The aerobic, water-assisted selective oxidation of methane over platinum-based catalysts

by

Sinqobile Vuyisile Lusanda Mahlaba

MSc in Chemistry, University of KwaZulu-Natal (2017)

BSc(Hons) in Chemistry, University of KwaZulu-Natal (2014)

BSc Applied Chemistry, University of KwaZulu-Natal (2013)

Thesis presented to the University of Cape Town in fulfilment of the requirements for the degree of

Dr of Philosophy in Chemical Engineering

Catalysis Institute, Department of Chemical Engineering

Faculty of Engineering and the Built Environment

University of Cape town

South Africa

August 2023

Declaration

I, **Sinqobile Vuyisile Lusanda Mahlaba**, certify that this submission is based on my original work, except for the inclusion of the contributions of others (who are duly acknowledged) and that neither the whole work nor any part has been, is being, or is to be submitted for another degree in this or any other university. I authorise the university to reproduce for the purpose of research either the whole or any portion of the contents in any manner whatsoever

Signature: Date: 05 August 2023

Ms. S.V.L. Mahlaba

Declaration for the inclusion of publications in thesis

I confirm that I have been granted permission by the University of Cape Town's Doctoral Degrees Board to include the following publication(s) in my PhD thesis, and where co-authorships are involved, my co-authors have agreed that I may include the publications:

1. **Mahlaba SVL,** Hytoolakhan Lal Mahomed N, Guo J, Govender A, Leteba GM, Cilliers PL, van Steen E "Platinum-catalysed selective aerobic oxidation of methane to formaldehyde in the presence of liquid water", *Angewandte Chemie International Edition*. 2022 Sept Vol. 62 No. 38, pe202206841.*
2. Van Steen E, Guo J, Hytoolakhan Lal Mahomed N, Leteba GM, **Mahlaba SVL** "Selective, aerobic oxidation of methane to formaldehyde over platinum-a review", *ChemCatChem*. 2023 April Vol. 15 No. 8 e202201238.*
3. **Mahlaba SVL**, Hytoolakhan Lal Mahomed N, Leteba GM, Govender A, van Steen E "Role of the support in the selective, aerobic methane oxidation to formaldehyde over Pt/TiO_2" (Submitted, in review)*

Signature: Signed by candidate Date: 05 August 2023

Student Name: Sinqobile Vuyisile Lusanda Mahlaba Student Number: MHLSIN018

Acknowledgements

I am deeply grateful to my supervisor Professor Eric van Steen for the enduring support, trust and confidence in my abilities to see the study to completion, and the opportunities he has given me to further my education. I would also like to thank my co-supervisor, Dr Alisa Govender from Sasol for her guidance and support, and her friendship throughout this journey.

The analytical lab at the university of Cape Town and the Materials Characterisation Group at Sasol are also acknowledged for providing access to instrumentation for characterisation of the catalysts reported in this thesis. A special thank you goes to A/Prof. Jaco Olivier for the extensive microscopy work for the alloys, and for his willingness to discuss the obtained data. Thank you to Dr Gerard Leteba for being a wonderful collaborator, a master nanoparticle synthesizer, and for his witticisms that made work enjoyable.

I would like to thank Junfeng Guo for reactor training when I initially arrived, and Nasseela for being a comrade in arms. I am grateful to Sandeeran, Yatesh, Tracey, Candace, Adli, Linathi, Nicholas and Thulani for their friendship, and members of the Reaction Engineering Group for being awesome colleagues. I also by extension like to thank everyone in the reactor lab for their support and assistance, particularly Portia Johnston, Chantal Le Roux, Rachel Cupido and Waldo Koorts of the technical team.

I am grateful to Sasol for funding my studies, and for providing me with a supportive network. Thank you to Dr Pheladi Mohlala, Dr Tanya Hughes, Dr Nishlan Govender and Dr Cathy Dwyer for their encouragement and faith in me. I would also like to thank Nkele Mokgothu and acknowledge the massive role she played in my move to Cape Town. The National Research foundation is also acknowledged for funding my studies, as well as the University of Cape Town Postgraduate Funding office and the Catalysis Society of South Africa (CATSA) for travel grants to attend conferences.

To my friends who have become family, Mandy, Khwezi, Maria, Betony, Sorrel, Jess and Hanna. Thank you for your support, understanding and encouragement. Thank you Sorrell and Jess for providing a home for me, for introducing me to rock climbing and weight training, for adventuring with me, and for feeding me. Thank you to Kareemah for being an awesome and dependable rock-climbing and belay partner. I would be remiss to not thank my furry friends; Izzy and Klanky (canines), Lu, Baby Cat and Ginny (felines) and Dougie (chicken) for keeping me company, and for insistent reminders to take a break. The long writing sessions were bearable because of their company.

I thank my siblings for being enduring pillars of support for all my endeavours.

To my siblings, for the three little mice

Synopsis

The direct, aerobic , selective oxidation of methane to liquid C_1-oxygenates presents an opportunity for the conversion of an abundantly available carbon source to value added products, without the need of additional, energetically intensive steps. This would also incentivise the conversion of bio methane from sustainable sources to value added products. The main issues encountered during the selective oxidation of methane to C_1-oxygenates are low productivities, and the difficulty in maintaining a high selectivity towards C_1-oxygenates such as methanol and formaldehyde at high methane conversions, which is referred to as the conversion/selectivity trade-off. Thus, the development of catalytic systems capable of attaining high methane conversion rates whilst maintaining high product selectivity is one of the remaining challenges in catalysis.

The objective of this PhD study is to investigate the selective oxidation of methane, using oxygen as an oxidant, over platinum-based catalysts at moderate temperature (220°C). The moderate temperature is chosen because at higher reaction temperatures, the conversion/selectivity trade-off becomes more pronounced, due to the more facile conversion of C_1-oxygenates to CO_2, the thermodynamically favoured product for methane oxidation. Low reaction temperatures on the other hand, result in high selectivity, albeit at a low productivity. Oxygen was chosen as an oxidant due to it being cheap, abundant and environmentally friendly.

The selective oxidation of methane in the presence of water was initially conducted in a gas-phase fixed bed reactor. Accidentally flooding the reactor resulted in the formation of selective oxidation products such as formaldehyde, methanol and 1,3,5-trioxane, hence a trickle-bed reactor was designed and commissioned. The oxidation of methane in the presence of liquid water was found to be selective towards the formation of formaldehyde when evaluated over 10 wt.% platinum supported on the rutile phase of titania. Increasing the amount of water in the feed enhanced the rate of methane consumption, whilst also enhancing the formaldehyde selectivity, achieving a maximum conversion of up to 1% with a formaldehyde selectivity of 90%. A similar observation was made over 10% Pt/Al_2O_3, which yielded a maximum methane conversion 0.5% with a formaldehyde selectivity of 65%.

Kinetic experiments over Pt/Al_2O_3 showed that the rate of methane conversion was zero order with respect to both the concentration of methane and that of oxygen. Thus, the reaction was

determined to be product desorption limited in accordance with DFT studies which indicated that the formation of a high stable di-σ hydroxy-methoxy species becomes likely under these conditions.

The unique role of the support was further demonstrated by performing the aerobic, selective oxidation of methane over platinum supported on carbon and P25. The carbon supported platinum (Pt/C) was the most active, achieving a conversion of up to 4% and a formaldehyde selectivity of 99%, whereas platinum supported on P25 yielded a reasonable activity but a different product slate (high selectivity towards the formation of CO_2 with some formation of methanal and methoxy methanol). The activity trend was in the order of Pt/Al_2O_3 (X_{CH_4} = 0.5%, TOF = 0.07 hr^{-1}, $S_{formaldehyde}$ = 65%) < Pt/TiO_2-P25 (X_{CH_4} = 0.6%, TOF = 0.10 hr^{-1}, $S_{methanol,\ methoxymethanol}$ = 10%) < Pt/TiO_2-Rutile (X_{CH_4} = 1%, TOF = 0.17 hr^{-1}, $S_{formaldehyde}$ = 90%) < Pt/C (X_{CH_4} = 4%, TOF = 0.41 hr^{-1}, $S_{formaldehyde}$ = 99%). Hydrophobic supports are more active, which is attributed to water preferential surrounding the metal particle, thereby facilitating product desorption. The selectivity is determined by the acid/base properties of the supports. Alumina and P25 also possessed the highest acid site density of the supported catalysts. Pt/P25 supported catalyst was mainly selective for the formation of methanol and methoxy methanol (although even this catalyst yielded initially some formaldehyde). The formation of methanol and methoxymethanol, albeit at low selectivity, was attributed to the secondary conversion of formaldehyde on the support acid/base sites. Furthermore, the adsorption of formaldehyde or methanediol (formaldehyde hydrate) on acid sites may result in further oxidation over P25.

The catalysts deactivate in the aerobic, selective oxidation of methane, Alumina transformed to boehmite under the strongly hydrothermal conditions applied in the reactor, induced by the presence of liquid water at 220°C. This caused the sintering of platinum due to the transformation of the support, and the resulting loss in the support surface area. Prolonged exposure of carbon to liquid water resulted in support gasification/oxidation, and again loss of platinum metal surface area. Platinum on titanium deactivated due to the formation of polyoxymethylene on the surface, which may have been formed on the acid sites present in the catalyst.

Platinum was alloyed with copper, silver and gold (yielding Pt_3M nanoparticles) using a surfactant based wet chemical synthesis route that involved the use of $Mo(CO)_6$ as a reducing

agent. The nanoalloys were synthesised in an effort to modify the binding strength of oxygen, and, by proxy, oxygenates on the catalyst surface. Pure platinum nanoparticles were synthesised as a reference material. The nanoparticles were deposited on the rutile phase of titania, since Pt/TiO_2-Rutile was the most productive and structurally stable catalyst. The alloys were however not stable at conditions required to remove the surfactants. Initial tests in the gas phase reactor yielded results in the following trend Pt_3Cu/TiO_2 (X_{CH_4} = 1.1%, TOF = 2.5 hr^{-1}, $S_{formaldehyde}$ = 66%) > Pt_3Au/TiO_2 (X_{CH_4} = 0.6%, TOF = 2.2 hr^{-1}, $S_{formaldehyde}$ = 65%) > Pt_3Ag/TiO_2 (X_{CH_4} = 0.3%, TOF = 0.5 hr^{-1}, $S_{formaldehyde}$ = 63%) = Pt/TiO_2 (X_{CH_4} = 0.3%, TOF = 2.2 hr^{-1}, $S_{formaldehyde}$ = 66%). The Pt_3Ag/TiO_2 and Pt_3Cu/TiO_2 catalysts were then tested in the trickle bed reactor, where the methane conversion and formaldehyde selectivity were enhanced further. The conversion of methane over Pt_3Cu/TiO_2 increased to 5% (TOF = 2.7 hr^{-1},) in the presence of liquid water ($S_{formaldehyde}$ = 78%) while a maximum methane conversion for 3% (TOF = 2.9 hr^{-1}) was obtained over Pt_3Ag/TiO_2 ($S_{formaldehyde}$ = 74%). The high, but constant TOF is attributed to the presence of molybdenum near the platinum site.

The high activity of platinum (possibly promoted) together with the favourable selectivity shows the potential of this route for the aerobic, selective oxidation of methane.

Table of Contents

List of Figures

List of Tables

List of Schemes

Glossary

Aerobic: Involving oxygen or air

Anaerobic: In the absence of oxygen or air

Eley-Rideal Mechanism: Mechanism where reactants are activated by adsorbed surface species rather than by bare metal active sites

Hydrophilic: Having a strong affinity for water

Hydrophobic: Having a poor affinity for water

Mars van Krevelen Mechanism: Activation of reactants by nucleophilic, lattice oxygen species

Methanediol: Hydrated form of formaldehyde

Methanotrophs: Bacteria that utilise methane as a source of energy

Product protection: conversion of methane to a form that is impervious to oxidation

Selective Oxidation Products: Products formed from the selective oxidation of methane such as methanol, formaldehyde, dimethyl ether, formic acid, etc.

Abbreviation/ nomenclature

ATR-IR	Attenuated total reflectance infrared spectroscopy
BET	Brunauer-Emmett-Teller
CO_2-TPD	Carbon dioxide temperature programmed desorption
DFT	Density functional theory
EDX	Energy dispersive X-ray spectroscopy
FBR	Fixed-bed reactor
FCC	Face centred cubic
FTR-IR	Fourier transform infrared spectroscopy
FID	Flame-ionisation detector
GC	Gas Chromatography
GHSV	Gas hourly space velocity
HRTEM	High-resolution transmission electron microscopy
ICP-OES	Inductively-couple plasma optical emission spectroscopy
IPA-TPD	Isopropylamine temperature programmed desorption
MFC	Mass flow controller
NADH	Nicotinamide adenine dinucleotide
NP	Nanoparticles
pMMO	Particulate methane monooxygenase
PXRD	Powder X-ray diffraction
sMMO	Soluble methane monooxygenase
TBR	Trickle bed reactor
TEM	Transmission electron microscopy
TOF	Turnover frequency
TPD	Temperature programmed desorption

Notations

d	Particle diameter, nm
D	Metal dispersion, %
p	Partial pressure, bar
P	Pressure, bar
-r	Rate of methane consumption, μmol/g/h
T	Temperature, K
S	Selectivity, %
$\mathbf{S_{sel.ox}}$	Selectivity to selective oxidation products
X	Conversion, %

Greek Notations

γ	Gamma, alumina phase
θ	Theta, Powder X-ray diffraction angle in °
μ	Micro, 10^{-6} of a unit

CHAPTER I: INTRODUCTION

1.1. CURRENT ENERGY LANDSCAPE: KEEPING TO OLD HABITS?

Hydrocarbons, in the form of crude oil, natural gas and coal (fossil fuels), form the bedrock of modern society; they are a source of carbon and hydrogen, which are used as cornerstones of energy-production [1-3]. Crude oil and coal have been heavily utilised to meet the demand for transportation fuels, chemicals and for electrical generation, while the use of, and demand for, natural gas has been increasing over the last two decades [4]. There has been, however, a paradigm shift in terms of meeting future energy needs, and the focus is now on moving away from fossil fuels to more sustainable fuel sources. This is mainly motivated by the harm to the environment caused by the combustion of fossil fuels for power generation and transportation, in addition to dwindling fossil fuel reserves. The development and use of solar-power, wind-energy and carbon-neutral fuel sources have been researched extensively, with minor gains having been made [5, 6]. The trends in energy consumption are presented in Figure 1.1. which shows that the fossil fuels (coal, natural gas and crude oil) still dominate. Although, there is a notable, albeit still minor increase in the usage of renewables in the form of solar and wind.

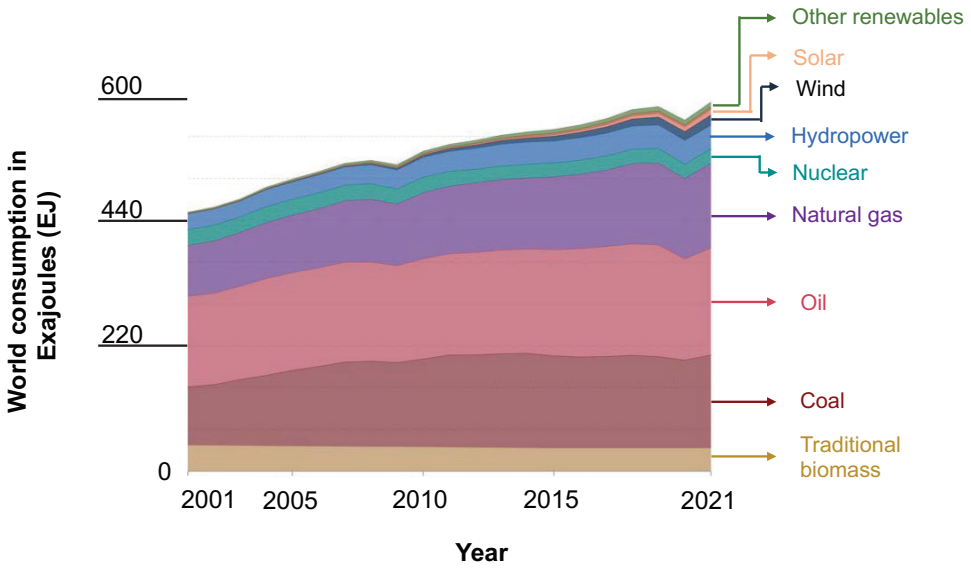

Figure 1.1: Trends in the global annual consumption of energy worldwide from 2001 to 2021, showing the emergence and increase in the usage of renewables, and a general increase in the usage of natural gas (downloaded from [7] and adapted from [4]).

The two main energy needs that fuel modern economies are power generation in the form of electricity, and fuels for transportation [8]. Current infrastructure favours the use of carbon-based fuels as energy vectors, with liquid fuels (with their high energy density) being especially important for transportation [6]. Hydrogen has been identified as a potential alternative fuel as it has a high specific energy (but a modest energy density), which would form the basis of a hydrogen economy. However, the main issue with hydrogen is the difficulty in storage and transportation [3], which poses difficulties in a seamless integration into existing energy infrastructure. A methanol-based economy has been proposed as an alternative [1, 3, 9], and entails the use of methanol and/or dimethyl-ether as energy carriers. Methanol is viewed as more viable than hydrogen due to its possible integration into existing infrastructure without needing major modifications [3], since it is a carbon-based liquid fuel. It is proposed that methanol could be obtained from the conversion of CO_2, with green hydrogen from water splitting. An alternative method for the production of methanol and other C_1-liquid oxygenates would be the direct conversion of methane to liquid products.

Methane, the main component of natural gas, is a readily available carbon source that can also be obtained via methane recovery technologies such as hydraulic fracturing [4, 10]. Methane is also emitted from municipal waste landfills, and can also be sustainably produced through the anaerobic digestion of biomass, particularly biowaste (a product referred to as biomethane) [11]. The increasing abundance of this cheap carbon resource, especially in the form of increasing accessible natural gas reserves, which is sometimes treated as a waste product, presents an opportunity for the development of technologies that can efficiently utilise methane. This is particularly relevant for Africa and South Africa, since most countries in the continent have agricultural-based economies and are experiencing an increase in the generation of municipal and agricultural waste [12]. Furthermore, Africa, being without significant oil refining capacity, stands to benefit from the generation of fuels, energy and chemicals from biomass [13].

1.2. METHANE AS A VALUABLE RESOURCE

Methane is mainly used as a fuel for heating, but it can also be used for the generation of chemicals. Industrially, methane, in the form of natural gas, is used indirectly as a feedstock for the generation of liquid fuels [14, 15]. Methane is first reformed to syngas (CO and H_2 mixture), which is then converted to liquid fuels and chemicals via the Fischer Tropsch process, or via the methanol synthesis process. The reforming of methane to syngas is a highly

energetically intensive process which becomes economical for large scale operations [16, 17], where methane is reformed in the presence of steam or CO_2 at high temperatures (~1000°C). Here, some of the natural gas is combusted to meet the energy demand of the process. Combustion of the feed also contributes to CO_2 emissions, which increases the carbon footprint of the methane reforming process [18]. It is hence desirable to directly convert methane to C_1-liquid oxygenates. Achieving the single-step conversion of methane to useful products such as methanol and formaldehyde would enable the production of high value chemicals from a relatively cheap feedstock in a single step, and, will provide a route for the efficient utilization of methane [15, 19]. The routes for the direct and indirect methane utilization are presented in Figure 1.2.The direct functionalisation of methane to methanol or formaldehyde could also enable the use of methane as a liquid organic hydrogen carrier. Formaldehyde and methanol could undergo dehydrogenation to obtain hydrogen, possibly over platinum or copper-based catalysts [20-22].

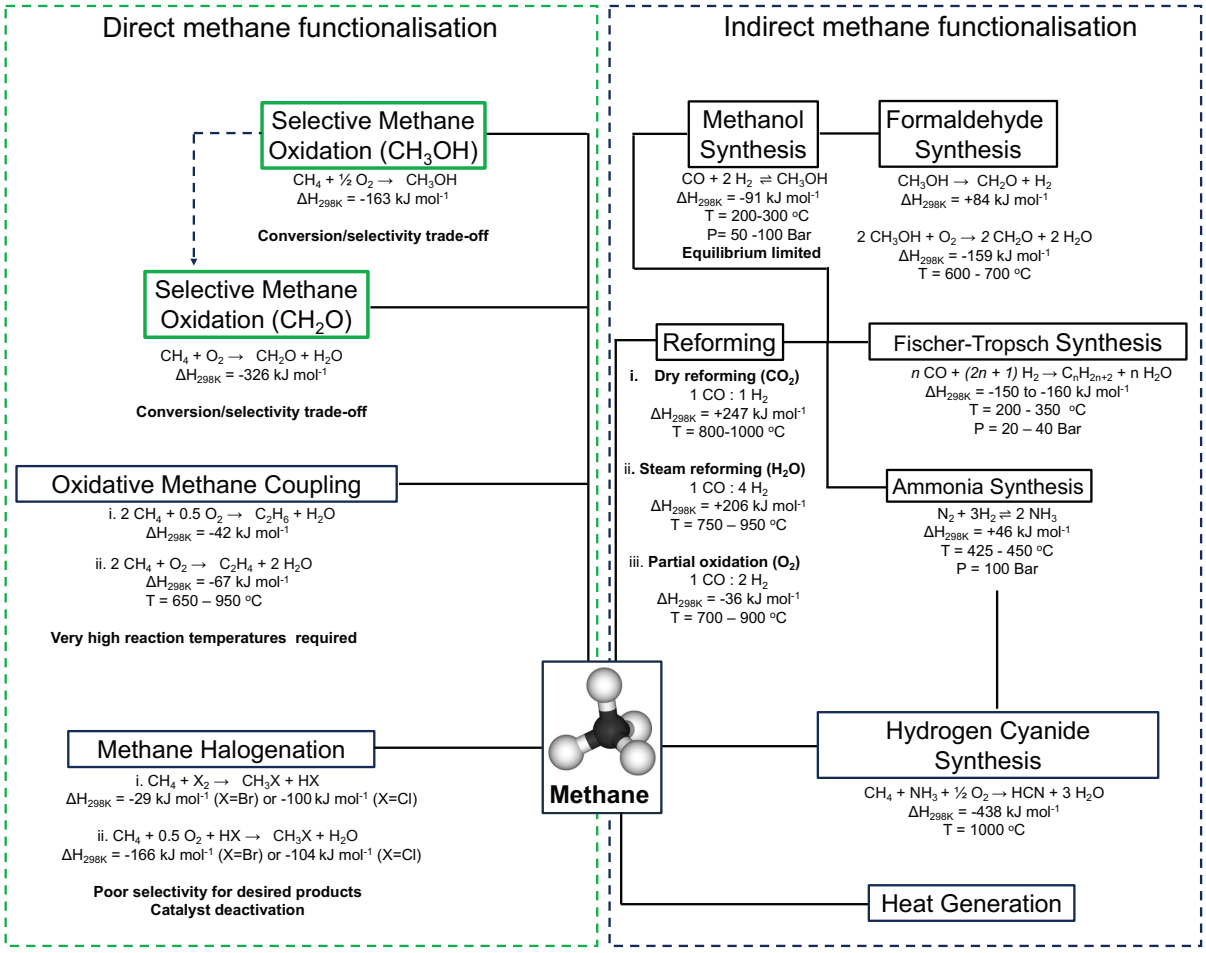

Figure 1.2: An outline of processes for the direct and indirect routes for methane functionalisation [14, 23, 24].

Methane is a highly symmetrical, non-polar molecule that is relatively inert, especially compared to long-chain hydrocarbons [25]. The activation of methane is, however, possible through the use of enzymatic, thermal or catalytic processes. The major issue encountered during the activation of methane, and attempts at methane functionalisation to C_1-oxygenates, stems from the difficulty in preventing the consecutive oxidation of the desirable product, viz. methanol and/or formaldehyde [26]. It has been widely reported that the selective oxidation of methane to oxygenates such as methanol and formaldehyde suffers from a conversion/selectivity conundrum, wherein the oxygenate selectivity decreases with increasing conversion, due to the facile conversion of the formed oxygenates to CO_2 [23, 27-29]. Hence, the selective oxidation of methane through selectively activating the H_3C-H bond has been referred to as the holy grail of chemistry.

1.3. THESIS AIM

This thesis aims to contribute to the search for a methane functionalisation process by documenting an experimental study in the development of metallic, platinum-based catalysts for the selective oxidation of methane to C_1-oxygenates, using oxygen as the oxidant, and water as a co-reactant.

1.4. THESIS OUTLINE

Chapter II presents a review of the existing literature on the various strategies explored for the selective oxidation of methane to C_1-oxygenates and presents the basis for the study presented in this thesis, **Chapter III** details the development of the strategies for the investigation of the selective oxidation of methane to C_1-oxygenates, encompassing the catalyst design, development of the experimental protocols and the product analyses which forms part of the catalyst evaluation. **Chapter IV** is a discussion on the in-depth study of the activity of platinum-based catalysts for the selective oxidation of methane in the presence of liquid water, while **Chapter V** details the investigation of the support effects on the selective oxidation of methane in the presence of liquid water. **Chapter VI** is an investigation of the effects of modifying the d-band of the catalytically active platinum via alloying on the rate of methane conversion and product selectivity. **Chapter VII** is the overall discussion that serves as a comparison of the different catalytic systems investigated, and **Chapter VIII** presents the conclusions and recommendations for the further improvement of this work.

CHAPTER II: LITERATURE REVIEW

THE SELECTIVE OXIDATION OF METHANE TO C_1-OXYGENATES

2. BACKGROUND AND INTRODUCTION

The first report on the selective oxidation of methane over a ferrous sulfate catalyst in the presence of hydrogen peroxide was made in 1930 [15]. The oxidation products formed were methanol, formaldehyde and formic acid. More systematic studies followed, particularly those reported by Boomer and Thomas [30-32], Newitt and Haffner [33] and Bone [34]. Despite over a century of research in the direct oxidation of methane to oxygenates [35], a commercial process is yet to be identified. Although a number of approaches have been investigated, none have met the activity and selectivity standards required for commercialisation, which specify a minimum single pass methane conversion of 5% and methanol selectivity of 80%, while a minimum selectivity of 50% is required for the formation of formaldehyde or acetic acid [36-38].

The challenge in the selective oxidation of methane stems from its chemistry. Methane is highly stable, symmetrical, non-polarisable and impervious to nucleophilic or electrophilic attack, with a C-H bond dissociation energy of 439 $kJ.mol^{-1}$ [39]. The C-H bond dissociation energies of the desired products, methanol or formaldehyde, are much lower with 402 $kJ.mol^{-1}$ and 369 $kJ.mol^{-1}$ respectively [39]. This means that, under conditions where methane is activated, the C-H bond in formed methanol and formaldehyde is more labile and would undergo further oxidation to CO_2 which is also the thermodynamically favoured product. This is particularly relevant for the high temperature gas phase activation of methane, since the initial cleavage of the methane C-H bond requires energy in the form of heat to speed up the reaction [40]. The relative potential energies of the product compounds in the conversion of methane to CO_2 is presented in Figure 2.1 [41, 42].

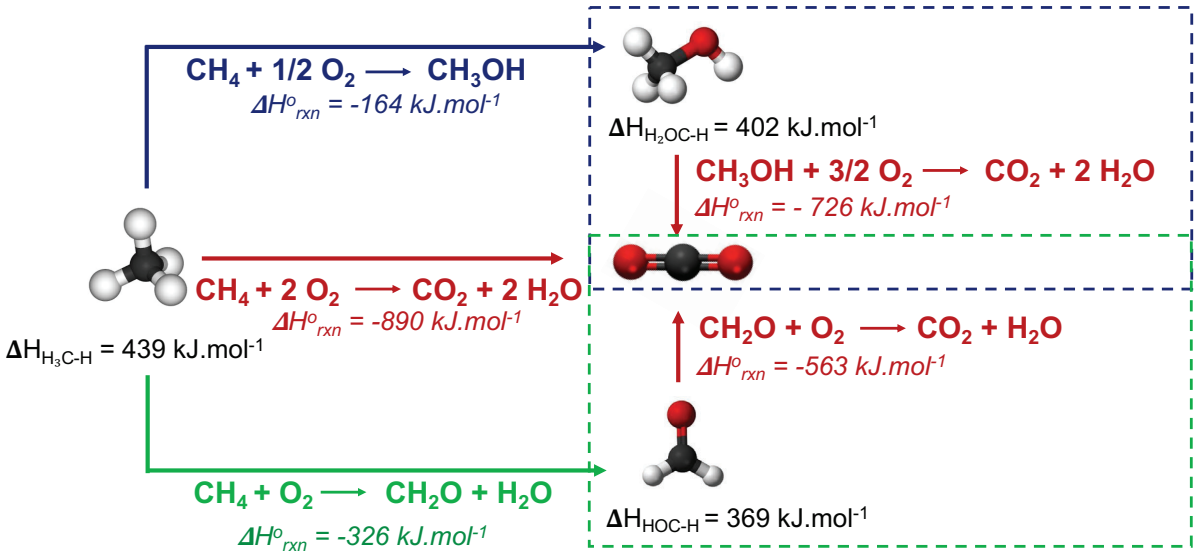

Figure 2.1: Schematic representation of the consecutive reaction of the formed oxygenates during the selective oxidation of methane, and the associated bond dissociation enthalpies of the C-H bonds of CH_4, CH_3OH and CH_2O [39].

The challenge in the selective oxidation of methane then lies in preventing the consecutive conversion of the formed oxygenates to CO_2. A number of approaches have been taken in solving this problem, ranging from tailoring reaction conditions, catalyst development and adopting product protection strategies [37, 43].

2.1 High temperature oxidation of methane

2.1.1. Homogeneous, gas phase oxidation of methane

Initial studies in the selective oxidation of methane were performed at high temperature in the presence or absence of a catalyst. In the absence of a catalyst, the reaction proceeds via a radical pathway [44, 45]. Briefly, methane is fed into the reactor in the presence of oxygen in a temperature range of 300 to 500°C at pressures ranging from 15 to 50 bar. The oxygen concentration is varied from 1 to 10% in order to stay above the upper explosion limit, since oxygen and methane mixtures become explosive in a certain concentration range [46, 47], and to ensure that oxygen remains the limiting reagent to prevent the complete combustion of methane to CO_2 [48]. The selectivity towards methanol seems to be sensitive to the oxygen concentration, with higher oxygen concentrations resulting in a higher methane conversion, but a lower selectivity for the formation of methanol [35, 49, 50].

Increasing the reaction pressure was found to favour methanol selectivity in the homogeneous oxidation of methane, whilst the increase in temperature had the opposite effect [48, 51]. Promising results for the autocatalytic oxidation of methane to methanol have been reported by Gesser et al. [52], Feng et al. [53] and Zhang et al. [54] with methanol selectivity in the range of 80 % at a methane conversion of around 8% [51]. Reproducibility of these experiments has however proven to be challenging [51]. This was attributed to differences in reactor designs [48, 54]. In essence, the difficulty in reproducing results from the autocatalytic oxidation of methane to methanol stems from the reaction pathway using radicals, which is difficult to control [44, 55, 56].

2.1.2. HIGH TEMPERATURE OXIDATION OF METHANE: EFFECTS OF SOLID CATALYSTS

Initial, high temperature studies investigating the use of solid catalysts were reported by Boomer and Thomas [30, 31], which focused on silver and copper-based catalysts at temperatures ranging from 300 to 500°C and pressures of 140 to 230 bar. The use of a copper catalyst had a positive effect on the methanol yield [30, 31]. Over these systems, the activation of methane was reported to be facilitated by activated, adsorbed oxygen on the catalyst surface or nucleophilic, lattice oxygen (equations 2.1 and 2.2.) at low oxygen concentrations [31]. The effect of the catalyst becomes less clear at high oxygen concentrations, particularly at high pressures, since the radical mechanism is suspected to be dominant under these conditions [32].

$$CH_4 + O_s \rightarrow CH_3OH \qquad \text{Equation 2.1}$$

$$CH_4 + Cu_2O \rightarrow CH_3OH + 2Cu \qquad \text{Equation 2.2}$$

Other high-temperature catalytic studies shifted towards the investigation of oxide-based systems, such as vanadium [57-61], molybdenum [62-64], iron [65] copper oxides [66, 67], and phosphates [68]. These systems operate at lower pressures and tend to favour the formation of formaldehyde, particularly when using O_2 as the oxidant. The dehydrogenation of methane, and addition of oxygen have been identified as the key steps in the selective oxidation of methane over these catalytic systems. The activation of methane over an oxide forms a weakly-bound methyl species adjacent to a surface-bound oxygen on the oxide, which rapidly reacts with the surface to form a methoxide species, which constitutes the oxygen insertion step [37, 69]. The methoxide species then decomposes to form formaldehyde and CO_x [69, 70].

An analysis of historical data of the high temperature methane oxidation over metal oxide catalysts yielding formaldehyde [66] showed that support contributions can mask the role of

the metal oxide in this selective oxidation of methane. The effect of the support was then minimised by using the least active support towards methane, which was determined to be β-silicon carbide. The selectivity for the formation of formaldehyde was ultimately correlated with a reduced electro-negativity of the transition metal involved, with increasing electronegativity favouring formaldehyde selectivity, implying the role of electron transfer in the reaction which was proposed to play a role during the activation of methane by H-abstraction [66, 71].

Mechanistic studies of the selective oxidation of methane over silica-supported MoO_3 catalysts showed the reaction to proceed via a Mars-van Krevelen mechanism, wherein methane is activated by lattice oxygen from MoO_3, which is replenished by oxygen from the gas phase [72]. At lower conversions and temperatures, the catalyst achieved a methane conversion of 0.1%, and a formaldehyde selectivity of 63%. Increasing the reaction temperature (from 550 to 630°C) led to an increase in the methane conversion (from 0.1 to 5.0%), but a decline in the formaldehyde selectivity (from 63 to 12.5%) [72]. The MoO_3 catalyst is sensitive to changes in the oxygen concentrations. Lower oxygen concentrations result in the reduction of MoO_3 to MoO_2, which reduces the formation of formaldehyde, thus reducing the selectivity of the process [73]. The speciation of molybdenum on the support, dictated by the molybdenum loading, also affects the catalytic activity. High activity is obtained at low molybdenum loadings, which is attributed to the presence of a highly-active, highly-dispersed mononuclear molybdate species [72].

Silica-supported vanadium oxide catalysts (V_2O_5) are capable of operating at lower reaction temperatures (460 to 500°C) in the selective oxidation of methane compared to MoO_3 systems, and are selective for the formation of both methanol and formaldehyde [74, 75]. V_2O_5 requires activation with N_2O for sufficient methane conversion [75] in contrast to molybdenum-based catalysts. Highly-dispersed monomeric VO_x species have been identified as the most active and selective for the selective oxidation of methane to formaldehyde and methanol [57, 75]. Phosphates and pyrophosphates have shown some promise for the selective oxidation of methane yielding formaldehyde [67, 68, 76, 77]. It has been proposed that methane over metal phosphates is activated by the redox-active Lewis acidic iron sites transferring the hydrogen to the weakly-basic surface phosphate groups [68].

The performance results of the various oxide and phosphate-based catalyst are compared with those of other systems in Table 2.1. The main issue with traditional metal-oxide based systems

is that high formaldehyde selectivities are obtained at low methane conversions; they are still affected by the conversion/selectivity trade-off (see Figure 2.2).

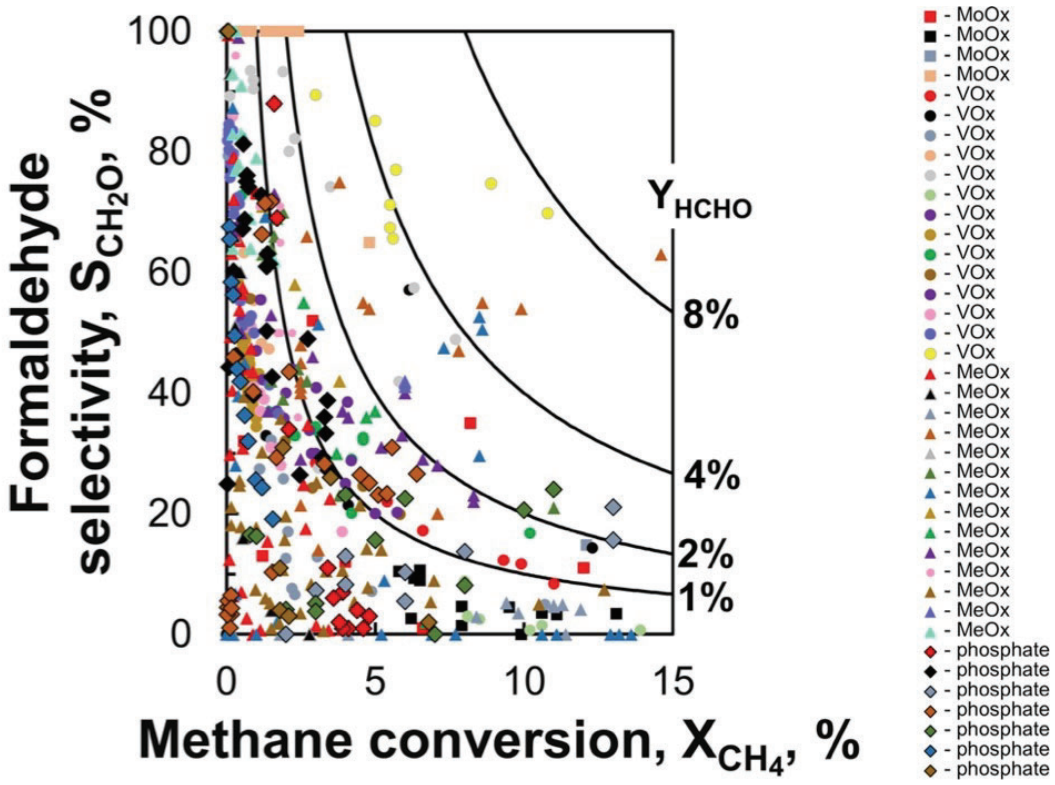

Figure 2.2: The conversion/selectivity relationship during the selective oxidation of methane to formaldehyde over molybdenum oxide, vanadium-oxide, metal-oxide and phosphate-based catalysts [78].

A B_2O_3-based system was recently reported for the selective oxidation of methane to CO and formaldehyde, achieving a 46% selectivity towards formaldehyde at a methane conversion of 6%. Although this system performs marginally better than known oxide systems, the process is still mostly selective towards the formation of CO [79]. The oxygenate selectivity was not negatively affected by an increase in the O_2/CH_4 ratio. In fact, an increase in the oxygen partial pressure positively impacted the rate of reaction. The activation of methane was determined through kinetic measurements and isotopic labelling experiments to occur via an Eley-Rideal mechanism [79]. The catalyst loading was 20 wt.% of B_2O_3 yielding multiple layers of boron oxide on the support, which is claimed to nullify any effects of the support identity on the catalytic performance. The reaction mechanism is presented in Figure 2.3. The activation of methane is thought to occur via an Eley-Rideal mechanism yielding a surface methoxy species, which undergoes H-abstraction by an adjacent hydroxyl group to yield formaldehyde.

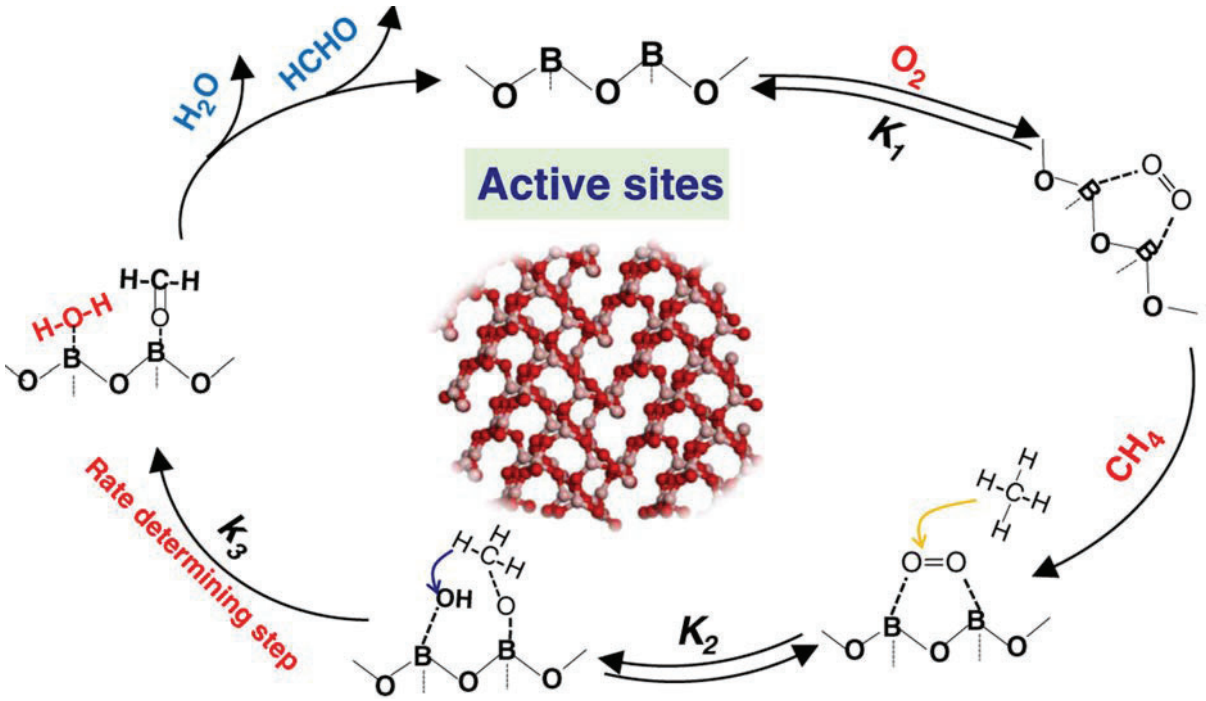

Figure 2.3: The reaction mechanism for the activation of methane to formaldehyde over the B_2O_3-based catalyst. Reproduced with permission from [79], © Springer Nature 2020.

2.2. Low-temperature Activation of Methane to Methanol

2.2.1 Enzymes and their Analogues

The selective oxidation of methane to methanol occurs readily in nature and is facilitated by methanotrophic bacteria, which utilize methane as a carbon and energy source. The formed methanol is an intermediate in the methanotroph metabolic pathway, and can be further converted to formaldehyde, formic acid, and ultimately, carbon dioxide (see Scheme 2.1) [80, 81]. The selective oxidation of methane to methanol (ΔG_{rxv} = -454 kJ.mol^{-1}) [82, 83] is catalysed by methane mono-oxygenase (MMO) which utilize oxygen as an oxidant and nicotinamide adenine dinucleotide (NADH) as a co-oxidant, according to equation 2.3 and 2.4 [84]. Two forms of MMO have been identified. One form is water soluble and contains a di-iron active centre (soluble methane monooxygenase, s-MMO) [85-87], while the other is membrane bound and possibly possesses a di-nuclear copper active centre (particulate methane monooxygenase, p-MMO) [88, 89].

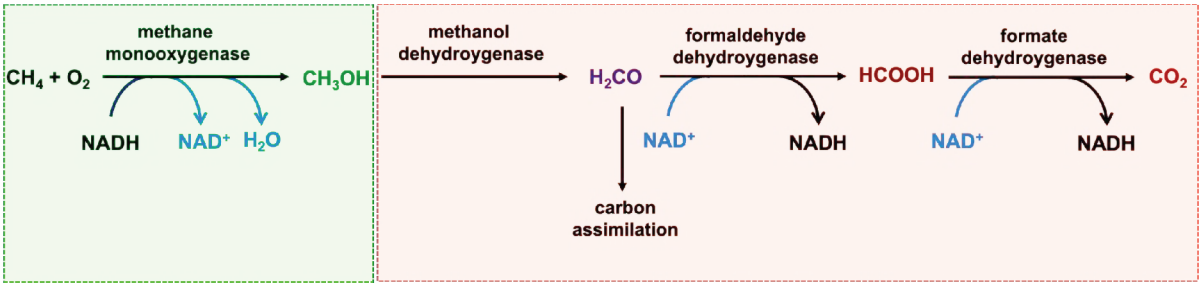

Scheme 2.1: Metabolic pathway for the oxidation of methane in methanotrophic bacteria adapted from [86].

$$2\ NADH \rightarrow 2\ NAD^{+} + 2\ H^{+} + 4\ e^{-} \qquad \text{Equation 2.3}$$

$$CH_4 + O_2 + 2\ e^{-} + 2\ H^{+} \xrightarrow{\textbf{MMO}} CH_3OH + H_2O \qquad \text{Equation 2.4}$$

Although p-MMO is the superior catalyst, it has not been studied as much as s-MMO due to loss of stability upon purification and difficulty in isolation [81, 90]. To that effect, most of the understanding of this biological process is obtained from s-MMO studies. The s-MMO protein comprises of three components, namely the hydroxylase, which is the active site containing a di-iron cluster (MMOH), the Fe_2S_2 cluster-containing reductase (MMOR) which facilitates electron transfer [91], and the regulatory protein (MMOB) which facilitates the access of the substrate to the active site [92]. The oxidation of methane by s-MMO is initiated by the activation of the di-iron μ-oxo centre, located within the hydroxylase unit, by O_2. This oxidises the di-iron (II) species, generating a di-iron (III) H_{peroxo} intermediate, which is referred to as the intermediate **P**. The intermediate evolves to form a di-iron (IV) species (commonly referred to as **Q**), which activates methane (see Figure 2.4) [93-95].

Methane is then introduced to the active site, where it undergoes hydroxylation to form an adsorbed methanol intermediate [81, 86]. Methanol is immediately eliminated after its formation, generating di-iron (III) species that are reduced by NADH associated with the reductase subunit, generating the Fe (II) di-iron cluster [94, 96].

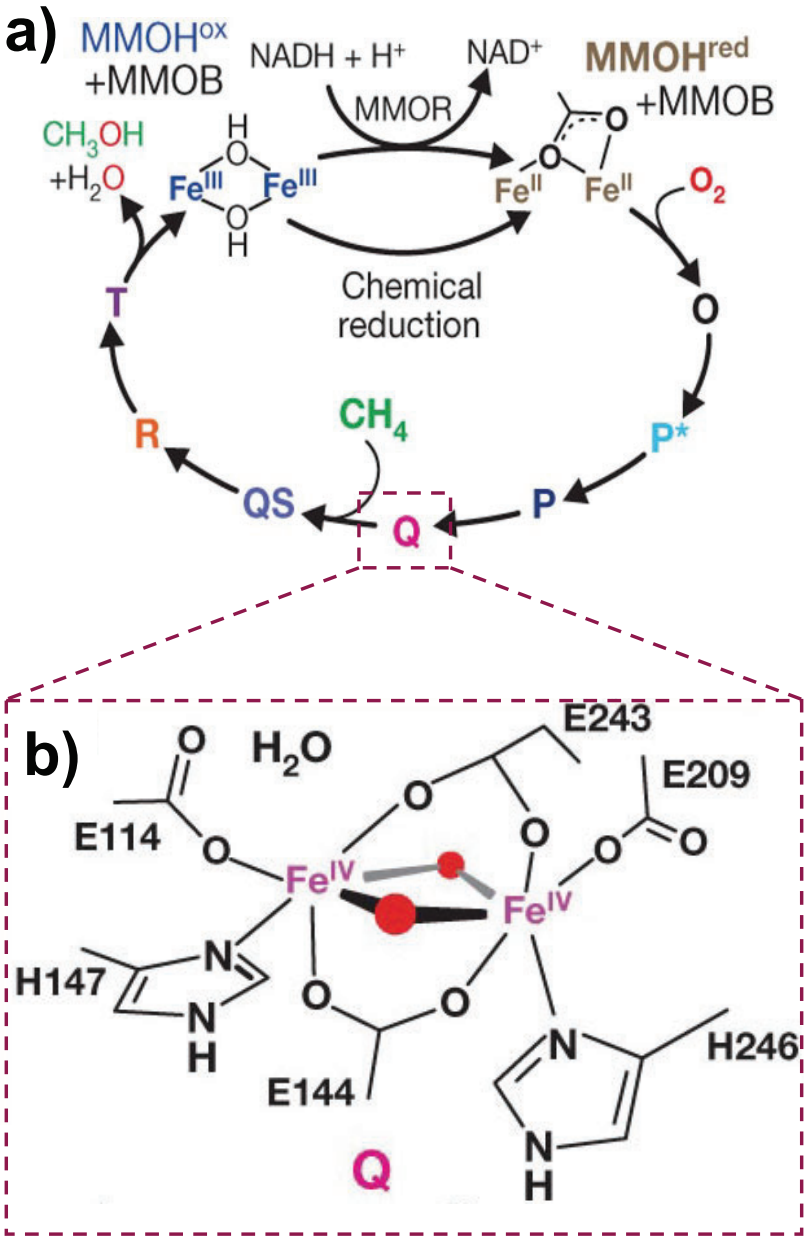

Figure 2.4: a) Catalytic cycle showing the activation of the di-iron MMO site with O_2, to form reactive intermediates and the activation of methane to methanol and b) the structure of Q, the di-iron (IV) reactive species. Reproduced with permission from [93], © 2014 Springer Nature.

The high efficiency displayed by MMO for methanol production is attributed to a) induction of a reactive oxidative reductive environment through the generation of highly reactive, high-spin metal species, b) a "gating mechanism" that imposes strict control of reactant access to the active site whilst also ensuring the transport of methanol away from the active site, and c) a carefully controlled and precisely timed electron transfer between MMOR and MMOH after

the formation of methanol has terminated, regenerating the active site [91, 97-99]. Access to the di-iron active site of MMOH is via either a hydrophilic pore that is involved in proton transfer, or a hydrophobic cavity [100, 101].

The enzymatic oxidation of methane to methanol is governed by the principle of site isolation and site control, whereby access of reactants to active sites is heavily restricted resulting in a highly selective process (i.e. S_{CH_3OH} = 100%, see Table 2.1) [102]. Although MMOs are efficient catalysts for methane oxidation under mild conditions, significant barriers to large scale implementation exist, such as low productivities, limited working temperature ranges, stability issues, poisoning of the enzymes by methanol (which limits their productivity) and high costs associated with expressing and purifying the proteins [81, 84, 103-105]. It is also important to remember that after synthesis, methanol undergoes further metabolic processes where it is ultimately converted to CO_2 as part of the respiration process of methanotrophs. Hence, to prevent this process, inhibitors will need to be applied, which adds further to the complexity of this process [106, 107]. Even so, the study of these enzymatic systems has lent insight that has informed the design of biomimetic catalyst systems [56, 81, 108].

2.2.1.1. BIO-INSPIRED ORGANOMETALLIC COMPLEXES

An example of a pMMO synthetic analogue is the tri-copper complex $[Cu^{I}\ Cu^{I}\ Cu^{I}$(**7-N-Etppz**)$]^{1+}$, which was found to be active for the selective oxidation of methane to methanol in acetonitrile at room temperature. The catalyst was activated by O_2 to form the highly reactive $[Cu^{II}\ Cu^{II}\ (\mu\text{-}O)_2Cu^{III}$(**7-N-Etppz**)$]^{1+}$ intermediate that is capable of activating methane. The reaction of methane with the oxidised active centre yields methanol, and reduces the complex to form a $[Cu^{I}\ Cu^{II}\ (\mu\text{-}O)_2Cu^{II}$ (**7-N-Etppz**)$]^{1+}$ species that requires reduction by hydrogen peroxide to reform the $[Cu^{I}\ Cu^{I}\ Cu^{I}$(**7-N-Etppz**)$]^{1+}$ complex (see Figure 2.5).

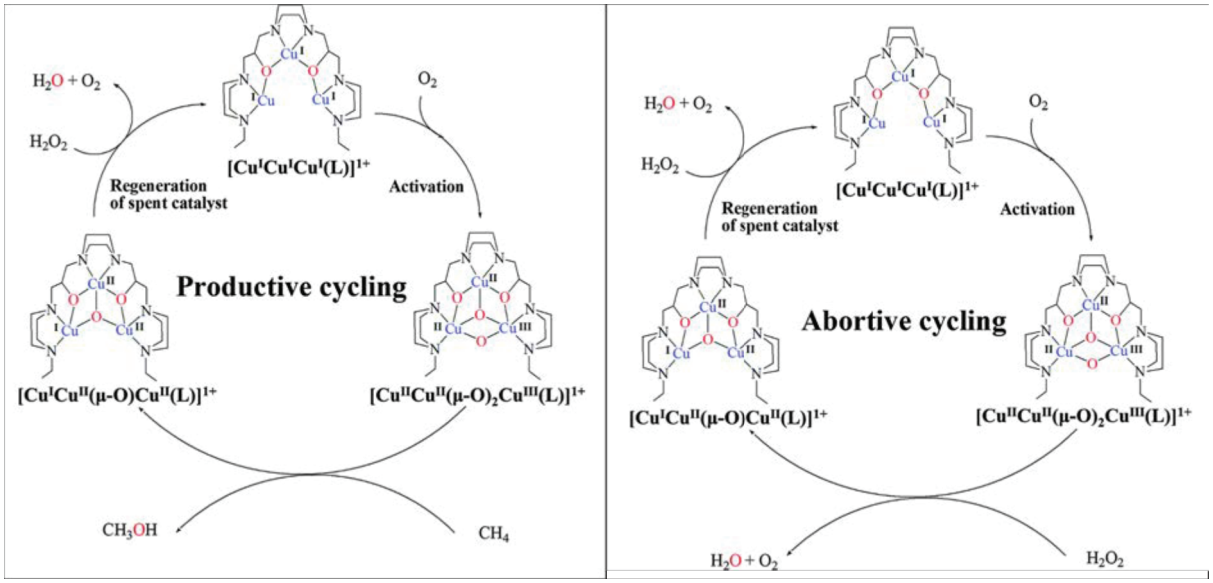

Figure 2.5: Catalytic cycle for the activation of the tri-copper complex, methane oxidation and site regeneration by H_2O_2 and the abortive cycle which occurs when CH_4 does not interact with the complex. H_2O_2 is then used to complete the abortive cycle [109].

The tri-copper complex possesses a hydrophobic alkane binding cleft at the base of the complex, which is selective to small, linear alkanes [110, 111]. Essentially, the architecture of this complex takes inspiration from methane monooxygenase, and is an attempt at designing a catalyst that works according to the principles of site-isolation in order to ensure controlled activation and functionalisation of methane. The catalyst is reported to be completely selective for the formation of methanol [109]. A turnover frequency of 0.05 s^{-1} (at a conversion of 0.1%) was obtained when H_2O_2 was used as an oxidant [112]. Immobilizing the complex on to mesoporous silica nanoparticles modified with alumina yielded a turnover frequency of 0.01 s^{-1} and a total conversion of 17.4% (over a period of three and a half hours) [110]. The catalysts progressively lost activity when subsequent reaction cycles were conducted, with an estimated 10% loss in activity per cycle. This was attributed to loss of the tri-copper complex, either through dissociation of the complex from the nanoparticles or decomposition of the complex [110].

Di-iron based s-MMO inspired synthetic analogues have proven to be challenging, due to the difficulty in generating stable, high valent bis (μ-oxo) diiron (IV) species which are active for methane activation [98, 113-115]. An alternative strategy that seems to have worked is the

design of nitrogen-bridged diiron phthalocyanine and porphyrin complexes, which have been found to be capable of stabilising high valent Fe(IV) oxo-species [116].

A nitrogen-bridged μ-nitrido iron tetra-*tert*-butylphthalocyanine complex ($[FePc(^tBu)_4]_2N$) containing two equivalent iron centres was found to be active for the selective oxidation of methane to formic acid and formaldehyde at low temperatures. The complex forms a $Fe^{IV}NFe^{III}OOH$ species upon activation with hydrogen peroxide, and converts methane at a turnover frequency of 0.001 s^{-1} [117]. Adding dilute sulfuric acid to the complex yields a strongly oxidising Fe^{IV}-N-Fe^{V}=O species which significantly improves activity, increasing the turnover frequency to 0.008 s^{-1} [113].

Biomimetic complexes also achieve low productivities despite excellent selectivity (especially displayed by the tri-copper complex). In addition, they require reactivation (with H_2O_2/H_2SO_4) to complete the catalytic cycle [98, 113] and are prone to decomposition [81, 113].

2.2.1.2. Fe and Cu Exchanged zeolites

Iron and copper containing zeolites have also been studied as solid analogues of sMMO (Fe) and pMMO (Cu). The zeolite-based systems are activated with nitrous oxide [118], hydrogen peroxide [119-121] or oxygen [122] to yield electrophilic metal-oxygen species capable of activating strong C-H bonds [97, 123]. Fe-based zeolites are unreactive towards O_2 and are instead activated by N_2O at 200-250°C to form reactive surface oxygen species, referred to as α-O sites [124-127]. The Fe(II) α-site is a mononuclear, extra-framework, high-spin square planar complex that is coordinated to anionic Al-O-Si ligands [126, 128]. The α-Fe(II) species undergoes activation to an α-O, a mononuclear high-spin Fe(IV)=O species that is highly active for the activation of the methane C-H bond [129-131]. The activation of methane occurs via hydrogen abstraction, yielding a Fe(III)-OH intermediate and methyl radical. The OH group then rotates away, followed by reaction with the methyl radical, forming the C-O bond which yields adsorbed methanol [132, 133]. Figure 2.6 shows the mechanism for the activation of methane over a α-O site. The oxygen is attached to the Fe(IV) species.

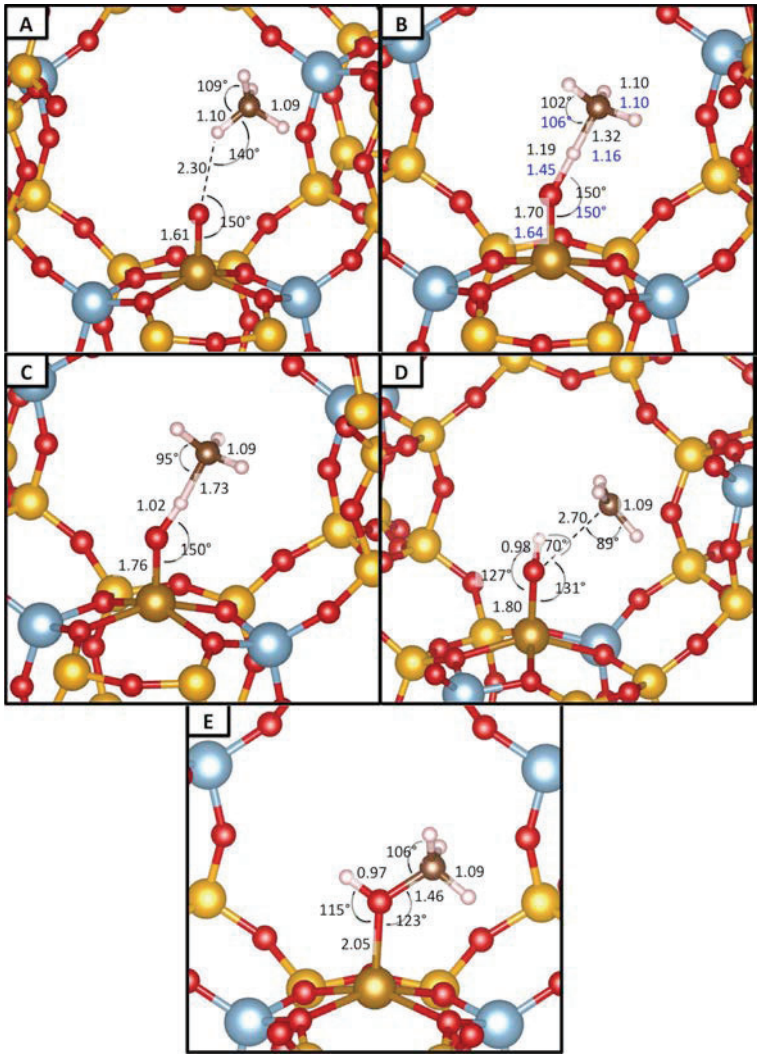

Figure 2.6: Activation of methane over the Fe(IV)=O site, with a) showing the coordination of methane to the Fe(VI)=O site, followed b) by hydrogen bonding to the Fe(IV)=O site, c) oxygen abstraction to form the Fe(III)-OH intermediate and methyl radical, d) rotation of the OH group and e) formation of the adsorbed methanol. Adapted with permission from [132], © 2016, the American Chemical Society.

The oxidation of methane over Fe exchanged zeolites follows a cyclical process [134-136], that is initiated by the pre-treatment of the zeolite at 800-900°C (forming reduced species via auto reduction that are inert to oxidation by O_2) [131, 136, 137], followed by activation with N_2O at 200-250°C. The zeolite is cooled to room temperature, upon which methane is introduced at room temperature. Methanol is extracted by hydrolysis with water [127] at 250°C [131, 138]. Thus, additional reagent needs to be introduced to facilitate product desorption at the end of

the reaction cycle. Furthermore, the entire process does not take place under similar conditions (i.e. cycling between different temperatures).

Parfenov et al. [118] attempted to close the catalytic cycle by conducting a series of experiments at temperatures above 200°C, where CH_4, N_2O and H_2O were introduced simultaneously over Fe-ZSM-5. Although desorption of the gas phase product was achieved without a separate hydrolysis step, the selectivity towards oxygenates decreased through coke formation, especially at high CH_4 conversions. The introduction of water was necessary to suppress coke formation. Better methanol yields were obtained at low conversions (conversion below 1 %) [118].

The selective oxidation of methane using N_2O as an oxidant over Fe-ZSM-5, Fe-Beta and Fe-FER catalysts in a fixed bed reactor resulted in the formation of dimethyl ether, formaldehyde, methanol (Fe-FER, $X_{CH_4} = 2.8$, $S_{Sel.\ Ox.} = 59\%$) and ethylene (Fe-ZSM-5, $X_{CH_4} = 2.2$, $S_{Sel.\ Ox.} = 40\%$) at a reaction temperature of 350°C in the absence of water [139]. The other catalysts were chiefly selective towards the formation of CO and CO_2 (see Table 2.1). The formation of ethylene over Fe-ZMS-5 was attributed to the conversion of methanol to dimethyl ether, followed by further conversion to ethylene. Although the reaction over Fe-based zeolites becomes catalytic above 200°C, this is achieved at the expense of oxygenate selectivity [118].

Hutchings addressed the problem of high temperature activation and product extraction by developing a process that occurs in an aqueous phase using H_2O_2 as the oxidant [119, 140]. This process is however not very selective to methanol, rather favouring the formation of methyl hydroperoxide (CH_3OOH), which subsequently decomposes into methanol [120, 140-144]. The active site of these zeolites is reported to be a dinuclear iron species that is activated to form a di-ferric active site with a ferryl (Fe(IV)=O) and an iron-hydroperoxy (Fe-OOH) site [56, 140]. The ferryl site serves to cleave the methane C-H bond, forming a methyl radical that reacts with the iron-hydroperoxy site to form the adsorbed methylhydroperoxyl, which desorbs in the presence of hydrogen peroxide. The hydrogen peroxide and N_2O routes are contrasted in Scheme 2.2 [140]. Replacing the oxidant with H_2O_2 results in overall higher productivities whilst keeping the selectivity towards the targeted product methanol high [145].

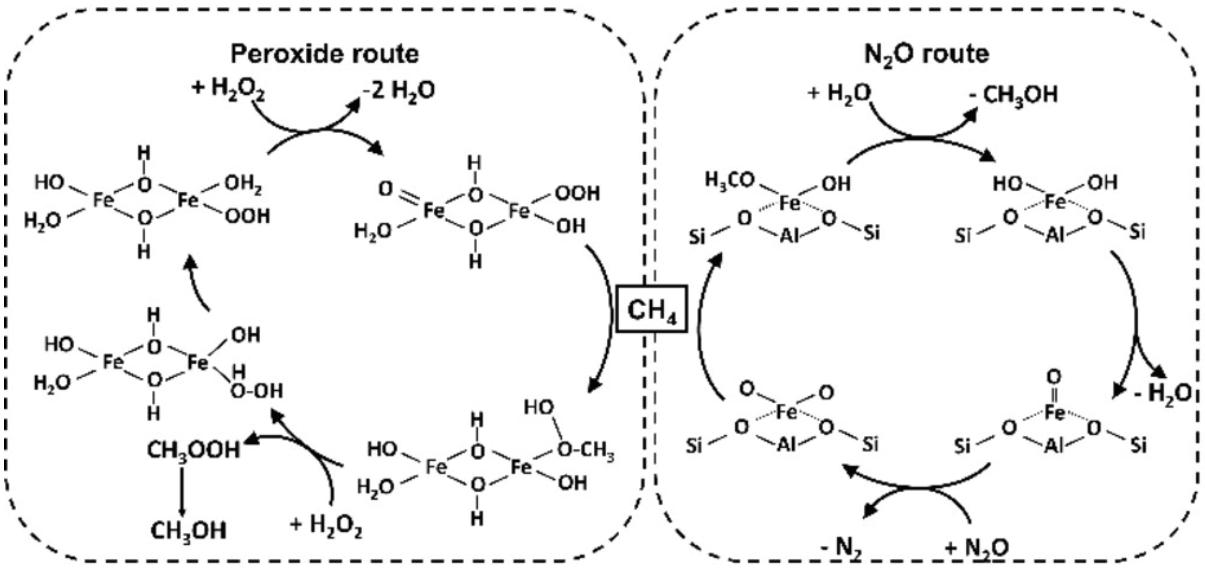

Scheme 2.2: Reaction mechanism for the catalytic, selective oxidation of methane over Fe-zeolites using hydrogen peroxide and N_2O as oxidants [37, 140].

The selective oxidation of methane over Cu-exchanged zeolites has received significant attention, particularly because the activation of Cu-based zeolites with oxygen can occur at lower temperatures (i.e. 300–650°C) compared to Fe-based zeolites (which require temperatures of up to 900°C) [146]. Dinuclear [147-149] and trinuclear [147, 150] copper active sites have been proposed, with a dinuclear Cu_2O_x site being identified as a more likely active site [148, 151-155]. Hence the mechanistic discussion is focused on the dinuclear copper active site. Activation of the copper active site with N_2O or oxygen forms a $[Cu_2O]^{2+}$ active site that is formed from two copper-ions bridged with an oxygen.

After activation, methane reacts with the catalyst at lower temperatures (125–200°C) [156]. Methane is activated on the bridging oxygen, and this reaction could occur via a radical or non-radical pathway. The radical pathway involves the formation of a methane radical that rebounds to the oxygen atom, while the non-radical pathway involves the migration of the cleaved methyl fragment to one of the copper atoms and subsequent recombination with the oxygen to form an adsorbed methanol intermediate. The removal of methanol is facilitated by water, which displaces the adsorbed methanol. The Cu sites require re-activation by cycling back to the activation temperature in order to remove the water from the active site. The reaction mechanism is presented in Scheme 2.3 [157]. The required high temperature for the activation of Cu based zeolites by O_2 results in a rather energy intensive process. Alternatively,

$[Cu_2(O)_2]^{2+}$ species may be generated at low temperatures in the presence of N_2O [147, 148], however, this still requires dehydration of Cu-ZSM-5 at 450°C in the presence of helium.

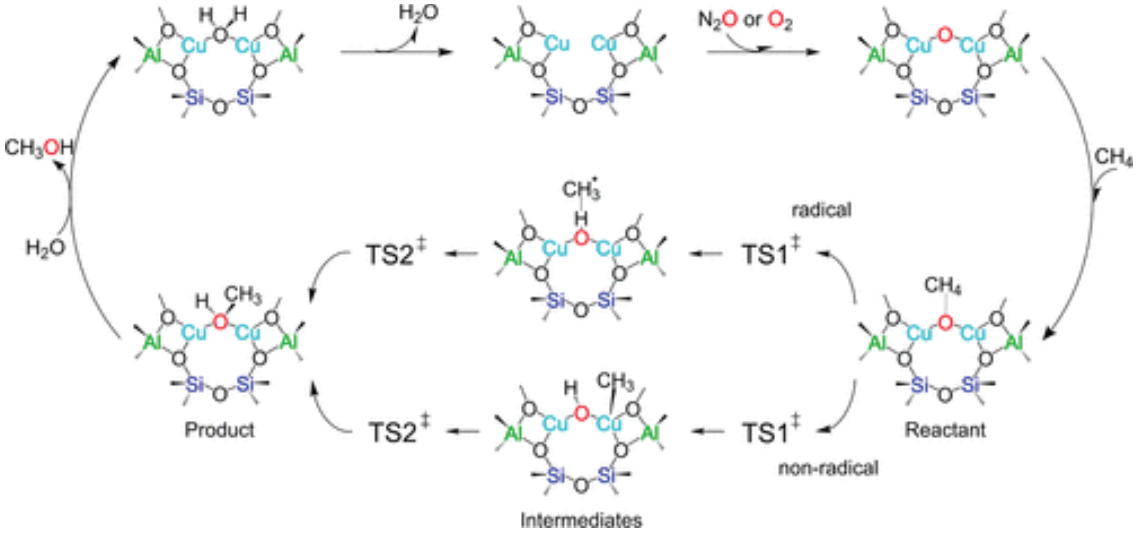

Scheme 2.3: Mechanism for the activation of the dinuclear Cu site to form the active $[Cu_2O]^{2+}$ species, and the subsequent oxidation of methane to methanol. Reproduced with permission from [157]. © 2018, the American Chemical Society.

Isothermal processes operating at low temperature have been investigated as alternatives to the tedious temperature cycling process [158-160]. Tomkins reported an isothermal process for the selective oxidation of methane over a Cu-exchanged zeolite. The zeolite activation, methane oxidation and product extraction all occurred at 200°C [158], which avoided temperature cycling (but still required reactant cycling). The catalyst did not require regeneration at high temperature, and was able to maintain a constant methanol yield during different reaction cycles, which indicated the stability of the catalyst. The same group reported the oxidation of methane over Cu-MOR using water as an oxidant. The process was cyclical, the results reported indicate the ability of using water as an oxidant, although the active site activation was still performed at 400°C [161].

An interesting study by the Romàn-Leshkov group investigated the stoichiometric and catalytic oxidation of methane over Cu-ZSM-5. The zeolite was first pre-treated at 550°C under flowing oxygen. The stoichiometric experiment involved first purging the zeolite with helium, followed by cooling and the subsequent introduction of methane for half an hour at 210°C. Thereafter, the methanol desorption was facilitated by the introduction of a $H_2O/O_2/CH_4$ mixture, which was sustained until all the methanol formed under the stoichiometric regime had desorbed, thereby entering a catalytic regime which showed sustained methanol production, albeit at

lower rates [162]. The changes in methanol productivity as the regime shifts from stoichiometric to catalytic are presented in Figure 2.7.

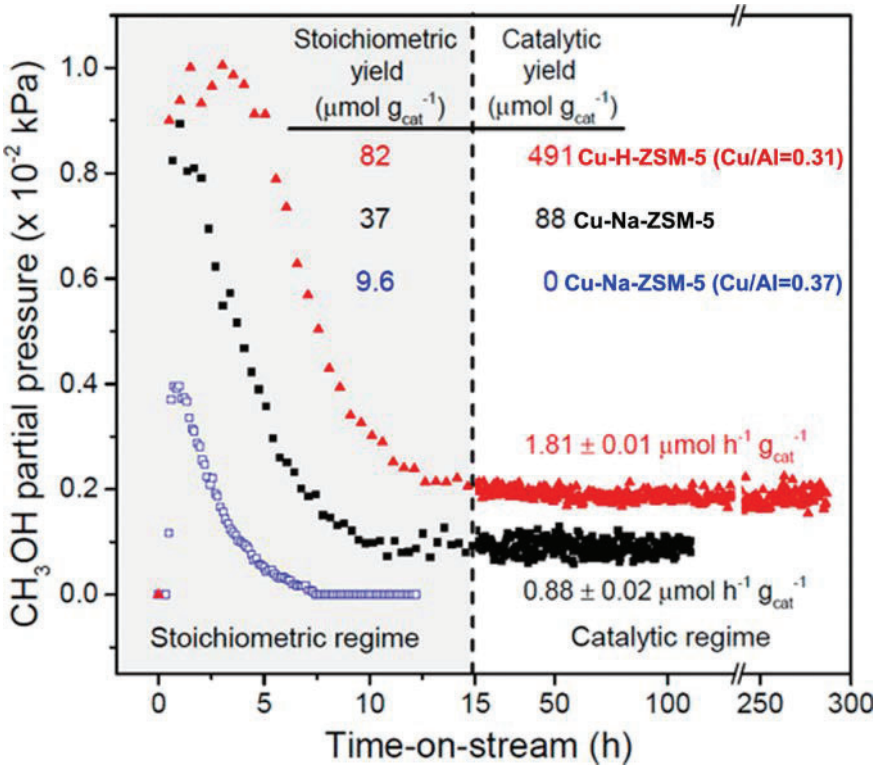

Figure 2.7: Changes in methanol productivity over Cu-ZSM-5. The stoichiometric section shows the desorption of the stoichiometrically-formed methanol, while the catalytic regime shows the catalytically-formed methanol after the complete desorption of the stoichiometric methanol. Reproduced with permission from [162]. © 2016, the American Chemical Society.

The major drawbacks to the application of zeolite-based catalysts are **a)** the need for expensive reagents such as N_2O and H_2O_2, or, when using oxygen as the oxidant **b)** incomplete catalytic cycles, and **c)** low methane conversion. Furthermore, the use of O_2 activated Cu zeolites as industrial catalysts is hindered by the requirement of cyclical temperature operation, which makes the process energy intensive. The process is also not fully catalytic and is rather stoichiometric, with catalytic regimes yielding low productivities (Table 2.1). The study of zeolites however highlighted not only the importance of site-isolation, but also brought to light the integral role water plays in the formation of selective oxidation products.

Table 2.1: Selected performance data on the selective oxidation of methane to C_1-oxygenates via different reaction strategies

	Catalyst	Oxidant	T, K	P, bar	$n_{CH4}/n_{oxidant}$	X_{CH4}, %	$S_{C1\text{-}oxygenate}$, %	Productivity[c-f]	TOF[a], hr^{-1}	Ref.
Autocatalytic	-	O_2	723	51	14	9.5	76 (CH_3OH)	900[c]	-	[52]
	-	O_2	673	30	39	3.1	47 (CH_3OH)	210[c]	-	[50]
	-	O_2	703	34	16	7	54 (CH_3OH)	87[c]	-	[163]
	-	O_2	723	51	10	13	63 (CH_3OH)	3490[c]	-	[54]
High temperature processes	$FePO_4/SiO_2$[b]	O_2	873	0.68	1	1.6	83 (HCHO)	3520[d]	-	[164]
	$FePO_4$	N_2O	673	1	1	2.6	85 (CH_3OH)	4064[d]	-	[77]
	Fe/SiO_2	O_2	873	1	19	0.47	60 (HCHO)	14500[d]	-	[165]
	$FePO_4$/SBA-15	O_2	773	1	2	0.56	81 (HCHO)	1230[d]	-	[166]
	$FePO_4$	O_2	723	1	7	0.11	66 (HCHO)	272[d]	-	[68]
	$FePO_4$	O_2	823	1	7	1.55	19 (HCHO)	1109[d]	-	[68]
	Cu-PO_x(50%)	O_2	873	1	1	1.9	31 (HCHO)	3201[d]	-	[167]
	Cu-PO_x(50%)	O_2	923	1	1	3.5	26 (HCHO)	4945[d]	-	[167]
	$MoCl_5$-R_4Sn/SiO_2	O_2	973	1	5	20	80 (HCHO)	4090[d]	-	[62]
	Cu-Fe-ZnO	O_2	973	1	5	0.8	14 (HCHO)	2530[d]	-	[168]
	Li-VPO	O_2	973	1	3.4	1.3	34 (HCHO)	650[d]	-	[169]
	MoO_3/SiO_2	O_2	863	1	7	0.7	72 (HCHO)	2520[d]	-	[63]
	MoO_3/β-SiC	O_2	923	1.5	3	1.7	36 (HCHO)	300[d]	-	[66]

[a] turnover frequency. [b] co-feeding water. [c] productivity in μmol/hr/cm^3 of reactor volume. [d] Productivity in μmol/hr/g of catalyst. [e] Productivity in μmol/hr/g dry cell. [f] Productivity in μmol/cycle/g catalyst.

Table 2.1 Continued…

	Catalyst	Oxidant	T, K	P, bar	$n_{CH4}/n_{oxidant}$	X_{CH4}, %	$S_{C1\text{-}oxygenate}$, %	Productivity[c-f]	TOF[a], hr^{-1}	Ref.
Enzymes and biomimetics	Methylosinus trichosporium OB3	O_2	303	1	1	-	100(CH_3OH)	51[e]	-	[170]
	([FePc(^{t}Bu)$_4$]$_2$N)	H_2O_2	333	32	-	-	31 (HCOOH)		28.8	
	[Cu_3(**7-N-Etppz**)]	O_2	298	1	10	17.4	100 (CH_3OH)	-	36	[109]
	Cu-MOR	O_2 (773K)	473	1	-	-	93 (CH_3OH)	169[f]	-	[171]
	Cu-MOR	O_2 (473K)	473	6	-	-	-(CH_3OH)	25[f]	-	[158]
	Cu-SSZ-13	O_2 (773K)	473	1	-	-	~85 (CH_3OH)	110[f]	-	[172]
	Cu-SSZ-13[b]	O_2	473	1	2	-	~50 (CH_3OH)	15[d]	-	[28]
	Cu-CHA[b]	O_2	573	1	2000	-	91 (CH_3OH)	195[d]	-	[173]
	Cu-MOR[b]	O_2	573	1	24	0.01	52 (CH_3OH+HCHO)	163[d]	0.5	[174]
	Cu-CHA[b]	O_2	573	1	24	0.06	60 (CH_3OH+HCHO)	920[d]	2.3	[175]
	Fe/Silicate + Cu-Silicate[b]	H_2O_2	343	3	0.36	10.1	93 (CH_3OH)	6014[d]	-	[140]
	Cu-Fe/ZSM-5[b]	H_2O_2	323	30	~3	-	80 (CH_3OH)	7015[d]	431	[145]
	Fe/ZSM-5 + Cu-ZSM-5[b]	H_2O_2	323	20	0.013	0.5	92 (CH_3OH)	75[d]		[119]
	Fe-FER	N_2O	623	1	4	2.8	59 (CH_3OH+CH_3OCH_3)	-	125	[139]

[a] turnover frequency. [b] co-feeding water. [c] productivity in μmol/hr/cm^3 of reactor volume. [d] Productivity in μmol/hr/g of catalyst. [e] Productivity in μmol/hr/g dry cell. [f] Productivity in μmol/cycle/g catalyst.

Table 2.1 Continued…

	Catalyst	Oxidant	T, K	P, bar	$n_{CH4}/n_{oxidant}$	X_{CH4}, %	$S_{C1\text{-}oxygenate}$, %	Productivity[c-f]	TOF[a], hr^{-1}	Ref.
Periana	(bpym)$PtCl_2$	H_2SO_4	493	34	~0.1	90	81 (CH_3OSO_3H)	85000[d]	36	[176]
	(bpym)$PtCl_2$/CTF	H_2SO_4	488	40	~0.2	-	81 (CH_3OH)	-	98	[177]
	Mn/TiO_2	$C_2HF_3O_2$	488	7	-	-	($C_3H_3F_3O_2$)	600[d]	-	[178]
Peroxyl route	1%-PdAu/TiO_2[b]	H_2O_2	343	30.5	-	-	89 (CH_3OOH)	1030[d]	14	[179]
	PdAu-colloids[b]	H_2O_2	323	30	-	-	89 (CH_3OOH)	29400[d]	-	[180]
	Pd@Pt-colloids[b]	H_2O_2	323	30	-	-	89 (CH_3OH)	89300[d]	-	[181]
	PdAu-colloids[b]	H_2O_2+O_2	323	30	-	-	90 (CH_3OOH)	39400[d]	-	[180]
	5%-PdAu/TiO_2[b]	H_2+O_2	343	30.5	44	-	89 (CH_3OH)	59[d]	0.16	[179]
	5%-PdAu/CNT[b]	H_2+O_2	323	33	5.9	-	73 (CH_3OH)	190[d]	-	[182]
	Pd_9Au-nanowires[b]	H_2+O_2	343	10	31	-	99 (CH_3OOH)	2890[d]	-	[183]
	0.5%AuPd/ZSM-5	H_2+O_2	323	34	-	-	100 (CH_3OH)	21.4[d]	0.57	[184]
	AuPd@ZSM-5-C_6	H_2+O_2	343	30	0.5	17.3	92 (CH_3OH)	4580[d]		[185]
Zeolites re-imagined	Au-ZSM-5	O_2+CO	513	24	20	-	100 (CH_3OH+CH_3COOH)	136[d]	-	[186]
	Rh-ZSM-5	O_2+CO	423	29	10	-	66(CH_3OH+CH_3COOH)	7098[d]	-	[187]
	Cu-SSZ-13/H-ZSM-5	O_2+H_2O	663	1		0.1	77 ($C_6H_5CH_3$)	102[d]	-	[188]

[a] turnover frequency. [b] co-feeding water. [c] productivity in μmol/hr/cm^3 of reactor volume. [d] Productivity in μmol/hr/g of catalyst. [e] Productivity in μmol/hr/g dry cell. [f] Productivity in μmol/cycle/g catalyst.

2.3. LIQUID PHASE ACTIVATION OF METHANE

2.3.1. HOMOGENEOUS COMPLEXES AND PRODUCT PROTECTION

The electrophilic activation of the methane C-H bond by an organometallic complex was first reported by Shilov in 1969. This was followed by a landmark article in 1972 which reported on the oxidation of methane in the presence of a $PtCl_4^{2-}/PtCl_6^{2-}$ system to form chloromethane, a "protected" intermediate which can undergo subsequent hydrolysis to methanol [189-191]. The authors proposed a three-step mechanism for the oxidation of methane to chloromethane, with the initial step being the electrophilic activation of the methane C-H bond forming a methyl fragment coordinated to the Pt(II) centre. The next step is the oxidation of the Pt(II) centre to Pt(IV). The final step is the reductive elimination of CH_3Cl.

The Shilov system is not suitable for practical application due to decomposition of the complex to metallic platinum or insoluble, polymeric Pt salts, and low overall yields [36, 192-194]. The Shilov system, however, inspired a paradigm shift in the approach of methane oxidation; instead of directly forming methanol, the strategy now shifted to the production of a protected methanol intermediate that is impervious to the consecutive oxidation to CO_2. This approach was employed by Periana et al. [194], who investigated the selective oxidation of methane (at 200-220°C) to a protected group in the presence of Hg(II) in concentrated sulfuric acid (the oxidant) to form a methanol derivative in the form of methyl esters (i.e. CH_3OSO_3H, methyl bisulfate). The reported methane conversion was 50 %, with a selectivity for the formation of methyl bisulfate of 85%, and thus a potential yield of methanol of 43% [194].

The use of a Pt(bis-1,2-dipyrimidal)Cl_2 complex (referred to as the Periana system) resulted in significant improvements to the process, with a methane conversion of up to 94% and a methyl bisulfate selectivity of 81% [176]. The mechanism for the platinum-catalysed conversion methane process (see Scheme 2.4) was proposed to occur in three steps, viz. initiation by the electrophilic activation of the methane C-H bond to form a CH_3-Pt(II) species, oxidation of the CH_3-Pt(II) species to CH_3-Pt(IV) species by SO_3, and, finally, the reductive elimination of the methyl ester [176] . The Periana system works well because of the formation of methyl bisulfate instead of methanol. The bisulfate groups are electron withdrawing, which protects the other C-H bonds of the methyl group from further electrophilic reactions [194, 195]. Methyl bisulfate can be hydrolysed to produce methanol [196] and dilute sulphuric acid formally closing the catalytic cycle (although the reaction requires concentrated sulphuric acid).

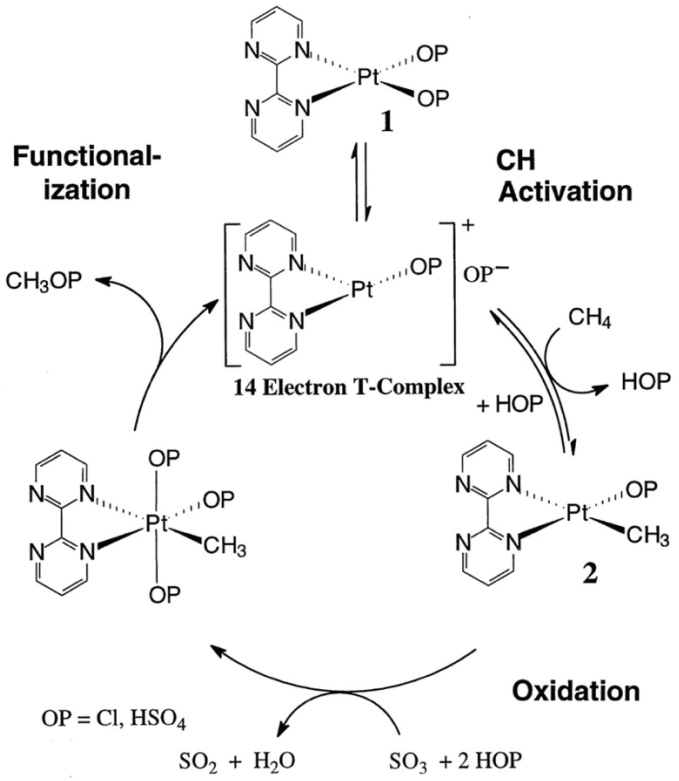

Scheme 2.4: Proposed catalytic cycle for the electrophilic functionalisation of methane. Reproduced from [176]. Reprinted with permission from AAAS.

The Periana system is however not suitable for large scale implementation despite its being one of the most selective and productive systems for the selective oxidation of methane to date (Table 2.1). The main drawback is its reliance on harsh, highly corrosive reagents and the need to oxidise SO_2 in order to recover SO_3 (the oxidising agent) [197]. The Periana system also requires energy intensive work-up of the dilute sulphuric acid formed after the reaction.

2.3.2. THE PEROXIDE ROUTE

The selective activation of a C-H bond to form oxygenates at low temperatures over metallic catalysts was first realized by Kesavan et al. [198], who reported the selective oxidation of toluene to oxygenates (benzyl benzoate, benzaldehyde, benzyl alcohol and benzoic acid) over AuPd alloy nanoparticles at 160°C with oxygen as the oxidant. It was hypothesized that the oxidation of toluene proceeds via the formation of a surface hydroperoxyl intermediate from the interaction of the metal active surface, O_2 and toluene. The surface hydroperoxyl intermediate is thought to be formed on the AuPd nanoparticles [199-202]. The selective oxidation of toluene over AuPd/TiO_2 could proceed at an even lower temperature (80°C) when tert-butyl hydroperoxide was used as the oxidant [203] illustrating the importance of surface-

stabilised reactive oxygen species, produced from the decomposition of peroxides, for the activation of C-H bonds [203].

Hutchings et al. further expanded on this work by investigating the performance of AuPd alloy nanoparticles for the selective oxidation of methane to methanol with H_2O_2 as the oxidant [179, 180, 182, 204, 205]. The gold-palladium nanoparticles are the catalytically active species as pure titania [179] is not active, whereas high activity is observed when using Au−Pd colloids [206], Au@Pd nanowires [183] and Pd@Pt nanoparticles [181] as the catalyst. The activity appears to be in line with the expected mass-based activity deduced from the mass loading of these nanoparticles on the support, although AuPd on titania catalyses the decomposition of H_2O_2 possibly at the metal-support interface [180], which may reduce the catalytic activity by reducing the H_2O_2 utilization efficiency.

The activity of the supported Au-Pd system appears to be support dependent; AuPd nanoparticles supported on the rutile phase of titania appears to be more active than AuPd particles supported on P25 [182] possibly due to the decomposition of hydrogen peroxide on the anatase phase. During the reaction, H_2O_2 possibly decomposes to form dissolved O_2, as well as surface bound hydroxyl and hydroperoxyl species [207]. The activity of the palladium and in particular the gold-palladium system may be linked to the stabilization of the hydroperoxyl species on the catalytically active surface(s), as Pd(111) stabilizes surface hydroperoxyl-species [180, 181]. The hydroxyl species may then activate methane to form a methyl radical that may react with hydroperoxyl species (the presence of the methyl and hydroxyl radicals was detected in the reaction mixture using EPR with DMPO as a radical scavenger, which did not detect hydroperoxyl radicals) [179] to yield methyl hydroperoxide. Alternatively, it may decompose into surface hydroxyl species (and a surface oxygen species), which then reacts further to form water (see Scheme 2.5).

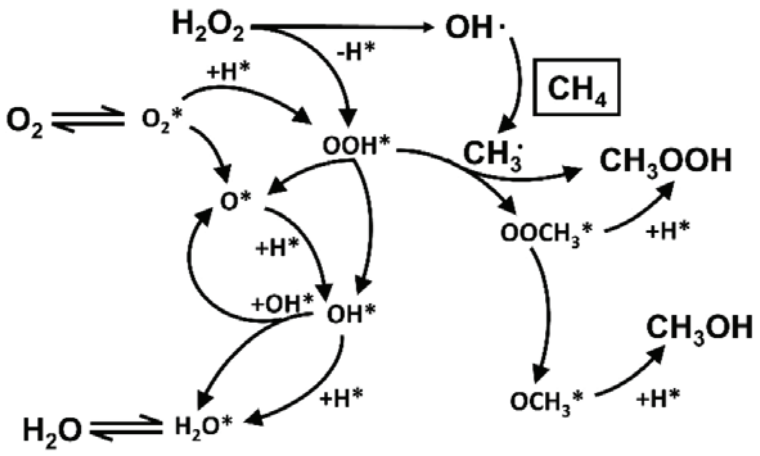

Scheme 2.5: Proposed mechanism for the selective oxidation of methane in the presence of H_2O_2 as the oxidant.

The presence of gold on the surface may moderate the strength of adsorption of oxygen containing species such as adsorbed hydroperoxyl (·OOH) [181], thus reducing their decomposition which could potentially favour the desorption of methyl hydroperoxide [179, 208]. Hydrogen peroxide was generated in-situ by feeding H_2 and O_2 as an attempt to boost the oxygenate productivity [179], as previous studies showed AuPd to be an effective hydrogen peroxide synthesis catalyst [209]. The oxidation of methane with in-situ generated hydrogen peroxide improves methanol selectivity and diminishes selectivity for methyl hydroperoxide, although the overall productivity is lower than that obtained when H_2O_2 is added in the feed (i.e. productivity of 0.28 $mol.kg_{cat}^{-1}.h^{-1}$ with preformed H_2O_2 vs 0.116 $mol.kg_{cat}^{-1}.h^{-1}$ when H_2/O_2 replaced H_2O_2) [179].

The in-situ generation of hydrogen peroxide proved to be beneficial in the continuous selective oxidation of methane in a capillary microreactor [210]. The improved activity was attributed to shorter residence times and faster hydrogen peroxide formation rates in the microcapillary reactor (contrasted with slower rates in a batch reactor, which utilised dilute H_2 and O_2 concentrations) [179, 210]. However, it could simply be that the activity is boosted by the use of hydrophobic silica in the capillary column, which would result in the improved local concentration of hydrogen peroxide around the AuPd nanoparticles [185], whereas the formed hydrogen peroxide in the batch reactor would be quite dilute since the reaction is carried out in water.

The effect of confining in-situ formed H_2O_2 around the AuPd active site was demonstrated by Jin et al. [185], who crystallised AuPd nanoparticles within zeolite crystals then modified the

zeolite surface with organosilanes, forming a hydrophobic sheath allowing the transport of hydrophobic species such as O_2, H_2 and CH_4 to the catalytically active site within the zeolite. However, the hydrophobic surface meant that diffusion of the formed H_2O_2 out of the zeolite is restricted, thereby confining hydrogen peroxide to the zeolite pore system, hence maintaining a high local concentration next to the AuPd active sites. This proved immensely beneficial for the conversion of methane and oxygenate selectivity (methanol and methyl-hydroperoxide). Figure 2.8 shows the effect of the zeolite modification on the methane conversion and oxygenate selectivity [185].

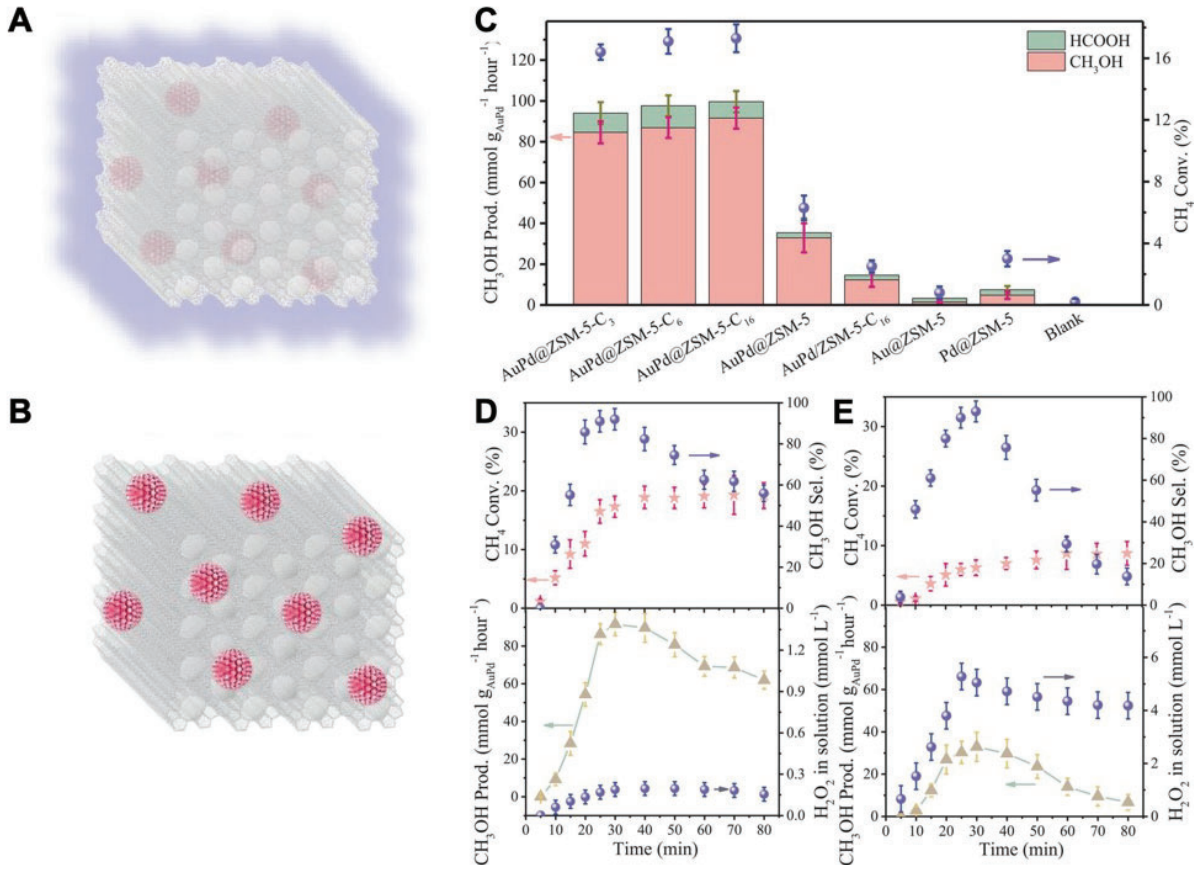

Figure 2.8: Conceptual presentation of A) the organosilane-modified zeolites showing the hydrophobic layer encapsulating the zeolite crystal, B) the unmodified zeolite crystal, C) the methane conversion and corresponding oxygenate selectivity/productivity over the unmodified and modified zeolite-supported catalyst in a batch reactor, D) and E) the influence of reaction time on the methane conversion, methanol productivity and hydrogen peroxide concentration over D) AuPd@ZSM-5-C_{16} and E) AuPd@ZSM-5. Adapted from [185]. Reproduced with permission from AAAS.

The selective oxidation of methane with in-situ formed hydrogen peroxide does not result in the formation of formic acid and CO_2 [184, 185, 211], instead, the process mainly favours the formation of methanol, especially in oxygen rich conditions. The formation of hydroperoxyl and hydroxyl radicals during the in-situ formation of hydrogen peroxide, and the presence of molecular oxygen, may contribute significantly to the reaction in addition to hydrogen peroxide.

The use of hydrogen peroxide as an oxidant for the selective oxidation of methane, although highly selective, is ultimately not economically viable as hydrogen peroxide is more expensive than methanol [78, 184]. The in-situ generation of hydrogen peroxide could provide a more economical process. The interesting thing to note is that even for in-situ produced hydrogen peroxide, it is important to maintain high methane concentrations in order to prevent the further oxidation of the formed methanol [212].

2.3.3. ZEOLITES RE-IMAGINED

Oxygen is a more desirable oxidant than H_2O_2. Shan et al. [213] reported the oxidation of methane to acetic acid and methanol using O_2 as an oxidant and CO as a co-reactant over single-site Rh catalysts supported on titania and ZSM-5. The zeolite-supported rhodium catalyst was selective for the formation of methanol, formic acid, acetic acid and CO_2. The selectivity towards acetic acid increased with decreasing oxygen concentrations (i.e. 2 bar O_2, 3 hrs reaction time, 65 % acetic acid selectivity and a total productivity of 673 $\mu mol.g_{cat}^{-1}.hr^{-1}$). The titania supported catalyst displayed a complete selectivity towards methanol, at a productivity of 77 $\mu mol.g_{cat}^{-1}.hr^{-1}$.

The catalyst was optimised by ensuring a high rhodium dispersion through removal of rhodium species from the pore mouths and external surface of the zeolite. This yielded a catalyst that was highly productive, achieving a productivity of up to 7300 $\mu mol.g_{cat}^{-1}.hr^{-1}$ and a selectivity of 60% towards the formation of acetic acid [213]. This reaction can be viewed as methane carbonylation, since the reaction involves the insertion of CO into methanol to form acetic acid, which can be catalysed by single-site Zn, Cu, Fe, Co, Ni, Ru, Pt and Pd, in addition to Rh [214-219]. Of course, Rh being a highly effective catalyst for carbonylation reactions, outperforms the other metals, followed by Ir and Ru [220]. The mechanism for the methane carbonylation is presented in Scheme 2.6.

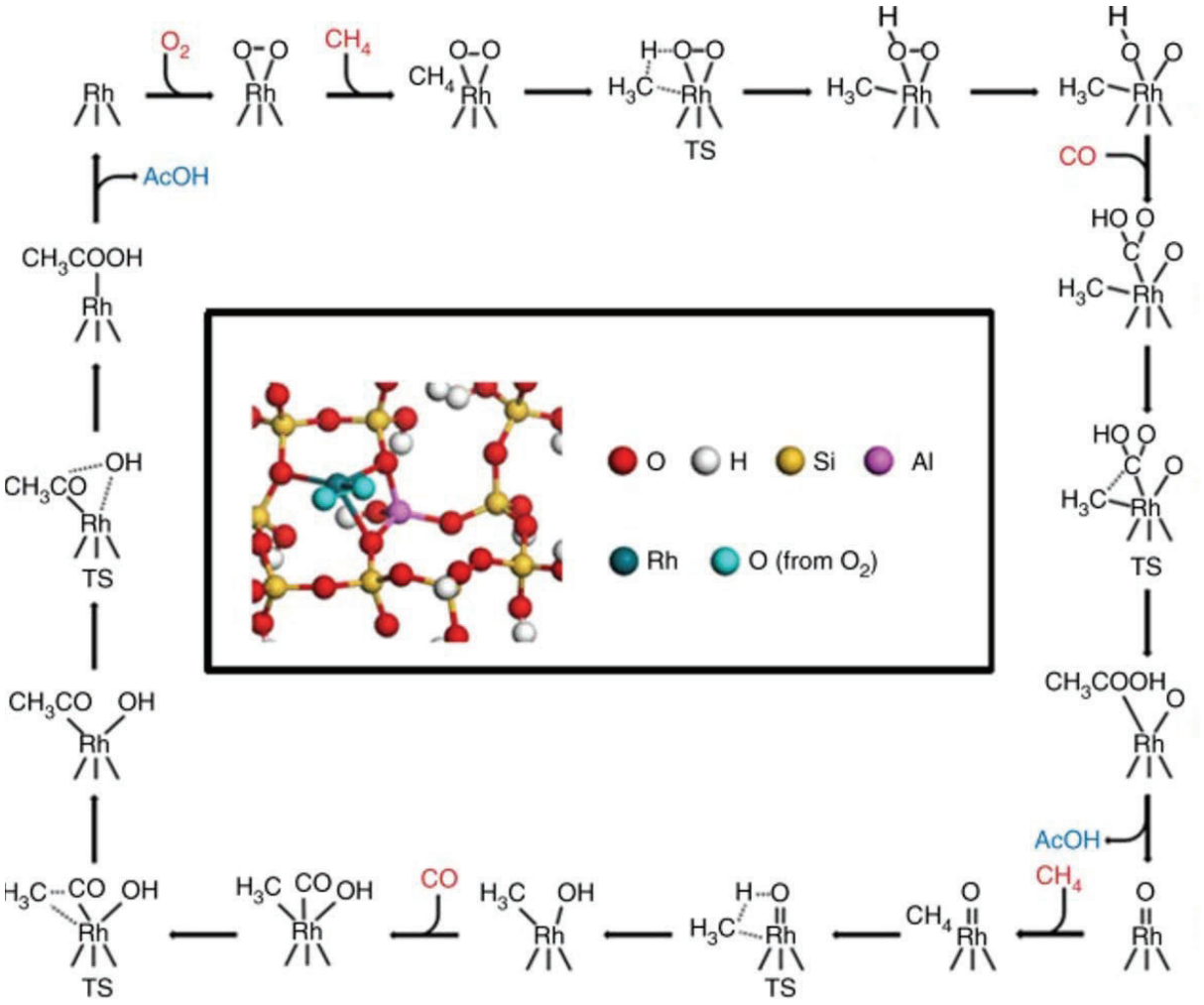

Scheme 2.6: Mechanism for the conversion of methane to acetic acid over Rh-exchanged zeolites, with the inset showing the activated rhodium active site. Adapted from [221], under a free-use licence © 2018, Springer-Nature

Further strategies for the protection of methanol formed from the zeolite-catalysed conversion of methane involve the use of tandem-catalysis for the functionalisation of the formed methane. This strategy is best illustrated by a study from the Romàn-Leshkov group [188], where the oxidation of methane over Cu-SSZ-13 was followed by using the formed methanol to alkylate benzene over H-ZSM-5. This boosted the selectivity towards oxygenate products even at slightly higher conversions, which was attributed to the functionalisation of methane to toluene, which was too large to diffuse into the SSZ-13 zeolite, thereby protecting the formed product from further oxidation [188]. However, the process still suffers from low conversions [188].

The Hutchings group have also continued with the development of catalytic processes using zeolites, with their latest attempt looking into the use of a Au-ZSM-5 catalyst for the selective

oxidation of methane, using oxygen as an oxidant [186] at moderate temperatures (120–240°C) in the presence of water. The catalyst was selective for the formation of methanol and acetic acid in the presence of CO. Contrary to existing reports, the presence of CO resulted in the formation of methanol, while the absence of CO favoured the formation of acetic acid. It is worth noting that Au was present in the form of 8.1 nm particles on the support. The difference between the single-site and nanoparticle-catalysed mechanism is that the activation of methane over Au nanoparticles is a surface-catalysed process, that involves the activation of methane over atomic oxygen, followed by functionalisation with molecularly-adsorbed oxygen, which forms intermediates that can form methanol, methyl hydroperoxide and acetic acid, as shown in scheme 2.7 [186].

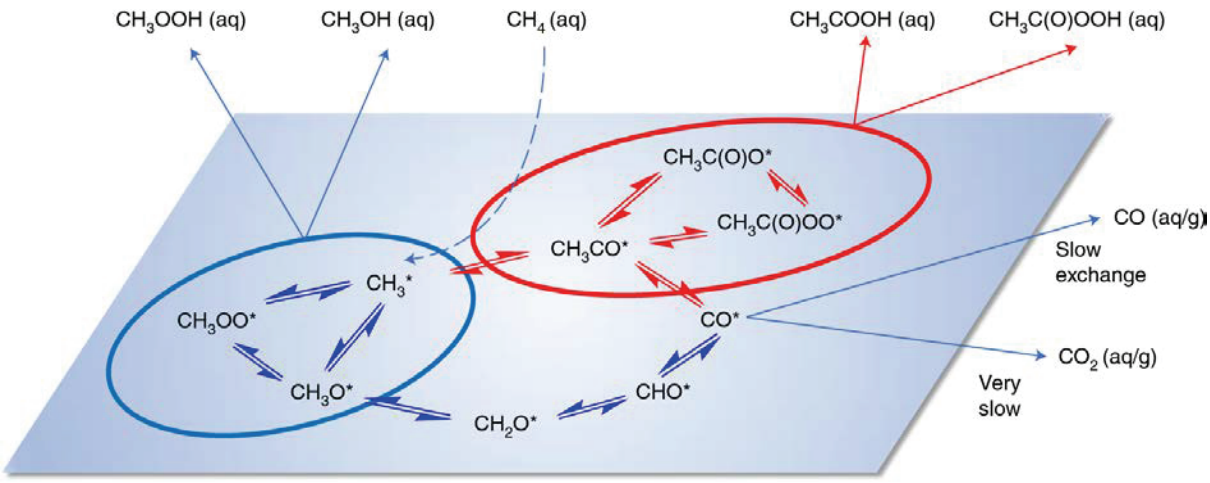

Scheme 2.7: The surface-catalysed conversion of methane to methanol, methyl-hydroperoxide and acetic acid over Au/ZSM-5 in the presence of oxygen and CO in water. Reproduced with permission from [186]. © 2022, Springer-Nature

The CO-assisted selective oxidation of methane to methanol and acetic acid presents a promising route for the direct functionalisation of methane, despite the reported low productivities.

2.4. AEROBIC OXIDATION OF METHANE OVER SOLID CATALYSTS AT MODERATE TEMPERATURES

Most studies reviewed have dealt with the activation of methane either at high (350 – 600°C) or low (25-120°C) temperatures. Operation at high temperatures suffer from poor selectivities, particularly at high methane conversions, while operation at lower reaction temperatures tend to suffer from poor productivities. Another issue to consider for an industrial process, is the

concept of heat recovery. Although the processes at low temperature are highly selective, it is worth keeping in mind that the oxidation of methane to methanol or formaldehyde is an exothermic reaction. As such, the heat generated during such reactions should ideally be recovered to improve thermal and exergetic efficiency of the process [222]. The recovered heat could be used to generate steam that could then be used to generate power. Hence, the ideal temperature operation region should be between 200 and 250°C [78].

Molecular oxygen is an ideal oxidant for oxidation reactions, due to its availability and cleanliness (producing environmentally benign by-products) [40, 223]. The main issue with the use of oxygen as an oxidant is the possible generation of free-radicals, a problem that has been encountered during the high-temperature autocatalytic oxidation of methane to methanol [223]. The main challenges with using oxygen are a) the activation of oxygen to make it reactive towards oxidation of the methane C-H bond, b) the selective activation of the methane C-H bond to form intermediates that are stable against over-oxidation and c) formation of the desired product without over-oxidation to CO_x products [40]. The activation of oxygen can be achieved through the use of transition metals or oxides [224-226]. Here we focus on the activation of oxygen and methane over metallic surfaces because metal oxides tend to bind the activated methane intermediates strongly, which makes them susceptible to further reaction with nucleophilic oxygen, leading to the formation of deep oxidation products via the Mars van Krevelen mechanism [23, 227].

2.4.1. THEORETICAL STUDIES OF METALLIC CATALYTIC SURFACES FOR THE SELECTIVE OXIDATION OF METHANE

The oxidation of methane to C_1 oxygenates using oxygen as an oxidant over metallic catalysts is not well researched experimentally, but has received a lot of attention in terms of model catalytic systems and density functional theory studies. Metallic catalysts are ideal candidates for the selective oxidation of methane under relatively mild reaction conditions, because a) they are capable of activating oxygen [225] which is usually the first step required for oxidative processes on metal surfaces, b) they tend to be more selective for oxidation reactions (i.e. they are less likely to completely oxidise a substrate to CO_x products) [23, 225], and require atomic oxygen (O) [228, 229] to initiate the oxidation reaction, and c) they are active for oxidative reactions under relatively mildly oxidising conditions, making them suitable for operation at lower temperatures, and conditions that are mild enough to favour the preservation of formed, selective methane oxidation products such as methanol and formaldehyde, which otherwise

oxidise further under strongly-oxidising conditions (i.e. high temperatures, and high oxygen partial pressures).

Theoretical studies have indicated the possibility of selectively oxidising methane to methanol over metallic catalysts using oxygen as an oxidant. A viable strategy involves the activation of methane over oxygen pre-covered surfaces [229-232]. This would drive the methane activation to occur via an Eley-Rideal type mechanism (see Figure 2.9). At low coverages, methane is activated over O* and an adjacent vacant site, forming adsorbed, surface-stabilised methyl and hydroxyl species (CH_3* + OH*). At high coverages, methane is activated over O*-O* pair sites via homolytic hydrogen abstraction to form surface adsorbed hydroxyl species, and a methoxy species that is stabilised by the vicinal O* (O*---CH_3 + OH*). This forms adsorbed methoxy (OCH_3*) and hydroxy (OH*) intermediate species [233-236].

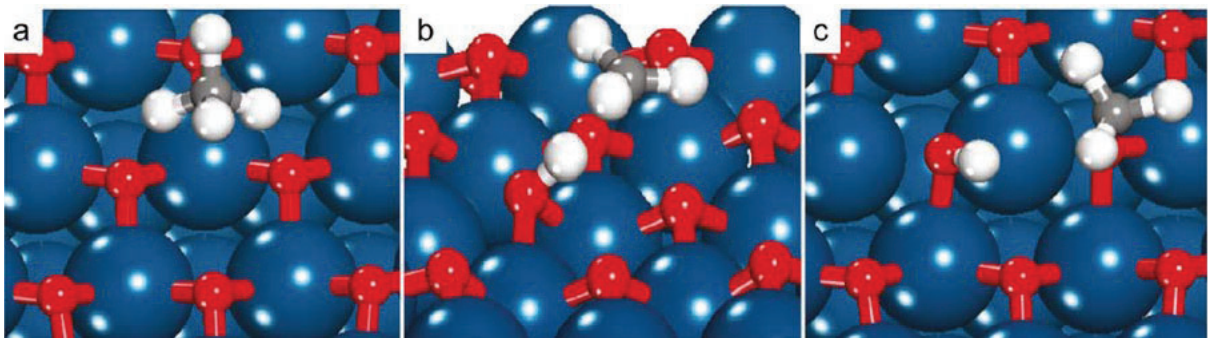

Figure 2.9: A conceptual representation of the activation of methane over an oxygen pre-covered surface (a) to yield an adsorbed hydroxyl intermediate (b) and a methoxy intermediate (c) via the Eley-Rideal mechanism. Reproduced with permission from [234]. © 2018, the American Chemical Society.

Yoo et al. [237] investigated routes for the formation of oxygenates over Pd, Pt, Ag, Au and Cu surfaces using DFT. Over a Pd (111) surface, methanol may form via a OH assisted hydrogenation of CH_3O* (CH_3* + OH* + O* → CH_3O* + OH* → CH_3OH + O*). The formaldehyde formation pathway on the same surface occurs via O* assisted dehydrogenation of CH_3O* (CH_3O* + O* → CH_2O + OH*) [237]. Platinum group metals (Pd, Pt, Rh) were found to be selective for the formation of CO and CH_2O. The authors correlated the differences in the preferential formation of products to the differences in steady state coverages of O*. Metals with higher O* coverages are more selective for CH_2O formation, via the O* assisted dehydrogenation of the adsorbed methoxy species. Coinage metals were found to favour the production of CH_2O and CH_3OH [237].

The formation and maintenance of OH* species on the catalyst surface has been proposed by the authors as the key to achieving methanol selectivity during CH_4 oxidation over coinage metals [237]. These conclusions are supported by Fratesi et al. [238], who studied the oxidation of methane to methanol over similar metals as investigated by Yoo et al. [237] (Pt, Pd, Rh, Cu, Ag, Au(111) surfaces).

2.4.2. WATER AS A CO-REACTANT

The use of water during the selective oxidation of methane plays a crucial role, and has been a fixture in most processes [16, 37]. Water plays many roles during reactions, either taking part in the catalytic cycle by displacing the product at the end of the reaction thus facilitating the removal of products from the catalytically active site (as in the case of zeolites); boosting the presence of active species which in turn correlates with increased catalytic activity (i.e. generate hydroxyls able to activate methane) [16, 239-241], acting as a medium for the removal of products through dissolving and solvating the products, and may even participate in the reaction either through stabilising reaction intermediates [242], or providing alternative, low energy pathways for the reaction to occur [239, 240, 243, 244]. Co-feeding water during selective oxidation of methane does not only prevent coke formation (thereby minimising catalyst deactivation), but has been found to promote the formation of selective oxidation products (i.e. methanol or formaldehyde) [245].

A detailed study on the role of water during the selective oxidation of methane over Cu-BEA zeolites was conducted using combined ab initio molecular dynamics simulations with isotope-labelling experiments [246]. Water was found to significantly boost the catalytic activity and methanol selectivity by creating a bridge between the adsorbed CH_3 and OH moieties (on the adjacent copper sites). This facilitated proton transfer from a water molecule to an adjacent water molecule, forming a H_3O^+ species and a hydroxyl intermediate, which then react with the methyl fragment forming an adsorbed methanol intermediate. The H_3O^+ intermediate meanwhile protonates the adjacent, copper-bound OH to re-form water. The simulated mechanism is presented in Scheme 2.8. The behaviour of water in this system is that of a co-catalyst, since water is regenerated at the end of the reaction cycle [247].

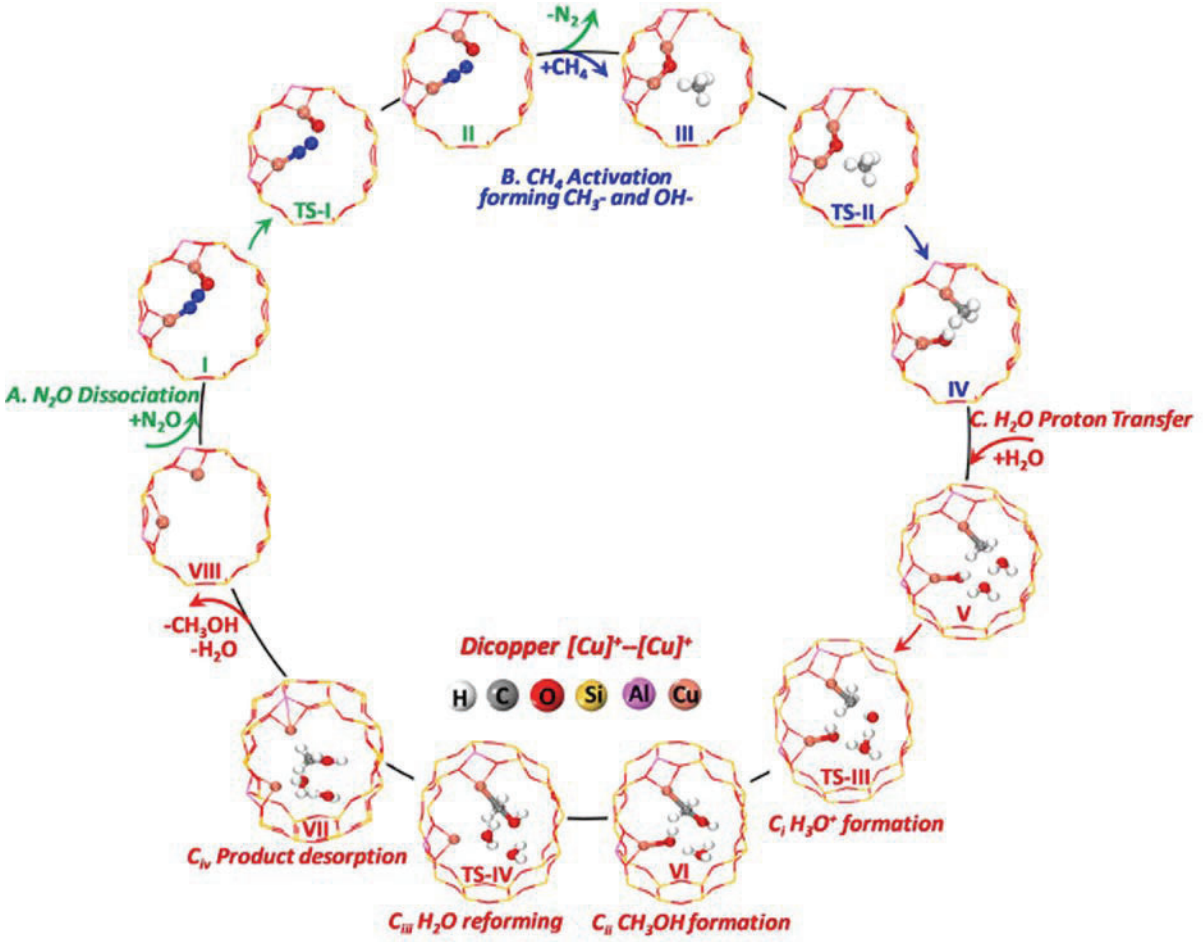

Scheme 2.8: Mechanism for the water-enhanced oxidation of methane to methanol over a dinuclear Cu_2O active site on Cu-BEA, showing the activation of the active site with N_2O, the reaction of the activated site with methane to yield adsorbed CH_3 and OH fragments, and the water-assisted desorption of methanol promoted by the formation of a proton-shuttling bridge. Adapted with permission from [246]. © 2021, Wiley-VCH.

The role of water during the surface-catalysed selective oxidation of methane over single crystals has been extensively studied by Rodriguez et al. [245, 248-251], in an attempt to elucidate the role of water in the reaction mechanism. Their earlier study [245] showed that the formation of methanol over a nickel surface supported on ceria was dependent on the presence of water. Water acted as a site-blocker (by forming OH surface groups), thus decreasing the interaction of methane with the metallic nickel surface and preventing the successive dehydrogenation of methane to carbon that would ultimately undergo a facile reaction with oxygen to form CO_x products. Furthermore, water acts as a directing agent that inhibits the dissociation of a methyl species that forms during the activation of methane, forcing the species

to form a methoxy species instead via interaction with adsorbed oxygen atoms. It was proposed that methanol forms via the hydrogenation of the surface bound methoxy species by water, which desorbs as methanol [245]. Water coordinates to the surface-bound methoxy species, forming a H-O-H----*CH_3O intermediate via hydrogen bonding. The bound methoxy intermediate is then protonated to form methanol which desorbs from the active site [245, 248-251].

CHAPTER III: SCOPE AND NOVELTY OF STUDY

3.1. CONTEXT AND PROBLEM STATEMENT

It is apparent from the previous studies that a catalyst is necessary in order to achieve a highly selective process for the selective oxidation of methane and to control the reaction mechanism. Operating at lower temperatures is crucial to prevent the successive oxidation of the formed oxygenates, as illustrated by the difficulty in attaining high oxygenate selectivities at high conversions over metal oxide catalysts [66, 78, 252]. The zeolite-based systems attempted to circumvent the selectivity problem by feeding an excess of methane, which results in very low productivities [97]. Although systems that use low reaction temperatures (<250°C) are the most productive to date, they require the use of either H_2O_2 or H_2SO_4 as oxidants, which imposes a cost constraint on the processes that renders them uneconomical at a large scale [16, 176]. Hence, the development of a fully-catalytic process for the selective oxidation of methane, using oxygen as an oxidant, at moderate reaction temperatures, is desirable.

This can be achieved by employing reaction conditions that should ideally support the survival of the formed oxygenate, which can encompass strategies such as moderate reaction temperatures and product protections [27, 253]. Furthermore, it has been noted that activating methane to form a methoxy intermediate is a crucial step in ensuring the formation of selective methane oxidation products [127, 254, 255]. Hence, development of this process should focus on designing a process that can activate methane at moderate reaction temperatures, using oxygen as an oxidant, to form a methoxy intermediate that can then be transformed to selective oxidation products. Moderate reaction temperatures (i.e. 150 - 250°C) are seen as desirable due to the possible limited reactivity of oxygenates at these temperatures, in addition to enabling the recovery of heat (in the form of steam) [78].

3.2. OBJECTIVES AND RATIONALE

The activation of methane using oxygen as an oxidant under moderate conditions is best achieved over metallic surfaces via a homolytic cleavage of the methane C-H bond by electrophilic atomic oxygen species. This was indicated by DFT calculations which showed the formation of a methoxy-intermediate through the activation of methane on atomic oxygen species adsorbed on metallic surfaces via an Eley-Rideal mechanism [234, 237, 238]. This is to enforce the interaction of methane with adsorbed oxygen (i.e., via an Eley-Rideal mechanism), and to prevent the activation of methane by nucleophilic oxygen species (typically

encountered for oxide-based systems). The activation of methane by electrophilic, adsorbed oxygen species could result in the formation of e.g. and adsorbed methoxy intermediate [228, 256]. This strategy requires the use of an oxygen-saturated surface, which would also prevent/minimise the formation of a methyl fragment, which is more likely to undergo facile oxidation to CO_2 via a dehydrogenation pathway [245, 257]. Hence, a metal that is capable of activating oxygen at moderate temperatures, can maintain high oxygen coverages, is stable against oxidation under reaction conditions, and does not bind oxygen too strongly to enable oxygen-assisted activation of the methane C-H bond is an ideal candidate for the active metal.

Platinum was chosen as the metal of choice due to its ability to activate oxygen and its stability against oxidation under mildly oxidising conditions [258]. It is however difficult to fully saturate a platinum surface with adsorbed oxygen atoms due to lateral interactions between the adsorbed oxygen atoms, which limits the saturation coverage to 0.3-0.5 monolayers [259, 260]. This limitation can be overcome by co-feeding water, which dissociates in the presence of oxygen to form adsorbed hydroxyl groups which significantly enhance the surface coverage [245, 261]. The presence of water has been shown to enhance the formation of selective oxidation products over metallic surfaces, which was attributed to the presence of surface hydroxyl groups [245, 248, 249]. These hydroxyl groups may act as site-blockers, preventing the successive dehydrogenation pathway that would lead to over-oxidation of methane [248, 262]. Water may also act as a protecting agent through the solvating effect, which may facilitate the desorption of the formed oxygenates whilst protecting them from further conversion to CO_2 [27, 246, 263].

3.3. PROJECT AIM

The key challenge in the selective oxidation of methane to C_1 oxygenates appears to be activating methane into an intermediate that will ultimately yield methanol and/or formaldehyde, without facilitating the formation of the total oxidation products, CO and CO_2, as well as employing reaction conditions that will limit the successive oxidation of the reaction products themselves [26]. This study thus aims to investigate the catalytic transformation of methane to C_1-oxygenates over platinum-based catalysts, using oxygen as an oxidant, employing a continuous catalytic process at a moderate temperature (i.e. 220°C), in the presence of water. Because the presence of water at moderately high temperatures and pressures creates a strongly hydrothermal environment, which may affect the catalyst support, different supports were also investigated. Platinum was supported on hydrophilic (i.e. Al_2O_3

and TiO_2-P25) and hydrophobic (activated carbon and TiO_2-rutile) supports to evaluate the stability of these catalysts under these conditions. Platinum also tends to bind atomic oxygen strongly, which would lower its reactivity towards activation of the C-H bond [228, 264]. The binding strength of atomic O can be tuned by either increasing the Pt particle size [265], or by alloying Pt with other metals [266]. Alloying Pt with non-precious metals has been observed to increase the activity and stability of methanol oxidation reaction catalysts which was attributed to the downshift in the d-band centre, brought about by the electron transfer from the less electronegative metal to Pt [267]. Hence, the effect of alloying platinum with group 11 metals on the rate of methane conversion was also investigated.

The project then investigates three main questions centring on activity, selectivity and stability;

I. How is the activity and the selectivity of a platinum catalyst influenced by the presence of water during the selective oxidation of methane?
II. How is the stability of the catalysts affected by the presence of water, and what is the role of the support in promoting the catalytic activity, stability and product selectivity?
III. How does modifying the platinum d-band centre affect the catalytic activity during the selective oxidation of methane?

3.4. SCOPE AND NOVELTY OF RESEARCH

This study is an investigation on the selective oxidation of methane to C_1-oxygenates, using oxygen as an oxidant, over platinum-based catalysts in the presence of water in the form of steam and liquid water. This was achieved by first conducting experiments in a fixed bed reactor with all reactants in the gas phase. This was followed by an investigation on the effects of liquid water on the conversion of methane and oxygenate selectivity over platinum-based catalysts in a dedicated trickle-bed reactor.

Catalyst stability tests were performed by running experiments over hundreds of hours regularly returning to baseline conditions. Structural aspects of the catalysts were investigated by comparing the initial state of the catalyst and that with the end-of-run catalyst.

The effect of modifying the platinum d-band on the catalytic activity was also investigated by alloying platinum with copper, gold and silver. The activity of the alloys was investigated in the gas-phase and trickle-bed reactors (see Appendix 1) to determine differences in

performance in the presence of steam and liquid water. The work presented herein is novel, based on the following points;

i. The use of a supported platinum catalyst for the aerobic, selective oxidation of methane in a continuous mode at moderate temperatures (200-250^{o}C), in the presence of co-fed water.
ii. The use of a trickle-bed reactor for the selective oxidation of methane (to investigate the effects of gas-phase vs liquid-phase water).
iii. Investigation on the effect of water on the activity and the stability of the catalyst, and the product selectivity
iv. Investigation on the effect of the partial pressure of methane and oxygen on the activity and selectivity in the selective oxidation of methane over platinum
v. Investigation on the effect of the support on the activity and the stability of the catalyst, and the product selectivity
vi. The investigation of nanoalloy Pt-based systems for the selective oxidation of methane using oxygen as an oxidant with the aim to tune the adsorption strength of oxygen (and oxygenate species) on the catalytic surface on the rate of methane conversion.

CHAPTER IV:

PLATINUM-CATALYSED SELECTIVE AEROBIC OXIDATION OF METHANE TO FORMALDEHYDE IN THE PRESENCE OF LIQUID WATER

Declaration:

The results reported herein have been adapted with permission from S.V.L. Mahlaba et al., Angew. Chem. Int. Ed. 61 (2022) e202206841. This manuscript has been included in the thesis with permission from the doctoral degrees board at the University of Cape Town, and the co-authors in the published version of this manuscript.

The density functional theory (DFT) calculations were performed by Prof. Eric van Steen (supervisor) and Pierre L. Cilliers (Co-author).

OVERVIEW

The aerobic, selective oxidation of methane to C_1-oxygenates remains a challenge, due to the more facile, consecutive oxidation of formed products to CO_2. Here, the aerobic selective oxidation of methane under continuous flow conditions, over platinum-based catalysts yielding formaldehyde with a high selectivity (reaching 90 % for Pt/TiO_2 and 65 % over Pt/Al_2O_3) upon co-feeding water is reported. The presence of liquid water under reaction conditions increases the activity strongly attaining a methane conversion of 1–3 % over Pt/TiO_2. Density-functional theory (DFT) calculations show that the preferential formation of formaldehyde is linked to the stability of the di-σ-hydroxy-methoxy species on platinum, the preferred carbon-containing species on Pt(111) at a high chemical potential of water. These findings provide insights into the reaction pathway for the Pt-catalysed, aerobic selective oxidation of CH_4.

4.1. JUSTIFICATION FOR THE AEROBIC, WATER ASSISTED PLATINUM CATALYSED OXIDATION OF METHANE

The challenge in the selective methane activation is often attributed to the limited reactivity of methane. However, enforcing formation of the desired product whilst at the same time limiting its consecutive conversion to CO_2, is at least as challenging [26]. For example, both the autocatalytic, homogeneous [45] and heterogeneously catalysed [66] oxidation of methane to formaldehyde show evidence of the fast consecutive oxidation of formaldehyde under those reaction conditions, thus requiring finetuning of the residence time to maximize its yield in these processes. The consecutive reactions in the oxidation of methane can be minimized by using alternative oxidants and/or carrying out the reaction at relatively low temperatures.

Some success in the selective oxidation of methane has been achieved using sulfuric acid [176], H_2O_2 [179] or N_2O [139] as the oxidant. However, the use of oxygen [161, 180, 186, 213, 245, 248-250, 268-270] or even air as the oxidant is necessary to make the process economically viable. It should be noted further that heat is an important side product in the selective methane oxidation (the oxidation of methane to formaldehyde releases 34 % of the lower heating value of methane), which will need to be recovered to obtain an energy-efficient process. Effective heat removal requires operating at somewhat elevated temperatures, typically in the range of 200–300 °C to co-generate medium to high pressure steam.

Water facilitates the selective oxidation of methane [27, 245, 248-250, 268, 269]. The mechanism for the observed enhancement may be system specific. The photo-catalytic oxidation of methane over single Au-atoms supported on black phosphorous nanosheets, is thought to be accelerated in the presence of water through the generation of hydroxyl radicals [268]. Rodriguez et al. [248-250] using inverse model catalysts ($MeO/Cu_2O/Cu(111)$ with Me=Ce, Zn) observed an improved selectivity for the formation of methanol in the conversion of methane upon co-feeding water over these model catalysts. Co-feeding water in the oxidation of methane did not only favour the formation of selective oxidation products, but also inhibited the formation of the complete oxidation products, CO_x. This was ascribed to the generation of active surface hydroxyl species facilitating the formation of surface methoxy species at the metal-oxide interface. The preferred formation of surface methoxy species over the formation of surface methyl species is necessary as the latter provides a pathway to CO_x [238, 245, 271], whereas the desorption of surface methoxy species could result in the formation of methanol [238, 245].

Hence, the characteristics of catalysts for the selective oxidation of methane can be defined as follows; they should be able to dissociate the C−H bond in methane, operate at somewhat elevated temperature (preferably 200–300 °C), to utilize a cheap oxidant, such as oxygen or air, and to yield surface methoxy species rather than surface methyl species upon activation of methane. The methoxy species should adsorb not too strongly so that desorption as a selective oxidation product remains feasible.

Here, the use of platinum for the selective oxidation of methane is explored. The formation of surface methoxy species may become preferred over surfaces saturated with oxygen containing species [238]. Full coverage of Pt(111) is difficult to achieve due to lateral interactions between adsorbed oxygen atoms [259] and a maximum coverage of adsorbed oxygen of ca. 0.44 ML has been reported [272]. It is, however, possible to increase the surface coverage with oxygen containing species by co-adsorbing water [273-275]. Hence, the role of water on the aerobic, selective oxidation of methane over supported catalysts containing 10 wt. % platinum is explored.

4.2. EXPERIMENTAL PROCEDURES

4.2.1. CATALYST PREPARATION AND CHARACTERISATION

The catalyst was prepared by wetness impregnation, as described in Section I, Appendix 2. The catalysts were characterised using ICP-OES to determine the elemental composition, powder-XRD to confirm the metallic phase of platinum after reduction, hydrogen and oxygen chemisorption to determine the metallic surface area, and transmission-electron microscopy to determine the particle-size distribution on the supports. Attenuated Total Reflectance infrared spectroscopy (ATR-IR) was also used to analyse the functional groups deposited on the recovered catalysts.

4.2.2. CATALYST TESTING

Catalytic tests were conducted in a fixed-bed gas phase reactor and a trickle-bed reactor (see Appendix 1). The reactor was connected to an Agilent 6890N gas chromatograph for online product analyses, which is equipped with a PolyArc oxidiser/methaniser interfaced with the flame-ionisation detector for the accurate quantification of methane, methanol, CO, CO_2, formaldehyde and other C_1-oxygenate derivatives. The calibration and analysis details of the GC-FID are explained in detail in Appendix I.

4.3. RESULTS AND DISCUSSION

The catalysts were prepared using incipient wetness impregnation of TiO_2 (rutile) and γ-Al_2O_3 with a platinic acid solution to obtain a metal loading of 10 wt.-% (as confirmed using ICP-OES—see Table A2.1) in the reduced catalyst (T_{red}=400°C, t_{red}=5 hrs). Representative transmission electron microscopy bright field (TEM-BF) images show spherical platinum nanoparticles, well-dispersed on the support materials (Fig. 4.1a and d). The particle size distributions were determined by measuring the size of 400 arbitrarily chosen nanoparticles on the images (Fig.4.1b and e). The average platinum particle size was 3.2±1.5 nm for Pt/TiO_2 and 3.6±3.5 nm for Pt/Al_2O_3. This corresponds to an initial platinum dispersion of 41 % in Pt/TiO_2 and 46 % in Pt/Al_2O_3, respectively, when considering the full particle size distribution. Powder X-ray diffraction (PXRD) patterns show that platinum in both Pt/TiO_2 (Fig. 4.1c) and Pt/Al_2O_3 (Fig. 4.1f) is present as metallic FCC-platinum. The average crystalline domain size of platinum in Pt/Al_2O_3 was determined to be 4.4 nm in good agreement with the average platinum particle size determined from the TEM-BF-images. The average crystalline domain size of platinum in Pt/TiO_2 could not be determined accurately due to the overlap of the diffraction lines.

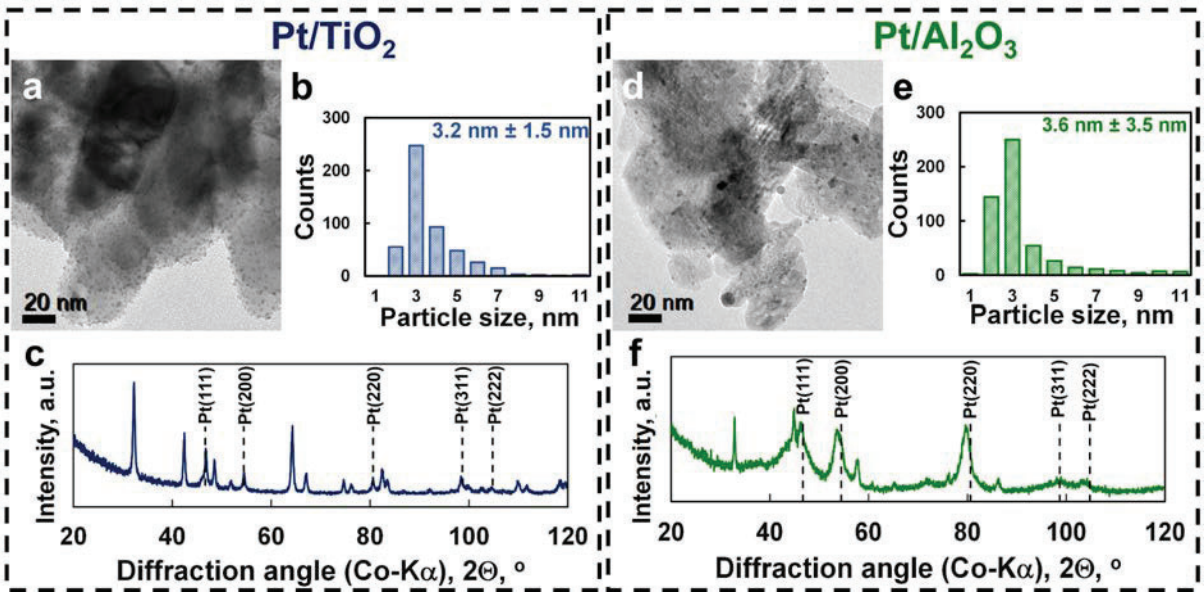

Figure 4.1: Transmission electron micrograph of the 10 wt. % Pt/TiO_2 catalyst (a) and the Pt/Al_2O_3 catalyst (d), particle size distribution of platinum on Pt/TiO_2 (b) and Pt/Al_2O_3 (e), and powder X-ray diffractogram of Pt/TiO_2 (c) and Pt/Al_2O_3 (f) showing the presence of FCC−Pt.

The catalysts were initially tested in a fixed bed reactor set-up with all components in the gas phase (see appendix 1 for detailed experimental procedures). The formation of interesting products, such as methoxy methanol and 1,3,5 trioxane, was observed when flooding the reactor (see Fig A2.1 and A2.2, appendix). Hence, a dedicated trickle bed reactor was constructed (see Appendix 1, Fig. A1.1 and A1.2) and the catalysts shown here were tested under continuous flow conditions for their activity and selectivity in the aerobic oxidation of methane in this set-up at 220°C. Water was added to the feed whilst keeping the inlet partial pressure of methane and oxygen constant at 0.5 bar and 1.5 bar, respectively. Typical runs lasted several hundreds of hours regularly returning to standard conditions (Fig. A2.3 and A2.5).

Fig. 4.2a–d shows the steady-state activity and selectivity in the oxidation of methane over the reduced platinum catalysts at 220°C as a function of the molar inlet ratio of water to methane. The introduction of water in the feed results in an initial 10 to 50-fold drop in the rate of methane consumption at steady-state. The drop in the catalytic activity was expected as the surface becomes increasingly more covered with adsorbed water and surface hydroxyl species [273-275], thus reducing the likelihood of the direct interaction of methane with the bare platinum surface. Increasing the ratio of water to methane in the feed further, but keeping the fluid phase as a gas phase, has a positive effect on the catalyst activity.

Interestingly, the rate of methane oxidation starts to increase more rapidly upon entering the trickle-bed regime i.e., with water now present as a liquid in the catalyst bed, which is observed at an inlet molar ratio of H_2O/CH_4 higher than 46 under the applied conditions. An activity of 35 $\mu mol/g_{cat}/h$ was obtained over Pt/TiO_2 with a feed ratio of H_2O/CH_4=204, which corresponds to a turnover frequency of 0.17 h^{-1} assuming a dispersion of platinum of 41 % (deduced from the particle size distribution in Fig. 4.1b). The obtained maximum rate of methane oxidation over Pt/Al_2O_3 was lower at 16 $\mu mol/g_{cat}/h$ (albeit at a lower inlet molar ratio of H_2O/CH_4 of 136).

The role of water in the aerobic, selective oxidation of methane was highlighted previously [27, 245, 248-250, 268, 269], but here we show unequivocally the need to perform the reaction in the presence of liquid water to accelerate the aerobic oxidation of methane. The increase in the activity upon entering the trickle bed regime changes gradually, possibly due to the incomplete wetting of the catalyst by liquid water [276]. The wetting efficiency (i.e., the fraction of surface covered by liquid water) increases with increasing superficial mass velocity

of the liquid, but under the applied reaction conditions the wetting efficiency is estimated [277] to be less than 40 % at the highest employed inlet molar ratio of H_2O/CH_4.

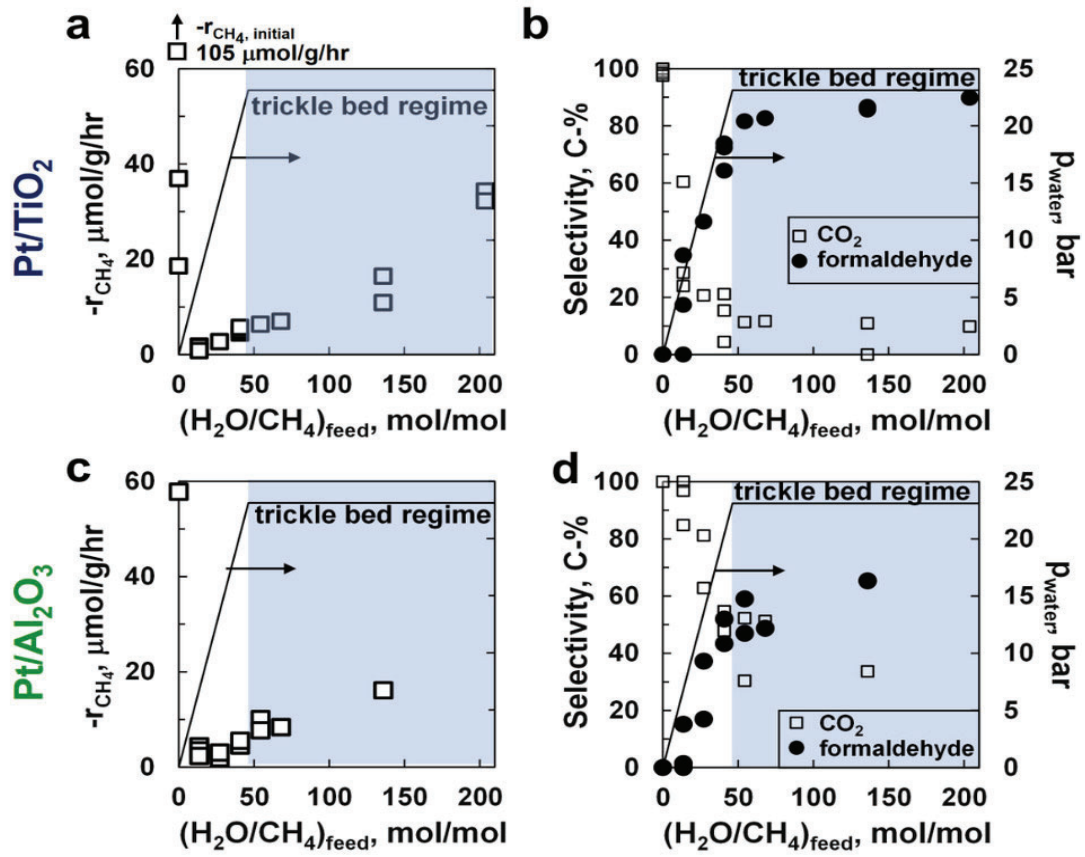

Figure 4.2: The rate of methane consumption over Pt/TiO_2 (a) and Pt/Al_2O_3 as a function of water partial pressure (c), and the corresponding selectivity for the formation of formaldehyde and CO_2 over Pt/TiO_2 (b) and Pt/Al_2O_3 (d). Operating conditions: $T_{reaction}$= 220°C, $p_{CH_4,\,inlet}$ = 0.5 bar, $p_{O_2,\,inlet}$ = 1.5 bar, $F_{CH_4,0}/W_{cat}$ = 3.23 mmol/g_{cat}/h.

The observed 3–20 times increase in the rate of methane oxidation upon partial wetting of the catalyst is surprising. The fugacity of water remains constant when moving into the trickle bed regime and thus the fraction of the surface covered with adsorbed water and species such as OH and O is not expected to change if these surface species are equilibrated with oxygen and water in the fluid phase. Various explanations for the observed strong increase in the rate of methane oxidation upon partial wetting of the catalyst can be put forward, viz. a change in the stability of the adsorbates through interaction with the liquid water [278], solvation effect of the product [27], or a kinetic effect if water is involved in the rate controlling step (wetting of the surface under the applied conditions results in a 100-fold increase in the concentration of

water near the catalytically active site). At this point no firm conclusions regarding the exact origin of this phenomenon can be made.

Increasing the water content in the feed induces a change in the product selectivity from forming only CO_2 in the absence of water to the selective formation of formaldehyde, with a selectivity of ca. 90 C-% when maintaining a H_2O/CH_4 ratio of ca. 100–200 in the feed over Pt/TiO_2. The high selectivity for the formation of formaldehyde is obtained before entering the trickle bed regime hinting at a decoupling between catalytic activity and selectivity.

The selective oxidation of methane often suffers from the so-called selectivity-conversion limitation [27, 28], wherein the selectivity of the desired selective oxidation product drops, often sharply, with increasing conversion. This can be rationalised by considering a common surface intermediate leading to the formation of the selective oxidation product and CO_x. Re-adsorption of the selective oxidation product will then result in enhanced formation of CO_x. A high rate for the consecutive oxidation of the common surface intermediate relative to the net rate of desorption of the selective oxidation product will result in a sharp drop in the selectivity for the formation of the selective oxidation product upon increasing the conversion of methane.

Limiting the rate for the consecutive reactions leading to the formation of CO_x relative to the net rate of desorption should ultimately yield an (almost) constant selectivity for the selective oxidation product as a function of the conversion. Transforming the obtained data at different inlet ratios of water to methane (Fig. A2.3 and A2.5) into a plot of the formaldehyde selectivity as a function of the methane conversion (Fig. 4.3) shows that the selectivity for the formation of formaldehyde is almost constant at a high $(H_2O/CH_4)_{feed}$ (>50) and does not decrease with increasing conversion (up to $X_{CH_4} \approx 3\%$ for Pt/TiO_2). The observed increase in the selectivity for the formation of formaldehyde with increasing conversion at lower conversion levels is attributed to the different kinetic regimes, to which the catalyst was exposed at the lower inlet ratios of methane to water.

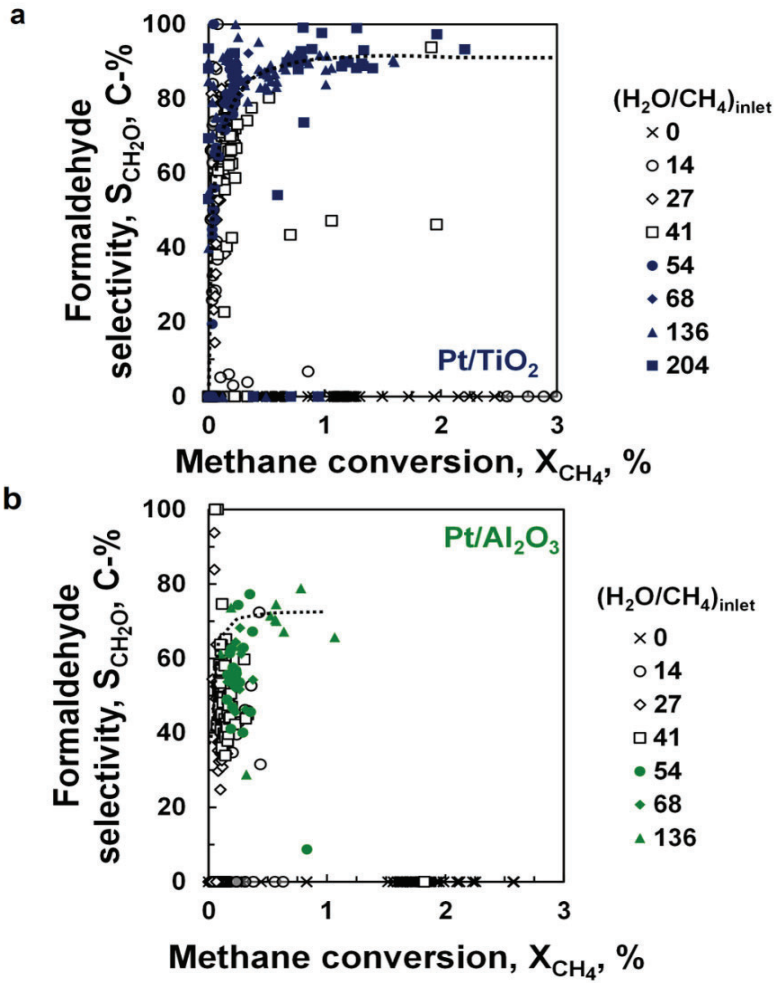

Figure 4.3: Selectivity of formaldehyde as a function of the methane conversion over Pt/TiO_2 (a) and Pt/Al_2O_3 (b) (x: without water in the feed; open symbols: gas phase reaction; solid symbols: trickle bed conditions). Operating conditions: $T_{reaction}$=493 K, $p_{CH_4,\,inlet}$ = 0.5 bar, $p_{O_2,\,inlet}$ = 1.5 bar, $F_{CH_4,0}/W_{cat}$ = 3.23 mmol/g_{cat}/h.

The formaldehyde selectivity over Pt/Al_2O_3 appears to be less than over Pt/TiO_2. Primarily formed formaldehyde can be further converted to CO_2, in particular over basic sites as present in boehmite [279], to which γ-Al_2O_3 transforms upon exposure to hydrothermal conditions at this temperature (vide infra). The conversion of formaldehyde may proceed directly or via a Cannizzaro-type of reaction involving formaldehyde and water (and indeed some methanol is sometimes observed under these conditions).

The kinetics of the selective oxidation of methane was further probed under trickle bed conditions (H_2O/CH_4=54) in a separate run starting with freshly reduced Pt/Al_2O_3 catalyst. The rate of methane consumption is independent of the partial pressure of methane (Fig. 4.4a). A first order dependency is expected if the reaction is limited by methane activation; a rate of

reaction independent of the methane partial pressure indicates that the rate determining step involves species whose surface concentrations are hardly affected by the change in the methane partial pressure (e.g., because their surface concentration is at its saturation level).

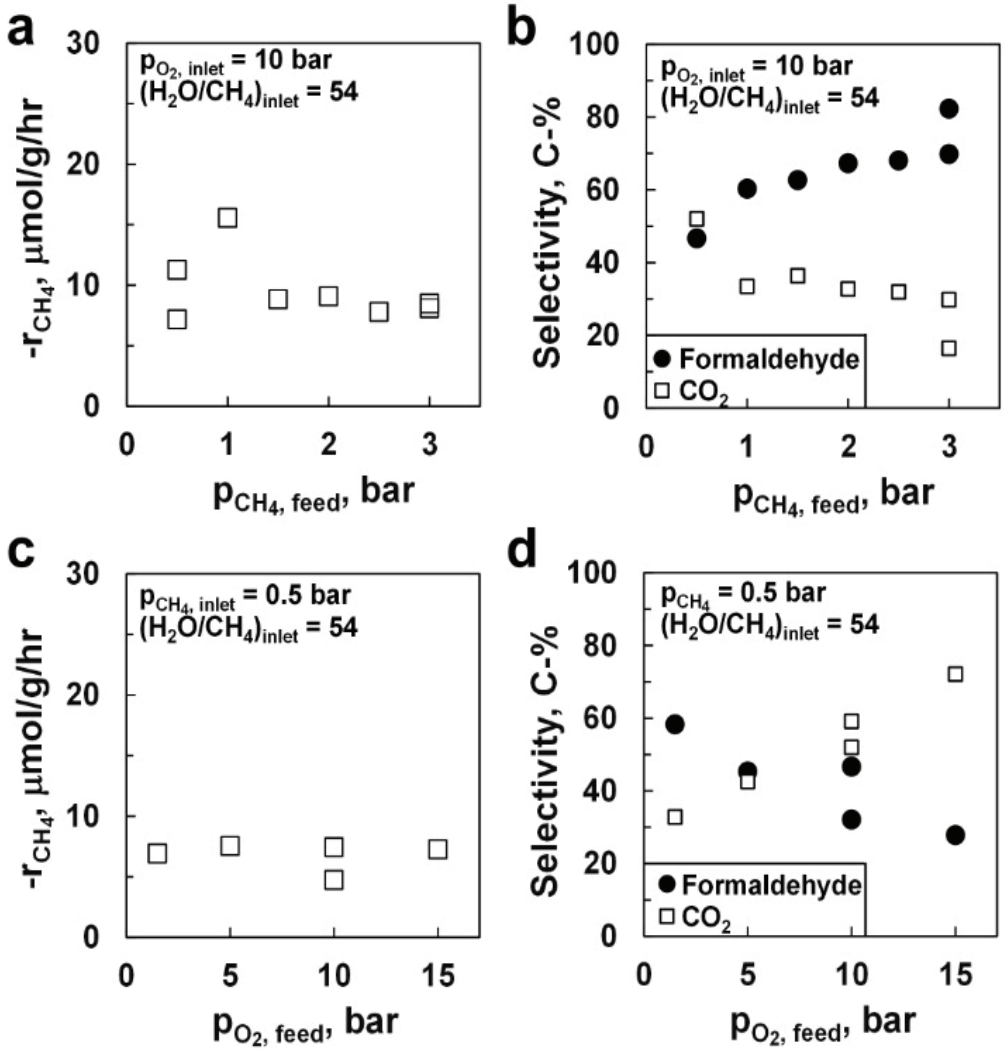

Figure 4.4: The effect of the methane partial pressure ($p_{O_2, inlet}$ =10 bar) on the rate of methane oxidation (a) and formaldehyde selectivity (b) over Pt/Al_2O_3, and the effect of the oxygen partial pressure ($p_{CH_4, inlet}$ =0.5 bar) on the rate of methane oxidation (c) and formaldehyde selectivity (d) over Pt/Al_2O_3 under trickle bed conditions at 220°C, p_{H_2O} =23.1 bar, $(H_2O/CH_4)_{feed}$ =54 and $F_{CH_4,0}/W_{cat}$ = 3.23 mmol/g_{cat}/h.

The rate of oxidation of methane under trickle bed conditions over Pt/Al_2O_3 is also independent of the oxygen partial pressure (Fig. 4.4c). This implies that the partial pressure of oxygen does not affect the surface coverage of the species involved in the rate determining step. The observed kinetic dependencies are consistent with the desorption of the selective oxidation

product being the rate controlling step in the aerobic oxidation of methane over Pt/Al_2O_3 under the applied conditions.

The selectivity for the formation of formaldehyde over Pt/Al_2O_3 increases first strongly and then gradually with increasing partial pressure of methane (Fig. 4.4b). A selectivity of 69 % for the formation of formaldehyde was observed when starting up the reaction and exposing the catalyst to a feed with $p_{CH_4,\,inlet}$ =3 bar (and $p_{O_2,\,inlet}$ =10 bar; $(H_2O/CH_4)_{feed}$=54). Subsequently, the methane partial pressure was dropped to 0.5 bar (keeping the partial pressure of oxygen and the feed ratio of water to methane constant) resulting in a drop in the selectivity of formation of formaldehyde to 47 % (the lower selectivity for the formation of formaldehyde at these inlet conditions was verified in an independent measurement). The inlet partial pressure of methane was subsequently increased stepwise resulting in an increase in the selectivity for the formation of formaldehyde. Returning to an inlet partial pressure of methane of 3 bar yielded a selectivity for the formation of formaldehyde of 82 % over this catalyst. This implies that the selectivity may not only be affected by the change in the partial pressure of methane but also by changes in the catalyst, although this does not affect the catalyst activity.

The selectivity for the formation of formaldehyde decreases with increasing partial pressure of oxygen (Fig. 4.4d). This might be attributed to a secondary conversion of primarily formed formaldehyde to CO_x [28, 237, 279].

The catalysts showed signs of deactivation (Fig. A2.3, A2.5 and A2.6), as indicated by activity loss during periodic returns to operating conditions in the absence of water and/or an inlet molar ratio of water to methane in the feed of 14. The platinum particle size distribution in the Pt/TiO_2 catalyst after exposing it to the strong hydrothermal conditions of methane oxidation for more than 300 hrs was almost unchanged (Fig. 4.5a) and a platinum dispersion of 39 % was determined (based on the whole particle size distribution in Fig. 4.5b). The powder X-ray diffraction pattern (PXRD) of Pt/TiO_2 shows that the titania support remained present in the rutile phase and platinum as FCC−Pt (Fig. 4.5c). The attenuated total reflectance-infrared (ATR-IR) spectrum of the recovered catalyst shows the appearance of a new strong absorption band at 999 cm^{-1} (Fig. 4.5d), which is attributed to C−O−C stretching in polyoxymethylene with a low degree of polymerization or paraformaldehyde [280, 281]. The absorption bands at 1417 cm^{-1} and 1472 cm^{-1} are indicative of the C−H bending mode in polyoxymethylene [282]. Deposition of the oligomers of formaldehyde or polyoxymethylene on Pt/TiO_2 may thus be the cause of the observed catalyst deactivation in this catalyst.

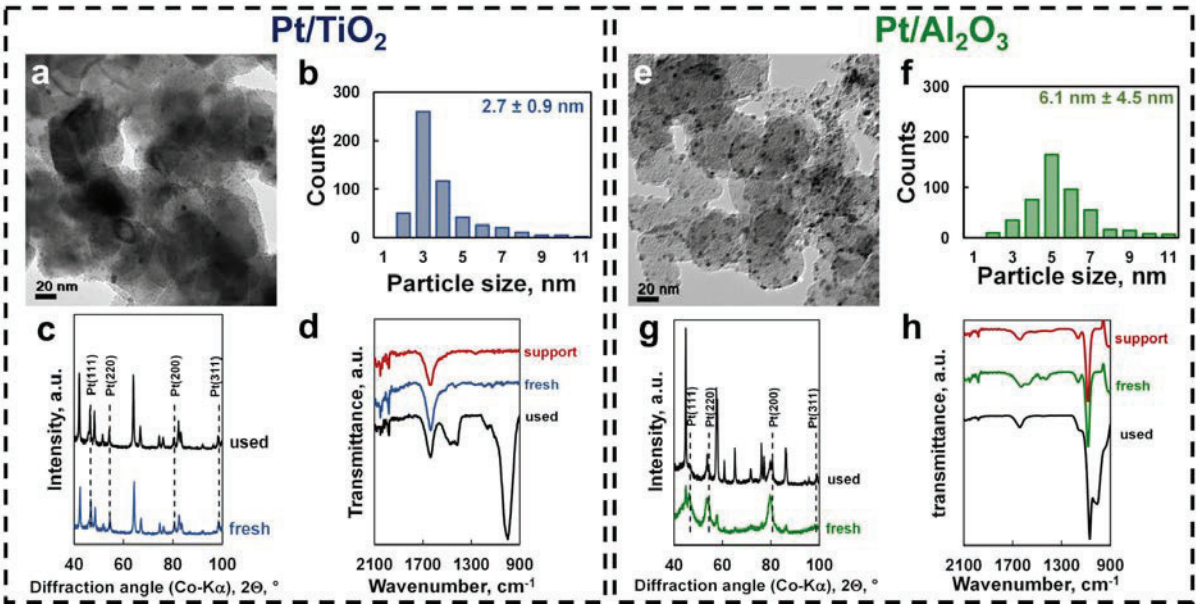

Figure 4.5: Transmission electron micrograph of the recovered 10 wt. % Pt/TiO_2 catalyst (a) and the Pt/Al_2O_3 catalyst (e), particle size distribution of platinum on Pt/TiO_2 (b) and Pt/Al_2O_3 (f), powder X-ray diffractogram of Pt/TiO_2 (c) and Pt/Al_2O_3 (g) before and after exposure to the hydrothermal condition of the selective, aerobic oxidation of methane, and the ATR-FTIR spectra of the support and the samples before and after testing Pt/TiO_2 (d) and Pt/Al_2O_3 (h) in the selective oxidation of methane.

Large changes are observed in the Pt/Al_2O_3 catalyst after exposure to the hydrothermal conditions of selective oxidation of methane (Fig. 4.5e–h). The platinum dispersion in the recovered Pt/Al_2O_3 catalyst decreases from 46 % to 24 %. Furthermore, the alumina support in the catalyst has undergone a phase transition and is present mainly as boehmite in the recovered catalyst (Fig. 4.5g). Platinum is still present as FCC−Pt. The phase transition of γ-Al_2O_3 to boehmite under the applied hydrothermal conditions is rapid [283, 284] and is typically associated with a loss in the surface area of the support as well sintering of the deposited platinum particles [283], and thus a loss in the metal surface area. The metal loading of the recovered catalyst did not change, indicating that leaching of platinum did not occur. The ATR-FTIR spectrum shows again the strong absorption band at 1000 cm^{-1}, but the characteristic bands at ca. 1420 and 1470 cm^{-1} indicative of the C−H bending mode in polyoxymethylene [282] are absent. The appearance of the band at 1000 cm^{-1} may be related to the structural change in the support when exposing the catalysts to liquid water under reaction conditions.

The decrease in catalyst activity seen over Pt/Al_2O_3 is (at least partly) attributed to the change in the platinum metal surface area.

Density functional theory (DFT) calculations were performed to further investigate the preferential formation of formaldehyde over platinum-based catalysts. The calculations focused on the Pt(111) surface as this surface is expected to be dominant on platinum nano-particles [285, 286]. Furthermore, oxygen-containing species are bonded weaker on Pt(111) than on Pt(100) [287], and product compounds adsorbed on Pt(111) may desorb more readily.

First, the phase space of the coverages with atomic oxygen, surface hydroxyl groups and adsorbed water were explored on a ($\sqrt{3}\times\sqrt{3}$)-Pt(111), a (2×2)-Pt(111) and a (3×3)-Pt(111) surface using ab initio thermodynamics [288] to map out conditions at which the surface could be fully covered with oxygen containing species (the selective oxidation of methane is thought to be facilitated when the surface is fully covered with oxygen containing species) [238]. Many different possible configurations have been probed (Table A2.2). This map gives thus a reasonable indication of the favourable reaction conditions for the selective aerobic oxidation of methane.

At a low chemical potential of water (corresponding to a low partial pressure of water), the coverage of Pt(111) with oxygen is limited to ca. 0.50 ML (Fig. 4.6a), a value in good agreement with the experimental saturation coverage with oxygen of 0.44 ML [272]. Higher surface coverage may be obtained by exposing the platinum surface to a mixture of water and oxygen as surface hydroxyl species can form a so-called honeycomb structure on the surface [273-275], in which 2/3 of the surface is covered with adsorbate. Surface coverages of 80–89 % have been reported experimentally [275] and they become thermodynamically stable at higher chemical potential of water and oxygen (i.e., at elevated partial pressures).

For instance, a structure containing 0.33 ML H_2O and 0.67 ML OH (Fig. 4.6a) was determined to be the most stable structure at 493 K and a chemical potential of oxygen of 0 eV (relative to the chemical potential of oxygen at 493 K and 1 bar) and a chemical potential of water of 0.04 eV (relative to the chemical potential of water at 493 K and 1 bar), which corresponds to a partial pressure of oxygen and water of 1 and 2.6 bar, respectively. In this structure, all surface platinum atoms on Pt(111) are covered with adsorbate species. The structure containing a coverage of 0.50 ML H_2O and 0.50 ML OH (as indicated in Fig. 4.6a) will not exist as water condenses out at a chemical potential of 0.133 eV relative to the chemical potential of water at 1 bar and 493 K.

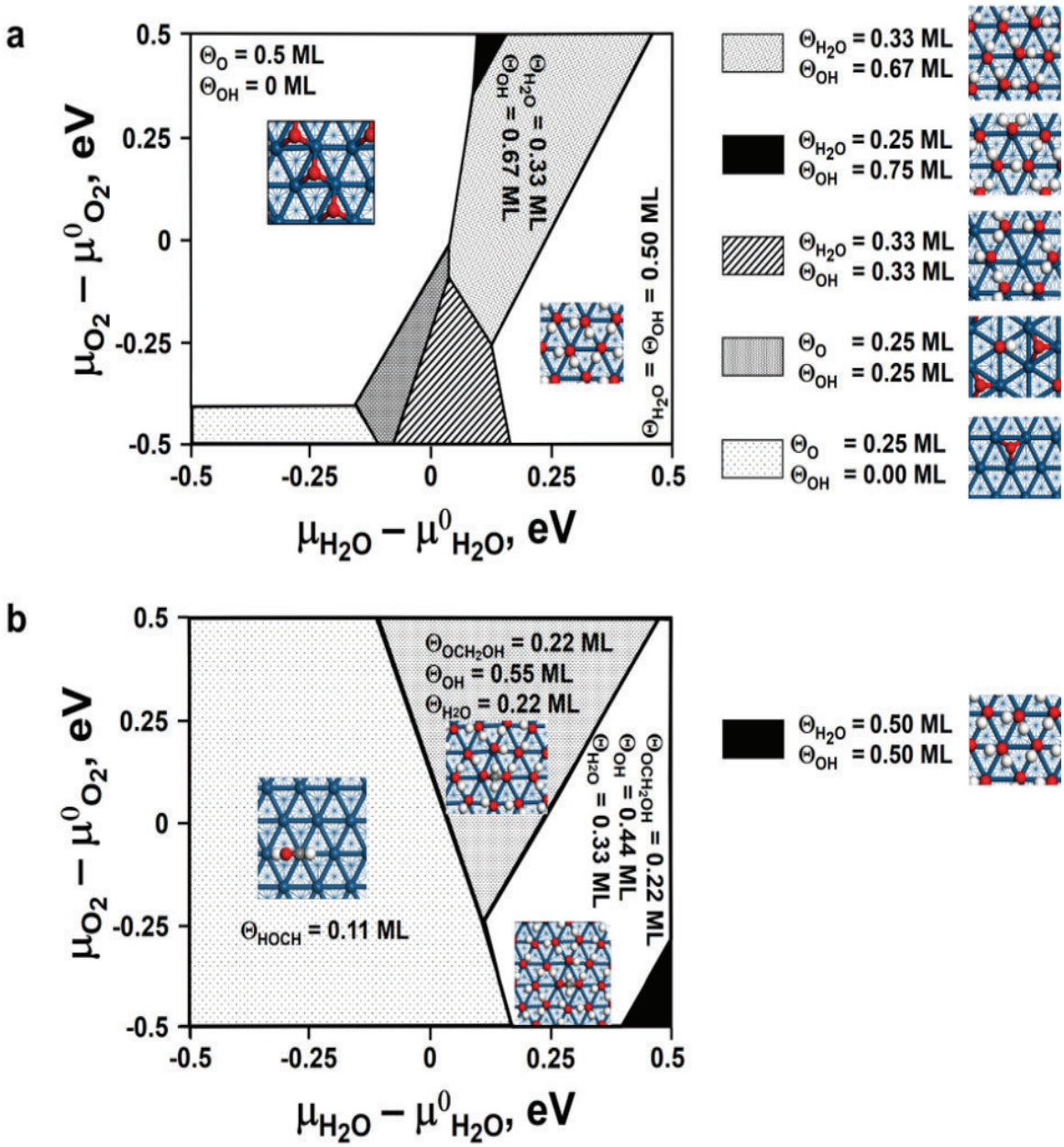

Figure 4.6: Surface phase diagram upon adsorption of H_2O and O_2 (a) and H_2O, O_2 in the presence of CH_4 ($p_{CH_4,\ inlet}$ =0.5 bar) (b) at 493 K on Pt(111) (chemical potential of O_2 and H_2O relative to their chemical potential at 493 K and 1 bar;—note water will condense at $\mu_{H_2O} - \mu_{H_2O}^0$ =0.133 eV and T = 493 K; hydrogen: white; oxygen: red; surface platinum: dark cyan).

The activation of methane on Pt(111) partially covered with adsorbed atomic oxygen may result in the formation of a surface methyl species, a surface methoxy species, adsorbed di-σ formaldehyde [289] or further decomposition products [290]. At a low chemical potential of oxygen and water and a partial pressure of methane of 0.5 bar (Fig. 4.6b), a surface hydroxy

methylene species is the most stable intermediate on Pt(111). Hydroxy methylene does not desorb as formaldehyde but rather decomposes to CO [291]. The interaction of methane with Pt(111) saturated with adsorbed H_2O and OH species, which is obtained at higher chemical potential of water, favours the formation of a very stable di-σ-hydroxy-methoxy species. Upon increasing the oxygen partial pressure, this intermediate becomes the most stable species at a lower partial pressure of water and may play an important role in the selective oxidation of methane.

The direct formation of formaldehyde with high selectivity (up to 90 C-% at a methane conversion of up to 3 % over Pt/TiO_2) is observed in the selective oxidation of methane over platinum. A pathway leading to the formation of methanol and formaldehyde can be easily established over a bare Pt(111) surface (Scheme 4.1a), if the activation of methane results in the formation of a surface methoxy species [238, 245]. Hydrogen transfer from either co-adsorbed water or surface hydroxyl species to the surface methoxy species would yield adsorbed methanol, and upon desorption yield methanol in the gas phase. Hydrogen transfer from the surface methoxy species to co-adsorbed hydroxyl species could result in the formation of adsorbed formaldehyde, CH_2O*, which could desorb resulting in the formation of formaldehyde is the gas phase. However, this reaction pathway cannot explain readily the preferred formation of formaldehyde over methanol as observed experimentally.

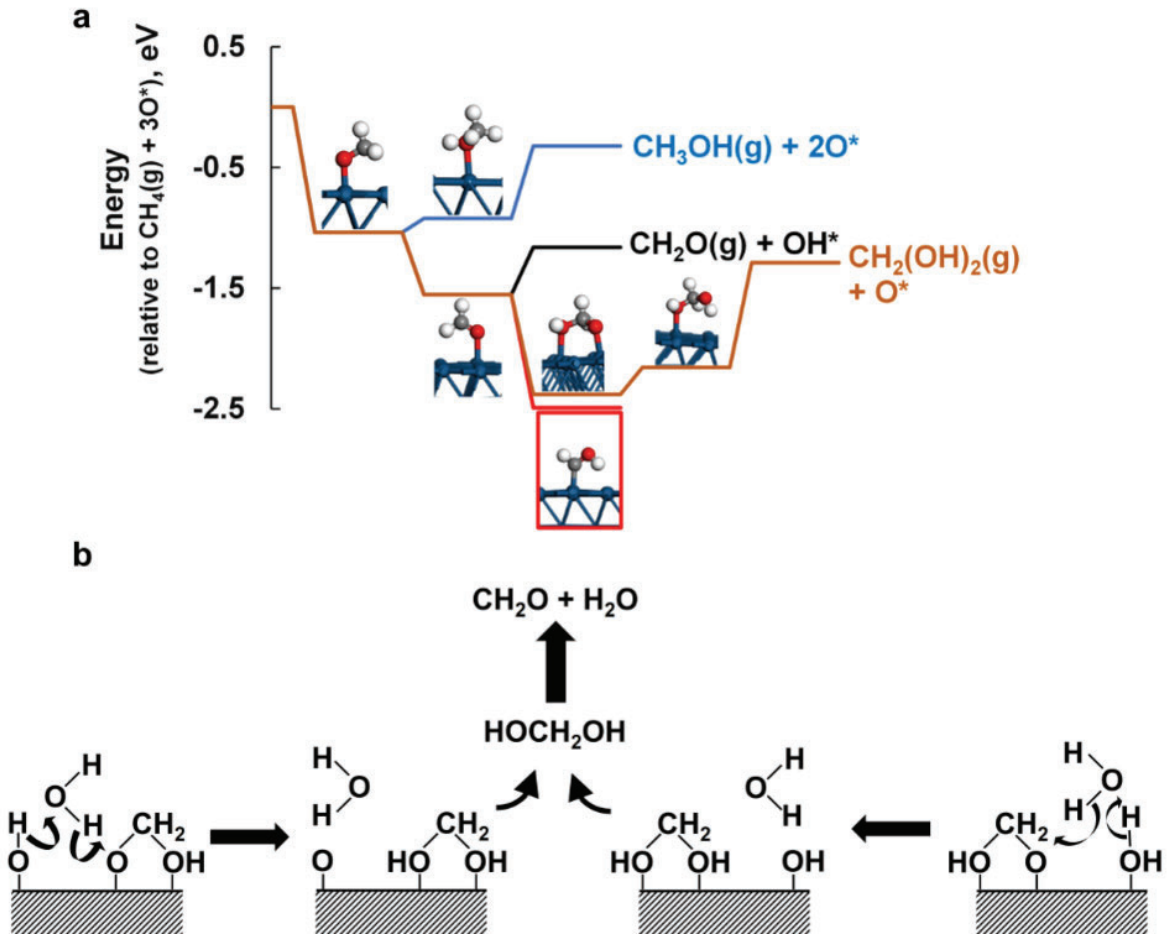

Scheme 4.1: Possible reaction pathway for product formation over Pt(111) in the selective oxidation of methane (a) and role of water as a H-transferring shuttle in the formation of methanediol (b).

The addition of a surface hydroxyl species to adsorbed formaldehyde may result in the formation of the stable di-σ-hydroxy-methoxy species. Hydrogen transfer from co-adsorbed water or surface hydroxyl species would result in the formation of adsorbed methanediol, which would desorb as the hydrated form of formaldehyde, methanediol [292]. The formation of the strongly adsorbed di-σ-hydroxy-methoxy species may explain the observed high selectivity for the formation of formaldehyde in the absence of formation of methanol. It may further result in the desorption (rather than methane activation) becoming the rate controlling step, in accordance with the observed zero order dependency of the rate of reaction with respect to the partial pressure of methane and oxygen.

The presence of liquid water in the selective oxidation of methane over Pt/TiO_2 and Pt/Al_2O_3 has been shown to enhance the rate of reaction. Various thermodynamic reasons for the

observed enhancement have been put forward [27, 278]; water may also have a kinetic effect, assisting in the hydrogen transfer between adsorbed surface intermediates, thereby enhancing product desorption (see Scheme 4.1b). Water will interact with adsorbed surface hydroxyl species, adsorbed water, and other surface species through H-bonding. Water in the liquid phase can orientate itself towards the surface species, thus maximizing its interaction with various surface species. Hydrogen transfer from a surface hydroxyl species or adsorbed water to a di-σ-hydroxy-methoxy species could be facilitated by a water molecule in the fluid phase interacting with both species, simultaneously accepting hydrogen from either an adsorbed hydroxyl species or adsorbed water and donating it to the di-σ-hydroxy-methoxy intermediate in a concerted reaction, which upon desorption would yield methanediol in the gas phase.

Methanediol can undergo various reactions in the reactor (and even in the reactor effluent). It may dehydrate resulting in the formation of formaldehyde [292], although its homogeneous uni-molecular decomposition rate is less than 2×10^{-6} s^{-1} [293] (but it may be facilitated by wall material). It may also polymerise/oligomerise resulting in catalyst deactivation (as evidence for polyoxymethylene was observed in the recovered Pt/TiO_2 catalyst).

4.4. CONCLUSION

The selective, aerobic oxidation of methane over platinum-based catalysts results in the selective formation of formaldehyde. The preferential formation of formaldehyde is thought to proceed via the strongly adsorbed di-σ-hydroxy-methoxy species on Pt(111) which would result in the formation of formaldehyde in its hydrated form, methanediol. The rate of reaction is independent of the partial pressure of methane and oxygen, but strongly affected by the presence of water in the feed. The reaction is further enhanced when the catalyst is in contact with liquid water. Water is thought not only to saturate the surface thus minimizing the presence of precursors for the formation of CO_x, but also to facilitate the desorption of the di-σ-hydroxy-methoxy intermediate yielding methanediol (formaldehyde hydrate) and formaldehyde.

Improved catalysts may be obtained by weakening the adsorption of the di σ-hydroxy-methoxy species, facilitating the desorption from the platinum surface as the desired product and reducing the extent of polymerisation on the surface. This may be achieved by alloying the catalytically active metal and altering the strength of oxygen/oxygen species adsorption by changing the d-band centre.

CHAPTER V:

IN SUPPORT OF SELECTIVE, AEROBIC METHANE OXIDATION TO FORMALDEHYDE: EFFECT OF CATALYST CARRIER ON ACTIVITY AND PRODUCT SELECTIVITY

Disclaimer:

The temperature programmed desorption studies were carried out at Sasol by Dr Alisa Govender (Co-Supervisor).

OVERVIEW

The influence of the support material (TiO_2, P25 and rutile, γ-Al_2O_3 and carbon black, C) on the performance and stability of platinum catalysts (10 wt.-% Pt) for the aerobic, selective oxidation of methane in the presence of liquid water was investigated. The catalysts were active for the oxidation of methane to CO_2 in the absence of water and became selective for the formation of oxygenates, particularly formaldehyde, upon the introduction of water in the feed. Platinum supported on carbon was the best performing catalyst, with a methane conversion of up to 4% and a selectivity for the formation of formaldehyde of up to 98%.

Over platinum supported on the rutile phase of TiO_2, a selectivity for the formation of formaldehyde of 90% was obtained at a conversion of methane of 1%. The Pt/Al_2O_3 catalyst achieved a maximum conversion of 0.5% and a formaldehyde selectivity of 65%. A high conversion (4%) and a high selectivity towards formaldehyde (99%) was obtained over Pt/C. The oxidation of methane over the Pt/TiO_2-P25 catalyst yields some methanol and methoxy-methanol, but performed poorly in terms of selectivity. The selectivity appears to be linked to the presence of acidic and basic sites in the catalyst.

The findings discussed here present an argument for the careful screening of an optimal support, particularly for use in the aerobic, selective oxidation of methane in the presence of water.

5.1. JUSTIFICATION FOR INVESTING THE EFFECT OF SUPPORT IDENTITY

A number of studies [28, 245, 248, 251, 262, 294] have noted the importance of water as a co-reactant in the selective oxidation of methane. Water may enhance the dissociation of molecularly adsorbed oxygen on a metallic catalyst surface [295], and may promote the formation of the precursors to the selective oxidation products (methanol or formaldehyde), such as adsorbed methoxy species, or di-σ-hydroxy-methoxy species [245, 248, 251, 262]. Furthermore, it may act as an extracting agent which assists the desorption of the selective oxidation products from the catalyst surface, thereby preventing their further oxidation [27, 262, 294, 296].

Although the nature of the catalytic site is of great importance, the selective oxidation of methane may also be affected by the type of support used, especially when water is used as a reaction medium [241, 297]. Water may interact with the support to generate Brønsted acid/base sites that may influence the selectivity during the selective oxidation of methane [298]. The wettability of the support may also influence the catalyst productivity and stability [185, 299]. Besides productivity, catalyst stability under process conditions is equally important [300], thus influencing the choice of material used as a catalyst support [284]. Reports on the selective oxidation of methane do not however specifically interrogate the role of the support, particularly with respect to stability, rather focusing on the active phase [65, 79, 205, 301].

In the previous chapter, it was observed that platinum supported on titania (rutile) resulted in a highly selective catalyst for the formation of formaldehyde in the selective oxidation of methane under trickle bed conditions. A lower selectivity for the formation of formaldehyde was obtained over platinum supported on alumina. The Pt/TiO_2-Rutile and Pt/Al_2O_3 catalysts also underwent significant deactivation with time. In this chapter, the effects of the support identity are probed further, focusing on their acid/base properties and affinity to water, and how these influence the behaviour of the catalyst with time, and product distribution during the selective oxidation of methane in the presence of liquid water. Furthermore, Pt/TiO_2-P25 was studied to compare the role of the titania crystal phase and Pt/C was studied as a possible alternative support.

5.2. EXPERIMENTAL PROCEDURE

The catalysts were prepared by wetness impregnation (see Appendix 2, Section I). The characterisation techniques and methodology, and catalyst activity evaluation procedures are explained in full in Appendix 3, sections I-III.

5.3. RESULTS AND DISCUSSION

5.3.1. CATALYST CHARACTERISATION

The platinum loading on all catalysts was confirmed to be 10 wt.-% using elemental analysis (Table 5.1) and thermogravimetric analysis (Figure A3.1). Figure 5.1(a-d) shows the XRD patterns of Pt/TiO_2-P25, Pt/TiO_2-Rutile, Pt/Al_2O_3 and Pt/C catalysts. All the freshly reduced catalysts show the diffraction lines at $2\theta = 46.4^o$, 54.3^o, 80.3^o, 98.3^o, 104.0^o, consistent with the presence of face-centred cubic (fcc) metallic Pt. The average crystallite domain size of platinum nanoparticles was difficult to determine due to peak overlap for the oxide supported catalysts. The X-ray diffractogram of Pt/C showed broad reflections due to the presence of small FCC-Pt nanoparticles as well as some sharp reflections indicating the presence of larger FCC-Pt particles (see Fig. 5.1d). Rietveld refinement resulted in a crystalline domain size for FCC-Pt of 1.1 nm (accounting for 95 wt.-% of platinum) and 26.1 nm (accounting for 5 wt.-%).

Transmission electron microscopy bright field (TEM-BF) images showed well-dispersed platinum nanoparticles on the support materials with well-defined near-spherical shapes (Fig. 5.2a-d). Histograms representing the size distributions of platinum nanoparticles measured from TEM images are shown as insets in Figure 5.2(a-d). The average platinum nanoparticle sizes were 2.8 ± 2.3 nm (Pt/TiO_2-P25), 3.2 ± 1.5 nm (Pt/TiO_2-Rutile), 3.6 ± 3.5 nm (Pt/Al_2O_3) and 1.7 ± 0.4 nm (Pt/C). Large particles as evidenced using XRD were not seen in the TEM images. Furthermore, the particle sizes calculated from the platinum dispersion using hydrogen chemisorption were determined to be 4.0 nm (Pt/TiO_2-P25), 4.9 nm (Pt/TiO_2-Rutile), 3.2 nm (Pt/Al_2O_3) and 2.7 nm (Pt/C). The larger particle sizes determined using chemisorption for Pt/C is consistent with the presence of larger Pt particles in the material as evidenced using XRD. The average particle sizes of these platinum nanoparticles calculated from both TEM-images and hydrogen chemisorption are summarized in Table 5.1.

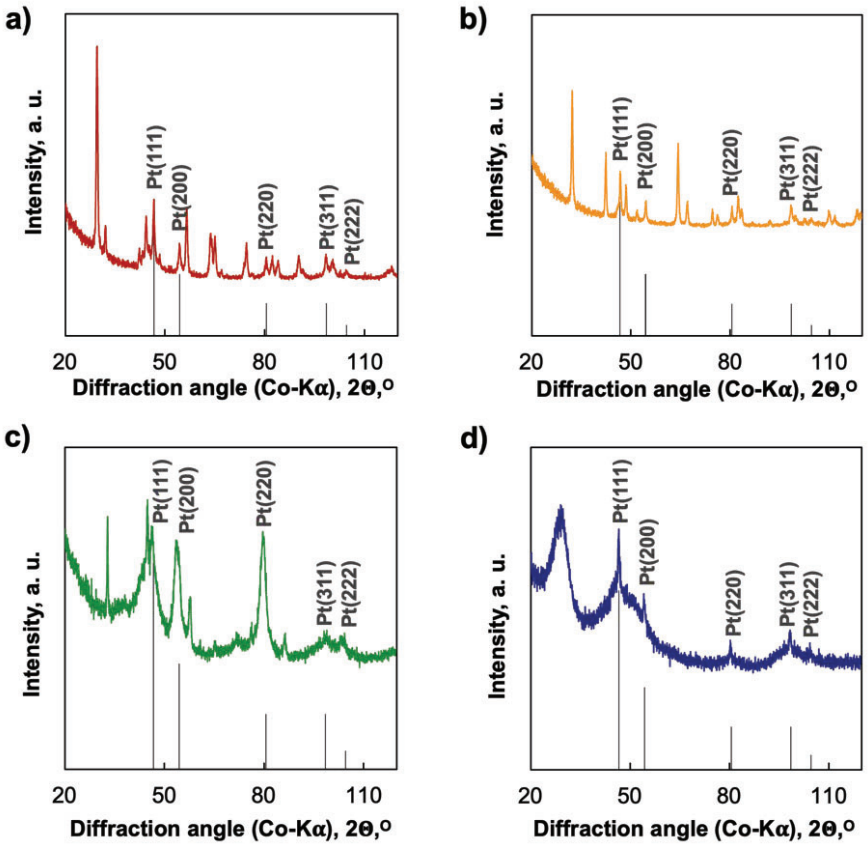

Figure 5.1: Powder X-ray diffraction patterns of the freshly reduced 10 wt.% platinum (Pt) supported on (a) TiO_2-P25, (b) TiO_2-Rutile, (c) Al_2O_3 and (d) carbon (C) before catalytic measurements showing the diffraction lines for FCC-Pt.

Table 5.1: Physico-chemical properties of the freshly reduced catalysts

Catalyst	**w_{Pt}[a] wt. %**	**S_{BET}[b] m^2/g**	**D_{Pt}[c] %**	**$d_{Pt,chem.}$[d] nm**	**$d_{Pt,TEM}$[e] nm**	**$n_{ads,\ IPA}$[f] µmol/g**	**$n_{ads,\ CO2}$[g] µmol/g**
Pt/TiO_2-P25	9.5	42 ± 0.07	28	4.0	2.8 ± 2.3	290	17
Pt/TiO_2-Rutile	10.0	24 ± 0.04	23	4.9	3.2 ± 1.5	75	28
Pt/Al_2O_3	10.2	51 ± 0.07	35	3.2	3.6 ± 3.5	394	293
Pt/C	10.0*	204 ± 0.7	42	2.7	1.7 ± 0.4	228	10

[a]Platinum loading determined using ICP-OES, [*]platinum loading determined from TGA-DSC; [b]BET-surface area of the catalyst; [c]Dispersion of platinum from hydrogen chemisorption assuming $H/Pt_{surface}=1$; [d]Platinum particle size estimated from $d_{Pt} = \frac{113}{Dispersion\ (\%)}$; [e]Platinum particle size distribution deduced from TEM-images; [f]Amount of isopropyl amine adsorbed as

an indicator for the number Brønsted acid sites; [g]Amount of CO_2 adsorbed as an indicator for the number basic sites.

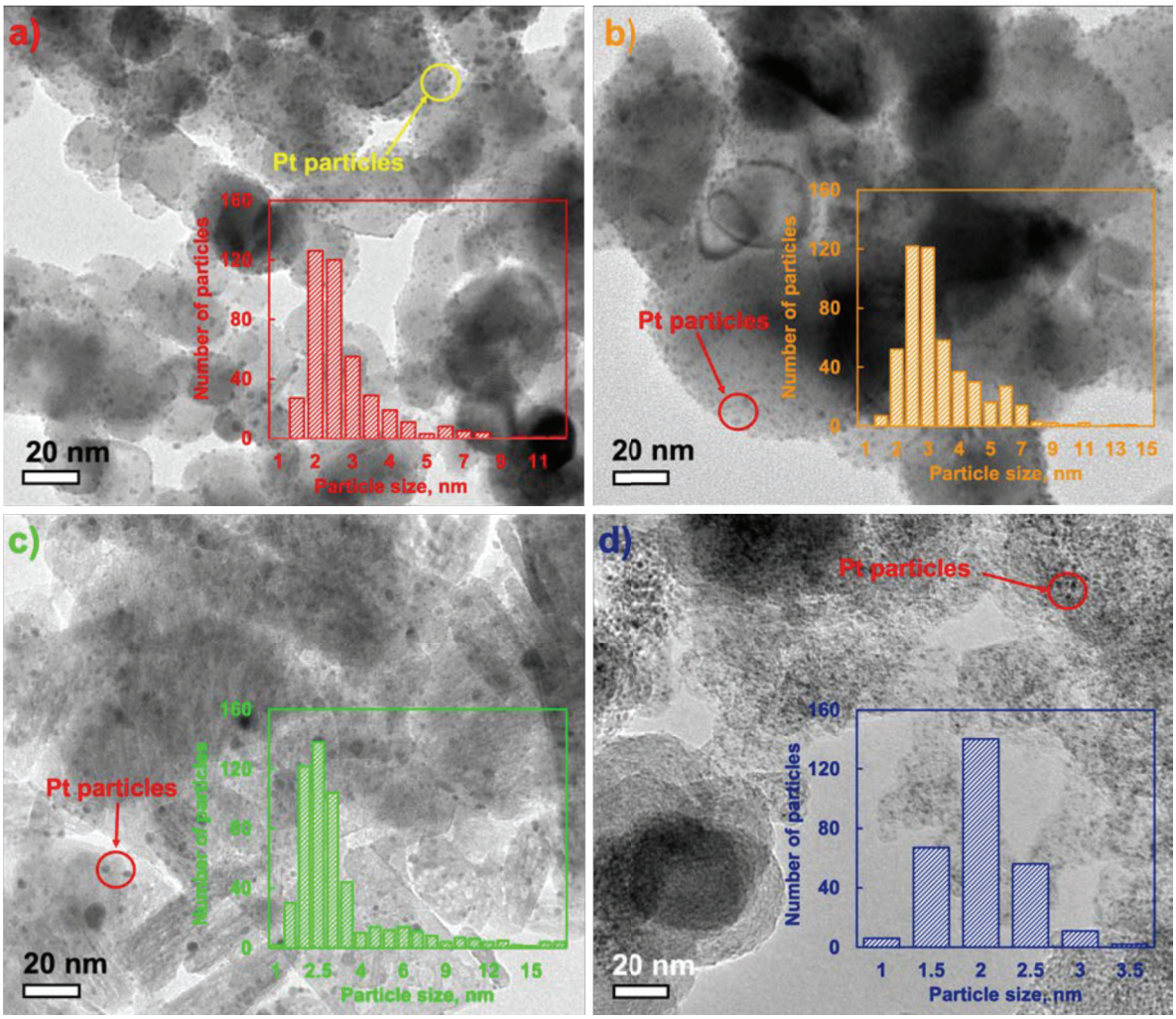

Figure 5.2: TEM-BF images of the freshly reduced (a) Pt/TiO_2-P25, (b) Pt/TiO_2-Rutile, (c) Pt/Al_2O_3 and (d) Pt/C catalysts. Insets are particle-size distribution histograms.

The acidity of the catalysts was probed using isopropylamine adsorption and the basicity was probed using CO_2 adsorption (see Table 5.1). The amount of isopropyl amine adsorbed per unit mass of catalyst, which can be correlated to the number of acid sites in the catalysts [302, 303], was lowest on the rutile supported catalyst, and highest on the alumina-supported catalyst (Table 5.1), but the number of acid sites per unit surface area was lowest on the carbon supported platinum catalyst (Table A3.1). The concentration of acid sites in Pt/TiO_2-P25 per unit surface area is twice the concentration of acid sites in Pt/TiO_2-Rutile. The strength of adsorption was probed using TPD. The temperature programmed desorption profiles of

isopropylamine decomposition products (i.e., ammonia and propylene), and water are shown in Figure 5.3 (a-c), together with the CO_2-TPD spectra (Fig. 5.3 d and e).

The evolution of ammonia (m/z=15) as a function of temperature during the TPD of isopropyl amine over the freshly reduced supported platinum containing catalysts (see Figure 5.3a) shows the occurrence of two events. The first desorption peak for ammonia coincides with the desorption of propene (m/z=41) and may be attributed to the dissociative desorption of adsorbed isopropyl amine on a Brønsted acid site via the well-known Hoffmann elimination [304]. The maximum for the first desorption peak (m/z=15 and m/z=41) for the oxide-supported catalysts is at similar temperatures (ca. 150°C) implying that they possess acid sites of similar strength. The presence of a second maximum for the desorption of both ammonia and propene indicates the presence of weaker acid sites as the Hoffman elimination occurs at higher temperatures. On Pt/Al_2O_3 the TPD of ammonia (m/z=15) shows a second maximum without the same desorption of propene. This could be explained by the desorption of ammonia formed in the Hoffmann elimination on vacated acid sites, which desorbs at higher temperatures.

A second maximum is observed in the TPD-spectrum of isopropyl amine over Pt/TiO_2-P25 for both ammonia (m/z=15, $T_{desorption}$= 302°C) and propene (m/z=41, $T_{desorption}$= 250°C), implying the presence of strong acid sites (catalysing the Hoffman elimination at ca. 150°C) and medium sites indicated by the desorption peak at ca. 250°C. Re-adsorption of ammonia does also affect the TPD spectrum of isopropylamine over Pt/TiO_2-P25, since the intensity of the 2nd desorption peak of propene (m/z=41) relative to the intensity of the 1st desorption peak of propene is less than the ratio of the two desorption peaks for ammonia (m/z=15) from this catalyst. Pt/TiO_2-Rutile also appears to have two types of acid sites, but re-adsorption of ammonia does appear to be less important (possibly due to the lower number of acid sites in this catalyst).
The acid sites on Pt/C appear to be weaker than on the oxide-supported catalysts as ammonia (m/z=15) and propene (m/z=41) appear at a higher temperature (ca. 220°) and thus the Brønsted acid sites on carbon catalyse the Hoffmann elimination less efficiently .

Water is also removed from the catalysts during the desorption of iso-propyl amine as evidenced by m/z=18 (Fig. 5.3b). One major desorption peak is observed for Pt/Al_2O_3 at 460°C as a consequence of the dehydroxylation of the alumina support [305]. The water desorption

profile from Pt/TiO_2-Rutile and Pt/C are marginal, while three desorption peaks are observed for Pt/TiO_2-P25 (140°C, 300°C and 450°C), which may correspond to the desorption of physisorbed water (~ 140°C), chemisorbed water (300°C) and dehydroxylation of the support (450°C) [306]. Significant evolution of water over Pt/Al_2O_3 and Pt/TiO_2-P25 was expected, since both supports are known to be hydrophilic [307, 308] and exposure of the freshly reduced catalyst to air may have resulted in water uptake.

CO_2-adsorption and its desorption were used to characterize the basicity of the support. The CO_2-uptake is generally low except on Pt/Al_2O_3, which adsorbs CO_2 in a similar amount as isopropylamine. Temperature programmed desorption profiles of CO_2 from the fresh catalysts are shown in Figure 5.3 (d and e). The molecular fragments monitored during CO_2-TPD are m/z=18 attributed to the desorption of water and m/z=44 attributed to the desorption of CO_2. Pt/TiO_2-P25 possesses medium to strong basic sites (with desorption peaks at 340°C and 550°C, respectively). The desorption profile of CO_2 from Pt/TiO_2-Rutile is rather flat, which may imply that the surface may not possess basic sites (or the basic site density is low). Pt/Al_2O_3 possesses medium and strong basic sites (420°C and 560°C) [309]. Determining the surface basicity of Pt/C from CO_2-TPD is not straightforward; desorption of CO_2 (m/z=44) from Pt/C is observed (see Fig. 5.3f), but the amount of CO_2 adsorbed was quite low (see Table 5.1). Hence, CO_2 observed in the TPD-profile may not originate from adsorbed CO_2 but might be a product of a partial decomposition of the carbon support.

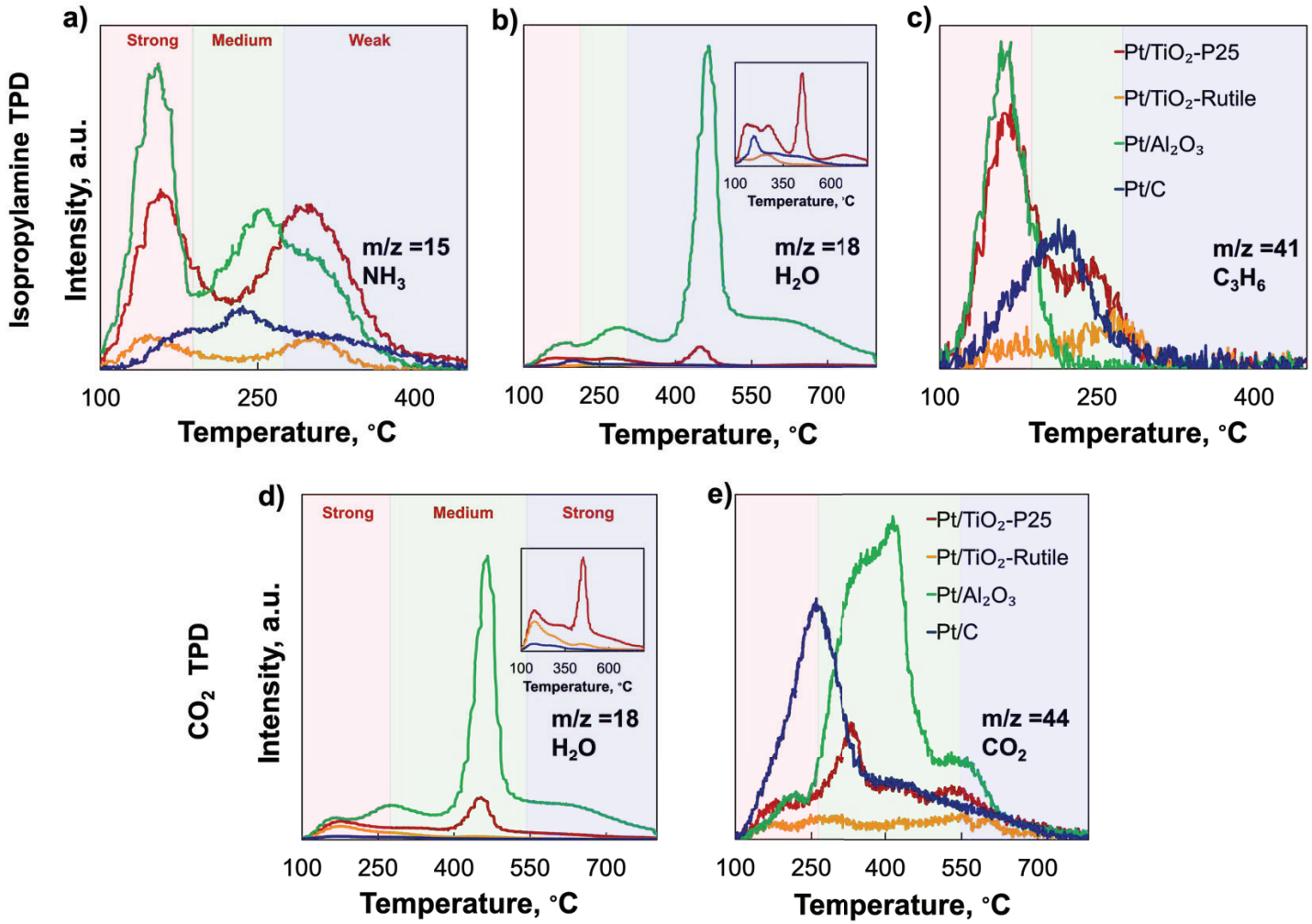

Figure 5.3: Desorption profiles of the fresh and recovered catalysts during the temperature programmed desorption of isopropyl amine (a-c) and carbon dioxide (d-f) showing the evolved molecular fragments of isopropyl amine and CO_2 desorption, in addition to the desorption of water from the catalyst samples.

5.3.2. CATALYTIC ACTIVITY AND SELECTIVITY

The catalytic activities of the different catalysts were evaluated in a trickle bed reactor (see Appendix I). The catalysts were exposed to varying amounts of water keeping the methane space velocity, and the inlet partial pressures of methane and oxygen constant. The performance of the catalyst is strongly dependent on the water to methane feed ratio. Figure 5.4 shows the catalytic activity obtained over the supported platinum catalysts as a function of the inlet feed ratio of water to methane (different datapoints at a fixed molar water to methane ratio have been collected at different times-on-line and thus correspond to different extent of catalyst deactivation; see Figures A3.2-A3.5 for the historical activity profiles of the catalysts).

The rate of methane conversion in the absence of water is high (see Fig. 5.4a, c, e, g), particularly for Pt/TiO_2. The initial activity was in the order of $Pt/C < Pt/Al_2O_3 < Pt/TiO_2$-Rutile $< Pt/TiO_2$-P25. The rate of methane consumption decreased strongly upon the introduction of water to the feed, but the subsequent increase in the molar ratio of water to methane in the feed resulted in an increase in the rate of methane conversion. The decrease in the rate of methane conversion upon the initial introduction of water can be attributed to the coverage of the catalytically active surface with surface OH or H_2O-species generated upon the interaction of water and oxygen with the platinum surface, thereby decreasing the number of sites available for the activation of methane on the metallic surface.

The rate of methane consumption increased substantially under trickle bed conditions ($H_2O/CH_4 > 46$ mol/mol), although the point at which the rate increased substantially differed for the various catalysts. The rate of methane consumption increases gradually over the oxide supported catalysts upon entering the trickle bed reactor regime, whereas the rate of methane consumption increases more strongly over Pt/C upon entering the trickle bed region. It is expected that the support material becomes partly wetted when approaching trickle-bed operation [276, 277]. Catalysts are inhomogeneous materials comprising of the metallic, catalytically active phase and the support. Over a more hydrophobic support, liquid water may be preferentially located around the metal particle, while it may be more evenly distributed in the case of a hydrophilic support [310].

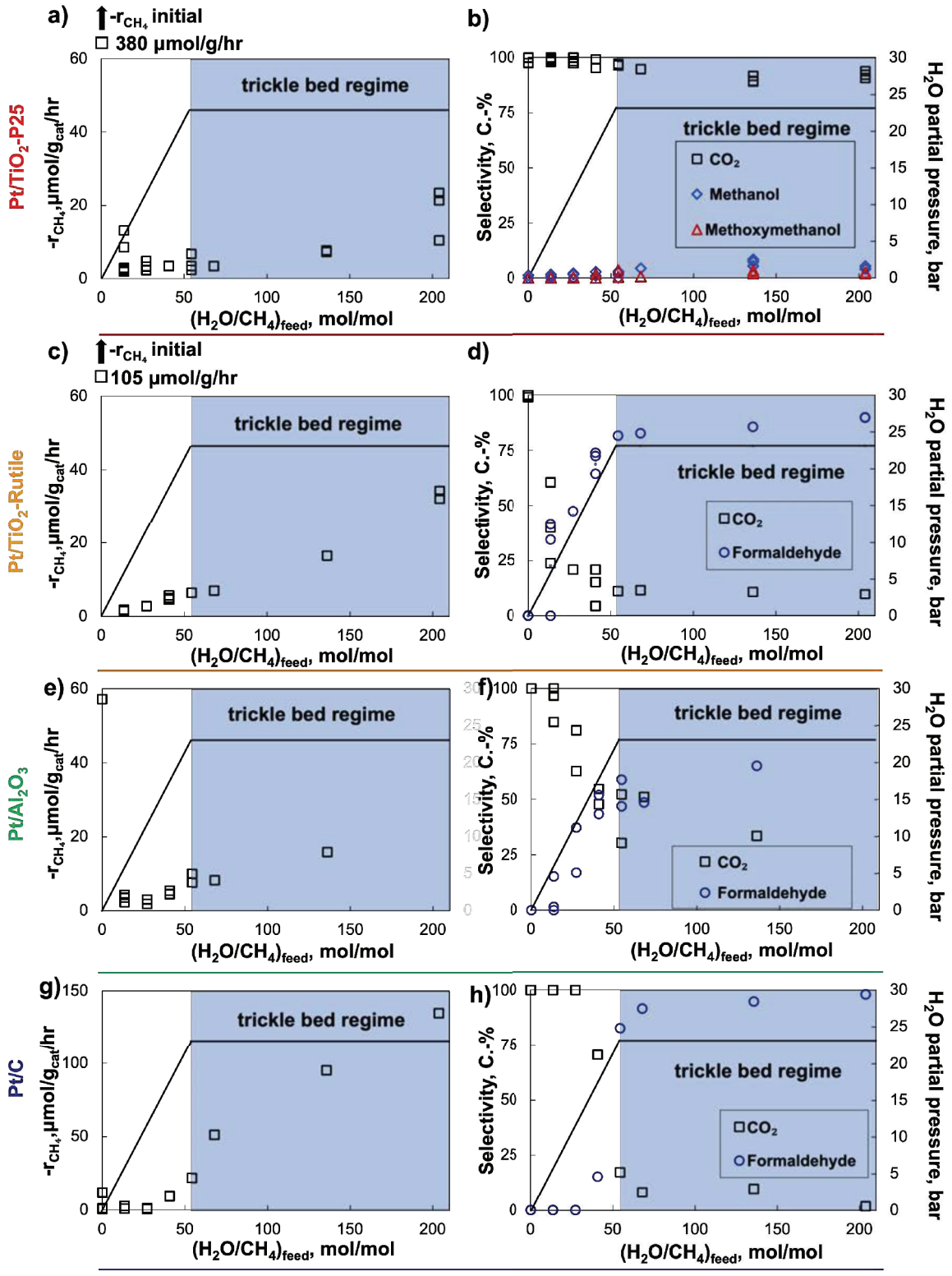

Figure 5.4: Rate of methane consumption and corresponding oxygenate selectivity as a function of the molar water/methane ratio in the feed over Pt/TiO_2-P25 (a, b), Pt/TiO_2-Rutile (c, d), Pt/Al_2O_3 (e, f) and Pt/C (g, h). Conditions: T=220°C, p=30 bar, $p_{CH_4,inlet}$=0.5 bar, $p_{O_2,inlet}$=1.5 bar, space velocity = 3.23 $CH_4/g_{catalyst}$/hr.

The introduction of water resulted in the formation of selective oxidation products such as methanol (CH_3OH), methoxy-methanol (CH_3O-CH_2OH) and mostly formaldehyde (CH_2O) over the supported catalysts (Fig. 5.4b, d, f and h). The first two products were only observed in the methane oxidation over Pt/TiO_2-P25 at a relatively low selectivity. However, even this catalyst initially showed the formation of formaldehyde (see also Figure A3.2), which switched to methanol and methoxy-methanol after pro-longed exposure to hydrothermal conditions.

The response of the formaldehyde selectivity to the increase in the H_2O/CH_4 mole ratio on the feed varies across the different catalysts. The formaldehyde response appears to be delayed on Pt/C, since even at a H_2O/CH_4 mole ratio of 27, the formaldehyde selectivity is still zero, while over Pt/TiO_2-Rutile and Pt/Al_2O_3 the formaldehyde selectivity is significant at this point. The formaldehyde selectivity undergoes a significant boost close to trickle-bed operation for the Pt/C catalyst (which is accompanied by an increase in the rate of methane conversion), and continues increasing in the trickle-bed regime. This may be an indication of the reaction rate being enhanced, which is caused by an increase in the rate of formaldehyde desorption, particularly when water is present in the liquid phase. Water may have a similar effect on the rutile-supported catalyst (which is also relatively hydrophobic).

The maximum selectivity for formation of formaldehyde in the selective oxidation of methane over Pt/Al_2O_3 is lower (65%) than over Pt/TiO_2-Rutile, which is lower than over Pt/C. The increase in the selectivity for the formation of formaldehyde appears to correlate with a decrease in the support acid/base properties (see Table 5.1) in addition to the support hydrophobicity. Hence, the difference in the selectivity for the formation of formaldehyde might be attributed to consecutive, support-catalysed conversion of formaldehyde to CO_2 via the possible formation of formate species, and their further conversion to CO_2 in the presence of oxygen, in addition to the conversion of formaldehyde to methanol and methoxymethanol [279]. Pt/TiO_2-Rutile showed a high selectivity for the formation of formaldehyde in the selective oxidation of methane In contrast to Pt/TiO_2-P25. Rutile is mildly acidic and lacks basicity compared to anatase (see also Table 5.1) [309]. This may have contributed to the sustained high selectivity for the formation of formaldehyde with extended reaction time (Figure A3.3).

The catalytic performance of the tested catalyst under trickle bed conditions, presented as productivity and turnover frequency (TOF), are summarized in Table 5.2. The turnover

frequency (determined based on the Pt-dispersion in the fresh catalyst) increases with the molar ratio of H_2O/CH_4 in the feed indicating an acceleration of the rate of reaction upon increasing the wetting efficiency on the catalyst [262]. The activation of methane over a platinum surface covered with H_2O and OH species in the presence of liquid water may yield a stable di-σ-hydroxy-methoxy intermediate, whose desorption may be facilitated by the presence of liquid water in its proximity [262].

It is interesting to note that the turnover frequencies obtained over Pt/TiO_2-Rutile and Pt/Al_2O_3 are similar whereas the TOF obtained over Pt/C is significantly higher under the same reaction conditions. The route for the activation of methane in this process is not yet clear. It may however be postulated that methane is activated over adsorbed oxygen atoms, which will, under these conditions, be present on the edge sites of platinum nanoparticles [287]. The fraction of surface sites present at the edge of nanoparticles is inversely related to size of the nanoparticles [311]. Hence, small platinum nanoparticles as present in Pt/C (with an average particle size of 1.7 nm) are expected to have a higher fraction of edge sites. This may result in a higher TOF over Pt/C compared to the TOF over the oxide-supported catalysts as the average Pt nanoparticle size on Pt/TiO_2-P25 is 2.8 nm, on Pt/TiO_2-Rutile 3.2 nm and on Pt/Al_2O_3 3.6 nm (Table 5.1).

Table 5.2: Summary of catalytic activity[a] for the aerobic conversion of methane under trickle bed conditions, the rate of formation of oxygen containing products over the supported platinum catalysts

Catalyst	**(CH_4/H_2O) mol/mol**	**X_{CH_4}, %**	**TOF[b], hr^{-1}**	**Productivity, µmol/g_{cat} /hr**			
				CH_3OH	**CH_3O-CH_2OH**	**CH_2O**	**CO_2**
Pt/TiO_2-P25	136	0.2 ± 0.01	0.04 ± 0.001	0.58 ± 0.12	0.22 ± 0.06	-	7.4 ± 0.1
	204	0.6 ± 0.2	0.10 ± 0.03	0.99 ± 0.48	0.46 ± 0.23	-	19 ± 6.8
Pt/TiO_2-Rutile	136	0.5 ± 0.05	0.08 ± 0.02	-	-	14 ± 8.7	1.8 ± 0.52
	204	1.0 ± 0.3	0.17± 0.02	-	-	30 ± 12	3.3 ± 2.0
Pt/Al_2O_3	136	0.5 ± 0.2	0.07 ±0.04	-	-	11 ± 6.9	5.8 ± 2.9
Pt/C	136	3.0 ± 0.75	0.29 ± 0.07	-	-	99 ± 23	0.3 ± 0.7
	204	4.2 ± 1.4	0.41 ± 0.13	-	-	132 ± 42	2.7 ± 0.6

[a] **Conditions**: T=220°C K, p=30 bar, $p_{CH_4,inlet}$=0.5 bar, $p_{O_2,inlet}$=1.5 bar O_2, space velocity = 3.23 $CH_4/g_{catalyst}$/hr; [b] Turnover frequency (TOF) based on the metal dispersion determined from $d_{Pt} = \frac{113}{Dispersion\ (\%)}$ of the fresh catalyst.

The selective oxidation of methane is often affected by the selectivity-conversion conundrum, in which high selectivity can be obtained at (very) low conversion, which drops (rapidly) upon increasing the conversion of methane [27, 28, 45, 252]. This is not observed upon changing the conversion of methane over Pt/TiO_2-Rutile, Pt/Al_2O_3 and Pt/C catalysts, when the conversion was changed by altering the inlet feed ratio of H_2O/CH_4. (see Fig. 5.5).

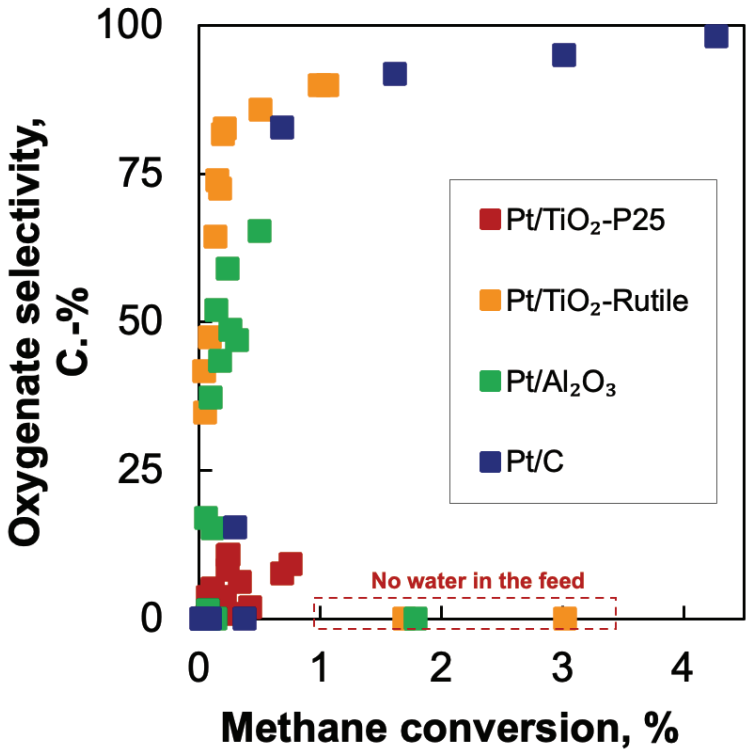

Figure 5.5: Selectivity for the formation of selective oxidation products as a function of the conversion of methane in the aerobic oxidation of methane in the presence of water (220°C, 30 bar, $p_{CH4,inlet}$=0.5 bar, $p_{O2,inlet}$=1.5 bar, space velocity = 3.23 mmol $CH_4/g_{catalyst}$/hr; conversion altered by changing $(H_2O/CH_4)_{inlet}$).

The selectivity for the formation of selective oxidation products over Pt/TiO_2-P25 increases slightly with increasing conversion, accompanied by a corresponding, but slight increase in the oxygenate selectivity (up to ca. 10%). A more pronounced, positive correlation between selectivity and conversion is obtained over Pt/Al_2O_3, Pt/TiO_2-Rutile (up to 1% conversion and formaldehyde selectivity of 90% for the latter) and Pt/C (4.2% conversion, 98% formaldehyde selectivity). These results and the trends compare favourably to those reported in literature (see Table A3.2).

5.3.3. CATALYST DEACTIVATION

The catalytic activity in the selective oxidation of methane was evaluated as a function of time-on-line varying the molar water/methane ratio. The extent of catalyst deactivation was determined by regularly returning to standard conditions (see Figs. A3.2-A3.5). Figure 5.6 shows the rate of methane consumption as a function of time-on line over all four catalysts at a standard condition (T=220°C, p=30 bar, $p_{CH_4,inlet}$=0.5 bar, $p_{O_2,inlet}$=1.5 bar, $(H_2O/CH_4)_{inlet}$=14). It should be noted that the catalyst was intermittently exposed to different $(H_2O/CH_4)_{inlet}$-ratios. At these conditions, all components are in the gas phase (p_{H_2O} = 6.8 bar). All four catalysts under investigation deactivated significantly. The extent of activity loss is in the order of Pt/TiO_2-Rutile (a_{loss}=84%) < Pt/C (a_{loss}=87%) < Pt/TiO_2-P25 (a_{loss}=88%) < Pt/Al_2O_3 (a_{loss}=94%).

The rate of deactivation appears to be catalyst specific with Pt/TiO_2-P25 deactivating gradually over the whole reaction time, whereas the other catalysts appear to deactivate more rapidly. Exposure of Pt/Al_2O_3 (and to a lesser extent Pt/C) to higher $(H_2O/CH_4)_{inlet}$-ratios appear to re-activate the catalyst temporarily. Post-mortem characterisation of the recovered catalyst (i.e. catalyst retrieved from the reactor after catalytic tests) was carried out to identify the likely cause of deactivation. Figure 5.7 shows the TEM-images and XRD-patterns of the recovered catalysts. Further physico-chemical characteristics of the recovered catalysts are summarized in Table 5.3.

The loss in activity over Pt/TiO_2-P25 as a function of the reaction time (Fig. 5.6a) is gradual, albeit quite extensive. This drop in activity cannot be attributed to a change in the available platinum surface area as the platinum dispersion as determined using hydrogen chemisorption hardly changes (ca. 26% in the recovered catalyst vs 28% in the freshly reduced catalyst). This is also confirmed by the platinum particle size distribution using TEM (2.6 ± 1.3 nm in the recovered vs 2.8 ± 2.3 nm in the freshly reduced catalyst, see Fig. 5.7a). Furthermore, platinum remains present as FCC-Pt as revealed by the XRD-pattern (see Fig. 5.7e).

Pt/TiO_2-Rutile loses its activity in the methane oxidation much more rapidly than Pt/TiO_2-P25 (see Fig. 5.6a and b). Again, the loss in activity cannot be attributed to a change in the available platinum surface area as the platinum dispersion as determined using hydrogen chemisorption hardly changes (ca. 24% in the recovered catalyst vs 23% in the freshly reduced catalyst), which is confirmed by the platinum particle size distribution determined using TEM (3.8 ±1.9

nm in the recovered catalyst vs 3.2 ±1.5 in the freshly reduced catalyst. Platinum also remains present as FCC-Pt which is indicated by the XRD-pattern (see Fig. 5.7f).

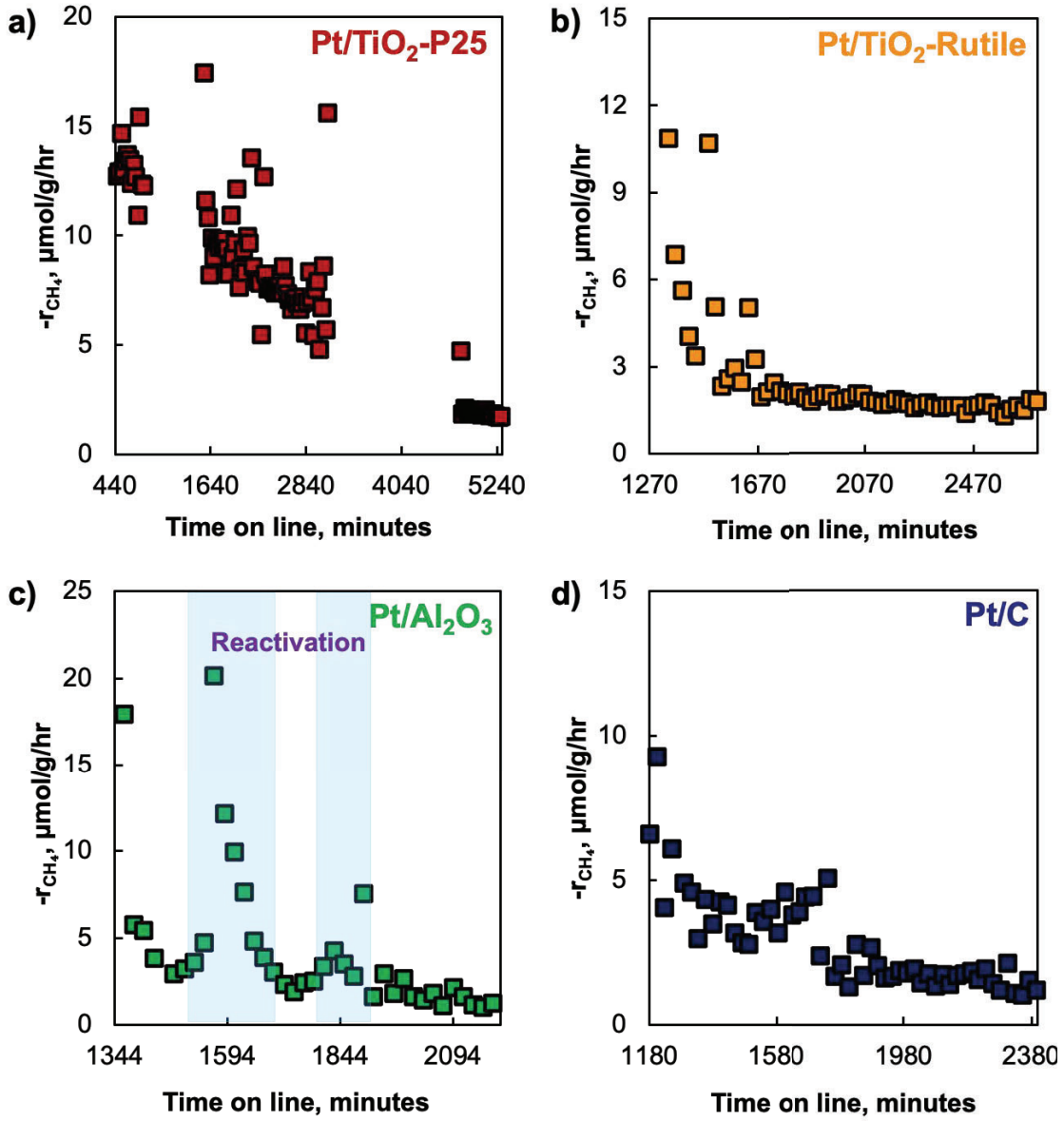

Figure 5.6: The loss of activity experienced by a) Pt/TiO_2-P25, b) Pt/TiO_2-Rutile, c) Pt/Al_2O_3 and d) Pt/C as determined at standard conditions (T=220°C, p=30 bar; $p_{CH_4,inlet}$=1.5 bar; $p_{O_2,inlet}$=1.5 bar, $p_{H_2O,inlet}$=6.8 bar, space velocity = 3.23 $CH_4/g_{catalyst}/hr$).

The activity of Pt/Al_2O_3 as a function of time-on-line at the standard conditions shows a more unusual behaviour; the catalyst appears to reactivate slightly (highlighted in blue), followed by deactivation. The catalyst shows evidence of severe sintering as the platinum dispersion determined from H_2-chemisorption decreases from 35% to 3.7%. Sintering is also evidenced

from the TEM-images showing a shift in the platinum particle size towards larger particles (see Fig. 5.7c). The extent of sintering may explain most of the observed deactivation. The strong change in the platinum dispersion may be related to the observed phase change of the support from γ-Al_2O_3 to boehmite, AlOOH (see Fig. 5.7g) upon exposure to these strong hydrothermal conditions [284, 312]. This is accompanied by a strong reduction in the number of acid sites in the catalyst [284].

Platinum on activated carbon (Pt/C) appears to deactivate more gradually than Pt/TiO_2-Rutile or Pt/Al_2O_3 (with some evidence of re-activation between 1560 and 1700 min online; see Fig. 5.6b, c and d). The catalyst showed excellent performance in the methane oxidation with a conversion of 4.2% and a selectivity for the formation of formaldehyde of 98% at 220°C and a molar inlet ratio of water to methane of 204 (vide infra). Increasing the feed ratio of water to methane further to 340 did not improve the formaldehyde yield, although the CO_2 yield increased strongly. The catalyst was subsequently unloaded, and the Pt-loading in the recovered catalyst was determined to be 30 wt.-% (see Table 3, and Fig. A3.1 a) implying a loss of the carbon support possibly due via gasification/combustion under the applied conditions.

The platinum dispersion in the recovered catalyst dropped from 42% to 6.9% (see Table 5.3) indicating that the loss of some of the carbon support material could have led to sintering [313]. This is also evidenced from the XRD-pattern, which showed sharp diffraction lines attributable to FCC-Pt (see Fig. 5.7h). The TEM-image (Fig. 5.7d) shows limited evidence of sintering possibly due to bias in sample preparation. The degradation of the support also results in an increase in the number of acid sites, despite a decrease in the BET-surface area (the area normalized number of acid sites increases from 1.2 μmol/m^2 to 4.7 μmol/m^2).

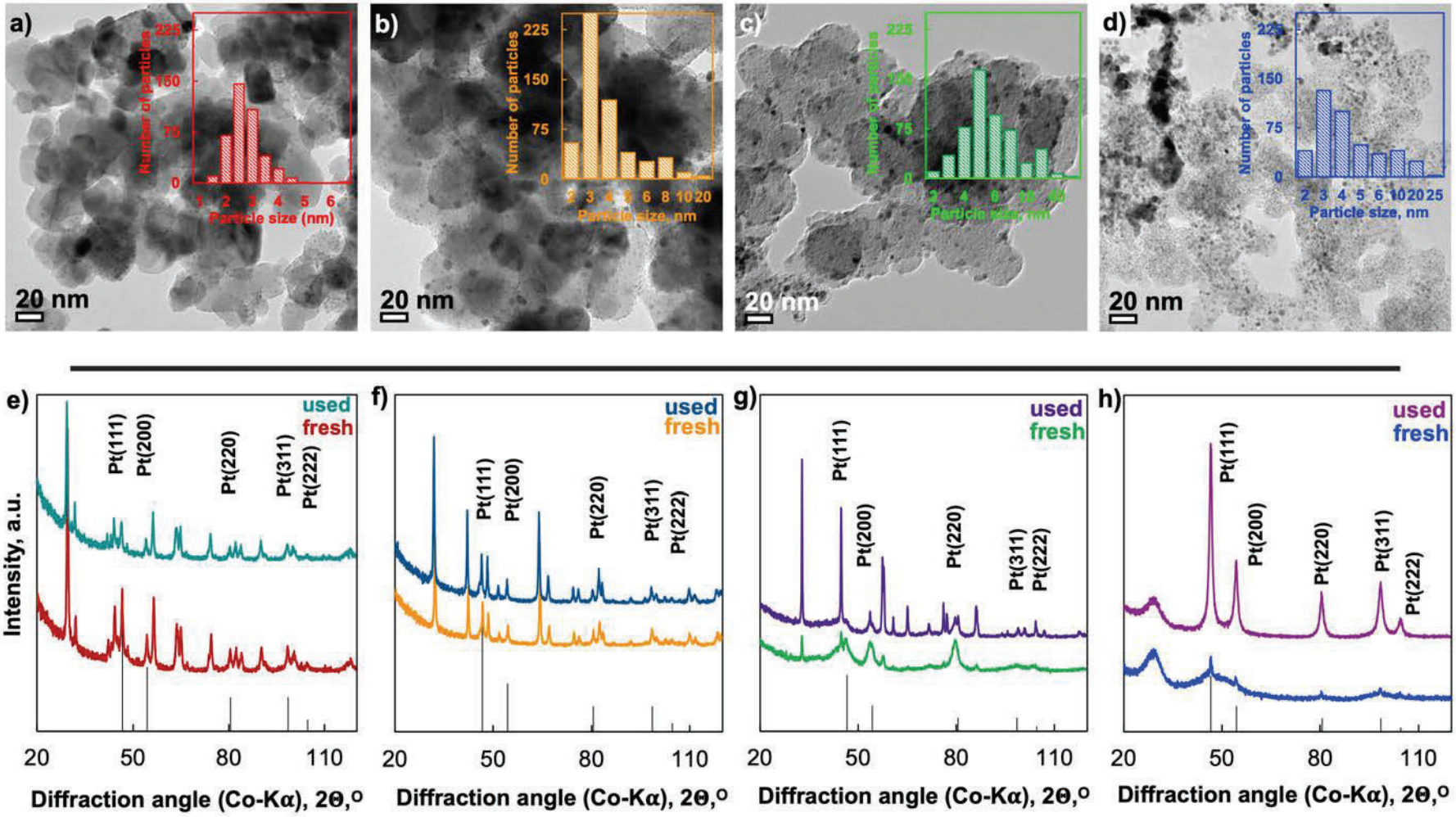

Figure 5.7: TEM-BF images of the recovered a) Pt/TiO_2-P25, b) Pt/TiO_2-Rutile, c) Pt/Al_2O_3 and d) Pt/C catalysts with Insets showing the particle-size distribution histograms and the PXRD patterns of the fresh and recovered e) Pt/TiO_2-P25, f) Pt/TiO_2-Rutile, g) Pt/Al_2O_3 and h) Pt/C catalysts.

Table 5.3: Physico-chemical properties of the recovered catalysts

Catalyst	w_{Pt}[a]	S_{BET}[b]	D_{Pt}[c], %	$d_{Pt,chem.}$[d]	$d_{Pt,TEM}$[e]	$n_{ads,\ IPA}$[f]
	wt.%	m^2/g		nm	nm	µmol/g
Pt/TiO_2-P25	9.6	52.6 ± 0.13	26	4.4	2.6 ± 1.3	200
Pt/TiO_2-Rutile	10.0	24.7 ± 0.04	24	4.6	3.8 ± 1.9	36
Pt/Al_2O_3	-[g]	32.1 ± 0,13	3.7	31.0	6.1 ± 4.5	89
Pt/C	30*	198.6 ± 1.65	6.8	16.7	4.4 ± 3.3	942

[a]Platinum loading determined using ICP-OES (and *platinum loading determined using TGA-DSC); [b]BET-surface area; [c]Dispersion of platinum from hydrogen chemisorption assuming $H/Pt_{surface}$=1; [d]Platinum particle size estimated from $d_{Pt} = \frac{113}{Dispersion\ (\%)}$; [e]Platinum particle size distribution deduced from TEM-images; [f]Amount of isopropyl amine adsorbed as an indicator for the number Brønsted acid sites.

The ATR-FTIR spectrum of the recovered Pt/TiO_2-P25 catalysts (Fig. 5.8a) shows the appearance of new absorbance bands at ca. 1046 cm^{-1}, 1136 cm^{-1}; a strongly skewed absorption band peaking at ca. 1412 cm^{-1} and a minor peak at ca. 1456 cm^{-1}. These bands are absent in the spectra of the fresh catalyst and the bare support, and may be caused by the presence of organic deposits on the catalyst surface. The absorption bands at 1046 cm^{-1} and 1136 cm^{-1} may be attributed to C-O-C stretching vibration, and the bands at 1412 cm^{-1} and 1456 cm^{-1} to CH_x bending [314]. This may indicate the presence of organic moieties containing (CH_2O) linkages similar to those in polyoxymethylene (it should be noted that the absorption bands attributable to CH_x-bending appear to be more intense than the absorption bands attributable C-O-C stretching vibrations).

Heating the recovered catalyst Pt/TiO_2-P25 in helium results in the release of H_2O (m/z=18), CO_2 (m/z=44) and CO (m/z=28) (see Fig. 5.8e). Water may evolve upon release of physisorbed or weakly chemisorbed water (at ca. 100-250°C) or from dehydroxylation (at ca. 450°C). Water in conjunction with the acid and basic sites on the catalyst may assist the decomposition of the organic deposits leading to the formation of CO/CO_2. These deposits may be associated with the presence of acid sites, as the concentration of acid sites over Pt/TiO_2-P25 reduces by 30% after the reaction (see Table 5.3). The presence of organic deposits in the oxidation of methane over Pt/TiO_2-P25 may contribute to the observed catalyst deactivation.

The ATR-FTIR spectrum of the recovered Pt/TiO_2-Rutile catalyst (see Fig. 5.8b) shows the appearance of new absorbance bands at ca. 1000 cm^{-1}, 1156 cm^{-1}, 1415 cm^{-1} and 1471 cm^{-1}, which are absent from the spectra of the fresh catalyst and the bare support. The new absorbance bands are similar to those observed in the recovered Pt/TiO_2-P25 catalysts with two obvious deviations, viz. a red shift of the main absorption band attributed to C-O-C stretching at ca. 1000 cm^{-1} and a strong increase in the intensity of the absorption band attributed to the C-O-C stretching band in comparison to the CH_x-bending mode. The red-shift in the band for the C-O-C may indicate a higher degree of polymerization of the deposit [280].

The presence of organic deposits is further confirmed by the desorption of decomposition products of organic molecules upon heating the recovered sample in helium (see Fig. 5.8f). It should be noted that some formation of decomposition products is observed only at low temperature, and not at ca. 400°C in contrast to the decomposition of organic deposits on Pt/TiO_2-P25. This may be attributed to the low amount of water formed due to dehydroxylation of Pt/TiO_2-Rutile compared to Pt/TiO_2-P25 (see also Fig. 5.3b and 5.3d). These deposits may be linked to the presence of acid sites on the rutile support as the concentration of acid sites (as determined from adsorption of isopropyl amine) is reduced by 50% in the recovered catalyst relative to the fresh catalyst (see Table 5.3), which could be a major contributor to the loss in catalyst activity (through occlusion of platinum active sites).

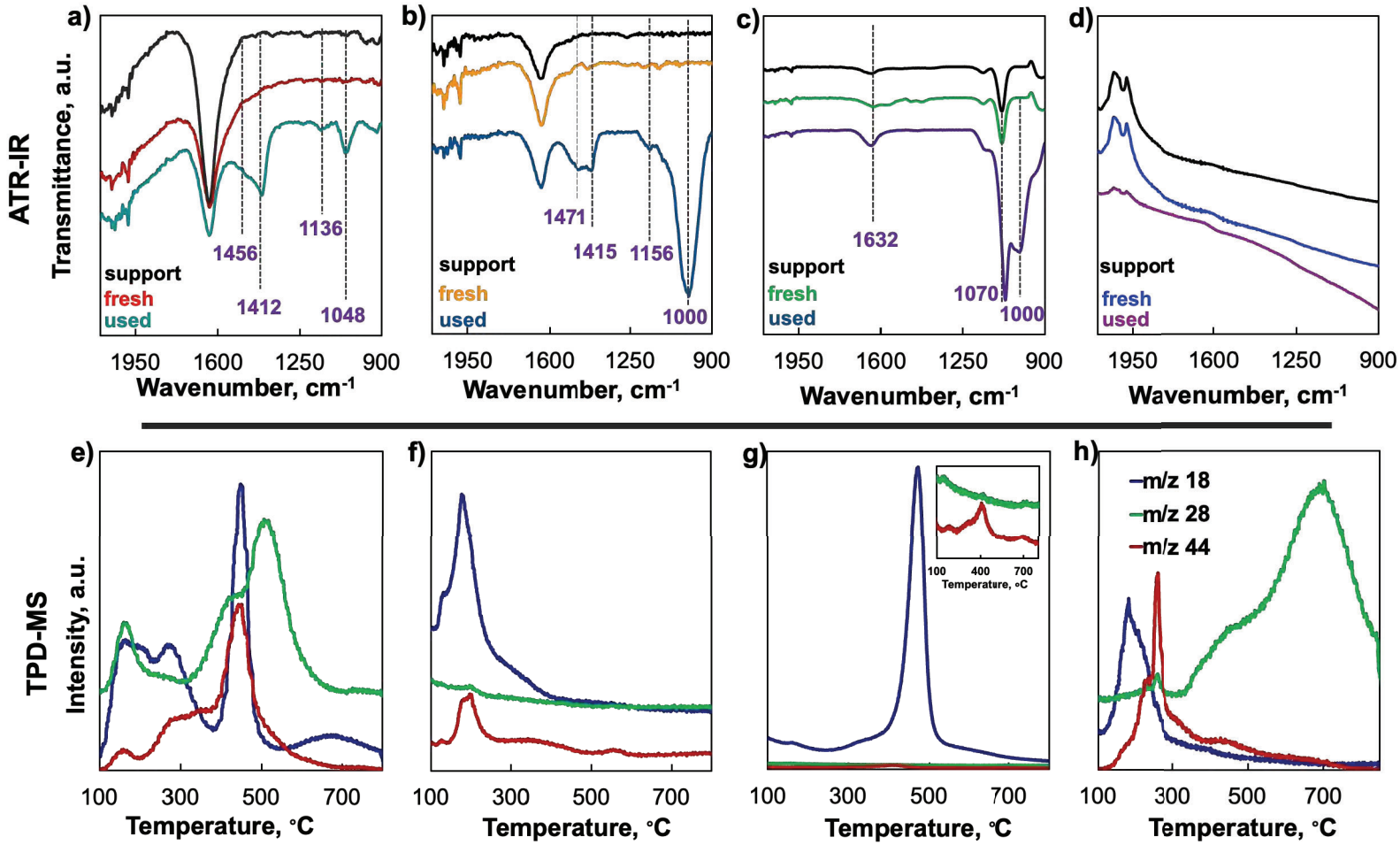

Figure 5.8: Attenuated total reflectance infrared spectra of the freshly reduced and recovered a) Pt/TiO_2-P25, b) Pt/TiO_2-Rutile, c) Pt/Al_2O_3, d) Pt/C catalysts and the accompanying TPD-MS profiles of the recovered e) Pt/TiO_2-P25, f) Pt/TiO_2-Rutile, g) Pt/Al_2O_3, and h) Pt/C catalysts.

The ATR-FTIR spectrum of the recovered Pt/Al_2O_3 catalyst (Fig. 5.8c) shows an absorption band at 1000 cm^{-1} and 1070 cm^{-1}, which is ascribed to the presence of boehmite in the sample [315]. Absorption bands in the region 1400-1500 cm^{-1} are absent implying the absence of CH_x-groups on the catalyst surface. The small amount of organic deposits on the recovered Pt/Al_2O_3 catalyst is further substantiated by the temperature programmed heating of this sample in helium (see Fig. 5.8g) which shows only a marginal amount of desorbed CO_2; the major contribution in the TPD profile appears to be from the dihydroxylation of the boehmite.

The ATR-FTIR of the recovered Pt/C catalyst does not show any evidence of organic deposits (see Fig. 5.8d) although heating up of the recovered catalyst in helium does result in the formation of CO (m/z=28, 700°C) and CO_2 (m/z=44, 260°C) possibly from the decomposition of the support (see Fig 5.8h), especially considering the high CO and CO_2 desorption temperatures [316].

5.3.4. INTERROGATING THE CONTRIBUTION OF THE SUPPORT

Formaldehyde is hypothesised to form over platinum active sites, and the presence of liquid water serves to facilitate the desorption of the formed formaldehyde via proton transfer and solvation [27, 246]. This means that the formed formaldehyde is expected to be concentrated in the liquid phase. If the catalytically active phase is supported on a hydrophobic support, it is suspected that the liquid phase is confined around the platinum nanoparticles with less contact with the support [310, 317, 318]. Water would then provide a physical barrier, which prevents contact between the water-solvated formaldehyde [319] (which is a polar molecule) and support active sites, hence protecting the formaldehyde from further conversions on the support active sites. The formaldehyde instead leaves the reactor with the rest of the liquid phase. Water, in essence, acts as a product protector in this scenario. This may then explain the high formaldehyde selectivity obtained over the relatively hydrophobic supports (TiO_2-Rutile and carbon).

Over a hydrophilic support, the liquid phase is likely in contact with both the active metal surface and with the support surface [320], which presents a pathway for the diffusion of the formaldehyde in the liquid phase to the support active sites. This therefore enables the further conversion of formaldehyde over the support acid/base sites. Because the liquid phase remains in contact with the catalyst bed as it trickles through the reactor, the conversion of formaldehyde is not only confined to the metal-support interface, but may occur over any support active sites that the formaldehyde comes in contact with.

From the catalytic data reported in Fig. 5.4, it can be observed that the P25-supported catalyst is the least productive in terms of oxygenate selectivity and yield. Initially, in the presence of water in the gas phase, the catalyst was selective towards formaldehyde. The selectivity changed with time, favouring the formation of methanol and methoxy-methanol. The oxidation of methane over the rutile, alumina and carbon supported catalysts, on the other hand, resulted in the formation of formaldehyde, with reasonable selectivities. The best performing catalyst was Pt/C. It is suspected that the selectivities achieved on the different supports is influenced by the support acid/base properties and the support hydrophobicity.

On carbon, the most hydrophobic support, the formaldehyde selectivity achieved under trickle bed conditions reached a maximum of 99%. On rutile, the second most hydrophobic support, the formaldehyde selectivity reached a maximum of 90% in the trickle-bed regime. Carbon and rutile were also determined to be the least acidic materials, with acid site densities of 1.2

$\mu mol_{IPA}.m_{cat}^{-2}$ for Pt/C (the recovered catalyst, after exposure to H_2O/CH_4=360 mol/mol has a relatively high acid density of 4.7 $\mu mol_{IPA}.m_{cat}^{-2}$, which may have contributed to the high CO_2 selectivity after exposure to these conditions), and 3.1 $\mu mol_{IPA}.m_{cat}^{-2}$ for Pt/TiO_2-Rutile (which reduced to 1.4 $\mu mol_{IPA}.m^{-2}$ in the recovered catalyst). The acid site density of Pt/TiO_2-P25 was determined to be 6.8 $\mu mol_{IPA}.m_{cat}^{-2}$ and declined to 3.8 $\mu mol_{IPA}.m_{cat}^{-2}$ in the recovered catalyst. The Pt/TiO_2-P25 catalyst showed a preference for the formation of CO_2 compared to Pt/C and Pt/TiO_2-Rutile. The formation of CO_2 may occur from the transformation of formaldehyde to dioxymethylene on bridging titania hydroxyl groups (classified as acid sites) which then undergoes oxidation to CO_2 [321], and may occur to a greater extent over Pt/TiO_2-P25 [322].

Pt/Al_2O_3 also contains a high acid site concentration (7.8 $\mu mol_{IPA}.m_{cat}^{-2}$), but this reduces to 2.8 $\mu mol_{IPA}.m_{cat}^{-2}$ in the recovered catalyst. The reduction in the acid site concentration may be caused by the transformation of alumina to boehmite. The formation of CO_2 over boehmite may be promoted by the presence of hydroxyl groups which catalyse the oxidation of formaldehyde via a formate pathway [279, 323].

The Pt/TiO_2-P25 catalyst was initially selective for the formation of formaldehyde, but this changed with increasing exposure to water, favouring the formation of methanol and methoxy-methanol instead. It is suspected that these products are formed from further conversion of formaldehyde, via a base-catalysed Cannizzaro-type reaction [321]. The P25 support may experience an increase in its surface acid/base character in the presence of water, through the generation of additional bridging and terminal hydroxyl groups [324-326]. The hydroxyl groups then catalyse the conversion of formaldehyde to methanol and CO_2 (and may also promote the oxidation of formaldehyde via the formate pathway). The P25 support is also quite hydrophilic, which may contribute to the successive conversion of formaldehyde over support acid sites.

The formation of the polyoxymethylene deposits may also be catalysed by support acid sites [321] via the polymerisation of formaldehyde, which is suspected to happen at the metal-support interface. Over Pt/C, the polymeric deposit is not visible on the ATR-IR spectrum of the recovered catalyst, while it is present on the spectra of Pt/TiO_2-P25 and Pt/TiO_2-Rutile catalysts. The ATR-IR spectrum of the recovered Pt/Al_2O_3 catalyst seems to be showing bands associated with boehmite. The observed absence of the deposit on boehmite may be due to the possible diminished acidity of the alumina support due to it transforming to boehmite, which is a basic material [327]. Hence, this makes it increasingly likely that the polyoxymethylene

formation is due to acidic sites. The mechanisms for the formation of acid and base-catalysed by-products over titania are presented in Scheme 5.1.

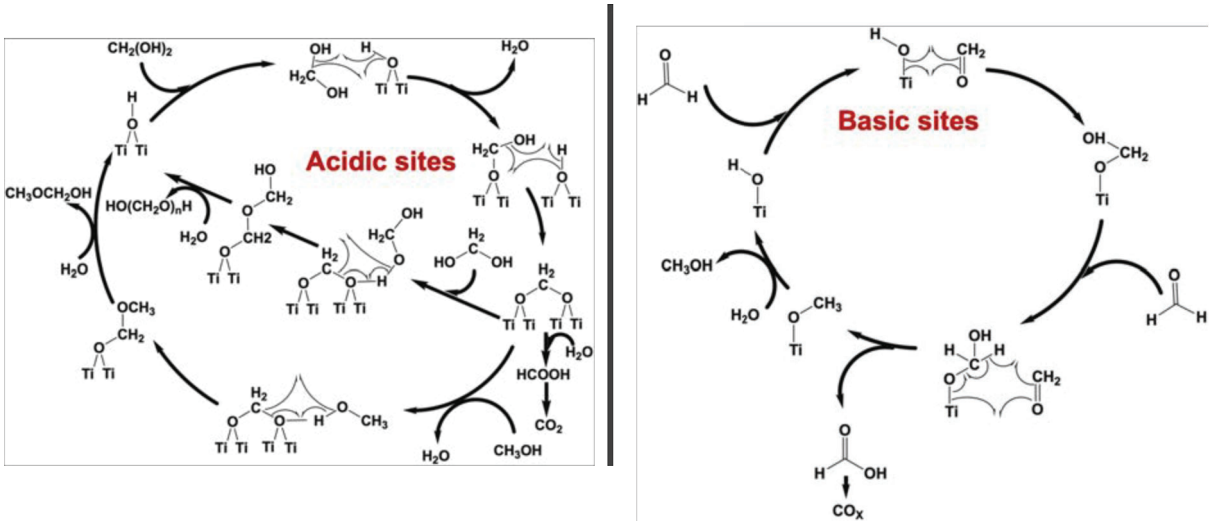

Scheme 5.1: Conceptual mechanism for the formation of by-products over acidic and basic sites on the titania support.

5.4. CONCLUSION

The influence of the support on the activity, selectivity and stability of platinum catalysts for the aerobic, selective oxidation of methane in the presence of liquid water was investigated. Platinum was supported on different oxides (TiO_2-Rutile, TiO_2-P25 and γ-Al_2O_3) and carbon black using wet impregnation. The results obtained from catalytic tests for the aerobic, water-assisted selective oxidation of methane demonstrate that the use of platinum nanoparticles on different support materials results in the formation of mainly formaldehyde under continuous flow of liquid water. High selectivity for formaldehyde formation (>90%) at a methane conversion of 1-4% was achieved over platinum supported on rutile and carbon black, which are relatively hydrophobic supports. Moderate selectivity towards formaldehyde was achieved over Pt/Al_2O_3 (65%) at a maximum conversion of 0.5%.

From the results presented here, it can be deduced that the catalytic activity is influenced by the metal active phase (i.e. the dispersion of platinum), and the conversion of methane may be structure sensitive. It is also deduced that the support influences the product selectivity. The support property that seems to have a large influence on the selectivity seems to be the hydrophilicity of the support, since if the support is hydrophobic, then the support acid/base properties may affect the selectivity less, since the contact between the support and the liquid phase is minimised.

The Pt/TiO_2-P25 catalyst was the least active, with a maximum methane conversion of 0.6%. The catalyst was initially selective towards formaldehyde but became increasingly selective towards methanol and methoxy-methanol with increasing reaction time, achieving a maximum oxygenate selectivity of 10%. The low oxygenate selectivity achieved by Pt/TiO_2-P25 was attributed to the further conversion of formaldehyde to methanol via the Cannizaro reaction over TiO_2-P25 and the oxidation of formaldehyde to CO_2 facilitated by the adsorption of formaldehyde on acid sites, which vastly reduced the selectivity of the catalyst towards selective oxidation products.

Although all four catalysts deactivated with time, the loss of activity over Pt/Al_2O_3 was caused by the reconstruction of the alumina support to boehmite under trickle-bed conditions, inducing sintering of platinum nanoparticles and thereby contributing to catalyst deactivation. The deactivation of the Pt/TiO_2-P25 catalyst was attributed to the deposition of oligomeric species on the catalyst. The use of more hydrophobic supports (Pt/TiO_2-Rutile and Pt/C) is suitable for the selective oxidation of methane under trickle-bed conditions. However, the carbon support

is susceptible to combustion under process conditions, leading to loss of the catalytically active surface sites of platinum.

From the results reported herein, it can be concluded that platinum as a catalyst for the selective oxidation of methane under trickle bed conditions should be highly dispersed on a support, and a suitable support should stabilize this catalytic active phase against sintering. The support must also be slightly hydrophobic and inert to water-induced structural reconstructions. The support must be impervious to combustion and gasification under reaction conditions, and ideally should not possess highly active acid sites that may polymerize formaldehyde to yield oligomeric deposits, nor possess highly active sites that catalyse the secondary conversion of formaldehyde, thereby reducing the formaldehyde yield. Based on the supports studied thus far, rutile seems to be more suitable based on the fact that the platinum nanoparticles did not undergo sintering over Pt/TiO_2-Rutile and the support did not undergo restructuring under process conditions. Carbon may also be suitable provided the loss of carbon surface area through combustion and gasification can be avoided.

CHAPTER VI:

AN INVESTIGATION OF PLATINUM-BASED NANO-ALLOYS FOR THE SELECTIVE OXIDATION OF METHANE

Declaration:

The high resolution transmission electron microscopy imaging was performed by Dr. Ezra Jaco Olivier at the Centre for High Resolution Transmission Electron Microscopy at the Nelson Mandela University, with virtual participation by the PhD candidate.

OVERVIEW

The selective oxidation of methane over platinum supported on rutile, P25, alumina and carbon black resulted in the selective formation of formaldehyde. Kinetic studies indicated that the rate of reaction was limited by the desorption of formaldehyde from the catalyst surface. Platinum was subsequently alloyed with copper, silver or gold (in a 3 Pt:1 M ratio) in an attempt to tune the adsorption strength of oxygen and by proxy, the adsorption strength of oxygenate species in an effort to enhance the rate of product desorption from the catalyst surface.

The nanoalloy catalysts were tested in the gas-phase reactor initially, and the catalytic activity was in the trend of Pt_3Ag < Pt < Pt_3Au << Pt_3Cu, with all of them attaining a formaldehyde selectivity of ca. 65%. The Pt_3Ag and Pt_3Cu catalysts were then tested in the trickle bed reactor. Although the Pt_3Cu/TiO_2 catalyst achieved a conversion of up to 5% in the presence of liquid water and a formaldehyde selectivity of 78%, the rate of methane conversion remained the same as in the gas phase reactor at ca. 300 μmol/g_{cat}/h. The activity of the Pt_3Ag catalyst was much improved in the trickle bed reactor, increasing from 43 μmol/g_{cat}/h (in the gas phase) to 271 μmol/g_{cat}/h in the trickle bed reactor.

The findings presented here show the potential of designing more active catalysts through alloying platinum with other metals, which also presents a strategy for reducing the platinum loading.

6.1. JUSTIFICATION FOR INVESTIGATING PLATINUM NANOALLOYS

The selective oxidation of methane yielding formaldehyde has been achieved over catalysts containing 10 wt.-% platinum. The use of the expensive platinum may be prohibitive for this interesting process. The amount of platinum may be reduced by alloying platinum and thus using less of the expensive metal. Platinum based alloy catalysts have been studied for the oxygen reduction reaction [328] and for the catalytic oxidation of organic compounds [329, 330]. For instance, alloys of platinum with 3d metals (Ni, Fe and Co) have been reported to have enhanced activity for the oxygen reduction reaction [331, 332]. Pt-Mo, Pt-Sb, Pt-Sn and Pt-Bi alloys have been reported to be active for the selective oxidation of organic compounds (such as glycerol). The Mo [333], Bi, Sn, Pb, and Sb adatoms [329, 334] may result in new active sites that adsorb hydroxyl groups, which may further enhance the oxygen coverage of bimetallic alloy catalysts.

Alloying may alter the reactivity of the catalytically active metal and can thus be used to tune the catalytic activity. The selective oxidation of methane to formaldehyde over platinum-based catalysts was determined to be zero order with respect to both methane and oxygen, which led to the conclusion that the reaction was desorption limited. Hence, it was hypothesised that modifying the binding strength of oxygenates on the catalyst surface could potentially enhance the rate of product desorption, thereby speeding up the kinetics of the overall reaction [78]. The binding strength of reactive species on the platinum surface can be modified by alloying platinum with another metal.

The binding strength of adsorbates on metal surfaces is governed by the proximity of the *d*-band centre energy to the Fermi level [335]. Metals whose d-band centre lies close to the Fermi level form stronger bonds with adsorbates. The interaction of the adsorbate with the *sp* states of the metal leads to a broadening of the adsorbate states. The broadened adsorbate states couple to the metal *d* states, giving rise to bonding and anti-bonding states [335, 336]. If the antibonding states are below the Fermi-level, the adsorbate-metal interaction is weakened, whereas if the antibonding states are above the Fermi-level, the adsorbate-metal bond is strengthened [337, 338].

Alloying can either cause an up-shift or downshift of the d-band centre, depending on the atomic radius of the promoter metal. Alloying with a metal of a larger atomic radius induces tensile strain, while an element with a smaller atomic radius induces compressive strain [267, 331, 339, 340]. Subjecting atoms to tensile strain expands the lattice thereby decreasing the

overlap between *d*-electrons on neighbouring metal atoms. The d-band then moves up in energy to keep the d-band occupancy fixed [341]. Compressive strain on the other hand lowers the energy the d-band by increasing the d-orbital overlap.

The surface composition of alloys can be quite different from the bulk composition. In the extreme case, it may lead to the formation of skin alloys, with the surface containing a single element. This will induce strain effects in the nanoparticle lattice experienced by the surface atom causing a shift in the position of the *d*-band centre of the metal [341, 342]. An upshift in the d-band centre of the surface atoms would result in a stronger interaction between the surface atoms and adsorbate, which would strengthen the binding strength of the adsorbates on the metal surface. A downshift in the d-band centre of the surface atoms would result in weaker binding of the adsorbates, on the other hand.

In the case of oxygen (and, by proxy, oxygenates), weakening the binding strength of oxygen on platinum-based systems seems to render them more active, particularly during oxidation and electrochemical reactions [291, 330, 343-346].

This chapter is an investigation on the effects of alloying Pt with Cu, Ag or Au on the catalytic activity and oxygenate selectivity in the selective oxidation of methane, based on the hypothesis that alloying platinum will tune the binding strength of the formaldehyde intermediate, thereby enhancing its rate of desorption. Alloying platinum with gold was included to determine if the upshift in the platinum d-band centre would result in a slower reaction. The alloys are supported on the rutile phase of titania, since a rutile-supported platinum catalysts was selective for the formation of formaldehyde, and did not undergo deactivation caused by deleterious changes in the support structure (i.e. the rutile is stable against phase-changes and combustion in the trickle-bed reactor, as per findings in Chapter V).

6.2. EXPERIMENTAL METHODOLOGY

The alloys were synthesized using a wet-chemical approach, wherein the nanoparticles were precipitated in their metallic form upon addition of molybdenum hexacarbonyl ($Mo(CO)_6$) to the solution after heating the metal precursors dissolved in a mixture of benzyl ether, oleylamine and oleic acid to 250°C [347]. More details on the catalyst synthesis, characterisation and testing methodologies are described in detail in Appendix 4.

6.3. MATERIAL CHARACTERISATION RESULTS

6.3.2. AS-SYNTHESISED NANOPARTICLES

The powder-X-ray diffraction patterns and bright-field transmission-electron microscopy images of the as-synthesised alloy nanoparticles, with element maps are presented in Figure 6.1. The diffraction patters of the nanoparticles show a face-centred cubic structure (fcc) that resembles that of metallic platinum (see Table 6.1). Rietveld refinement was used to determine the crystal lattice parameters and the crystalline domain sizes of the as synthesised Pt, Pt_3Cu, Pt_3Ag and Pt_3Au nanoparticles.

The synthesised Pt nanoparticles have a lattice parameter corresponding to FCC platinum and an average crystalline domain size of 6.8 nm (see Table 6.1). The diffraction lines of Pt_3Cu are slightly shifted to higher angles in comparison to the diffraction lines of FCC-Pt (see Figure 6.1). A reduced lattice parameter of 0.382 nm was determined for the Pt_3Cu- lattice as a result of the incorporation of the smaller Cu atom in the platinum lattice [348]. The molar ratio of platinum to copper is estimated to be 2.3 assuming the validity of Vegard's law [349]. The average size of the crystalline domain as estimated using the Scherrer equation was determined to be 3.9 nm (see Table 6.1). The TEM image for the unsupported Pt_3Cu nanoparticles (Fig. 6.1 c) shows the presence of nanoparticles mostly in the 4-5.5 nm size range. The average particle size was determined to be 5.2 ± 2.3 nm (see Fig. A4.1a and Table 6.1), which is slightly larger than the size determined using Rietveld refinement. This may indicate that the observed particles consist of different crystalline domains. The element map of the as-synthesised Pt_3Cu nanoparticles appears to show areas of copper surface-enrichment for the larger nanoparticles (see Figure 6.1f), while some regions seem to show a random distribution of Cu and Pt, indicating a random-alloy structure.

The Pt_3Ag-nanoparticles yield a PXRD-pattern corresponding to a FCC-structure, which is best described with Gaussian peaks (see Figure 6.1a). The diffraction lines appear to be shifted to

lower 2θ angles indicating an increase in the d-spacing [350] to 0.397 nm (see Table 6.1). This indicates an expansion of the platinum lattice, caused by the incorporation of the larger Ag atom in the platinum lattice, thereby increasing the lattice constant (to 0.399 nm) due to the formation of an alloy between Pt and Ag. The molar ratio of platinum to silver is estimated to be 1.5 assuming the validity of Vegard's law [351]. The average crystalline domain size of the FCC-structure was determined to be 2.4 nm from Rietveld refinement. The TEM image of the unsupported, Pt_3Ag nanoparticles shows the presence of small, spherical nanoparticles with a narrow particle size distribution averaging around 4.3 ± 0.8 nm (Table 6.1, Fig. A4.1b), which is larger than the size determined from XRD analysis. This again may indicate the presence of multiple crystalline domains within a particle. Pt_3Ag appears to be a true alloy with a homogeneous distribution of platinum and silver (see Figure 6.1g).

Table 6.1: The lattice constants of the nanoalloy as calculated from XRD analyses and the composition determined from Vegard's law for the nanoparticles

nanoalloy	**FCC(111) diffraction line, 2θ, °**	**a[a] nm**	**x_{Pt}[b]**	**x_M[b]**	**d_{Pt_3M}[c] nm**	**$d_{Pt_3M,\ TEM}$[d] nm**
Pt	46.87	0.392	1	0	6.8	5.8 ± 1.0
Pt_3Cu	47.14	0.382	0.70	0.30	3.9	5.2 ± 2.3
Pt_3Ag	45.97	0.399	0.60	0.40	2.4	4.3 ± 0.8
Pt_3Au	46.10	0.394	0.800	0.200	3.9	9.3 ± 1.1

[a] lattice parameter from Rietveld refinement; [b] mole fraction of metal; [c] determined from Rietveld refinement in XRD; [d] determined from TEM.

The Pt_3Au-nanoparticles also yield a PXRD-pattern corresponding to a FCC-structure, which best described with Gaussian peaks. Similar to that of Pt_3Ag, the PXRD pattern of Pt_3Au shows peaks that appear to have shifted to lower 2θ angles which indicate the formation of an alloy between Au and Pt. The lattice parameter was determined to be 0.394 nm, which indicates an expansion of the platinum lattice. The molar ratio of platinum to gold is estimated to be 4.0 assuming the validity of Vegard's law [352], in reasonable agreement with their molar ratios in the synthesis mixture. The average crystalline domain size of Pt_3Au was determined to be 3.9 nm using Rietveld refinement. The TEM image of unsupported, as synthesized Pt_3Au nanoparticles shows the presence of spherical nanoparticles that seem to be uniformly sized. The average particle size was determined to be 9.3± 1.1 nm (See Fig. A4.1c), which is

substantially larger than the particle size diameter determined from Rietveld refinement, implying that the nanoparticles contain multiple crystalline domains. The Pt_3Au-alloy appears to be inhomogeneous with region with a high gold content and regions with a low gold content (see Figure 6.1i).

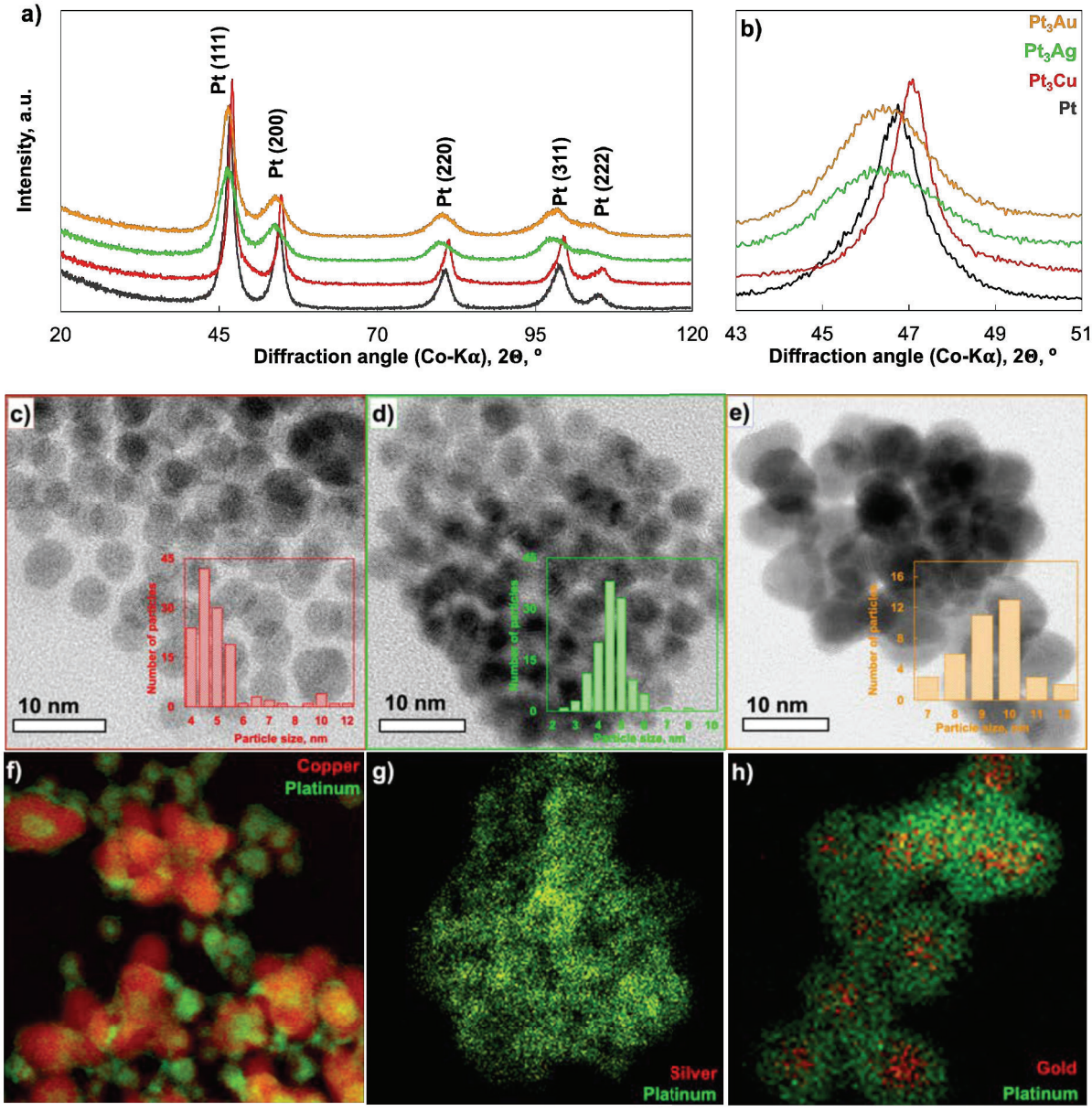

Figure 6.1: a) Powder X-ray patterns of the unsupported, as synthesised nanoalloy catalysts, b) the Pt(111) diffraction lines of the platinum nanoparticles and the as-synthesised alloys, the bright field TEM image of the unsupported nanoparticles and the particle size distribution of Pt_3Cu (c), Pt_3Ag (d), Pt_3Au (e) and the corresponding elemental maps of the as-synthesised, unsupported Pt_3Cu (f), Pt_3Ag (g) and Pt_3Au (h).

6.3.3. SUPPORTED AND PRE-TREATED NANOPARTICLES

The nanoparticles were supported on the rutile phase of titania. The metal loading of the supported catalysts was determined using elemental analysis (see Table 6.2). The platinum loading across all catalysts was around 7 wt.% while the Cu, Ag and Au loadings were 0.68, 1.5 and 0.66 wt.% respectively, which was close to the targeted Pt_3M composition for both Pt_3Ag and Pt_3Cu. The Pt-Au composition was determined to be $Pt_{11}Au$, which may be an error in the analysis (Note this composition also appears to be in contradiction to the composition determined using Vegard's law). Hence, the Pt_3Au naming convention will be maintained.

The metal dispersion of the supported catalysts was determined through oxygen chemisorption, as presented on Table 6.2. The Pt_3Cu/TiO_2 catalyst was found to have a higher dispersion, followed by Pt_3Ag/TiO_2, then Pt_3Au. However, the low oxygen uptake on the P_3Ag and Pt_3Au nanoalloys may be due to Ag and Au occupying surface sites, which may impede oxygen adsorption. The low oxygen uptake on both Pt_3Au and monometallic Pt may be due to sintering of the metallic phase during pre-treatment (the samples are pre-treated at 350°C in the flow of oxygen/helium to remove residual surfactants that may remain after synthesis). The sintering of the metallic phase on Pt_3Au during annealing can be seen on the TEM images of the annealed samples.

Table 6.2: Dispersion and particle sizes of the metallic phases of the supported nanoparticles

Catalyst	**w_{Pt}[a] wt.%**	**w_M[a] wt.%**	**Pt:M, mol/mol**	**$n_{O_2,\ ads}$, $\mu mol/g_{cat}$**	**d_{Pt_3M}[c] nm**	**$d_{Pt_3M,\ TEM}$[d] nm**
Pt	6.5	-	-	17.6 ± 0.9	10.7	6.6 ± 2.8
Pt_3Cu/TiO_2	7.0	0.68	3.4:1	55.4 ± 3.6	4.8	6.0 ± 3.5
Pt_3Ag/TiO_2	7.7	1.8	2.4:1	46.6 ± 3.2	5.0	10.3 ± 20.6
Pt_3Au/TiO_2	7.3	0.66	11:1	22.8 ± 0.5	8.5	19.0 ± 30.7

[a] Metal loading in catalyst as determined using ICP-OES; [b] O_2-chemisroption measurement assuming dissociative adsorption of O_2 at 220°C ; [c] O_2-chemisorption; [d]TEM measurements of the annealed samples.

Prior to reaction, the nanoparticles are typically pre-treated at 350°C in the presence of oxygen diluted in helium (10% v/v) to remove any residual surfactants from the nanoparticle synthesis.

Hence, the catalysts were analysed with XRD and TEM after this pre-treatment to observe changes in the particle morphology and dispersion after the annealing treatment.

Figure 6.2 shows the powder X-ray diffraction patterns of the unsupported nanoparticles, the supported nanoparticles, and the pre-treated Pt_3Cu/TiO_2 (6.2a), Pt_3Ag/TiO_2 (6.2b) and Pt_3Au/TiO_2 (6.2c) catalysts. The powder XRD pattern (Fig. 6.2a) of the supported Pt_3Cu nanoparticles shows the presence of small peaks that were determined to have a crystalline domain size of 4.5 nm and a lattice constant of 0.382 nm, which corresponds to a Pt:Cu ratio of 2.3. The Powder diffraction pattern of the annealed sample shows an increase in the intensities of the diffraction lines which indicates an increase in the crystalline domain size (which was determined to have grown to be 21 nm using Rietveld refinement). The lattice parameter also increased to 0.391 nm (Table A4.1), which corresponds to pure platinum and may indicate a partial de-alloying of the nanoparticles resulting in the formation of platinum enriched phases [353]. The copper-enriched particles may be too small and are possibly below the instrument limit of detection.

A similar behaviour is seen in the PXRD pattern of the annealed Pt_3Ag/TiO_2 catalyst (see Figure 6.2b). The diffraction lines appear narrower and are slightly shifted to higher diffraction angles. This may indicate a growth of the size of the crystalline domain (which increased from 2 nm for the unannealed sample to 8.9 nm for the pre-treated sample). The lattice parameter decreased to 0.393, which indicates a partial segregation of the alloy, forming predominantly phases with a Pt:Ag composition of 4 [351]. The PXRD pattern of the annealed Pt_3Au/TiO_2 catalyst also shows an increase in the average size of the crystalline domain of the metallic phase (Fig. 6.2c). The crystalline domain size increased from 3.4 nm to 27 nm. The lattice parameter did not change for this system.

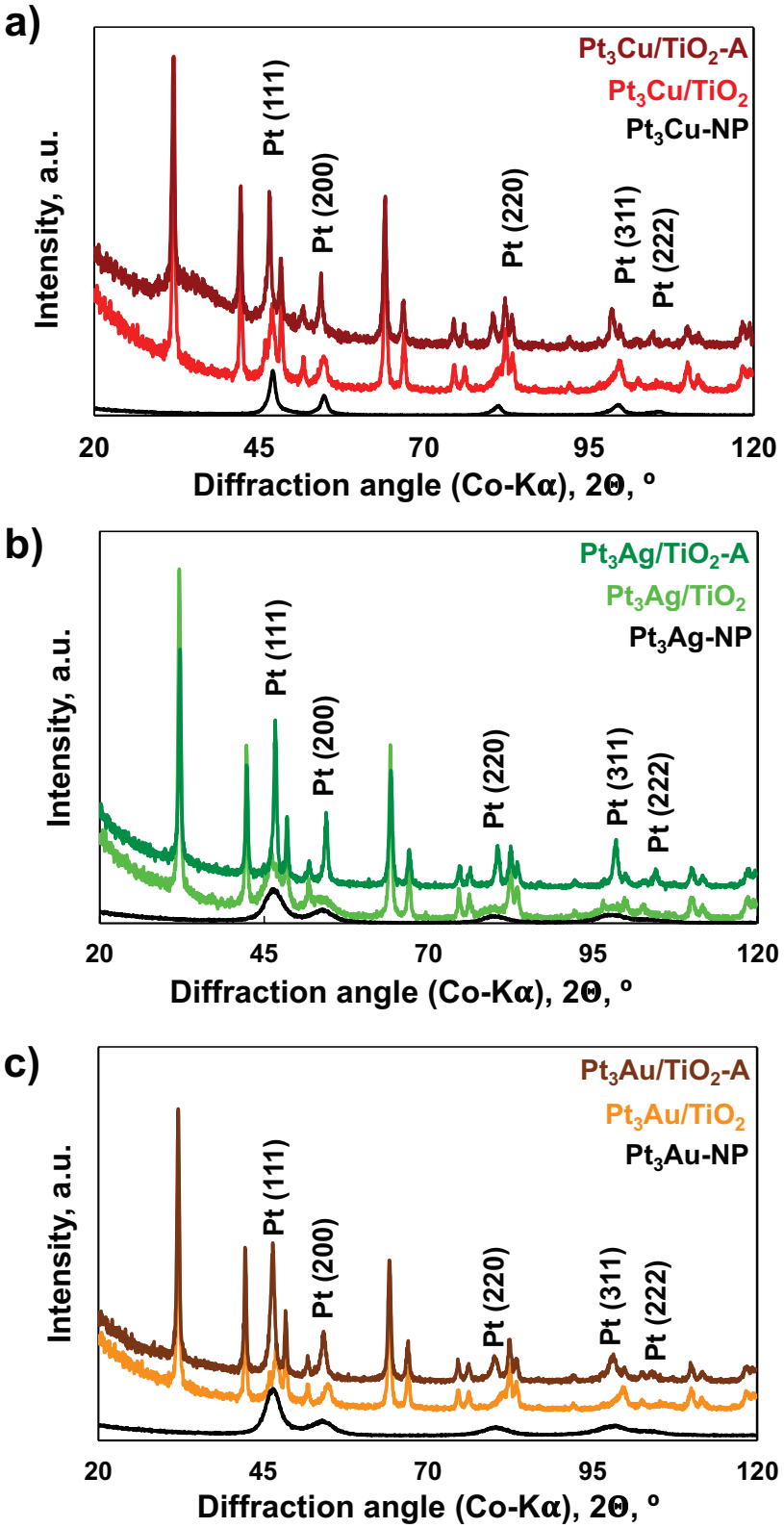

Figure 6.2: PXRD patterns of the nanoparticles before deposition on the support (denoted NP), the supported nanoparticles and the supported, annealed (A) Pt_3Cu (a), Pt_3Ag (b) and Pt_3Au (c) nanoparticles and supported catalysts.

The transmission electron microscopy images of the supported, pre-treated catalysts are presented in Figure 6.3. The TEM images obtained for Pt_3Cu shows the presence of well-dispersed, bimodal particles ranging from small to medium in particle size, which were determined to largely lie in the 3-6 nm range, with some particles being as large as 19 nm (Fig. 6.3 a and g).

The TEM images obtained for Pt_3Ag/TiO_2 show the presence of large clusters (Fig. 6.3b-h). The images show a heterogeneous distribution of metal particles, with some regions showing highly-dispersed, small particles in the 4-8 nm range, and some regions with large metal clusters. The particle-size distribution histogram shows a log-normal distribution of the particle sizes (Fig. 6.3h), with particles ranging from 2-14 nm, but some particles as large as 200 nm.

The bright-field TEM images of the pre-treated Pt_3Au/TiO_2 catalyst also show notable signs of sintering, with metal-enriched regions (i.e. occupied by large clusters of metal), while some regions show the presence of small, well-distributed nanoparticles (Fig. 6.3c and i). The particle size distribution histogram shows a random distribution of particle sizes, which can be best be grouped into three distinct sizes, which are small particles (2-6 nm), medium particles (7-15 nm) and large clusters (20-250 nm). The image in Fig.6.3f shows the presence of small, ~2nm particles and a 10 nm particle.

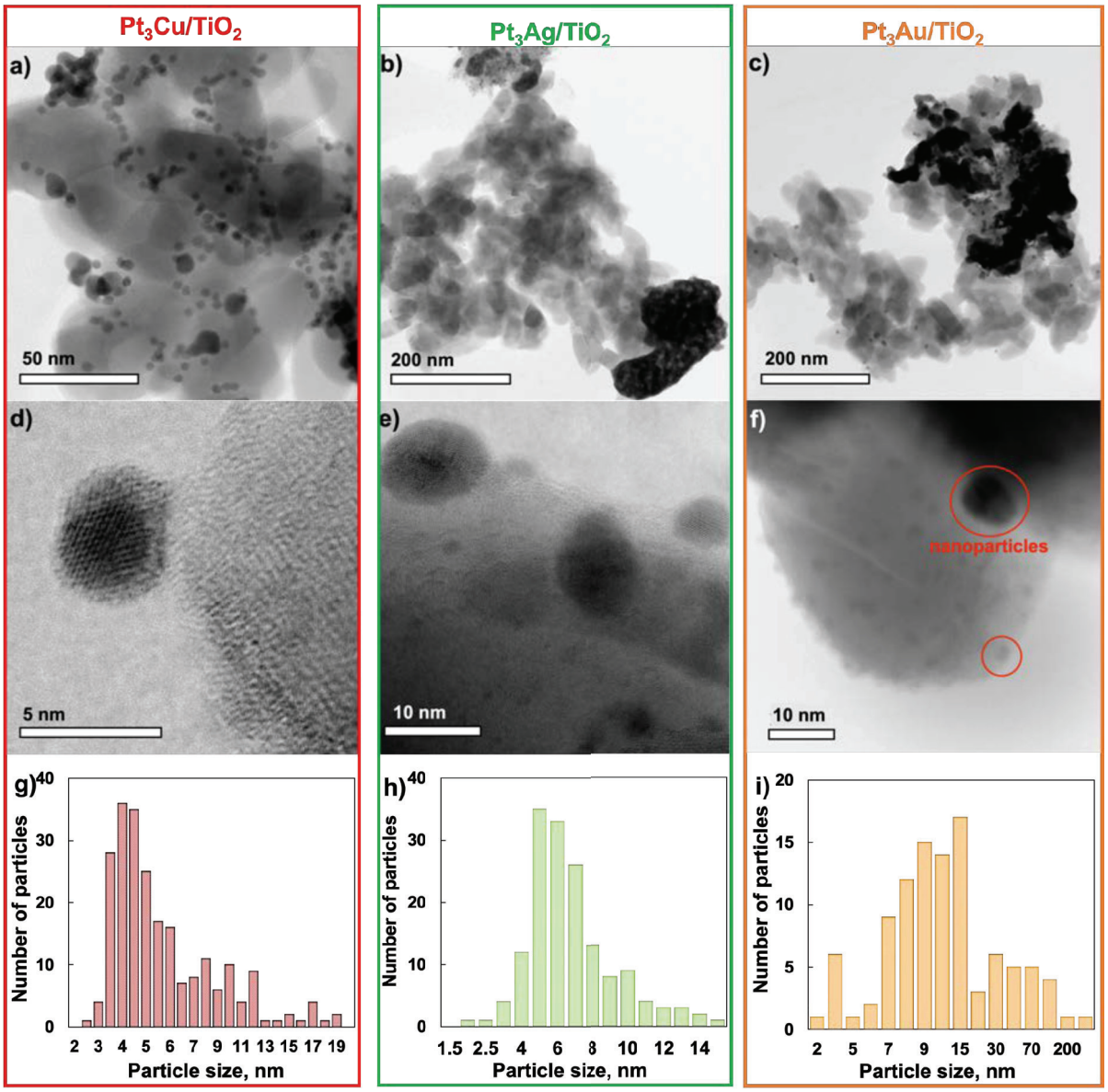

Figure 6.3: Bright-field TEM image (a - c), high magnification image (d-f) and particle size distribution histograms of the pre-treated Pt_3Cu/TiO_2, Pt_3Ag/TiO_2 and Pt_3Au/TiO_2 catalysts.

Scanning transmission electron microscopy coupled with electron dispersive X-ray analyses on some selected areas was used to determine the metallic distribution on the pre-treated catalysts (see Figure 6.4). From the Pt_3Cu/TiO_2 spectra (Fig. 6.4 a-c), it can be observed that the small nanoparticles are copper-enriched, while the large particles are platinum enriched. The presence of small, copper particles has also been observed (Figure 2 in appendix 4, (Fig. A4.2)), which may be due to complete segregation of the copper from the copper-enriched particles (see Fig. 6.1f). The diffusion of copper out of the alloy structure of platinum-copper

alloys in an oxidising environment has been reported before, which resulted in the formation of small copper islands on the platinum surface [354].

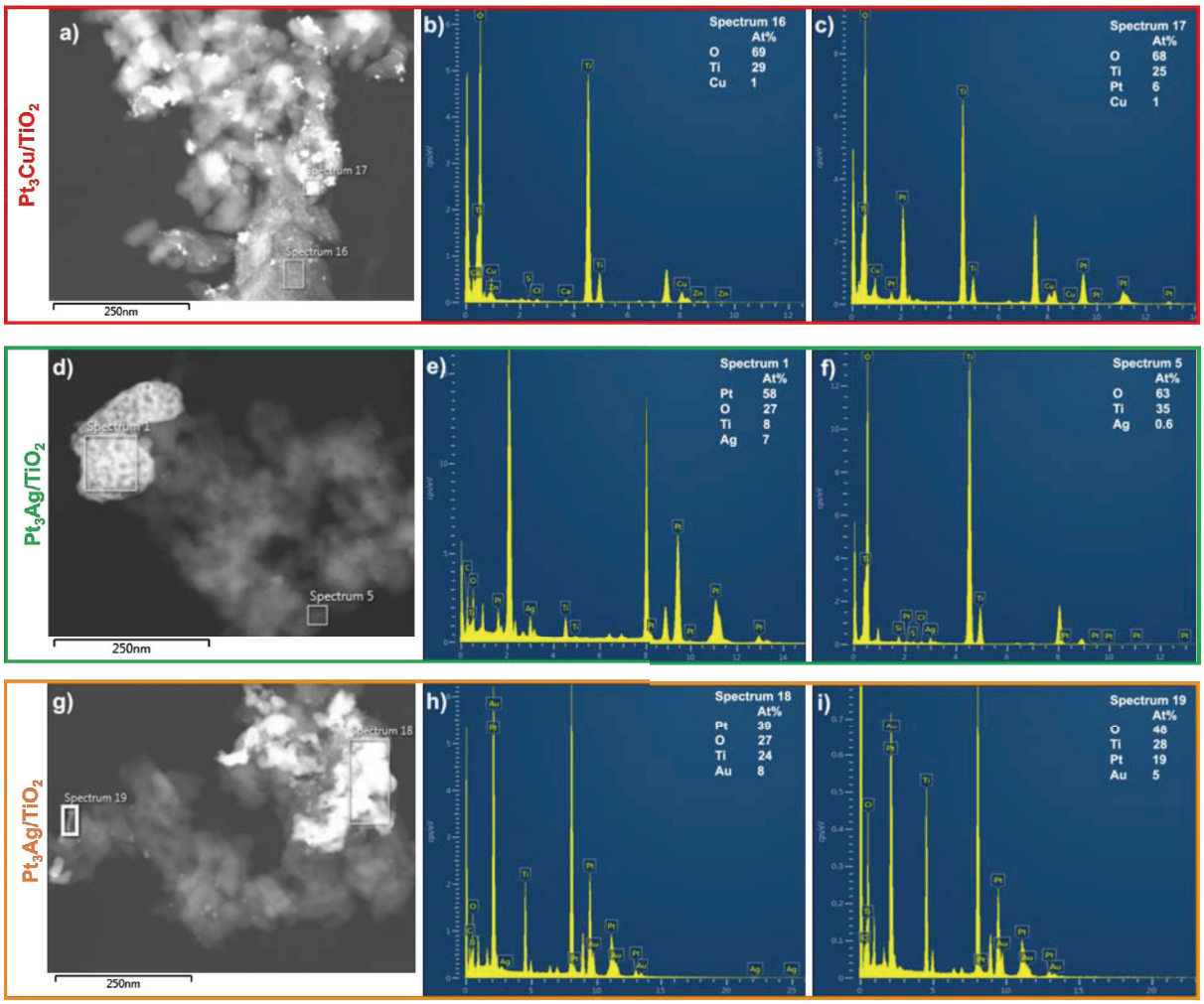

Figure 6.4: STEM-EDX scans showing the association between platinum and the alloying element for the annealed Pt_3Cu/TiO_2 (a-c), Pt_3Ag/TiO_2 (d-f) and Pt_3Au/TiO_2 (g-i) catalysts.

The annealed Pt_3Ag/TiO_2 dark-field image and corresponding EDX spectra (Fig. 6.4d-f) shows that the large metallic cluster is platinum-rich, while the small, flat particles are isolated silver nanoclusters. There are also small, silver-rich particles with trace amounts of platinum (Fig. A4.2), particles in the 2-8 nm size range with a molar platinum-silver composition ranging from 1:1 to 8:1, and large clusters greater than 15 nm that are enriched in platinum. A variability in the platinum-silver content within particles (as determined from STEM-EDX spot analyses) was observed for the unannealed sample (Fig.A4.3) [351].

The dark-field image of the annealed Pt_3Au/TiO_2 catalyst and corresponding EDX spectra (see Figure 6.4g-i) shows the presence of large clusters and small nanoparticles. The Pt:Au ratio is 5:1 for the large cluster, and 4:1 for the elongated, wire-shaped nanoparticle. Scans of smaller nanoparticles (in the 2 nm size range) show gold enriched platinum-gold nanoparticles, and some platinum-enriched nanoparticles (Fig.A4.4). The compositions determined using EDX are in line with compositions from Vegard's law.

6.4. CATALYTIC TESTING RESULTS

The selective oxidation of methane in the fixed bed, gas phase reactor over monometallic platinum and the bimetallic platinum nanoalloy catalysts resulted in the formation of formaldehyde (see Figure 6.5). Platinum nanoparticles supported on rutile were tested to compare the effects of alloying platinum on the rate of methane conversion and C_1-oxygenate selectivity. The rate of methane conversion over Pt/TiO_2 at 220°C ($p_{CH_4,inlet}$ = 0.2 bar, $p_{O_2,inlet}$ = 1.5 bar) is 65 μmol/g_{cat}/hr in the absence of water over Pt/TiO_2 (Fig. 6.5a). The introduction of water causes a slight increase to a maximum rate of methane conversion of 95 μmol/g_{cat}/hr at a maximum $(H_2O/CH_4)_{feed}$ ratio of 87.1 mol/mol ($p_{H_2O,\ inlet}$ = 16 bar). This could be due to an enhanced desorption of formaldehyde in the presence of steam, which may regenerate some metallic catalytically active sites. In the absence of water, the catalyst is selective towards the formation of CO_2 (Fig. 6.5b, 85%) and CO (15%). The introduction of water immediately leads to the formation of formaldehyde, which reaches a maximum of 66% at a $(H_2O/CH_4)_{feed}$ ratio of 87.1 mol/mol. The selectivity towards CO over this catalyst at $(H_2O/CH_4)_{feed}$ ratio of 87.1 mol/mol is 6%.

The catalytic activity over Pt_3Cu/TiO_2 (see Figure 6.5c) increased gradually upon the introduction of water, going from 30 μmol/g_{cat}/hr at a $(H_2O/CH_4)_{feed}$ ratio of 10.8 mol/mol (p_{H_2O} = 2.8 bar) to 53 μmol/g_{cat}/hr at a $(H_2O/CH_4)_{feed}$ ratio 32.6 mol/mol (p_{H_2O} = 8.5 bar). The rate of methane conversion then increased rapidly when the water was increased further, almost tripling to 147 μmol/g_{cat}/hr at a $(H_2O/CH_4)_{feed}$ ratio of 43.5 mol/mol (p_{H_2O} = 13.2 bar). Further increasing the amount of water in the feed increased the rate of methane conversion, with a maximum rate of methane conversion of 292 μmol/g_{cat}/hr obtained at a $(H_2O/CH_4)_{feed}$ ratio of 87.1 mol/mol (p_{H_2O} = 16 bar). In the absence of water, the catalyst was mainly selective for the formation of CO (24%) and CO_2 (76%). The introduction of water (Fig. 6.5d) initially resulted in an increase in the CO selectivity and a slight decline in the CO_2 selectivity. Further increase

in the water resulted in the formation of formaldehyde, which gradually increased to a maximum of 65% at a $(H_2O/CH_4)_{feed}$ ratio of 54.4 mol/mol.

Over the Pt_3Ag/TiO_2 catalyst (see Figure 6.5e), the rate of methane conversion decreased upon the initial introduction of water. Increasing the amount of water in the feed gradually increased the rate of methane conversion (albeit very slowly) to a maximum of 68 $\mu mol/g_{cat}/hr$ at a $(H_2O/CH_4)_{feed}$ ratio of 76 mol/mol (p_{H_2O} = 15.4 bar), which then declined to a rate of 43 $\mu mol/g_{cat}/hr$ at a H_2O/CH_4 ratio of 87 mol/mol (p_{H_2O} = 16 bar). In the absence of water, the catalyst was completely selective for the formation of CO_2 (see Figure 6.5f). The introduction of water initially led to an increase in the CO selectivity at the expense of the CO_2 selectivity. The formation of formaldehyde was observed when the $(H_2O/CH_4)_{feed}$ ratio in the feed reached 21.7 mol/mol. The formaldehyde selectivity gradually increased, reaching a maximum of 71.6% at a H_2O/CH_4 ratio of 65, then declined to a final value of 63 at a H_2O/CH_4 ratio of 87.1 mmol/mol. The decline in methane conversion and formaldehyde selectivity show a similar trend, which may indicate possible catalyst deactivation.

The Pt_3Au/TiO_2 catalyst was initially not as active as Pt_3Cu/TiO_2 (23 $\mu mol/g_{cat}/hr$) and Pt_3Ag/TiO_2 (23 $\mu mol/g_{cat}/hr$), with an initial activity of 9 $\mu mol/g_{cat}/hr$ (Fig. 6.5g). The activity increased gradually with the introduction of water, similar to the other catalysts, reaching a maximum methane conversion rate of 103 $\mu mol/g_{cat}/hr$ at a $(H_2O/CH_4)_{feed}$ ratio of 87.1 mol/mol. The selectivity trend also follows that of the other catalysts, with Pt_3Au/TiO_2 being chiefly selective for the formation of CO_2 in the absence of water (Fig. 6.5h). The formaldehyde selectivity also increased with an increase in the amount of water in the feed, reaching a maximum of 64% at a $(H_2O/CH_4)_{feed}$ ratio of 87.1 mol/mol.

The selectivity towards formaldehyde was in the order of Pt_3Au (64%) $\approx$ Pt (66%) $\approx$ Pt_3Cu (66%) < Pt_3Ag (72%). However, at the highest water partial pressure, the formaldehyde selectivity decreased to 63% for Pt_3Ag. The rate of methane conversion was in the order of Pt_3Cu (292 $\mu mol/g_{cat}/hr$) > Pt_3Au (103 $\mu mol/g_{cat}/hr$) $\geq$ Pt (95 $\mu mol/g_{cat}/hr$) while Pt_3Ag was the least active, with a maximum activity of 68 $\mu mol/g_{cat}/hr$.

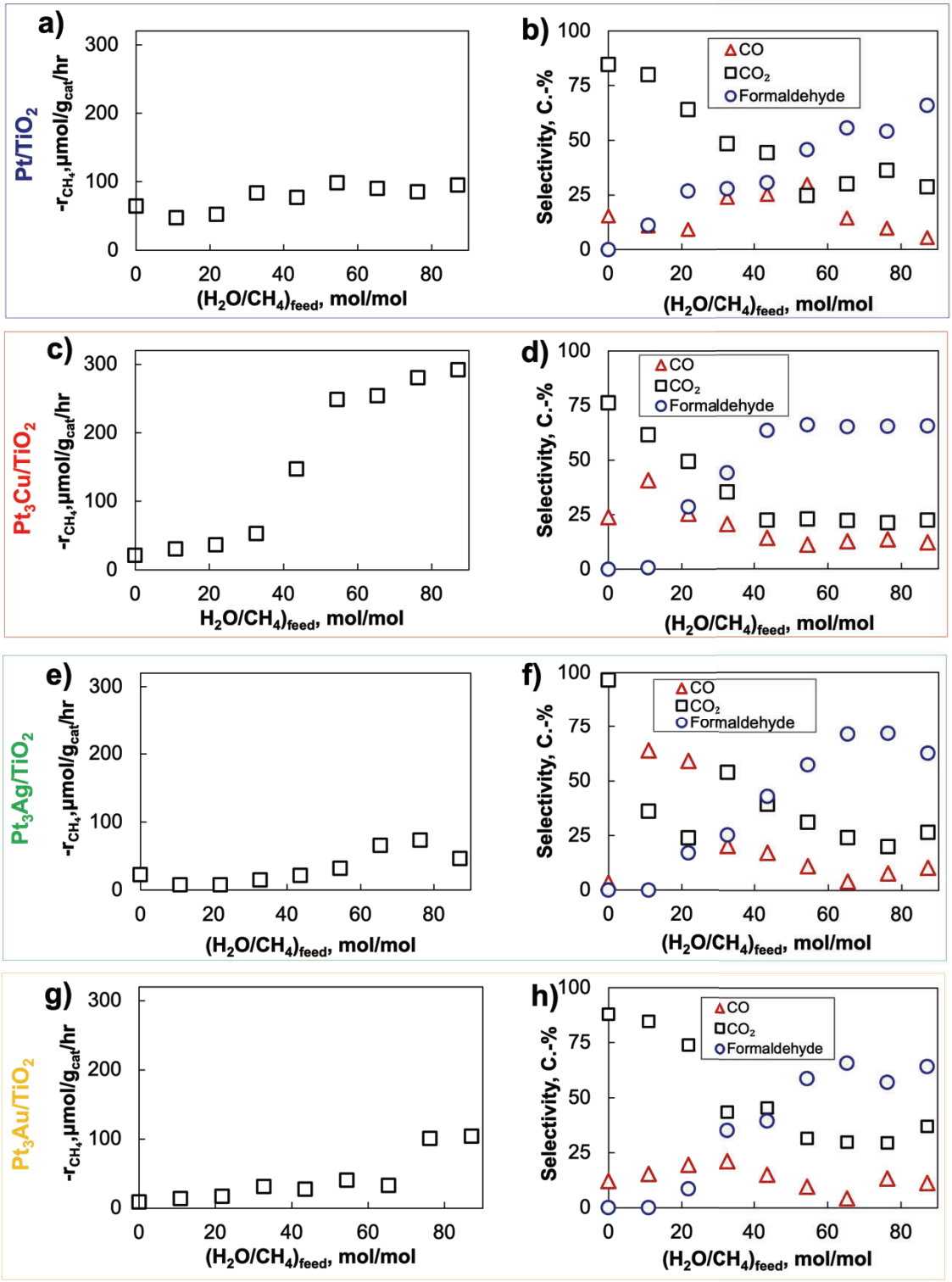

Figure 6.5: The rate of methane conversion over a) Pt/TiO_2-rutile, c) Pt_3Cu/TiO_2, e) Pt_3Ag/TiO_2 and g) Pt_3Au/TiO_2 and the corresponding CO, CO_2 and formaldehyde selectivities obtained over b) Pt/TiO_2, d) Pt_3Cu/TiO_2, f) Pt_3Ag/TiO_2 and h) Pt_3Au/TiO_2. Conditions: Conditions: T=220°C, P_{total}=20 bar, p_{CH_4} = 0.2 bar, p_{O_2} = 1.5 bar.

The activity and selectivity of Pt_3Cu/TiO_2 and Pt_3Ag/TiO_2 for the selective oxidation of methane in the presence of liquid water were further investigated in the trickle bed reactor. The rate of methane conversion and corresponding CO, CO_2 and formaldehyde selectivities are presented in Figure 6.6. The activity displayed by Pt_3Cu/TiO_2 for the rate of methane conversion (Fig. 6.6a) increased to 320 μmol/g_{cat}/hr, which is slightly larger than obtained in the gas-phase reactor (Fig. 6.5a). The formaldehyde selectivity also increased, from 65% in the gas phase (Fig. 6.6, b) to 78% in the trickle bed reactor. Some methanol was formed as well, obtaining a maximum methanol selectivity of 2% (bringing the oxygenate selectivity to 80%), which was not observed in the gas-phase reactor. The increase in the formaldehyde selectivity in the presence of liquid water, over Pt_3Cu/TiO_2 may be due to water inhibiting the re-adsorption of formaldehyde on the catalyst surface, thereby preventing the further oxidation of the formed formaldehyde.

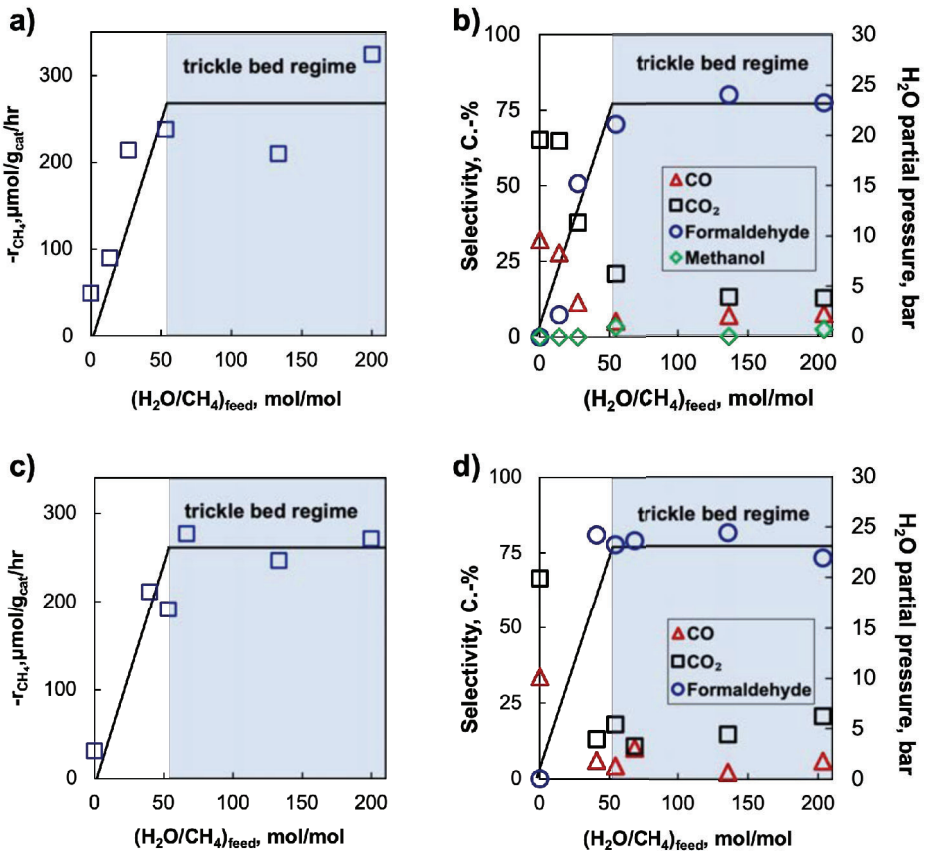

Figure 6.6: The rate of methane conversion as a function of the water to methane mole ratio in the feed over Pt_3Cu (a) and Pt_3Ag (c) and the corresponding oxygenate selectivity over Pt_3Cu (b) and Pt_3Ag (d). Conditions: T=220°C, P_{total}=30 bar, p_{CH_4} = 0.5 bar, p_{O_2} = 1.5 bar.

Testing Pt_3Ag/TiO_2 in the presence of liquid water resulted in a three-fold increase in the rate of methane conversion, increasing from 68 μmol/g_{cat}/hr to 271 μmol/g_{cat}/hr (see Figure 6.6c), with an increase in the formaldehyde selectivity from 63% (Fig. 6.5d) in the gas phase to 73 in the presence of liquid water (Fig. 6.6d), with a maximum selectivity of 81% at $(H_2O/CH_4)_{feed}$ mol/mol ratio of 136). The presence of water could also have possibly removed residual surfactant, which would effectively clean the catalyst, thereby enhancing the rate of methane conversion. The historical time on line activities of the catalysts are presented in Figure A4.5-A4.8 in Appendix 4.

6.4.1. CHARACTERISATION OF THE RECOVERED CATALYSTS

After testing, the catalysts recovered from the gas phase reactor were characterised with powder X-ray diffraction to determine reaction-induced changes in the catalyst, TEM to visualize changes in particle morphology and FTIR to monitor the formation of organic deposits.

Figure 6.7 shows the XRD patterns of the recovered nanoalloy catalysts, accompanied by the dark-field TEM images and particle-size distribution histograms of the recovered catalysts. The PXRD pattern of the recovered Pt_3Cu/TiO_2 catalyst shows the presence of sharper peaks, which may indicate an increase in the crystalline domain size, which was indeed determined to be 16 nm via Rietveld refinement. This may indicate further sintering of the nanoparticles on the support which occurred during the selective oxidation of methane. The diffraction lines belonging to the FCC-structure also appear to be shifted to lower diffraction angles, possibly indicating further dealloying of the platinum-copper nanoparticles. The lattice parameter was determined to be 0.391 nm, which represents an expansion of the lattice, and corresponds to a platinum-enriched phase (Pt:Cu ~ 9).

The PXRD pattern of the recovered Pt_3Ag/TiO_2 catalyst shows the presence of sharp diffraction lines indicating the presence of crystalline metallic phases. The peak associated with the Pt(111) line appears to have broadened in the direction of lower diffraction angles and resembles the profile of the unannealed samples, which may indicate different platinum-silver crystalline phases and/or species, and the presence of Ag enriched phases. The crystalline domain size was determined to be 11 nm (which is slightly larger than that of the annealed sample). The lattice parameter of the recovered sample is 0.393 nm, which is the same as that of the annealed sample, which may indicate that no further Pt and Ag compositional changes occurred during the reaction.

The PXRD pattern of the recovered Pt_3Au/TiO_2 catalyst does not show signs of significant changes in the crystalline structure. The crystalline domain size was determined to be 5.5 nm, and the lattice parameter remains 0.394 nm.

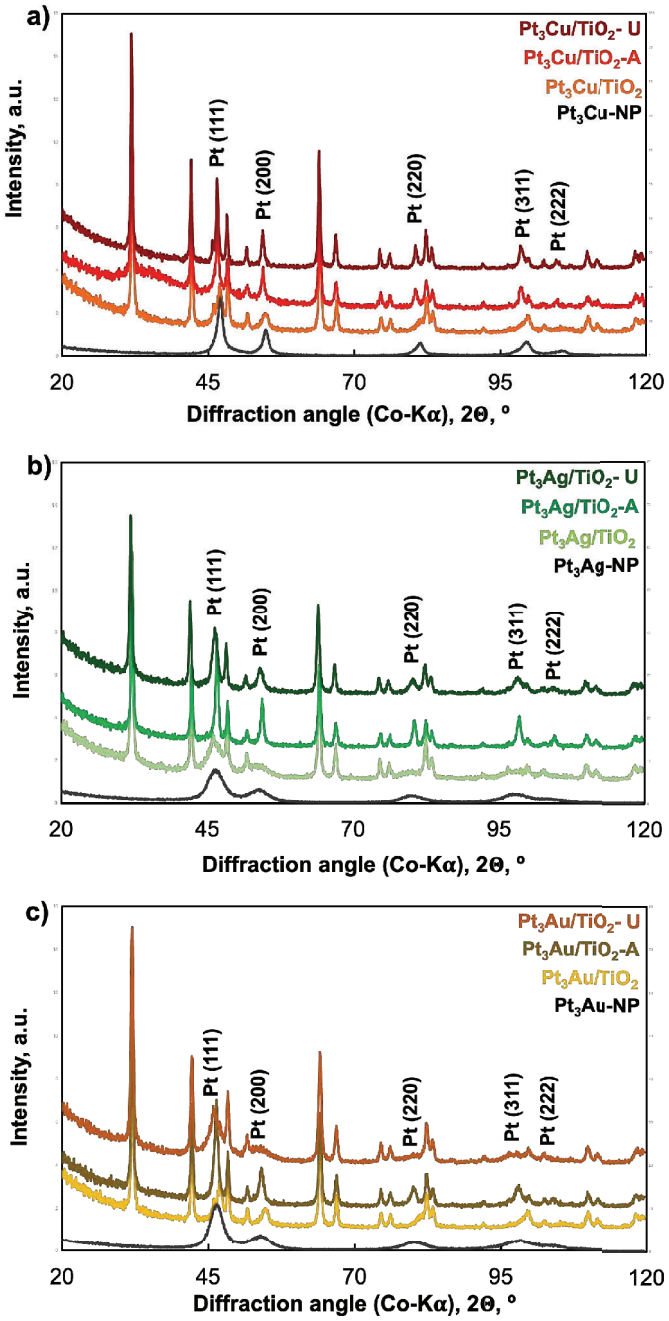

Figure 6.7: PXRD patterns of the nanoparticles before deposition on the support (denoted NP), the supported nanoparticles and the supported, annealed (A) and recovered (R) Pt_3Cu (a), Pt_3Ag (b) and Pt_3Au (c) nanoparticles and supported catalysts.

Transmission electron microscopy images were obtained for the recovered catalysts, and are presented in Figure 6.8. The TEM images of the Pt_3Cu/TiO_2 (Fig. 6.9 a-c)catalyst show well-dispersed particles in the 5-15 nm size range, which indicates that no further sintering occurred in-situ. The TEM images of the recovered Pt_3Ag catalyst on the other hand shows presence of nanoparticles in the 2-3 nm, 4-7 nm and 10-35 nm size range (Fig. A4.5).

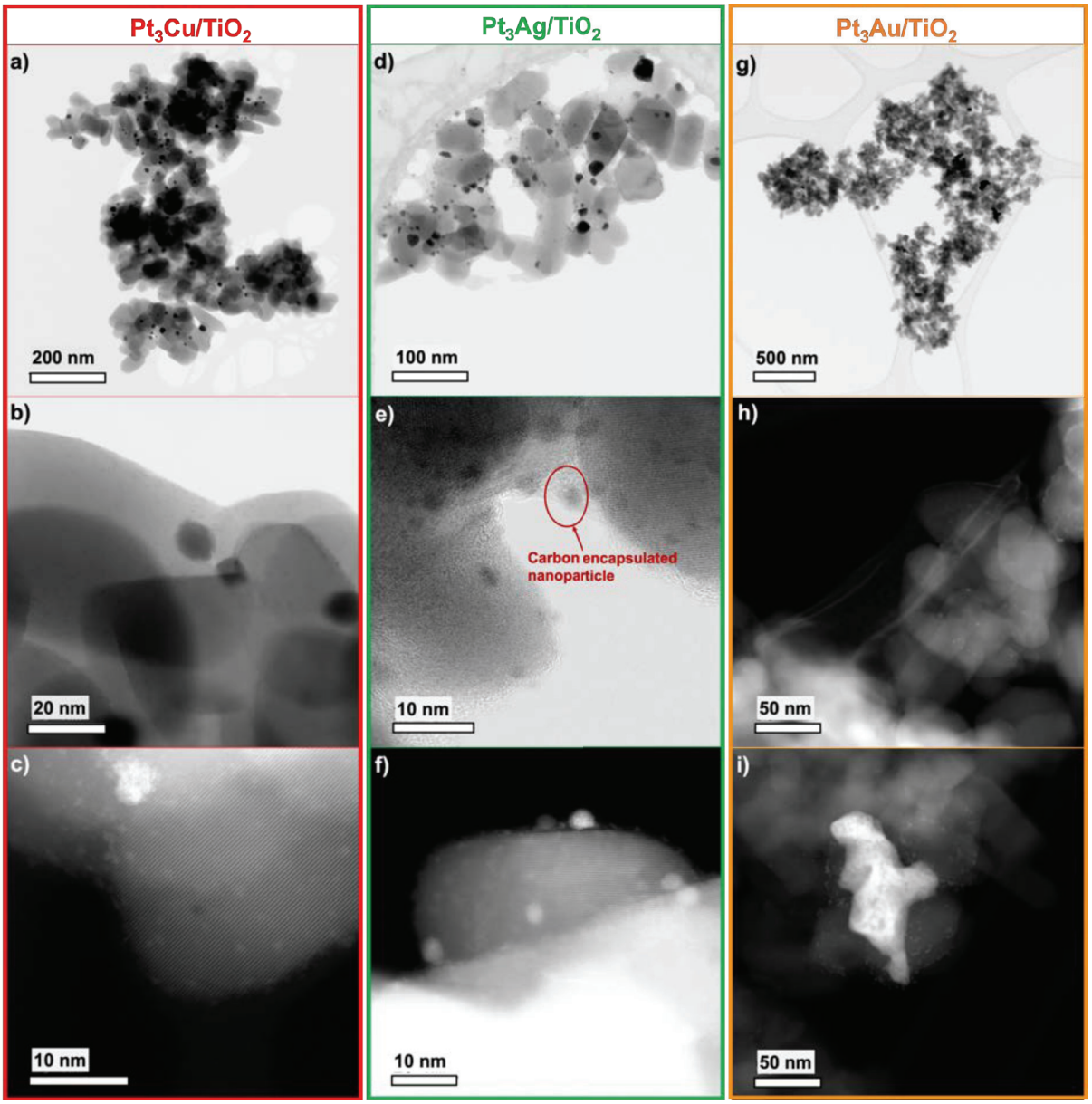

Figure 6.8: Bright-field transmission electron microscopy and images obtained at high magnification images of the recovered Pt_3Cu/TiO_2 (a-c), Pt_3Ag/TiO_2 (d-f) Pt_3Au/TiO_2 (g-i) catalysts recovered from the gas-phase reactor.

The most surprising TEM images were those obtained for the recovered Pt_3Au/TiO_2 catalyst, which shows the presence of irregular particles in the size range of 50 nm (see Fig. A4.9c), and small particles and nanowires in the 3-4 nm size range (Figures 6.8 h and i). However, there are regions with irregularly shaped, 0.5 μm sized particles (Fig.A4.4e). These results are in contradiction to those obtained from XRD, which show the crystalline domain size to be much smaller than the sizes determined from TEM. However, despite a polynomial particle size distribution, it seems most of the Pt_3Au nanoparticles are in the range of 2-6 nm (Fig. A4.9,

PSD). This may indicate the large clusters break apart during the reaction and become re-dispersed.

The Pt_3Ag/TiO_2 (Figures 6.8 d and e) and Pt_3Au/TiO_2 (Figure 6.8 h) show signs of carbon deposition. The deposit on Pt_3Ag/TiO_2 seems to originate from the metal-support interface, as the deposit is found between the metal and the support. It eventually encapsulates the metal nanoparticles, removing them from the support (Fig. 6.8 e). Figure 6.9 shows a high resolution image of a metal nanoparticle on a titania particle (showing the (110) crystallographic plane of TiO_2-rutile with d-spacing of 0.32 nm) [355]. Deposits can be seen at the base of the platinum nanoparticle and appear to be located at the metal-support interface. The material is seemingly absent on the recovered Pt_3Cu/TiO_2 catalyst, and was not visible on the TEM images obtained prior to reaction, indicating that the material may have been formed during the reaction.

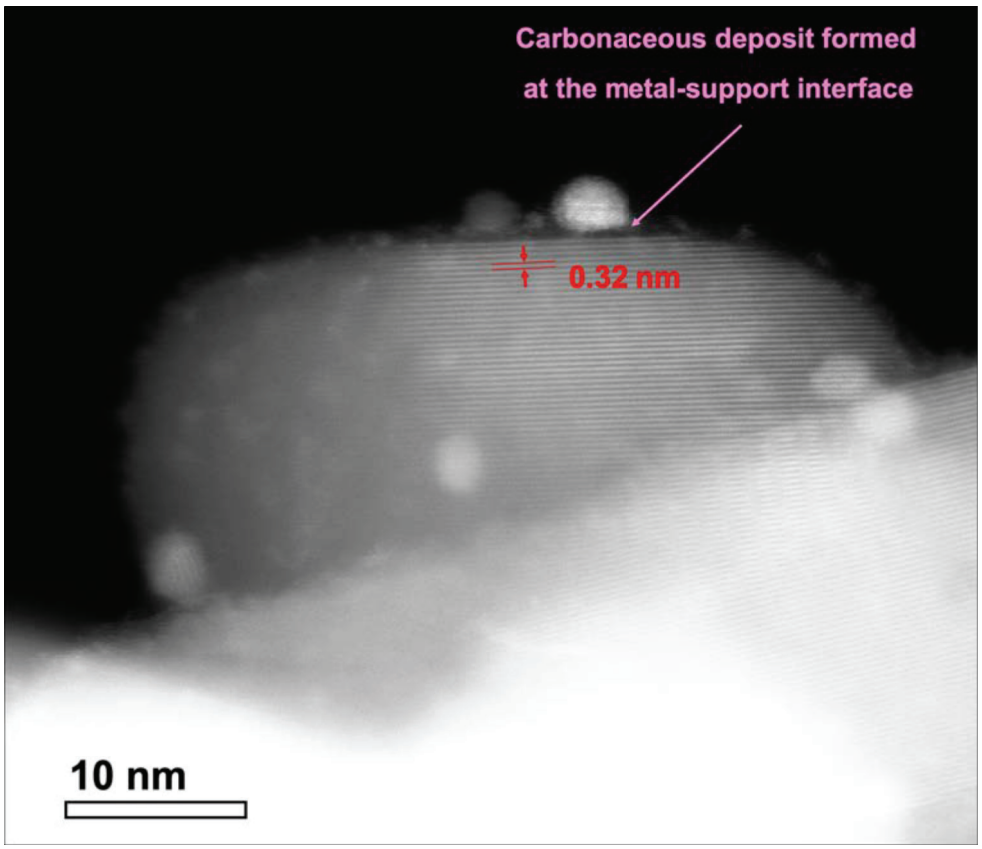

Figure 6.9: High-resolution dark field TEM image of the recovered Pt_3Ag/TiO_2 from the gas phase reactor showing the carbonaceous film at the metal-support interface.

STEM EDX spectra of the recovered catalysts recovered from the gas phase reactor are shown in Figure 6.10. The EDX spectra of the recovered Pt_3Cu/TiO_2 catalyst (Fig. 6.10a-c) shows

large, platinum-enriched clusters and small particles that consist of platinum alloyed with copper.

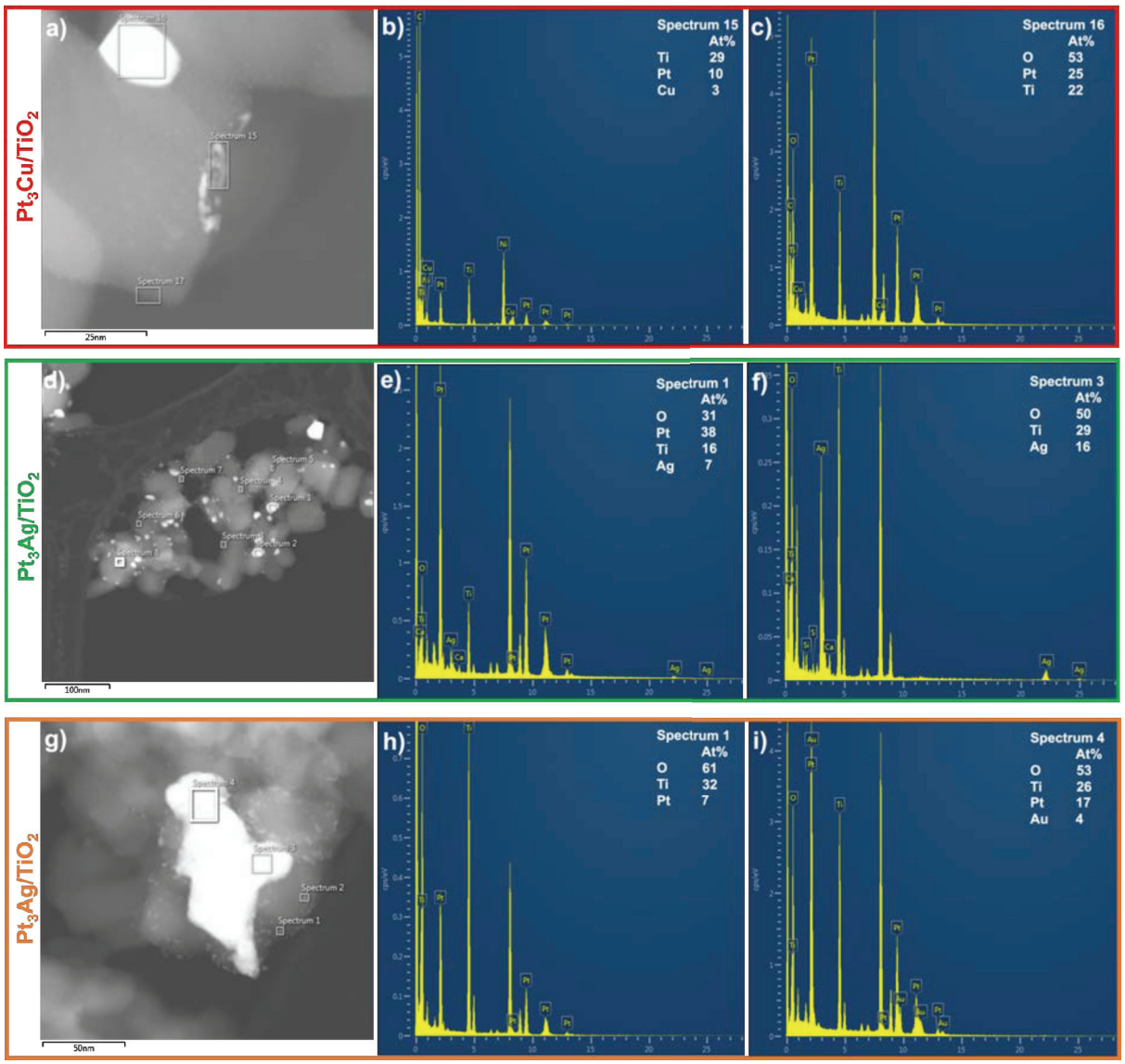

Figure 6.11: STEM-EDX scans showing the association between platinum and the alloying element for the recovered Pt_3Cu/TiO_2 (a-c), Pt_3Ag/TiO_2 (d-f) and Pt_3Au/TiO_2 (g-i) catalysts.

The EDS spectra of the recovered Pt_3Ag/TiO_2 catalyst (Fig. 6.10 d-f) shows the presence of particles with a size of ca. 10 nm that are composed of platinum and silver, but with a relative high platinum content (Pt : Ag = 5:1), and small, flattened silver nanoparticles in the 2 nm size range. The spectra obtained for the recovered Pt_3Au/TiO_2 catalyst shows a large, platinum-rich cluster that is composed of platinum and silver (Fig. 6.10 g-i). Interestingly, there are nanowires around this particle, which are seemingly pure platinum nanoparticles, in the 2-nm range. The

EDX spectra of the amorphous material observed in Figure 6.8 e and h indicated that the material is composed of carbon (Fig.A4.10).

The attenuated total reflectance – infrared (ATR-IR) spectra of the fresh, pre-treated and recovered Pt_3Ag/TiO_2 catalyst was obtained, since this catalyst showed obvious signs of carbon deposition. The recovered catalyst samples were obtained from the gas-phase and trickle-bed reactors, in order to determine if the higher activity and selectivity obtained in the trickle-bed reactor was due to hydrolysis of the carbonaceous species in the presence of liquid water (Fig. 6.11). The Pt_3Cu/TiO_2 and Pt/TiO_2 spectra are included for reference. The FBR and TBR coding refers to the reactor the catalyst was recovered from. The ATR-IR spectra of both catalysts, before pre-treatment, shows the presence of peaks that are associated with the surfactant used during the synthesis of the nanoparticles, which disappear after annealing.

The ATR-IR spectrum of the recovered Pt_3Cu/TiO_2 catalyst does not show any additional bands, and resembles that of the pre-treated catalyst. The spectra of the recovered Pt_3Ag/TiO_2 catalyst, on the other hand, shows the presence of bands that indicate the deposition of carbon-based species on the catalyst. The sample that was recovered from the gas-phase reactor (Pt_3Ag/TiO_2-R-FBR) shows new absorbance bands at 1018 and 1203 cm^{-1}, while the catalyst recovered from the trickle bed reactor (Pt_3Ag/TiO_2-R-TBR) shows a new band at 1018 and a shoulder at 1104 cm^{-1}. The bands at 1018-1104 cm^{-1} correspond to C-O-C stretching vibrations while the bands at ca. 1200 cm^{-1} potentially correspond to CH_2 rocking transitions [314]. The presence of these bands further confirms the presence of carbonaceous species on the recovered Pt_3Ag/TiO_2 catalyst, as indicated by the TEM image. Similar absorbance bands were observed on the recovered, Pt/TiO_2 catalyst (Fig. A4.11f), which appeared slightly shifted to higher wavenumbers (1030 and 1220 cm^{-1}).

The extent of carbon deposition on the catalyst tested in the trickle-bed reactor seems to be less than that of the catalyst tested in the fixed bed reactor, which may possibly indicate the removal of the carbonaceous species in the trickle bed reactor with liquid water. Water may also prevent carbon-deposition through facilitating the efficient desorption of formaldehyde, which would minimise the formation of the polyoxymethylene polymer. This would then prevent encapsulation of the metal nanoparticles, thereby preventing the deactivation of the catalytic active sites by protecting them from occlusion by the carbonaceous deposit. This could possibly explain the improved catalytic activity obtained over Pt_3Ag/TiO_2 in the trickle-bed reactor, compared to the activity obtained in the fixed reactor. Furthermore, the Pt_3Ag/TiO_2 catalyst

was found to deactivate to a significant extent in the fixed-bed reactor (Fig. A4.12a), while the catalytic activity was more stable in the trickle-bed reactor (Fig. A4.12b).

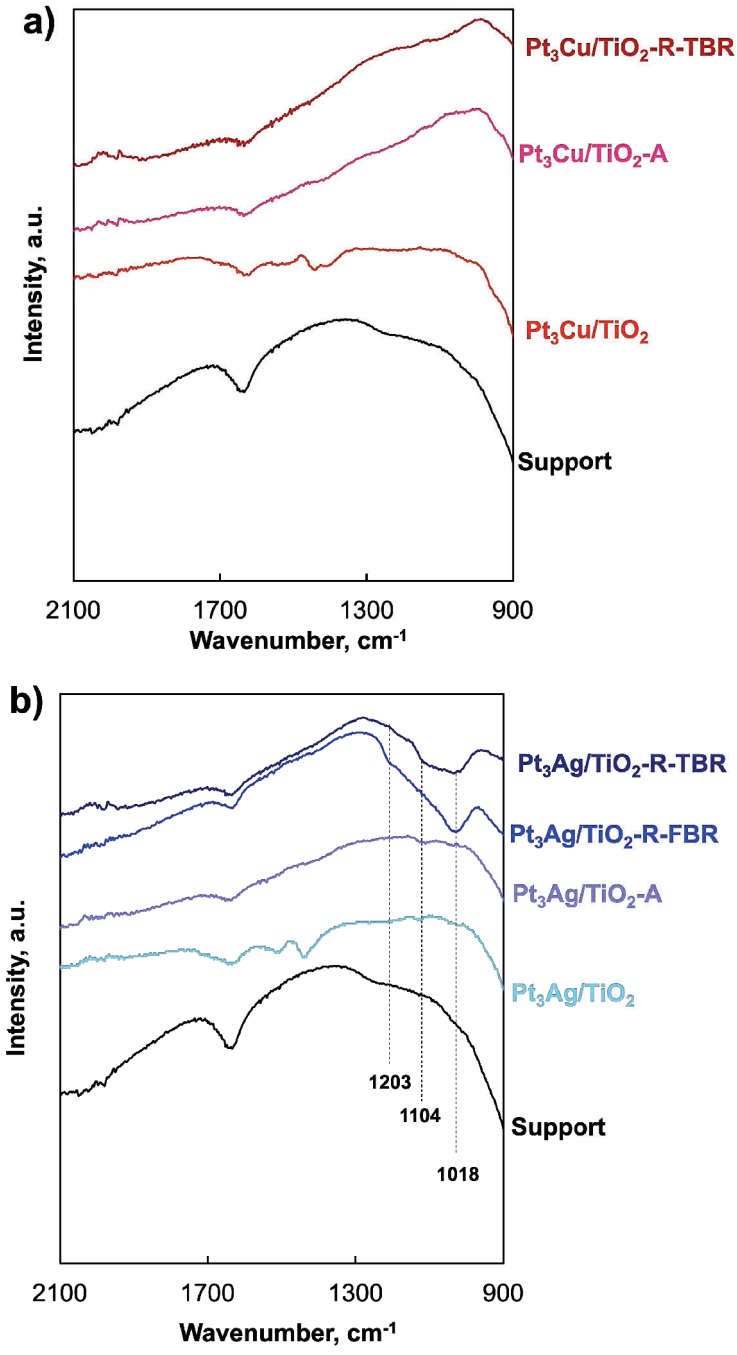

Figure 6.11: ATR-IR spectra of the Pt_3Cu/TiO_2 (a) and Pt_3Ag/TiO_2 (b) catalysts. The spectra were obtained for the supported nanoparticles, the pre-treated (annealed) catalysts, and for the recovered catalysts.

6.5. DISCUSSION

The selective oxidation of methane over platinum and platinum nanoalloy catalysts yielded with good selectivity formaldehyde in the presence of water. The main finding from these experiments is that the formation of formaldehyde requires the presence of water, and that water in the liquid phase greatly enhances the formaldehyde selectivity, and enhances catalyst stability (see Figure A4.6). Alloying platinum with copper resulted in a catalyst that was highly active, achieving a rate of reaction that is three times that of the pure platinum catalyst, and a similar formaldehyde selectivity. The platinum-gold catalyst displayed a similar activity to the pure platinum catalyst, while the platinum silver catalyst deactivated, obtaining the lowest rate of methane conversion. The turnover frequency achieved with the Pt-based catalysts reported herein is ca. 2 h^{-1} (Table 6.3). The turnover frequencies and productivities achieved herein are comparable to those achieved over the Cu-MOR and Cu-CHA systems [28, 173] and some of the PdAu systems [182, 184].

Table 6.3: Summary of the activity and productivity for CO, CO_2 and formaldehyde obtained over the platinum nanoalloy catalysts in the fixed-bed and trickle-bed reactors

Catalyst	**X_{CH_4} %**	**$-r_{CH_4}$ $\mu mol/g_{cat}/hr$**	**TOF h^{-1}**	**Oxygenate productivity $\mu mol/g_{cat}/hr$[d]**		
				CO	**CO_2**	**CH_2O**
Pt/TiO_2[a]	0.3 ± 0.27	95 ± 80	2.2 ± 1.9[c]	5.0 ± 3.5	27 ± 7.7	63 ± 83
Pt_3Cu/TiO_2[a]	1.1 ± 0.19	292 ± 47	2.5 ± 0.42[c]	35 ± 34	66 ± 10	192 ± 38
Pt_3Cu/TiO_2[b]	*5.1± 2.7*	*320 ± 158*	*2.6 ± 1.3[c]*	*24 ± 2.6*	*40 ± 5.0*	*250 ± 155*
Pt_3Ag/TiO_2[a]	0.3 ± 0.10	43 ± 18	0.5 ± 0.1[c]	5.0 ± 1.7	11 ± 2.6	27 ± 13
Pt_3Ag/TiO_2[b]	*3.0 ± 0.62*	*271± 55*	*2.9± 0.5 [c]*	*16 ± 3.1*	*55 ± 11*	*198 ± 55*
Pt_3Au/TiO_2[a]	0.6 ± 0.16	103 ± 28	2.3 ± 0.6[c]	12 ± 3.0	39 ± 7.7	67 ± 19

[a] Fixed-bed reactor, 220°C, P_{total}=20 bar, p_{CH_4} = 0.2 bar, p_{O_2} = 1.5 bar, p_{H_2O}=16 bar, $(H_2O/CH_4)_{feed}$=87 mol/mol; [b] Tested in a trickle bed reactor at 220°C, P_{total}=30 bar, p_{CH_4} = 0.5 bar, p_{O_2} = 1.5 bar, p_{H_2O}=23 bar, $(H_2O/CH_4)_{feed}$=204 mol/mol; [c] Turnover frequency (TOF) based on the metal dispersion determined from the metal dispersion measured with oxygen.

The more facile desorption of formaldehyde due to the effects of alloying platinum with copper, may have also reduced the likelihood of the transformation of formaldehyde to polymeric deposits on the support active sites, particularly in the presence of liquid water. This may

explain the absence of polymeric deposits on the Pt_3Cu/TiO_2 catalyst (see Figure 6.11b, and Figures A4.4 - A4.5).The correspondingly lower catalytic activity over Pt_3Ag/TiO_2 in the gas phase could be attributed to the formation of a polymeric deposit on the catalyst surface, which eventually encapsulated the metallic nanoparticles, causing their removal from the titania support (see Fig. 6.8d). The catalyst was slightly more active in the trickle-bed reactor, which may indicate that water prevents the formation of a deactivating polyoxymethylene deposit, thereby improving the catalytic activity, albeit slightly.

Previously, it was postulated that formaldehyde may form from a di-σ-hydroxy-methoxy intermediate, that desorbs as methane diol which undergoes dehydration to formaldehyde in the gas phase [262]. The slow desorption of this intermediate may thus result in its polymerisation at the metal-support interface, leading to the formation of the oligomeric material that has been detected with TEM and infrared analyses. This may be more likely to form over the Pt/TiO_2, Pt_3Ag/TiO_2 and Pt_3Au/TiO_2 catalysts since the binding strength of oxygenates on these metal surfaces is expected to be stronger. Platinum is known to bind oxygen atoms strongly [229], while alloying platinum with gold and silver is likely to cause an upshift in the platinum d-band centre, which may further increase the binding strength of oxygenates on the metallic surface [356, 357].

It is interesting to note that the presence of liquid water greatly enhanced the activity and oxygenate selectivity of the Pt_3Ag/TiO_2 catalyst. The activity increased by a factor of 6 in the trickle bed reactor, whilst the formaldehyde selectivity increased slightly from 63% to 73%. The increase in catalytic activity and stability with the presence of liquid water may be due to the liquid water acting as a hydrogen shuttle that aids in the desorption of the adsorbed di-σ-hydroxy-methoxy intermediate [78]. Rutile is a relatively hydrophobic support [358] which means that under trickle bed operation, water may be localised around the metallic phase, with minimal interaction between water and the rutile support. The water surrounding the metallic active phase (upon which the di-σ-hydroxy-methoxy intermediate is adsorbed) will effectively transfer a hydrogen to the di-σ-hydroxy-methoxy intermediate, converting it to methanediol. Methanediol is then dissolved (i.e. solvated) in the aqueous phase, thus facilitating its removal from the metallic active site [27, 319, 359].

It is also possible that the enhanced activity is due to liquid water removing residual surfactant more effectively than the gas-phase pre-treatment. This could result in an improvement in the catalytic activity as observed over both Pt_3Cu/TiO_2 and Pt_3Ag/TiO_2 in the trickle-bed reactor.

Some polymeric deposits are formed on the Pt_3Ag/TiO_2 catalyst upon exposure to conditions of the selective oxidation of methane in a trickle bed reactor (Fig. 6.12b), which indicate that some of the di-σ-hydroxy-methoxy intermediate undergoes polymerisation at the metal-support interface, although not to the same extent as that observed in the fixed-bed reactor.

6.6. CONCLUSION

The selective oxidation of methane over platinum-based nanoalloy catalysts using oxygen as an oxidant, in the presence of steam, resulted in the formation of formaldehyde, CO and CO_2. The presence of steam was necessary for the formation of formaldehyde, since in the absence of steam, the catalysts were chiefly selective for the formation CO_2. The catalytic activity of the Pt_3Cu/TiO_2 catalyst in the selective oxidation of methane in the gas phase was superior ($-r_{CH_4} = 292$ μmol/g_{cat}/hr), followed by that of the Pt_3Au/TiO_2 catalyst ($-r_{CH_4} = 103$ μmol/g_{cat}/hr), Pt/TiO_2 ($-r_{CH_4} = 95$ μmol/g_{cat}/hr), with Pt_3Ag/TiO_2 catalyst being the least active catalyst ($-r_{CH_4} = 43$ μmol/g_{cat}/hr). The latter was ascribed to the formation of deposits on the catalyst surface, that served to occlude the catalytically active sites through encapsulation.

Testing Pt_3Cu/TiO_2 in the trickle bed reactor resulted in an improvement in the oxygenate selectivity, with the formaldehyde selectivity increasing from 66 % to 78%, while the catalyst became selective for the formation of methanol (with a 2.3% selectivity). The activity of the Pt_3Ag/TiO_2 catalyst increased markedly in the presence of liquid water ($-r_{CH_4} = 277$ μmol/g_{cat}/hr), which was accompanied by a slight increase in the formaldehyde selectivity (from 63% in the gas phase to 73% in the presence of liquid water). The presence of liquid water also enhanced the catalyst stability to a significant extent, while the catalyst deactivated in the gas-phase.

From the results reported herein, it can be concluded that alloying platinum with copper enhances the desorption of methanediol to form formaldehyde, which enhances the rate of reaction. The presence of liquid water is important since it enhances the formaldehyde selectivity, and prevents catalyst deactivation by minimising the formation of formaldehyde oligomers on the catalyst surface. The best performing catalyst in this series was the platinum-

copper nanoalloy, and it warrants further investigation in order to probe further the effects of liquid water.

CHAPTER VII: GENERAL DISCUSSION

The selective oxidation of methane using oxygen as an oxidant is a challenging reaction, whose reaction pathway needs to occur via a mechanism which facilitates the formation of a surface methoxy-intermediate, a key intermediate in the formation of selective oxidation products [238, 248, 255]. DFT studies indicate that the formation of a methoxy intermediate can be achieved by the activation of methane via a homolytic cleavage of the methane C-H bond with electrophilic oxygen species [238]. Thus, the selective oxidation of methane would necessitate the activation of methane over an oxygen-covered surface [234, 235].

To achieve the oxygen covered surface, it is necessary to use a metal that is active for the dissociation of oxygen. The metal must also be stable against oxidation, in order to prevent phase changes during the reaction, and to prevent the activation of methane by nucleophilic oxygen species, which would occur via a heterolytic pathway yielding a methyl fragment, which may result in the formation of deep oxidation products [235]. Hence, platinum was seen as a rational starting point for the design of metal-based selective oxidation of methane [225].

7.1. RATIONALE FOR PLATINUM AS AN ACTIVE METAL

The selective oxidation of methane to C_1-oxygenates using oxygen as an oxidant was first attempted over platinum-based catalysts in a fixed-bed reactor equipped with an evaporator for the generation of steam. In the absence of steam, the catalysts were active for the total oxidation of methane to CO_2. The introduction of steam resulted in the formation of selective oxidation products such as formaldehyde, methanol, methoxy-methanol and trioxane, albeit at a very low conversion of ca. 0.1%. Accidentally flooding the reactor resulted in enhanced product selectivity, spurring us to perform the reaction under (controllable) trickle bed conditions.

At the same time, findings from an MSc DFT-based study in our research group [257] proposed a method for obtaining a high surface coverage of platinum with oxygen containing species by co-feeding water with oxygen, as a full coverage of platinum with only adsorbed oxygen atoms is difficult to achieve due to lateral interactions between the adsorbed oxygen atoms [259]. These findings were then consolidated to design a process for the selective, aerobic oxidation of methane using oxygen as an oxidant. A trickle-bed reactor was designed and commissioned to investigate the effect of liquid water on the selectivity towards C_1-oxygenates.

7.2. MECHANISTIC AND KINETIC EFFECTS OF WATER

In the absence of water, the oxidation of methane over platinum-based catalysts only yielded the deep oxidation products, CO_2 and CO. The oxidation of methane over metal surfaces proceeds via the activation and cleavage of the methane C-H bond to form an adsorbed OH species, and adsorbed methyl (CH_3) species at low surface coverages [234, 360]. The methyl species undergoes facile dehydrogenation over bare metal surfaces, followed by oxidation with O_{ads} to form CO_2 or CO, as presented in Scheme 7.1. [360, 361]. The key then lies in preventing the formation of adsorbed $CH_{3(ads)}$ species during the C-H bond cleavage step and instead promoting the formation of an adsorbed CH_3O intermediate, which can be achieved through the addition of water [248, 251].

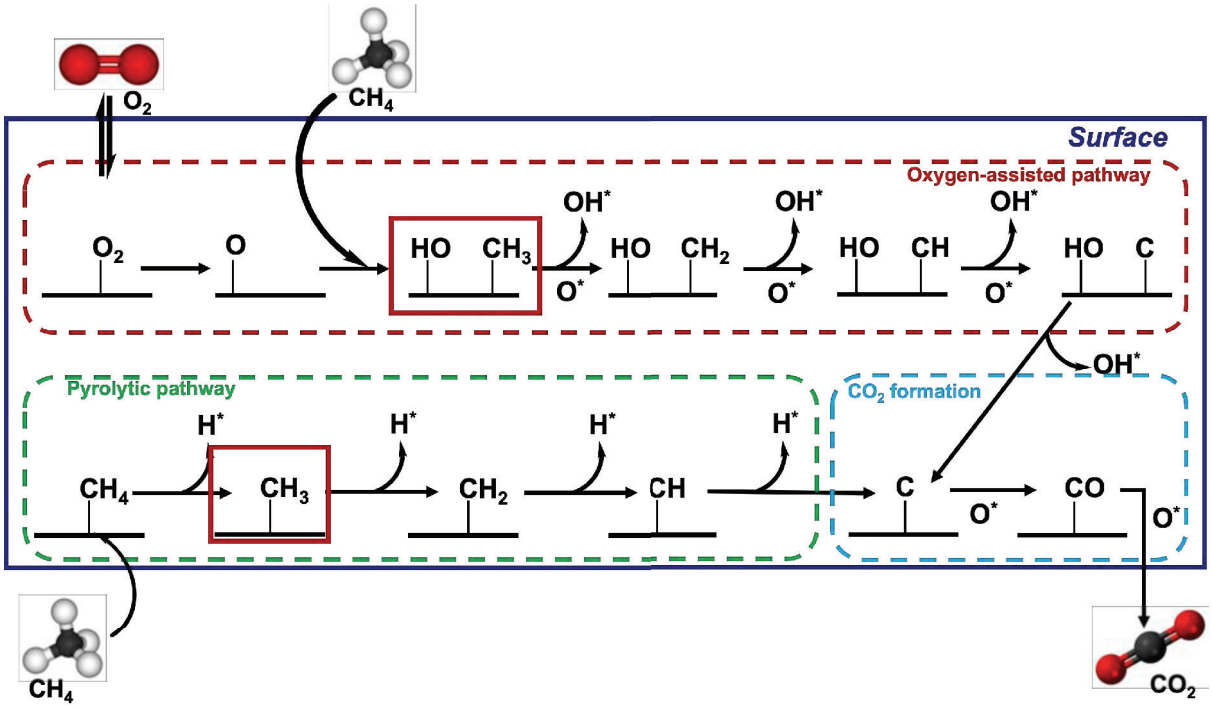

Scheme 7.1: Proposed mechanism for the formation of CO and CO_2 during the oxidation of methane over metal surfaces.

Co-feeding water resulted in the formation of formaldehyde. Increasing the H_2O/CH_4 ratio in the feed enhanced not only the formaldehyde selectivity, but also the rate of methane consumption. DFT calculations showed that water reacts with adsorbed oxygen species to form adsorbed OH groups on the Pt(111) surface, which enhances the surface coverage on platinum [273]. These hydroxyl groups have been identified to act as site-blockers that facilitate the formation of adsorbed methoxy species through enforcing interaction of methane with adsorbed oxygen atoms rather than bare metallic sites which would otherwise yield surface

methyl species [245, 248]. Hydroxyl groups also play a role in the formaldehyde formation pathway through reacting with the methoxy species to form a di-σ-hydroxy-methoxy intermediate which has been identified as a formaldehyde or formaldehyde hydrate precursor [262]. The proposed mechanism for the formation of formaldehyde in the presence of water is presented in Scheme 7.2.

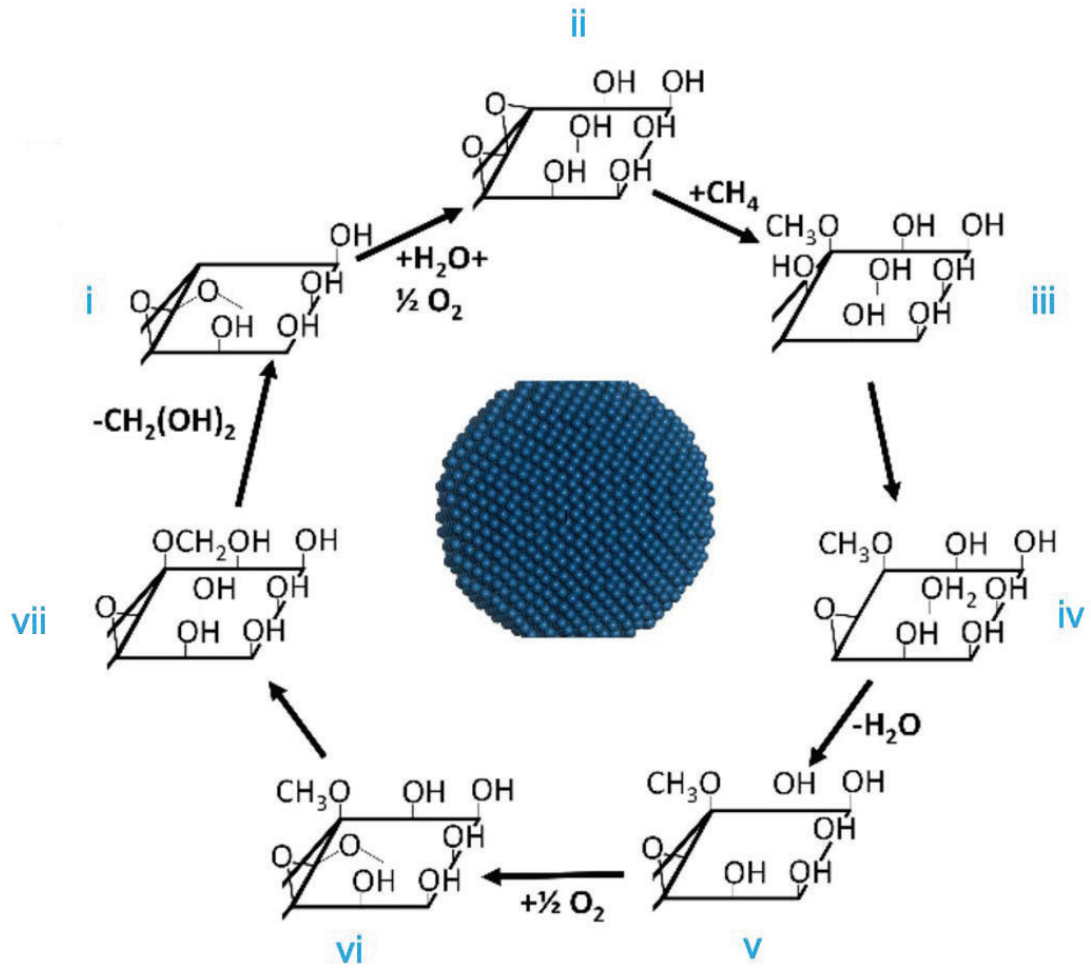

Scheme 7.2: Mechanism for the formation of formaldehyde over a metal surface in the presence of water and oxygen [78].

It has been previously shown that edge sites are preferentially covered with adsorbed oxygen atoms [362]. Hence, it is postulated that methane is initially activated on oxygen atoms located on the platinum edge sites to yield an adsorbed methoxy species (CH_3O_{ads}) and an adsorbed hydroxy species (OH_{ads}) located on the edge sites. The surface hydroxyl species undergoes deprotonation by an adjacent adsorbed hydroxyl species to yield an adsorbed water molecule and O_{ads} located on the edge site. The water molecule desorbs, leaving a vacant site that can subsequently be occupied by an oxygen atom. This oxygen atom dehydrogenates the CH_3O_{ads}

species, which then couples with an adjacent OH_{ads} fragment to yield the di-σ-hydroxy-methoxy intermediate. Water can thus be identified as a co-reactant that directs the reaction pathway towards the formation of the precursor for formaldehyde (in the form of a surface bound di-σ-hydroxy-methoxy species) [78, 248]. Hydrogen transfer from either adsorbed water or adsorbed hydroxyl groups to the di-σ-hydroxy-methoxy intermediate yields methanediol, which desorbs and dehydrates in the gas phase to form formaldehyde.

Alternatively, the formed methanediol may not desorb to form formaldehyde, instead undergoing acid/base catalysed transformations at the metal-support interface to yield species such as dioxymethylene, trioxane and polyoxymethylene [321]. Trioxane was observed to be a dominant product during the selective oxidation of methane over platinum-based catalysts (dispersed on the rutile phase of titania) in the gas-phase reactor, where water was introduced as steam instead of liquid water (Fig. A2.2) [78]. Hence, the second function of water is that of a desorption facilitator via solvation of the methanediol [247]. The increase in the rate of methane conversion typically observed when the H_2O/CH_4 ratio increases in the feed is attributed to the enhancement of the rate of product desorption, which regenerates the platinum active sites thus availing them for the next catalytic cycle.

7.3. INFLUENCE OF THE SUPPORT

The formation of C_1 oxygenates is not only tied to the presence of water but was found to also be influenced by the identity of the support used to disperse the active phase. The primary role of a support is to disperse the catalytically active platinum nanoparticles. Carbon-black, which possessed the highest surface area, yielded the most dispersed catalyst, while the metal dispersions on alumina (Al_2O_3) and titania (rutile and P25) were similar. The rate of methane consumption achieved over Pt/C was significantly higher than that of platinum supported on oxides. The higher catalytic activity obtained over Pt/C might be due to the high dispersion of platinum on this catalyst, which exposes a higher concentration of corner and edge sites which are postulated to be highly active for the dissociative activation of oxygen [287]. This would indicate that the reaction may be structure-sensitive [78, 363], although the obtained catalytic activity may be obscured by the extent of catalyst deactivation as well.

C_1-oxygenates belong to a class of rather reactive organic molecules, which may undergo further conversion via support-catalysed reactions [364, 365]. Hence, the acid/base properties of the catalyst carrier are an important consideration. This was highlighted by the discrepancy in the oxygenate selectivities obtained over the different catalysts. The density of acid sites per

unit mass of catalyst (as a measure for the number of acid sites loaded into the reactor) as determined using the adsorption of isopropyl amine on the fresh catalyst follows the order Pt/Al_2O_3 > Pt/TiO_2-P25 > Pt/C > Pt/TiO_2-Rutile whereas the density per unit surface area follows the order Pt/Al_2O_3 > Pt/TiO_2-P25 > Pt/TiO_2-Rutile > Pt/C. The density of basic sites per unit mass of catalyst as determined from CO_2 pulse adsorption on the fresh catalyst follows the order Pt/Al_2O_3 >> Pt/TiO_2-Rutile > Pt/TiO_2-P25 > Pt/C. It should be noted that alumina underwent severe phase transformation upon exposure to the severe hydrothermal conditions resulted in a 75% decrease in the number of acid sites present in the catalyst.

The least acidic, most hydrophobic support yielded the most active and most selective catalyst (Pt/C), which was attributed to a) the high dispersion of platinum on the carbon support, b) the low concentration of support acid/base sites which could catalyse the conversion of formaldehyde to other C_1-derivatives that would adversely affect the formaldehyde selectivity, and, c) the efficient desorption of the formed formaldehyde from the catalytically active phase into liquid water, thereby increasing the catalyst turnover. The enhanced desorption of formaldehyde from the metal surface is due to preference of water to being located around the platinum active site rather than spread out over the support [310, 317, 366], since carbon black is hydrophobic and the liquid hold-up is only a function of the gas and liquid velocity and not of properties of the support [367]. The localisation of water around the platinum active sites may ensure a high local concentration of water around platinum nanoparticles on the carbon supported catalyst, thereby confining formaldehyde to the liquid phase (see Scheme 7.3). This may have also prevented the interaction of the formed formaldehyde with the support active sites, thereby preventing the further conversion of formaldehyde.

Titania (P25) used as a support becomes bifunctional in the presence of water; water hydroxylates the anatase surface, yielding additional hydroxyl sites [325, 326] that may enhance the acid/base properties of the P25 support [324]. P25 is also hydrophilic, which means that a film of water may form over both the metal and the support in the presence of liquid water, which may enable diffusion between the metal active sites and the support active sites [320]. This may present a pathway for the diffusion of methanediol from the metal active sites to the support active sites, where it may undergo support-catalysed reactions. It is hypothesized that the poor oxygenate selectivity observed for the Pt/TiO_2-P25 catalyst is due to the further conversion of formaldehyde over support active sites yielding CO_2 (and methanol) (see Scheme 5.1) [321, 322].

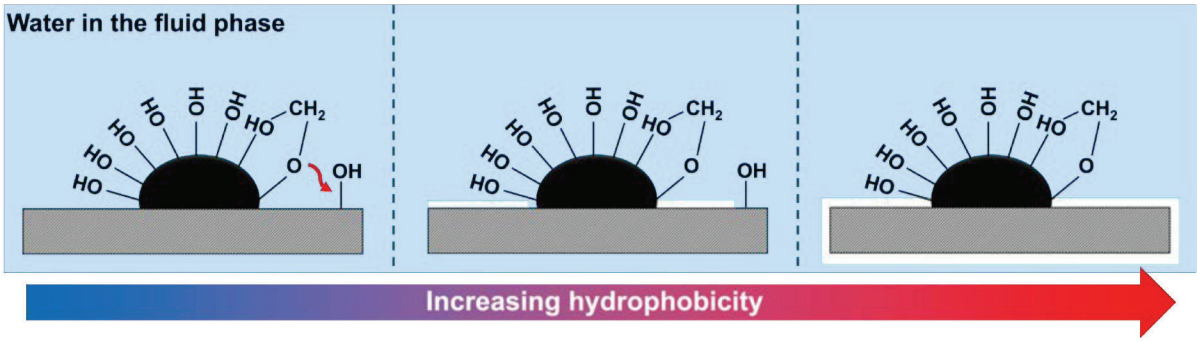

Scheme 7.3: Conceptual representation of the interaction of water with hydrophilic and hydrophobic supports showing diminishing interaction of water with the support as the support hydrophobicity increases.

The secondary conversion of formaldehyde over the rutile phase of the titania support was not as extensive as that observed over P25, due to the rutile phase of titania being relatively hydrophobic in comparison to anatase [368]. The rutile phase of titania does contain less acid sites than P25, which is expected to lessen the likelihood of support-catalysed conversion of formaldehyde towards the formation of CO_2 (and methanol).

The selective oxidation of methane takes place under quite strongly hydrothermal conditions and the support needs to be stable under those conditions. It was shown that γ-Al_2O_3 transforms under the applied conditions to boehmite, which resulted in the growth of the platinum nanoparticles on the support. Carbon was a surprising support which showed great activity and selectivity. Upon obtaining a conversion of 4% of methane with a selectivity for the formation of 98% using a liquid water flow rate of 0.3 ml/min (T = 220°C, $p_{CH_4,inlet}$=0.5 bar, $p_{O_2,inlet}$=1.5 bar O_2, space velocity = 3.23 mmol $CH_4/g_{catalyst}$/hr). The methane conversion was further increased by increasing the liquid flow rate of water further to 0.5 ml/min. This resulted in a strong increase in the rate of formation of CO_2, whilst the rate of formaldehyde formation remained the same. Analysis of the recovered catalyst indicated the gasification of the carbon support.

7.4. EFFECTS OF ALLOYING PLATINUM WITH GROUP 11 METALS

Kinetic experiments over the alumina-supported catalysts showed that the rate of methane conversion is independent of both the methane or oxygen partial pressures, although the formaldehyde selectivity increased with the increase in the methane partial pressure and decreased with the increase in the oxygen partial pressure. This indicated that the reaction was limited by the rate of formaldehyde desorption, which may be influenced by the binding strength of oxygenate species and, by proxy, of oxygen on the catalytically active metal oxygen. The binding strength of oxygen on the catalyst surface can be tuned by alloying platinum with group 11 metals.

Platinum was alloyed with copper, silver and gold were synthesized in a wet-chemical process using molybdenum hexacarbonyl [346, 369] (platinum nanoparticles were synthesized in the same manner for comparison). The bimetallic catalysts were dispersed on the rutile phase of titania since the carbon support proved to be unstable during time-on stream experiments and the rutile-supported catalyst was the second best in terms of performance. Upon heating the catalysts in oxygen at 350°C to remove the residual surfactants, the alloys segregated.

The rate of methane conversion over Pt_3Cu/TiO_2 in the presence of liquid water was not significantly different to that obtained in the presence of water in the gas phase, while there was a notable improvement in the formaldehyde selectivity. The improvement in the formaldehyde selectivity may be due to a more facile desorption of the formaldehyde from the active metal surface, which is enhanced by the presence of liquid water. The oligomers observed on the Pt_3Ag/TiO_2 catalyst were seemingly absent on Pt_3Cu/TiO_2 (or it may be below the instrument detection limit).

It is suspected that the polyoxymethylene polymeric species forms at the metal-support interface and may be initiated by the interaction of a $HO(CH_2)$-O^* species with hydroxyl groups on the support (suspected to be acid sites) at the metal-support interface. If the desorption of this intermediate into the liquid phase is facile, then the interaction between the $HO(CH_2)$-O^* species is less likely, thereby improving the formaldehyde selectivity. However, if the desorption is not facile, then the likelihood of the $HO(CH_2)$-O^* species interacting with support active sites is increased, resulting in the formation of the polyoxymethylene deposit, as depicted in Scheme 7.4. The $HO(CH_2)$-O^* species may also react with some bridging hydroxyls to form dioxymethylene, which may convert to a formate species over terminal hydroxyl groups [322,

326]. The formate species may result in the formation of CO_2, which also reduces the formaldehyde selectivity (see Scheme 5.1 for the detailed mechanism).

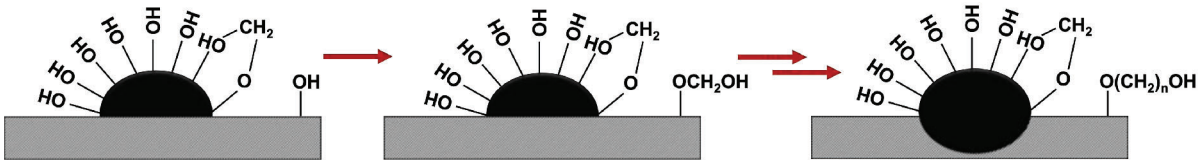

Scheme 7.4: Formation of polyoxymethylene at the metal-support interface.

The true test of the effectiveness of alloying platinum with other metals lies in the improvement in the intrinsic activity of catalytically active sites, which is indicated by the turnover frequency (TOF, h^{-1}) [370, 371]. The turnover frequency of the bimetallic catalysts is overall greater than that of the monometallic catalysts. The observed turnover frequency of the platinum catalysts presented in Table 7.1. At the moment, it is unclear whether the improvement in the turnover frequency displayed by the catalysts prepared using a wet chemical approach is due to the alloying effect of Cu, Ag and Au, or if it is due to the presence of residual molybdenum, which originates from the addition of molybdenum hexacarbonyl (the reducing agent used during the synthesis of the nanoparticles).

The turnover frequency obtained over the nanoalloy and Pt nanoparticle catalysts was plotted against the shift in the d-band center for isolated platinum in an impurity surface. From the plot presented in Figure 7.1, it seems there is a beneficial, albeit minor effect when platinum is alloyed with copper, silver and gold.

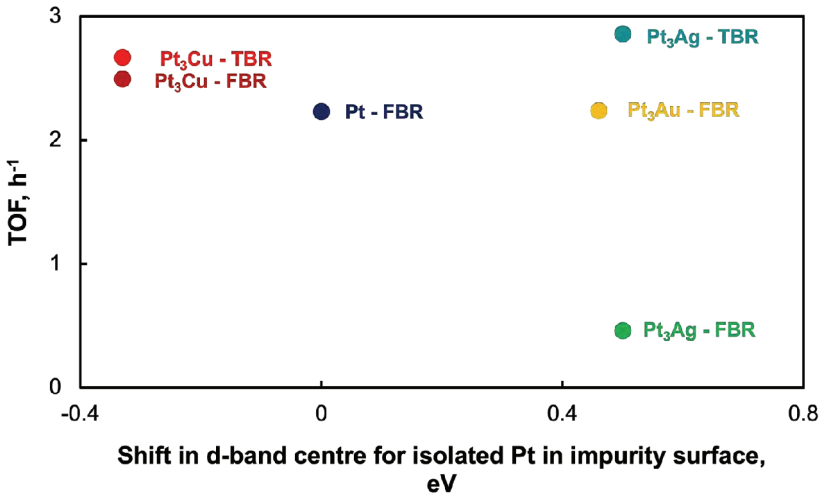

Figure 7.1: Observed turnover frequency as a function of the d-band center on platinum [335].

Table 7.1: Catalytic performance of platinum-based catalysts for the selective, aerobic oxidation of methane in the gas-phase and trickle bed reactor

Catalyst	w_{Pt}[a] %	Reactor[b]	X_{CH_4} %	$-r_{CH_4}$ μmol/g/hr	TOF h^{-1}	S_{CH_2O} %	Productivity[c] μmol/g/hr
Pt/TiO_2-P25	9.5	trickle	0.6	21	0.10	-	-
Pt/TiO_2-Rutile	10.0	trickle	1.0	32	0.17	90	30
Pt/Al_2O_3	10.2	trickle	0.5	16	0.07	65	11
Pt/C	10.0	trickle	4.2	135	0.41	99	132
Pt/TiO_2-Rutile[d]	6.5	gas	0.3	95	2.2	66	63
Pt_3Cu/TiO_2-Rutile[d]	7.0	gas	1.1	292	2.5	66	192
Pt_3Ag/TiO_2-Rutile[d]	7.7	gas	0.3	43	0.5	63	27
Pt_3Au/TiO_2-Rutile[d]	7.3	gas	0.6	103	2.3	65	67
Pt_3Cu/TiO_2-Rutile[d]	7.0	trickle	5.1	320	2.7	78	250
Pt_3Ag/TiO_2-Rutile[d]	7.7	trickle	3.0	271	2.9	74	198

[a] platinum loading; [b] catalyst tested in either the trickle bed reactor of gas phase reactor; [c] formaldehyde productivity; [d] nanoparticles prepared via a solution-phase, colloidal method using molybdenum hexacarbonyl as a reducing agent.

CHAPTER VIII:

CONCLUDING REMARKS AND RECOMMENDATIONS FOR CONTINUATION OF STUDY

8.1. CONCLUSION

The selective oxidation of methane to C_1-oxygenates, using oxygen as an oxidant, remains one of the grand challenges in catalysis [37, 372], which was initially attributed to the activation of the methane C-H bond. However, the challenge may not only lie in the energetically demanding activation of the methane C-H bond, but also in controlling the selectivity through ensuring desorption of the selective oxidation products, whilst at the same time minimizing its secondary conversion [26, 255]. A selective route for the aerobic oxidation of methane over metallic platinum catalysts was hence developed through a multi-pronged approach, viz. i) directing the methane activation pathway to occur via an Eley-Rideal mechanism and avoiding the formation of surface methyl species [234, 238], ii) co-feeding liquid water which facilitated product desorption through solvation [247], and iii) optimising the catalyst support.

The methane activation pathway was re-directed from a total oxidation reaction pathway to a selective oxidation pathway via co-feeding water. DFT calculations have shown that co-adsorbing water with oxygen significantly enhances the oxygenate coverage on the Pt(111) surface, thereby enforcing the activation of methane with activated oxygen species adsorbed on corner and edge sites, yielding CH_3O_{ads} and HO_{ads} species which form a di-σ-hydroxy-methoxy intermediate that desorbs as formaldehyde in the presence of water. The efficiency in the product desorption was found to be heavily influenced by the presence of liquid water. Furthermore, increasing the H_2O/CH_4 ratio in the feed enhanced the rate of methane reaction and formaldehyde selectivity, which was tied to an increase in the efficiency of product desorption as the reaction approaches the trickle-bed regime, which regenerates the catalytically active site. Mechanistically, water is proposed to act as a hydrogen shuttle which facilitates the desorption of formaldehyde, and as a solvating agent that protects formaldehyde from further conversion in the gas phase.

Surprisingly, the support identity was also found to be crucial. Supporting platinum on P25, a mixture of anatase and rutile resulted in the least active, but more importantly the least

selective catalyst under trickle bed conditions, with a turnover frequency of 0.1 h^{-1} and a maximum oxygenate selectivity of 10%. The low activity, especially under trickle bed conditions, is attributed to the hydrophilicity of support, which results in less water surrounding the metal nano-particles, thereby lessening the catalytic activity. The acidity of the support resulted in the secondary conversion of formaldehyde to methanol, carbon dioxide and methoxy-methanol. Basic sites in the catalyst are thought to be linked to the formation of formaldehyde oligomers on the catalyst surface, which may have contributed further to the low activity of the Pt/TiO_2-P25 catalyst. The hydrophilicity of the support also means that the liquid phase that contained the desorbed formaldehyde remained in contact with the support, thereby enabling the interaction between formaldehyde and support active sites that facilitated the secondary formaldehyde reactions.

Supporting platinum on alumina resulted in a catalyst that deactivated under trickle-bed conditions. This was attributed to the phase transformation of alumina to boehmite, which resulted in sintering of platinum nano-particles. The presence of acid sites negatively affected the formaldehyde selectivity, limiting it to ca. 65%.

The hydrophobic supports on the other hand fared better, with the rutile phase supported catalyst obtaining a turnover frequency (TOF) of 0.17 h^{-1} in the presence of liquid water, and a formaldehyde selectivity of 90%. The catalyst did however undergo deactivation, which was attributed to the presence of formaldehyde oligomers on the catalyst surface. Carbon supported catalyst achieved the best performance (compared to the rest of the impregnated catalysts), with a TOF of 0.41 h^{-1} and a maximum formaldehyde selectivity of 98%. It should be noted that this catalyst underwent deactivation at a high H_2O/CH_4 ratio induced by combustion/gasification of the support, which led to sintering of the active phase.

The rate of reaction was found to be independent of the methane and oxygen partial pressure, which indicated that the rate limiting step was associated with product desorption. To enhance the rate of formaldehyde desorption, platinum was alloyed with copper, silver and gold. Platinum nanoparticles were also synthesised using a similar method and tested as a reference (TOF = 2.2 h^{-1}, S_{CH_2O} = 66%). The nanoalloy catalysts all displayed similar turnover frequencies; however, the Pt_3Cu/TiO_2 catalyst was the most productive, with productivities comparable to those achieved by Cu-CHA and Cu-MOR systems [28, 171, 173] and PdAu systems which uses in situ generated H_2O_2 [182, 184].

8.2. NOVELTY AND IMPACT OF STUDY

This study set out to selectively oxidise methane to C_1-oxygenates, over supported metallic catalysts, in a truly catalytic process (where the oxygen activation, methane functionalisation and product desorption occur at the same temperature, and all the reactive gases are co-fed into the reactor) [373]. This was successfully achieved. The selective oxidation of methane to oxygenates is notorious for the infamous conversion-selectivity limitations, where an increase in the methane conversion is usually achieved at the cost of C_1-oxygenate selectivities. This has led to selectivities being seen as more important than high conversions. In this study, we have managed to reach a maximum methane conversion of 5% at a formaldehyde selectivity of 78% over the Pt_3Cu/TiO_2 catalyst. Over the impregnated Pt/C catalyst, a conversion of 4.1% was obtained with a selectivity for the formation of formaldehyde of 99%, although the support was not stable.

The reaction conditions employed are also novel; the reaction is carried out at 220°C in the presence of liquid water in a trickle-bed reactor. The temperature employed herein is relatively mild compared to temperatures typically employed in the methane oxidation yielding formaldehyde when oxygen is used as an oxidant. The recovered temperature range would allow for recovery of the heat generated in the reaction via co-generation of medium pressure steam, The coupling of oxygen as an oxidant and the use of a metallic catalytic system is also rarely reported.

A mechanistic pathway for the formation of formaldehyde over platinum and CO_2 over the support has been outlined stressing the importance of acidic and basic sites on the support. The acid sites are thought to be linked to the formation of CO_2, polyoxymethylene and methoxymethanol, while the basic sites are linked to the formation of methanol and some CO_2 via a Cannizzaro type reaction. Furthermore, it was shown that the rate of reaction may be altered by changing the d-band centre of the catalytically active metal, platinum, through alloying.

8.3. RECOMMENDATIONS

Although this study represents a great progress in the aerobic, selective oxidation of methane in the presence of water over metallic catalysts yielding formaldehyde, there are a number of questions that are yet to be addressed, which can be achieved in the continuation of this project. The first question pertains to the effect of the support wettability and liquid holdup on the catalytic activity and formaldehyde selectivity. Although the different supports provide hints on the effect of support hydrophobicity, it is worth exploring the interaction of support with water further to gain a better understanding of the actual effect of support wettability.

The tested catalysts have shown a large decrease in activity with time on line. This could be partly attributed to sintering upon collapse of the support, but also to the formation of oligomers/polymer on the catalyst. The prevailing hypothesis is that adsorbed methanediol forms on the catalyst surface, which may desorb as formaldehyde in the gas phase. Methanediol polymerises on acidic sites at the metal-support interface, forming surface-bound formaldehyde polymeric species. The mechanism for the formation of these polymers should be studied further in order to optimise the catalyst system and to prevent their formation.

The catalyst support needs to be optimised. Although rutile is a good starting point for further exploration based upon this work, other hydrophobic, more thermally stable supports should be explored, in addition to rutile-modified surfaces. The desired support materials should be hydrophobic, hydrothermally stable, and contain a minimal amount of acidic sites and basic sites. Reasonable potential supports may be carbon-based materials that are functionalised for stability under oxidising environments [284]. Graphitic carbon nitride may be a likely candidate, since it can be tailored to be relatively hydrophobic and is relatively stable in the presence of oxygen, and may be tailored to be weakly acidic/basic [374, 375].

The catalysts contain a large amount of platinum. The platinum dispersion should be improved through the synthesis of smaller platinum or Pt_3Cu nanoparticles. The platinum loading may be reduced by introducing platinum skin catalysts on a support.

REFERENCE LIST

REFERENCES

[1] G.A. Olah, Goeppert, A. and Prakash, G.K.S., Methanol and Dimethyl Ether as Fuels and Energy Carriers in Beyond Oil and Gas: The Methanol Economy, G.A. Olah, A. Goeppert, G.K. S. Prakash (Eds.), Wiley & Sons (2009) pp. 185-231.

[2] A. Davies, M.D. Simmons, Energy Rep. 7 (2021) 4483-4497.

[3] G.A. Olah, Angew. Chem. Int. Ed. 44 (2005) 2636-2639.

[4] BP, Statistical Review of World Energy, BP, 2018.

[5] H.J. Schellnhuber, S. Rahmstorf, R. Winkelmann, Nat. Clim. Change 6 (2016) 649-653.

[6] S.J. Davis, N.S. Lewis, M. Shaner, S. Aggarwal, D. Arent, I.L. Azevedo, S.M. Benson, T. Bradley, J. Brouwer, Y.-M. Chiang, C.T.M. Clack, A. Cohen, S. Doig, J. Edmonds, P. Fennell, C.B. Field, B. Hannegan, B.-M. Hodge, M.I. Hoffert, E. Ingersoll, P. Jaramillo, K.S. Lackner, K.J. Mach, M. Mastrandrea, J. Ogden, P.F. Peterson, D.L. Sanchez, D. Sperling, J. Stagner, J.E. Trancik, C.-J. Yang, K. Caldeira, Science 360 (2018) eaas9793.

[7] H. Ritchie, How have the world's energy sources changed over the last two centuries?, 2021, https://ourworldindata.org/global-energy-200-years (accessed 25/07/2023).

[8] L. Hammarström, AMBIO, 41 (2012) 103-107.

[9] G.A. Olah, Angew. Chem. Int. Ed. 52 (2013) 104-107.

[10] L.B. Conglin Xu, Oil Gas J. 116 (2018) 20-23.

[11] L. Hamelin, H.B. Møller, U. Jørgensen, Renew. Sustain. Energy Rev. 138 (2021) 110506.

[12] T.N.O. Mensah, A.S. Oyewo, C. Breyer, Renew. Energy 173 (2021) 297-317.

[13] S. Dasappa, Energy Sustain. Dev. 15 (2011) 203-213.

[14] P. Tang, Q. Zhu, Z. Wu, D. Ma, Energy Environ. Sci. 7 (2014) 2580-2591.

[15] M. Ravi, M. Ranocchiari, J.A. van Bokhoven, Angew. Chem. Int. Ed. 56 (2017) 16464-16483.

[16] S.J. Freakley, N. Dimitratos, D.J. Willock, S.H. Taylor, C.J. Kiely, G.J. Hutchings, Acc. Chem. Res. 54 (2021) 2614-2623.

[17] J. Baltrusaitis, W.L. Luyben, ACS Sustainable Chem. Eng. 3 (2015) 2100-2111.

[18] A.P. Simpson, A.E. Lutz, Int. J. Hydrog. Energy 32 (2007) 4811-4820.

[19] Z. Guo, B. Liu, Q. Zhang, W. Deng, Y. Wang, Y. Yang, Chem. Soc. Rev. 43 (2014) 3480-3524.

[20] L. Chu, S. Gu, Q. Jin, P. Zhu, Y. Shen, P. Li, Int. J. Hydrog. Energy 45 (2020) 28752-28763.

[21] P.T. Aakko-Saksa, C. Cook, J. Kiviaho, T. Repo, J. Power Sources 396 (2018) 803-823.

[22] Z. Dong, A. Mukhtar, H. Lin, Top. Catal. 64 (2021) 481-508.

[23] A.I. Olivos-Suarez, À. Szécsényi, E.J.M. Hensen, J. Ruiz-Martinez, E.A. Pidko, J. Gascon, ACS Catal. 6 (2016) 2965-2981.

[24] J.S. Valente, R. Quintana-Solórzano, H. Armendáriz-Herrera, J.-M.M. Millet, ACS Catal. 13 (2023) 1693-1716.

[25] R. Horn, R. Schlögl, Catal. Lett. 145 (2015) 23-39.

[26] M. Ravi, V.L. Sushkevich, A.J. Knorpp, M.A. Newton, D. Palagin, A.B. Pinar, M. Ranocchiari, J.A. van Bokhoven, Nat. Catal. 2 (2019) 485-494.

[27] A.A. Latimer, A. Kakekhani, A.R. Kulkarni, J.K. Nørskov, ACS Catal. 8 (2018) 6894-6907.

[28] K.T. Dinh, M.M. Sullivan, K. Narsimhan, P. Serna, R.J. Meyer, M. Dincă, Y. Román-Leshkov, J. Am. Chem. Soc. 141 (2019) 11641-11650.

[29] P. Schwach, X. Pan, X. Bao, Chem. Rev. 117 (2017) 8497-8520.

[30] E.H. Boomer, J.W. Broughton, Can. J. Res. 15b (1937) 375-382.

[31] E.H. Boomer, V. Thomas, Can. J. Res. 15b (1937) 401-413.

[32] E.H. Boomer, V. Thomas, Can. J. Res. 15b (1937) 414-433.

[33] D.M. Newitt, A.E. Haffner, W.A. Bone, Proc. Roy. Soc. (Lond.) 134 (1932) 591-604.

[34] W.A. Bone, Nature 127 (1931) 481-481.

[35] H.D. Gesser, N.R. Hunter, C.B. Prakash, Chem. Rev. 85 (1985) 235-244.

[36] E.G. Chepaikin, Activation and Oxidative Functionalization of Alkanes with Noble-Metal Catalysts: Molecular Mechanisms in Alkane Functionalization, A.J.L. Pombeiro, M.F.C. Guedes da Silva, Eds. John Wiley & Sons (2019) pp. 17-46.

[37] N.F. Dummer, D.J. Willock, Q. He, M.J. Howard, R.J. Lewis, G. Qi, S.H. Taylor, J. Xu, D. Bethell, C.J. Kiely, G.J. Hutchings, Chem. Rev. (2022).

[38] G.A. Foulds, B.F. Gray, Fuel Process. Technol. 42 (1995) 129-150.

[39] S.J. Blanksby, G.B. Ellison, Acc. Chem. Res. 36 (2003) 255-263.

[40] E. Roduner, W. Kaim, B. Sarkar, V.B. Urlacher, J. Pleiss, R. Gläser, W.-D. Einicke, G.A. Sprenger, U. Beifuß, E. Klemm, C. Liebner, H. Hieronymus, S.-F. Hsu, B. Plietker, S. Laschat, ChemCatChem 5 (2013) 82-112.

[41] S. Lervold, R. Lødeng, J. Yang, J. Skjelstad, K. Bingen, H.J. Venvik, Chem. Eng. J. 423 (2021) 130141.

[42] T. Yumura, T. Amenomori, Y. Kagawa, K. Yoshizawa, J. Phys. Chem. A 106 (2002) 621-630.

[43] J. Bao, G. Yang, Y. Yoneyama, N. Tsubaki, ACS Catal. 9 (2019) 3026-3053.

[44] V. Arutyunov, Chapter 5 - Key Features of the Mechanism, in: V. Arutyunov (Ed.) Direct Methane to Methanol, Elsevier (2014) pp. 75-83.

[45] E.M. Turan, E. van Steen, K.P. Möller, Chem. Eng. Sci. 241 (2021) 116718.

[46] H.D. Gesser, N.R. Hunter, Catal. Today 42 (1998) 183-189.

[47] C. Liao, N. Saito, Y. Saso, Y. Ogawa, Fire Saf. J. 27 (1996) 49-68.

[48] R. Burch, G.D. Squire, S.C. Tsang, J. Chem. Soc., Faraday Trans. 1 85 (1989) 3561-3568.

[49] P.S. Casey, T. McAllister, K. Foger, Ind. Eng. Chem. Res.33 (1994) 1120-1125.

[50] G.A. Foulds, B.F. Gray, S.A. Miller, G.S. Walker, Ind. Eng. Chem. Res. 32 (1993) 780-787.

[51] C.L. Rasmussen, P. Glarborg, Ind. Eng. Chem. Res. 47 (2008) 6579-6588.

[52] P.S. Yarlagadda, L.A. Morton, N.R. Hunter, H.D. Gesser, Ind. Eng. Chem. Res. 27 (1988) 252-256.

[53] W. Feng, F.C. Knopf, K.M. Dooley, Energy Fuels 8 (1994) 815-822.

[54] Q. Zhang, D. He, J. Li, B. Xu, Y. Liang, Q. Zhu, Appl. Catal. A: Chem. 224 (2002) 201-207.

[55] P. Khirsariya, R.K. Mewada, Procedia Eng. 51 (2013) 409-415.

[56] C. Hammond, S. Conrad, I. Hermans, ChemSusChem 5 (2012) 1668-1686.

[57] H. Berndt, A. Martin, A. Brückner, E. Schreier, D. Müller, H. Kosslick, G.U. Wolf, B. Lücke, J. Catal. 191 (2000) 384-400.

[58] J.A. Barbero, M.C. Alvarez, M.A. Bañares, M.A. Peña, J.L.G. Fierro, Chem. Commun. (2002) 1184-1185.

[59] P. Wallis, S. Wohlrab, V.N. Kalevaru, M. Frank, A. Martin, Catal. Today 278 (2016) 120-126.

[60] T.T.H. Dang, D. Seeburg, J. Radnik, C. Kreyenschulte, H. Atia, T.T.H. Vu, S. Wohlrab, Catal. Commun. 103 (2018) 56-59.

[61] K. Shimura, T. Fujitani, Appl. Catal. A: Chem. 577 (2019) 44-51.
[62] V. Amir-Ebrahimi, J.J. Rooney, J. Mol. Catal. 50 (1989) L17-L22.
[63] M.A. Banares, H.C. Hu, I.E. Wachs, J. Catal. 155 (1995) 249-255.
[64] Y. Kim, T.Y. Kim, C.K. Song, K.R. Lee, S. Bae, H. Park, D. Yun, Y.S. Yun, I. Nam, J. Park, H. Lee, J. Yi, Nano Energy 82 (2021) 105704.
[65] K. Wachi, T. Yabe, T. Suzuki, K. Yonesato, K. Suzuki, K. Yamaguchi, Appl. Catal. B: Environ. 314 (2022) 121420.
[66] M.J.G. Fait, A. Ricci, M. Holena, J. Rabeah, M.M. Pohl, D. Linke, E.V. Kondratenko, Catal. Sci. Technol. 9 (2019) 5111-5121.
[67] T. Akiyama, R. Sei, S. Takenaka, Catal. Sci. Technol. 11 (2021) 5273-5281.
[68] A. Matsuda, H. Tateno, K. Kamata, M. Hara, Catal. Sci. Technol. 11 (2021) 6987-6998.
[69] H.F. Liu, R.S. Liu, K.Y. Liew, R.E. Johnson, J.H. Lunsford, J. Am. Chem. Soc. 106 (1984) 4117-4121.
[70] T.J. Hall, J.S.J. Hargreaves, G.J. Hutchings, R.W. Joyner, S.H. Taylor, Fuel Process. Technol. 42 (1995) 151-178.
[71] G. Fu, X. Xu, X. Lu, H. Wan, J. Am. Chem. Soc. 127 (2005) 3989-3996.
[72] M.A. Banares, I. Rodriguez-Ramos, A. Guerrero-Ruiz, J.L.G. Fierro, Stud. Surf. Sci. Catal. 75 (1993) 1131-1144.
[73] N.D. Spencer, C.J. Pereira, AIChE Journal 33 (1987) 1808-1812.
[74] K.J. Zhen, M.M. Khan, C.H. Mak, K.B. Lewis, G.A. Somorjai, J. Catal. 94 (1985) 501-507.
[75] S.Y. Chen, D. Willcox, Ind. Eng. Chem. Res. 32 (1993) 584-587.
[76] X. Wang, Y. Wang, Q. Tang, Q. Guo, Q. Zhang, H. Wan, J. Catal. 217 (2003) 457-467.
[77] V.D.B.C. Dasireddy, D. Hanzel, K. Bharuth-Ram, B. Likozar, RSC Adv. 9 (2019) 30989-31003.
[78] E. van Steen, J. Guo, N. Hytoolakhan Lal Mahomed, G.M. Leteba, S.V.L. Mahlaba, ChemCatChem 15 (2023) e202201238.
[79] J. Tian, J. Tan, Z. Zhang, P. Han, M. Yin, S. Wan, J. Lin, S. Wang, Y. Wang, Nat. Commun. 11 (2020) 5693.
[80] J.-S. Han, C.-M. Ahn, B. Mahanty, C.-G. Kim, Appl. Biochem. Biotechnol. 171 (2013) 1487-1499.
[81] V.C.C. Wang, S. Maji, P.P.Y. Chen, H.K. Lee, S.S.F. Yu, S.I. Chan, Chem. Rev. 117 (2017) 8574-8621.

[82] P. Promoppatum, V. Viswanathan, ACS Sustainable Chem. Eng. 4 (2016) 1736-1745.
[83] P. Atkins, J. De Paula, Physical Chemistry 9th edition, Oxford University Press (2010).
[84] T.J. Lawton, A.C. Rosenzweig, J. Am. Chem. Soc. 138 (2016) 9327-9340.
[85] A.C. Rosenzweig, C.A. Frederick, S.J. Lippard, P. Nordlund, Nature 366 (1993) 537-543.
[86] M. Merkx, D.A. Kopp, M.H. Sazinsky, J.L. Blazyk, J. Müller, S.J. Lippard, Angew. Chem. Int. Ed. 40 (2001) 2782-2807.
[87] R. Banerjee, J.C. Jones, J.D. Lipscomb, Annu. Rev. Biochem. 88 (2019) 409-431.
[88] A.A. Shteinman, Kinet. Catal. 61 (2020) 339-359.
[89] R. Balasubramanian, A.C. Rosenzweig, Acc. Chem. Res. 40 (2007) 573-580.
[90] H. Thi Quynh Le, E.Y. Lee, Bioresour. Technol. 384 (2023) 129296.
[91] D.A. Kopp, G.T. Gassner, J.L. Blazyk, S.J. Lippard, Biochem. 40 (2001) 14932-14941.
[92] V. Srinivas, R. Banerjee, H. Lebrette, J.C. Jones, O. Aurelius, I.-S. Kim, C.C. Pham, S. Gul, K.D. Sutherlin, A. Bhowmick, J. John, E. Bozkurt, T. Fransson, P. Aller, A. Butryn, I. Bogacz, P. Simon, S. Keable, A. Britz, K. Tono, K.S. Kim, S.-Y. Park, S.J. Lee, J. Park, R. Alonso-Mori, F.D. Fuller, A. Batyuk, A.S. Brewster, U. Bergmann, N.K. Sauter, A.M. Orville, V.K. Yachandra, J. Yano, J.D. Lipscomb, J. Kern, M. Högbom, J. Am. Chem. Soc. 142 (2020) 14249-14266.
[93] R. Banerjee, Y. Proshlyakov, J.D. Lipscomb, D.A. Proshlyakov, Nature 518 (2015) 431-434.
[94] B.J. Brazeau, J.D. Lipscomb, Biochem. 39 (2000) 13503-13515.
[95] B.F. Gherman, M.-H. Baik, S.J. Lippard, R.A. Friesner, J. Am. Chem. Soc. 126 (2004) 2978-2990.
[96] I.Y. Hwang, S.H. Lee, Y.S. Choi, S.J. Park, J.G. Na, I.S. Chang, C. Kim, H.C. Kim, Y.H. Kim, J.W. Lee, E.Y. Lee, J. Microbiol. Biotechnol. 24 (2014) 1597-1605.
[97] K.T. Dinh, M.M. Sullivan, P. Serna, R.J. Meyer, M. Dincă, Y. Román-Leshkov, ACS Catal. 8 (2018) 8306-8313.
[98] G. Xue, R. De Hont, E. Münck, L. Que Jr, Nat. Chem. 2 (2010) 400.
[99] W. Wang, R.E. Iacob, R.P. Luoh, J.R. Engen, S.J. Lippard, J. Am. Chem. Soc. 136 (2014) 9754-9762.
[100] S.J. Lee, M.S. McCormick, S.J. Lippard, U.-S. Cho, Nature 494 (2013) 380-384.
[101] W. Wang, A.D. Liang, S.J. Lippard, Acc. Chem. Res. 48 (2015) 2632-2639.
[102] J. Colby, D.I. Stirling, H. Dalton, Biochem. J. 165 (1977) 395-402.
[103] E.B. Charlotte, D.D. Paul, P. Jagroop, AIMS Bioeng. 5 (2018) 1-38.

[104] J. Lee, B.K. Soni, R.L. Kelley, Biotechnol. Lett. 18 (1996) 897-902.
[105] P.J. Strong, S. Xie, W.P. Clarke, Environ. Sci. Technol. 49 (2015) 4001-4018.
[106] S.-y. Park, C.-g. Kim, J. Mater. Cycles Waste Manag. 21 (2019) 415-422.
[107] H. In Yeub, H. Dong Hoon, L. Jae Hoon, P. Chang-Ho, C. In Seop, L. Jin Won, J. Microbiol. Biotechnol. 25 (2015) 375-380.
[108] J. Baek, B. Rungtaweevoranit, X. Pei, M. Park, S.C. Fakra, Y.-S. Liu, R. Matheu, S.A. Alshmimri, S. Alshehri, C.A. Trickett, G.A. Somorjai, O.M. Yaghi, J. Am. Chem. Soc. 140 (2018) 18208-18216.
[109] S.I. Chan, Y.-J. Lu, P. Nagababu, S. Maji, M.-C. Hung, M.M. Lee, I.-J. Hsu, P.D. Minh, J.C.-H. Lai, K.Y. Ng, S. Ramalingam, S.S.-F. Yu, M.K. Chan, Angew. Chem. Int. Ed. 52 (2013) 3731-3735.
[110] C.-C. Liu, C.-Y. Mou, S.S.F. Yu, S.I. Chan, Energy Environ. Sci. 9 (2016) 1361-1374.
[111] S.I. Chan, S.S.F. Yu, C.-C. Liu, C.-Y. Mou, Curr. Op. Green Sustain. Chem. 22 (2020) 39-46.
[112] P. Nagababu, S.S.F. Yu, S. Maji, R. Ramu, S.I. Chan, Catal. Sci. Technol. 4 (2014) 930-935.
[113] A.B. Sorokin, E.V. Kudrik, D. Bouchu, Chem. Commun. (2008) 2562-2564.
[114] S. Shaik, Nat. Chem. 2 (2010) 347.
[115] S. Friedle, E. Reisner, S.J. Lippard, Chem. Soc. Rev. 39 (2010) 2768-2779.
[116] P. Afanasiev, A.B. Sorokin, Acc. Chem. Res. 49 (2016) 583-593.
[117] Ü. İşci, A.S. Faponle, P. Afanasiev, F. Albrieux, V. Briois, V. Ahsen, F. Dumoulin, A.B. Sorokin, S.P. de Visser, Chem. Sci. 6 (2015) 5063-5075.
[118] M.V. Parfenov, E.V. Starokon, L.V. Pirutko, G.I. Panov, J. Catal. 318 (2014) 14-21.
[119] J. Xu, R.D. Armstrong, G. Shaw, N.F. Dummer, S.J. Freakley, S.H. Taylor, G.J. Hutchings, Catal. Today 270 (2016) 93-100.
[120] G.J. Hutchings, Top. Catal. 59 (2016) 658-662.
[121] Á. Szécsényi, G. Li, J. Gascon, E.A. Pidko, ACS Catal. 8 (2018) 7961-7972.
[122] Y. Kim, T.Y. Kim, H. Lee, J. Yi, Chem. Commun. 53 (2017) 4116-4119.
[123] M.H. Mahyuddin, Y. Shiota, K. Yoshizawa, Catal. Sci. Technol. 9 (2019) 1744-1768.
[124] P.J. Smeets, J.S. Woertink, B.F. Sels, E.I. Solomon, R.A. Schoonheydt, Inorg. Chem. 49 (2010) 3573-3583.
[125] K.A. Dubkov, V.I. Sobolev, E.P. Talsi, M.A. Rodkin, N.H. Watkins, A.A. Shteinman, G.I. Panov, J. Mol. Catal. A: Chem. 123 (1997) 155-161.

[126] B.E.R. Snyder, P. Vanelderen, M.L. Bols, S.D. Hallaert, L.H. Böttger, L. Ungur, K. Pierloot, R.A. Schoonheydt, B.F. Sels, E.I. Solomon, Nature 536 (2016) 317-321.

[127] E.V. Starokon, M.V. Parfenov, S.S. Arzumanov, L.V. Pirutko, A.G. Stepanov, G.I. Panov, J. Catal. 300 (2013) 47-54.

[128] M.L. Bols, S.D. Hallaert, B.E.R. Snyder, J. Devos, D. Plessers, H.M. Rhoda, M. Dusselier, R.A. Schoonheydt, K. Pierloot, E.I. Solomon, B.F. Sels, J. Am. Chem. Soc. 140 (2018) 12021-12032.

[129] B.E.R. Snyder, M.L. Bols, R.A. Schoonheydt, B.F. Sels, E.I. Solomon, Chem. Rev. 118 (2018) 2718-2768.

[130] M.L. Bols, B.E.R. Snyder, H.M. Rhoda, P. Cnudde, G. Fayad, R.A. Schoonheydt, V. Van Speybroeck, E.I. Solomon, B.F. Sels, Nat. Catal. 4 (2021) 332-340.

[131] E.V. Starokon, M.V. Parfenov, L.V. Pirutko, S.I. Abornev, G.I. Panov, J. Phys. Chem. C, 115 (2011) 2155-2161.

[132] F. Göltl, C. Michel, P.C. Andrikopoulos, A.M. Love, J. Hafner, I. Hermans, P. Sautet, ACS Catal. 6 (2016) 8404-8409.

[133] M.H. Mahyuddin, A. Staykov, Y. Shiota, K. Yoshizawa, ACS Catal. 6 (2016) 8321-8331.

[134] G.I. Panov, V.I. Sobolev, K.A. Dubkov, V.N. Parmon, N.S. Ovanesyan, A.E. Shilov, A.A. Shteinman, React. Kinet. Catal. Lett. 61 (1997) 251-258.

[135] N.S. Ovanesyan, K.A. Dubkov, A.A. Pyalling, A.A. Shteinman, J. Radioanal. Nucl. Chem. 246 (2000) 149-152.

[136] P.P. Knops-Gerrits, W.A. Goddard, J. Mol. Catal. A: Chem. 166 (2001) 135-145.

[137] E.V. Starokon, K.A. Dubkov, L.V. Pirutko, G.I. Panov, Top. Catal. 23 (2003) 137-143.

[138] B.R. Wood, J.A. Reimer, A.T. Bell, M.T. Janicke, K.C. Ott, J. Catal. 225 (2004) 300-306.

[139] G. Zhao, E. Benhelal, A. Adesina, E. Kennedy, M. Stockenhuber, J. Phys. Chem. C, 123 (2019) 27436-27447.

[140] C. Hammond, M.M. Forde, M.H. Ab Rahim, A. Thetford, Q. He, R.L. Jenkins, N. Dimitratos, J.A. Lopez-Sanchez, N.F. Dummer, D.M. Murphy, A.F. Carley, S.H. Taylor, D.J. Willock, E.E. Stangland, J. Kang, H. Hagen, C.J. Kiely, G.J. Hutchings, Angew. Chem. Int. Ed. 51 (2012) 5129-5133.

[141] Z. Fang, H. Murayama, Q. Zhao, B. Liu, F. Jiang, Y. Xu, M. Tokunaga, X. Liu, Catal. Sci. Technol. 9 (2019) 6946-6956.

[142] C. Hammond, M.M. Forde, M.H. Ab Rahim, A. Thetford, Q. He, R.L. Jenkins, N. Dimitratos, J.A. Lopez-Sanchez, N.F. Dummer, D.M. Murphy, Angew. Chem. Int. Ed. 51 (2012) 5129-5133.

[143] C. Hammond, N. Dimitratos, R.L. Jenkins, J.A. Lopez-Sanchez, S.A. Kondrat, M. Hasbi ab Rahim, M.M. Forde, A. Thetford, S.H. Taylor, H. Hagen, E.E. Stangland, J.H. Kang, J.M. Moulijn, D.J. Willock, G.J. Hutchings, ACS Catal. 3 (2013) 689-699.

[144] C. Hammond, N. Dimitratos, J.A. Lopez-Sanchez, R.L. Jenkins, G. Whiting, S.A. Kondrat, M.H. ab Rahim, M.M. Forde, A. Thetford, H. Hagen, E.E. Stangland, J.M. Moulijn, S.H. Taylor, D.J. Willock, G.J. Hutchings, ACS Catal. 3 (2013) 1835-1844.

[145] T. Yu, Z. Li, L. Lin, S. Chu, Y. Su, W. Song, A. Wang, B.M. Weckhuysen, W. Luo, ACS Catal. 11 (2021) 6684-6691.

[146] M.H. Groothaert, J.A. van Bokhoven, A.A. Battiston, B.M. Weckhuysen, R.A. Schoonheydt, J. Am. Chem. Soc. 125 (2003) 7629-7640.

[147] P.J. Smeets, R.G. Hadt, J.S. Woertink, P. Vanelderen, R.A. Schoonheydt, B.F. Sels, E.I. Solomon, J. Am. Chem. Soc. 132 (2010) 14736-14738.

[148] J.S. Woertink, P.J. Smeets, M.H. Groothaert, M.A. Vance, B.F. Sels, R.A. Schoonheydt, E.I. Solomon, Proc. Nat. Acad. Sci. 106 (2009) 18908.

[149] X. Liu, J. Zhang, C. Huang, X. Sun, J. Phys. Chem. C 122 (2018) 28645-28651.

[150] K.D. Vogiatzis, G. Li, E.J.M. Hensen, L. Gagliardi, E.A. Pidko, J. Phys. Chem. C 121 (2017) 22295-22302.

[151] D.K. Pappas, A. Martini, M. Dyballa, K. Kvande, S. Teketel, K.A. Lomachenko, R. Baran, P. Glatzel, B. Arstad, G. Berlier, C. Lamberti, S. Bordiga, U. Olsbye, S. Svelle, P. Beato, E. Borfecchia, J. Am. Chem. Soc. 140 (2018) 15270-15278.

[152] P. Vanelderen, R.G. Hadt, P.J. Smeets, E.I. Solomon, R.A. Schoonheydt, B.F. Sels, J. Catal. 284 (2011) 157-164.

[153] P. Vanelderen, B.E.R. Snyder, M.-L. Tsai, R.G. Hadt, J. Vancauwenbergh, O. Coussens, R.A. Schoonheydt, B.F. Sels, E.I. Solomon, J. Am. Chem. Soc. 137 (2015) 6383-6392.

[154] D. Plessers, A.J. Heyer, H.M. Rhoda, M.L. Bols, E.I. Solomon, R.A. Schoonheydt, B.F. Sels, ACS Catal. 13 (2023) 1906-1915.

[155] M.A. Newton, A.J. Knorpp, V.L. Sushkevich, D. Palagin, J.A. van Bokhoven, Chem. Soc. Rev. 49 (2020) 1449-1486.

[156] B. Ipek, R.F. Lobo, Chem. Commun. 52 (2016) 13401-13404.

[157] M.H. Mahyuddin, Y. Shiota, A. Staykov, K. Yoshizawa, Acc. Chem. Res. 51 (2018) 2382-2390.

[158] P. Tomkins, A. Mansouri, S.E. Bozbag, F. Krumeich, M.B. Park, E.M.C. Alayon, M. Ranocchiari, J.A. van Bokhoven, Angew. Chem. Int. Ed. 55 (2016) 5467-5471.

[159] T. Sheppard, C.D. Hamill, A. Goguet, D.W. Rooney, J.M. Thompson, Chem. Commun. 50 (2014) 11053-11055.

[160] P. Tomkins, M. Ranocchiari, J.A. van Bokhoven, Acc. Chem. Res. 50 (2017) 418-425.

[161] V.L. Sushkevich, D. Palagin, M. Ranocchiari, J.A. van Bokhoven, Science 356 (2017) 523-527.

[162] K. Narsimhan, K. Iyoki, K. Dinh, Y. Román-Leshkov, ACS Cent. Sci. 2 (2016) 424-429.

[163] A.S. Chellappa, S. Fuangfoo, D.S. Viswanath, Ind. Eng. Chem. Res.36 (1997) 1401-1409.

[164] G.O. Alptekin, A.M. Herring, D.L. Williamson, T.R. Ohno, R.L. McCormick, J. Catal. 181 (1999) 104-112.

[165] T. Kobayashi, N. Guilhaume, J. Miki, N. Kitamura, M. Haruta, Catal. Today 32 (1996) 171-175.

[166] Y. Wang, X. Wang, Z. Su, Q. Guo, Q. Tang, Q. Zhang, H. Wan, Catal. Today 93-95 (2004) 155-161.

[167] T. Akiyama, M. Shimakawa, S. Takenaka, Chem. Lett. 51 (2022) 511-514.

[168] Z. Sojka, R.G. Herman, K. Klier, Chem. Commun. (1991) 185-186.

[169] M.L. Granados, E.E. Wolf, Appl. Catal. A: Chem. 131 (1995) 263-281.

[170] C. Duan, M. Luo, X. Xing, Bioresour. Technol. 102 (2011) 7349-7353.

[171] M. Dyballa, D.K. Pappas, K. Kvande, E. Borfecchia, B. Arstad, P. Beato, U. Olsbye, S. Svelle, ACS Catal. 9 (2019) 365-375.

[172] D.K. Pappas, E. Borfecchia, M. Dyballa, I.A. Pankin, K.A. Lomachenko, A. Martini, M. Signorile, S. Teketel, B. Arstad, G. Berlier, C. Lamberti, S. Bordiga, U. Olsbye, K.P. Lillerud, S. Svelle, P. Beato, J. Am. Chem. Soc. 139 (2017) 14961-14975.

[173] L. Sun, Y. Wang, C. Wang, Z. Xie, N. Guan, L. Li, Chem 7 (2021) 1557-1568.

[174] J. Ohyama, A. Hirayama, Y. Tsuchimura, N. Kondou, H. Yoshida, M. Machida, S. Nishimura, K. Kato, I. Miyazato, K. Takahashi, Catal. Sci. Technol. 11 (2021) 3437-3446.

[175] A. Hirayama, Y. Tsuchimura, H. Yoshida, M. Machida, S. Nishimura, K. Kato, K. Takahashi, J. Ohyama, Catal. Sci. Technol. 11 (2021) 6217-6224.

[176] R.A. Periana, D.J. Taube, S. Gamble, H. Taube, T. Satoh, H. Fujii, Science 280 (1998) 560-564.

[177] R. Palkovits, M. Antonietti, P. Kuhn, A. Thomas, F. Schüth, Angew. Chem. Int. Ed. 48 (2009) 6909-6912.

[178] Y. Ji, A.N. Blankenship, J.A. van Bokhoven, ACS Catal. 13 (2023) 3896-3901.

[179] M.H. Ab Rahim, M.M. Forde, R.L. Jenkins, C. Hammond, Q. He, N. Dimitratos, J.A. Lopez-Sanchez, A.F. Carley, S.H. Taylor, D.J. Willock, D.M. Murphy, C.J. Kiely, G.J. Hutchings, Angew. Chem. Int. Ed. 52 (2013) 1280-1284.

[180] N. Agarwal, S.J. Freakley, R.U. McVicker, S.M. Althahban, N. Dimitratos, Q. He, D.J. Morgan, R.L. Jenkins, D.J. Willock, S.H. Taylor, C.J. Kiely, G.J. Hutchings, Science 358 (2017) 223.

[181] J. Chen, S. Wang, L. Peres, V. Collière, K. Philippot, P. Lecante, Y. Chen, N. Yan, Catal. Sci. Technol. 11 (2021) 3493-3500.

[182] C. Williams, J.H. Carter, N.F. Dummer, Y.K. Chow, D.J. Morgan, S. Yacob, P. Serna, D.J. Willock, R.J. Meyer, S.H. Taylor, G.J. Hutchings, ACS Catal. 8 (2018) 2567-2576.

[183] Y. Xu, D. Wu, P. Deng, J. Li, J. Luo, Q. Chen, W. Huang, C.M. Shim, C. Jia, Z. Liu, Y. Shen, X. Tian, Appl. Catal. B: Environ. 308 (2022) 121223.

[184] F. Ni, T. Richards, L.R. Smith, D.J. Morgan, T.E. Davies, R.J. Lewis, G.J. Hutchings, ACS Org. Inorg. Au (2023).

[185] Z. Jin, L. Wang, E. Zuidema, K. Mondal, M. Zhang, J. Zhang, C. Wang, X. Meng, H. Yang, C. Mesters, F.-S. Xiao, Science 367 (2020) 193-197.

[186] G. Qi, T.E. Davies, A. Nasrallah, M.A. Sainna, A.G.R. Howe, R.J. Lewis, M. Quesne, C.R.A. Catlow, D.J. Willock, Q. He, D. Bethell, M.J. Howard, B.A. Murrer, B. Harrison, C.J. Kiely, X. Zhao, F. Deng, J. Xu, G.J. Hutchings, Nat. Catal. 5 (2022) 45-54.

[187] J. Shan, M. Li, L.F. Allard, S. Lee, M. Flytzani-Stephanopoulos, Nature 551 (2017) 605-608.

[188] K.T. Dinh, M.M. Sullivan, P. Serna, R.J. Meyer, Y. Román-Leshkov, ACS Catal. 11 (2021) 9262-9270.

[189] V.N. Cavaliere, D.J. Mindiola, Chem. Sci. 3 (2012) 3356-3365.

[190] G.B. Shul'pin, Dalton Trans. 42 (2013) 12794-12818.

[191] A. Sen, M.A. Benvenuto, M. Lin, A.C. Hutson, N. Basickes, J. Am. Chem. Soc. 116 (1994) 998-1003.

[192] M.J. da Silva, Fuel Process. Technol. 145 (2016) 42-61.

[193] R. Palkovits, C. von Malotki, M. Baumgarten, K. Müllen, C. Baltes, M. Antonietti, P. Kuhn, J. Weber, A. Thomas, F. Schüth, ChemSusChem 3 (2010) 277-282.

[194] R.A. Periana, D.J. Taube, E.R. Evitt, D.G. Löffler, P.R. Wentrcek, G. Voss, T. Masuda, Science 259 (1993) 340-343.

[195] B.G. Hashiguchi, S.M. Bischof, M.M. Konnick, R.A. Periana, Acc. Chem. Res. 45 (2012) 885-898.

[196] J.T. Fuller, S. Butler, D. Devarajan, A. Jacobs, B.G. Hashiguchi, M.M. Konnick, W.A. Goddard, J. Gonzales, R.A. Periana, D.H. Ess, ACS Catal. 6 (2016) 4312-4322.

[197] N.J. Gunsalus, A. Koppaka, S.H. Park, S.M. Bischof, B.G. Hashiguchi, R.A. Periana, Chem. Rev. 117 (2017) 8521-8573.

[198] L. Kesavan, R. Tiruvalam, M.H.A. Rahim, M.I. bin Saiman, D.I. Enache, R.L. Jenkins, N. Dimitratos, J.A. Lopez-Sanchez, S.H. Taylor, D.W. Knight, C.J. Kiely, G.J. Hutchings, Science 331 (2011) 195-199.

[199] N. Dimitratos, J.A. Lopez-Sanchez, G.J. Hutchings, Chem. Sci. 3 (2012) 20-44.

[200] D.I. Enache, J.K. Edwards, P. Landon, B. Solsona-Espriu, A.F. Carley, A.A. Herzing, M. Watanabe, C.J. Kiely, D.W. Knight, G.J. Hutchings, Science 311 (2006) 362-365.

[201] J.A. Lopez-Sanchez, N. Dimitratos, P. Miedziak, E. Ntainjua, J.K. Edwards, D. Morgan, A.F. Carley, R. Tiruvalam, C.J. Kiely, G.J. Hutchings, Phys. Chem. Chem. Phys.10 (2008) 1921-1930.

[202] J. Pritchard, L. Kesavan, M. Piccinini, Q. He, R. Tiruvalam, N. Dimitratos, J.A. Lopez-Sanchez, A.F. Carley, J.K. Edwards, C.J. Kiely, G.J. Hutchings, Langmuir 26 (2010) 16568-16577.

[203] M.I. bin Saiman, G.L. Brett, R. Tiruvalam, M.M. Forde, K. Sharples, A. Thetford, R.L. Jenkins, N. Dimitratos, J.A. Lopez-Sanchez, D.M. Murphy, D. Bethell, D.J. Willock, S.H. Taylor, D.W. Knight, C.J. Kiely, G.J. Hutchings, Angew. Chem. Int. Ed. 51 (2012) 5981-5985.

[204] M.H. Ab Rahim, R.D. Armstrong, C. Hammond, N. Dimitratos, S.J. Freakley, M.M. Forde, D.J. Morgan, G. Lalev, R.L. Jenkins, J.A. Lopez-Sanchez, S.H. Taylor, G.J. Hutchings, Catal. Sci. Technol. 6 (2016) 3410-3418.

[205] M.H. Ab Rahim, M.M. Forde, C. Hammond, R.L. Jenkins, N. Dimitratos, J.A. Lopez-Sanchez, A.F. Carley, S.H. Taylor, D.J. Willock, G.J. Hutchings, Top. Catal. 56 (2013) 1843-1857.

[206] Y. He, J. Liang, Y. Imai, K. Ueda, H. Li, X. guo, G. Yang, Y. Yoneyama, N. Tsubaki, Catal. Today 352 (2020) 104-110.

[207] F. Bonino, A. Damin, G. Ricchiardi, M. Ricci, G. Spanò, R. D'Aloisio, A. Zecchina, C. Lamberti, C. Prestipino, S. Bordiga, J. Phys. Chem. B 108 (2004) 3573-3583.

[208] K. Harrath, X. Yu, H. Xiao, J. Li, ACS Catal. 9 (2019) 8903-8909.

[209] J.K. Edwards, B. Solsona, E.N. N, A.F. Carley, A.A. Herzing, C.J. Kiely, G.J. Hutchings, Science 323 (2009) 1037-1041.

[210] A. Delparish, S. Kanungo, J. van der Schaaf, M.F. Neira d'Angelo, Catal. Sci. Technol. 9 (2019) 5142-5149.

[211] S.J. Freakley, N. Agarwal, R.U. McVicker, S. Althahban, R.J. Lewis, D.J. Morgan, N. Dimitratos, C.J. Kiely, G.J. Hutchings, Catal. Sci. Technol. 10 (2020) 5935-5944.

[212] R. Serra-Maia, F.M. Michel, T.A. Douglas, Y. Kang, E.A. Stach, ACS Catal. 11 (2021) 2837-2845.

[213] J. Shan, M. Li, L.F. Allard, S. Lee, M. Flytzani-Stephanopoulos, Nature 551 (2017) 605.

[214] M.A. Artsiusheuski, R. Verel, J.A. van Bokhoven, V.L. Sushkevich, ACS Catal. 13 (2023) 5864-5875.

[215] H. Li, Y. Shen, X. Xiao, H. Jiang, Q. Gu, Y. Zhang, L. Lin, W. Luo, S. Zhou, J. Zhao, A. Wang, T. Zhang, B. Yang, ACS Catal. 13 (2023) 1197-1206.

[216] F. Wen, J. Zhang, Z. Chen, Z. Zhou, H. Liu, W. Zhu, Z. Liu, Catal. Sci. Technol. 11 (2021) 1358-1364.

[217] K. Narsimhan, V.K. Michaelis, G. Mathies, W.R. Gunther, R.G. Griffin, Y. Román-Leshkov, J. Am. Chem. Soc. 137 (2015) 1825-1832.

[218] N.V. Kolesnichenko, Y.M. Snatenkova, T.I. Batova, O.V. Yashina, K.B. Golubev, Microporous Mesoporous Mater. 330 (2022) 111581.

[219] X. Wang, G. Qi, J. Xu, B. Li, C. Wang, F. Deng, Angew. Chem. Int. Ed. 51 (2012) 3850-3853.

[220] T. Moteki, N. Tominaga, M. Ogura, ChemCatChem 12 (2020) 2957-2961.

[221] Y. Tang, Y. Li, V. Fung, D.-e. Jiang, W. Huang, S. Zhang, Y. Iwasawa, T. Sakata, L. Nguyen, X. Zhang, A.I. Frenkel, F. Tao, Nat. Commun. 9 (2018) 1231.

[222] A.M. Bahmanpour, A. Hoadley, A. Tanksale, Rev. Chem. Eng. 30 (2014) 583-604.

[223] E.V. Rybak-Akimova, Mechanisms of Oxygen Binding and Activation at Transition Metal Centers, in: A. Bakac (Ed) Physical Inorganic Chemistry, John Wiley & Sons (2010) pp. 109-188.

[224] X. Liu, Y. Ryabenkova, M. Conte, Phys. Chem. Chem. Phys. 17 (2015) 715-731.

[225] M.M. Montemore, M.A. van Spronsen, R.J. Madix, C.M. Friend, Chem. Rev. 118 (2018) 2816-2862.

[226] S. Kwon, P. Deshlahra, E. Iglesia, J. Catal. 377 (2019) 692-710.

[227] J. Xu, X.-M. Cao, P. Hu, J. Phys. Chem. C 123 (2019) 28802-28810.

[228] J.S. Yoo, T.S. Khan, F. Abild-Pedersen, J.K. Nørskov, F. Studt, Chem. Commun. 51 (2015) 2621-2624.

[229] B. Xing, X.-Y. Pang, G.-C. Wang, J. Catal. 282 (2011) 74-82.

[230] M. Valden, N. Xiang, J. Pere, M. Pessa, Appl. Surf. Sci. 99 (1996) 83-89.

[231] S. Nave, A.K. Tiwari, B. Jackson, J. Phys. Chem. A 118 (2014) 9615-9631.

[232] T.V. Choudhary, E. Aksoylu, D. Wayne Goodman, Catal. Rev. 45 (2003) 151-203.

[233] G. Lee, W. Zheng, K.A. Goulas, I.C. Lee, D.G. Vlachos, Ind. Eng. Chem. Res. 58 (2019) 17718-17726.

[234] Y.-H. Chin, C. Buda, M. Neurock, E. Iglesia, J. Am. Chem. Soc. 133 (2011) 15958-15978.

[235] Y.-H. Chin, C. Buda, M. Neurock, E. Iglesia, J. Am. Chem. Soc. 135 (2013) 15425-15442.

[236] Y.-H. Chin, M. García-Diéguez, E. Iglesia, J. Phys. Chem. C 120 (2016) 1446-1460.

[237] J.S. Yoo, J. Schumann, F. Studt, F. Abild-Pedersen, J.K. Nørskov, J. Phys. Chem. C 122 (2018) 16023-16032.

[238] G. Fratesi, P. Gava, S. de Gironcoli, J. Phys. Chem. C, 111 (2007) 17015-17019.

[239] S. Zhao, Y. Wen, X. Liu, X. Pen, F. Lü, F. Gao, X. Xie, C. Du, H. Yi, D. Kang, X. Tang, Nano Res. 13 (2020) 1544-1551.

[240] L. Lin, Y. Ge, H. Zhang, M. Wang, D. Xiao, D. Ma, JACS Au 1 (2021) 1834-1848.

[241] T.V. Andrushkevich, E.V. Ovchinnikova, Mol. Catal. 484 (2020) 110734.

[242] N. Akiya, P.E. Savage, Chem. Rev. 102 (2002) 2725-2750.

[243] B.N. Zope, D.D. Hibbitts, M. Neurock, R.J. Davis, Science 330 (2010) 74-78.

[244] M.B. Boucher, M.D. Marcinkowski, M.L. Liriano, C.J. Murphy, E.A. Lewis, A.D. Jewell, M.F.G. Mattera, G. Kyriakou, M. Flytzani-Stephanopoulos, E.C.H. Sykes, ACS Nano 7 (2013) 6181-6187.

[245] P.G. Lustemberg, R.M. Palomino, R.A. Gutiérrez, D.C. Grinter, M. Vorokhta, Z. Liu, P.J. Ramírez, V. Matolín, M.V. Ganduglia-Pirovano, S.D. Senanayake, J.A. Rodriguez, J. Am. Chem. Soc. 140 (2018) 7681-7687.

[246] R. Xu, N. Liu, C. Dai, Y. Li, J. Zhang, B. Wu, G. Yu, B. Chen, Angew. Chem. Int. Ed. 60 (2021) 16634-16640.

[247] G. Li, B. Wang, D.E. Resasco, ACS Catal. 10 (2020) 1294-1309.

[248] Z. Liu, E. Huang, I. Orozco, W. Liao, R.M. Palomino, N. Rui, T. Duchoň, S. Nemšák, D.C. Grinter, M. Mahapatra, P. Liu, J.A. Rodriguez, S.D. Senanayake, Science 368 (2020) 513-517.

[249] Z. Zuo, P.J. Ramírez, S.D. Senanayake, P. Liu, J.A. Rodriguez, J. Am. Chem. Soc. 138 (2016) 13810-13813.

[250] E. Huang, I. Orozco, P.J. Ramírez, Z. Liu, F. Zhang, M. Mahapatra, S. Nemšák, S.D. Senanayake, J.A. Rodriguez, P. Liu, J. Am. Chem. Soc. 143 (2021) 19018-19032.

[251] E. Huang, N. Rui, R. Rosales, J. Kang, S. Nemšák, S.D. Senanayake, J.A. Rodriguez, P. Liu, ACS Catal. (2022) 11253-11262.

[252] E.V. Kondratenko, T. Peppel, D. Seeburg, V.A. Kondratenko, N. Kalevaru, A. Martin, S. Wohlrab, Catal. Sci. Technol. 7 (2017) 366-381.

[253] M. Ahlquist, R.J. Nielsen, R.A. Periana, W.A. Goddard III, J. Am. Chem. Soc. 131 (2009) 17110-17115.

[254] K. Kvande, S. Prodinger, F. Schlimpen, P. Beato, P. Pale, S. Chassaing, S. Svelle, Top. Catal. (2022).

[255] M.C. Simons, S.D. Prinslow, M. Babucci, A.S. Hoffman, J. Hong, J.G. Vitillo, S.R. Bare, B.C. Gates, C.C. Lu, L. Gagliardi, A. Bhan, J. Am. Chem. Soc. 143 (2021) 12165-12174.

[256] M.F. Fellah, I. Onal, Catal. Today 171 (2011) 52-59.

[257] P.L. Cilliers, Phase diagram for the co-adsorption of O and OH on Pt(100) and Pt(111) as determined by DFT, MSc dissertation, University of Cape Town, Cape Town, (2017).

[258] M.A. van Spronsen, J.W.M. Frenken, I.M.N. Groot, Nat. Commun. 8 (2017) 429.

[259] H. Tang, A. Van Der Ven, B.L. Trout, Mol. Phys. 102 (2004) 273-279.

[260] N.A. Saliba, Y.L. Tsai, C. Panja, B.E. Koel, Surf. Sci. 419 (1999) 79-88.

[261] M. Mäkinen, K. Laasonen, Surf. Sci. 734 (2023) 122305.

[262] S.V.L. Mahlaba, N. Hytoolakhan Lal Mahomed, A. Govender, J. Guo, G.M. Leteba, P.L. Cilliers, E. van Steen, Angew. Chem. Int. Ed. 61 (2022) e202206841.

[263] Y. Shi, S. Liu, Y. Liu, W. Huang, G. Guan, Z. Zuo, Catal. Rev. 62 (2020) 313-345.

[264] E. Becker, P.-A. Carlsson, L. Kylhammar, M.A. Newton, M. Skoglundh, J. Phys. Chem. C 115 (2011) 944-951.

[265] L.G. Verga, J. Aarons, M. Sarwar, D. Thompsett, A.E. Russell, C.K. Skylaris, Faraday Discuss. 208 (2018) 497-522.

[266] M.P. Hyman, J.W. Medlin, J. Phys. Chem. C 111 (2007) 17052-17060.
[267] R. Zhang, W. Xia, W. Kang, R. Li, K. Qu, Y. Zhang, B. Chen, H. Wang, Y. Sun, H. Li, ChemistrySelect 3 (2018) 3615-3620.
[268] L. Luo, J. Luo, H. Li, F. Ren, Y. Zhang, A. Liu, W.-X. Li, J. Zeng, Nat. Commun. 12 (2021) 1218.
[269] Y. Lyu, J.N. Jocz, R. Xu, O.C. Williams, C. Sievers, ChemCatChem 13 (2021) 2832-2842.
[270] K. Zhu, S. Liang, X. Cui, R. Huang, N. Wan, L. Hua, H. Li, H. Chen, Z. Zhao, G. Hou, M. Li, Q. Jiang, L. Yu, D. Deng, Nano Energy 82 (2021) 105718.
[271] R.J. Bunting, P.S. Rice, J. Thompson, P. Hu, Chem. Sci. 12 (2021) 4443-4449.
[272] H. Steininger, S. Lehwald, H. Ibach, Surf. Sci. 123 (1982) 1-17.
[273] C. Clay, S. Haq, A. Hodgson, Phys. Rev. Lett. 92 (2004) 046102.
[274] W. Lew, M.C. Crowe, E. Karp, O. Lytken, J.A. Farmer, L. Árnadóttir, C. Schoenbaum, C.T. Campbell, J. Phys. Chem. C 115 (2011) 11586-11594.
[275] W. Lew, M.C. Crowe, C.T. Campbell, J. Carrasco, A. Michaelides, J. Phys. Chem. C 115 (2011) 23008-23012.
[276] I. Iliuta, F. Larachi, B.P.A. Grandjean, Chem. Eng. Res. Des. 77 (1999) 759-763.
[277] M.H. Al-Dahhan, M.P. Duduković, Chem. Eng. Sci. 50 (1995) 2377-2389.
[278] S.K. Desai, M. Neurock, Phys. Rev. B 68 (2003) 075420.
[279] Z. Yan, Z. Yang, Z. Xu, L. An, F. Xie, J. Liu, J. Colloid Interface Sci. 524 (2018) 306-312.
[280] T. Kitazawa, H. Tadokoro, T. Matsumoto, I. Imazu, Kobunshi Kagaku 19 (1962) 148-153.
[281] F. Duvernay, G. Danger, P. Theulé, T. Chiavassa, A. Rimola, Astrophys. J. 791 (2014) 75.
[282] F.X.L.i. Xamena, C.O. Areán, S. Spera, E. Merlo, A. Zecchina, Catal. Lett. 95 (2004) 51-55.
[283] K. Koichumanova, A.K.K. Vikla, D.J.M. de Vlieger, K. Seshan, B.L. Mojet, L. Lefferts, ChemSusChem 6 (2013) 1717-1723.
[284] J. Huo, J.-P. Tessonnier, B.H. Shanks, ACS Catal. 11 (2021) 5248-5270.
[285] N.V. Long, N.D. Chien, T. Hayakawa, H. Hirata, G. Lakshminarayana, M. Nogami, Nanotechnology 21 (2010) 035605.
[286] V. Tripković, I. Cerri, T. Bligaard, J. Rossmeisl, Catal. Lett. 144 (2014) 380-388.
[287] T.G. Gambu, M.A. Petersen, E. van Steen, Catal. Today 312 (2018) 126-131.

[288] K. Reuter, M. Scheffler, Phys. Rev. B 65 (2001) 035406.
[289] P. Błoński, N. López, J. Phys. Chem. C 116 (2012) 15484-15492.
[290] J. Greeley, M. Mavrikakis, J. Am. Chem. Soc. 126 (2004) 3910-3919.
[291] J. Greeley, I.E.L. Stephens, A.S. Bondarenko, T.P. Johansson, H.A. Hansen, T.F. Jaramillo, J. Rossmeisl, I. Chorkendorff, J.K. Nørskov, Nat. Chem. 1 (2009) 552-556.
[292] N. Matubayasi, S. Morooka, M. Nakahara, H. Takahashi, J. Mol. Liq. 134 (2007) 58-63.
[293] D.R. Kent, IV, S.L. Widicus, G.A. Blake, W.A. Goddard, III, J. Chem. Phys. 119 (2003) 5117-5120.
[294] B. Kunkel, S. Wohlrab, Catal. Commun. 155 (2021) 106317.
[295] A. Kunene, T. van Heerden, T.G. Gambu, E. van Steen, ChemCatChem 12 (2020) 4760-4764.
[296] J. Ohyama, D. Abe, A. Hirayama, H. Iwai, Y. Tsuchimura, K. Sakamoto, M. Irikura, Y. Nakamura, H. Yoshida, M. Machida, S. Nishimura, T. Yamamoto, S. Matsumura, K. Takahashi, J. Phys. Chem. C 126 (2022) 1785-1792.
[297] Y.-F. Ding, L.-Y. Pan, Q. Wan, S.-F. Yin, M.-Q. Cai, J. Org. Chem. 88 (2023) 6304-6312.
[298] T.Y. Yun, B.D. Chandler, ACS Appl. Mater. Interfaces 15 (2023) 6868-6876.
[299] J. Zhao, Z. Li, P. Wang, P. Miao, R. Shi, G.I.N. Waterhouse, T. Zhang, Nano Energy 110 (2023) 108350.
[300] S.L. Scott, ACS Catal. 8 (2018) 8597-8599.
[301] T. Sheppard, H. Daly, A. Goguet, J.M. Thompson, ChemCatChem 8 (2016) 562-570.
[302] J.G. Tittensor, R.J. Gorte, D.M. Chapman, J. Catal. 138 (1992) 714-720.
[303] C. Manrique, A. Guzmán, R. Solano, A. Echavarría, Energy Fuels 33 (2019) 3483-3491.
[304] A.G. Palkhiwala, R.J. Gorte, Catal. Lett. 57 (1999) 19-23.
[305] X. Liu, J. Phys. Chem. C 112 (2008) 5066-5073.
[306] D.A. Solís-Casados, L. Escobar-Alarcón, L.M. Gómez-Oliván, E. Haro-Poniatowski, T. Klimova, Fuel 198 (2017) 3-10.
[307] S.D. Kim, S.C. Baek, Y.-J. Lee, K.-W. Jun, M.J. Kim, I.S. Yoo, Appl. Catal. A: Chem. 309 (2006) 139-143.
[308] N. Aranda-Pérez, M.P. Ruiz, J. Echave, J. Faria, Appl. Catal. A: Chem. 531 (2017) 106-118.

[309] M. Watanabe, Y. Aizawa, T. Iida, R. Nishimura, H. Inomata, Appl. Catal. A: Chem. 295 (2005) 150-156.
[310] D.J. Trevoy, H. Johnson, Jr., J. Phys. Chem. 62 (1958) 833-837.
[311] W. Chen, J. Ji, X. Feng, X. Duan, G. Qian, P. Li, X. Zhou, D. Chen, W. Yuan, J. Am. Chem. Soc. 136 (2014) 16736-16739.
[312] R.M. Ravenelle, J.R. Copeland, W.-G. Kim, J.C. Crittenden, C. Sievers, ACS Catal. 1 (2011) 552-561.
[313] Q. Liu, P. Rzepka, H. Frey, J. Tripp, A. Beck, L. Artiglia, M. Ranocchiari, J.A. van Bokhoven, Mater. Today Nano 20 (2022) 100273.
[314] T. Kecskés, J. Raskó, J. Kiss, Appl. Catal. A: Chem. 273 (2004) 55-62.
[315] K.A. Wickersheim, G.K. Korpi, J. Chem. Phys. 42 (1965) 579-583.
[316] F. Herold, J. Gläsel, B.J.M. Etzold, M. Rønning, Chem. Mater. 34 (2022) 8490-8516.
[317] S. Gim, K.J. Cho, H.-K. Lim, H. Kim, Sci. Rep. 9 (2019) 14805.
[318] A. Hodgson, S. Haq, Surf. Sci. Rep. 64 (2009) 381-451.
[319] S. Dong, P.K. Dasgupta, Environ. Sci. Technol. 20 (1986) 637-640.
[320] L. Shenjie, H. Zelin, M. Na, G. Zhi, S. Kangzhong, W. Tongtong, L. Long, L. Licheng, Appl. Surf. Sci. 620 (2023) 156815.
[321] G. Busca, J. Lamotte, J.C. Lavalley, V. Lorenzelli, J. Am. Chem. Soc. 109 (1987) 5197-5202.
[322] X. Chen, G. He, Y. Li, M. Chen, X. Qin, C. Zhang, H. He, ACS Catal. 10 (2020) 9706-9715.
[323] Z. Xu, J. Yu, M. Jaroniec, Appl. Catal. B: Environ. 163 (2015) 306-312.
[324] W. Xue, Z. Yan, Q. Bao, W. Zhang, D. Mei, Mol. Simul. 48 (2022) 829-843.
[325] W. Li, D. Du, T. Yan, D. Kong, J. You, D. Li, J. Colloid Interface Sci. 444 (2015) 42-48.
[326] T. Wei, X. Zhao, L. Li, L. Wang, S. Lv, L. Gao, G. Yuan, L. Li, ACS Omega 7 (2022) 25491-25501.
[327] P. Lv, Y. Dong, Z. Wang, M. Zhang, Catal. Lett. 153 (2023) 2398-2405.
[328] Y. Xu, A.V. Ruban, M. Mavrikakis, J. Am. Chem. Soc. 126 (2004) 4717-4725.
[329] T. Mallat, Z. Bodnar, P. Hug, A. Baiker, J. Catal. 153 (1995) 131-143.
[330] A. Kunene, G. Leteba, E. van Steen, Catal. Lett. 152 (2022) 1760-1768.
[331] A.S. Nair, B. Pathak, J. Phys. Chem. C 123 (2019) 3634-3644.
[332] E. Antolini, J.R.C. Salgado, E.R. Gonzalez, Appl. Catal. B: Environ. 63 (2006) 137-149.

[333] C. Sener, T.S. Wesley, A.C. Alba-Rubio, M.D. Kumbhalkar, S.H. Hakim, F.H. Ribeiro, J.T. Miller, J.A. Dumesic, ACS Catal. 6 (2016) 1334-1344.

[334] X. Ning, Y. Li, H. Yu, F. Peng, H. Wang, Y. Yang, J. Catal. 335 (2016) 95-104.

[335] B. Hammer, J.K. Norskov, Nature 376 (1995) 238-240.

[336] A. Ruban, B. Hammer, P. Stoltze, H.L. Skriver, J.K. Nørskov, J. Mol. Catal. A: Chem. 115 (1997) 421-429.

[337] B. Hammer, J.K. Nørskov, Surf. Sci. 343 (1995) 211-220.

[338] B. Hammer, J.K. Nørskov, Adv. Catal. (2000) 71-129.

[339] L.A. Kibler, A.M. El-Aziz, R. Hoyer, D.M. Kolb, Angew. Chem. Int. Ed. 44 (2005) 2080-2084.

[340] X. Yang, Y. Wang, X. Tong, N. Yang, Adv. Energy Mater. 12 (2022) 2102261.

[341] M. Mavrikakis, B. Hammer, J.K. Nørskov, Phys. Rev. Lett. 81 (1998) 2819-2822.

[342] J.R. Kitchin, J.K. Nørskov, M.A. Barteau, J.G. Chen, Phys. Rev. Lett. 93 (2004) 156801.

[343] D.F. van der Vliet, C. Wang, D. Li, A.P. Paulikas, J. Greeley, R.B. Rankin, D. Strmcnik, D. Tripkovic, N.M. Markovic, V.R. Stamenkovic, Angew. Chem. Int. Ed. 51 (2012) 3139-3142.

[344] X. Jin, H. Yan, C. Zeng, P.S. Thapa, B. Subramaniam, R.V. Chaudhari, Ind. Eng. Chem. Res. 56 (2017) 13157-13164.

[345] G.M. Leteba, D.R.G. Mitchell, P.B.J. Levecque, L. Macheli, E. van Steen, C.I. Lang, ACS Appl. Nano Mater. 3 (2020) 5718-5731.

[346] G.M. Leteba, D.R.G. Mitchell, L. Macheli, P.B.J. Levecque, B.P. Doyle, E. van Steen, C.I. Lang, ACS Appl. Energy Mater. 5 (2022) 15102-15113.

[347] G.M. Leteba, D.R.G. Mitchell, P.B.J. Levecque, E. van Steen, C.I. Lang, Nanomater. 11 (2021) 1825.

[348] X. Sun, K. Jiang, N. Zhang, S. Guo, X. Huang, ACS Nano 9 (2015) 7634-7640.

[349] F. Chang, Y. Liu, Q. Zhang, Z. Jia, X. Wang, L. Yang, Z. Bai, Inorg. Chem. Front. 9 (2022) 249-258.

[350] K.M.K. Yu, D. Thompsett, S.C. Tsang, Chem. Commun. (2003) 1522-1523.

[351] Z. Peng, H. Yang, J. Solid State Chem. 181 (2008) 1546-1551.

[352] V. Petkov, B.N. Wanjala, R. Loukrakpam, J. Luo, L. Yang, C.-J. Zhong, S. Shastri, Nano Lett. 12 (2012) 4289-4299.

[353] X. Ge, L. Chen, J. Kang, T. Fujita, A. Hirata, W. Zhang, J. Jiang, M. Chen, Adv. Funct. Mater. 23 (2013) 4156-4162.

[354] H.-Y. Su, X.-K. Gu, X. Ma, Y.-H. Zhao, X.-H. Bao, W.-X. Li, Catal. Today 165 (2011) 89-95.

[355] M. Rehan, X. Lai, G.M. Kale, CrystEngComm 13 (2011) 3725-3732.

[356] E. Bus, J.A. van Bokhoven, J. Phys. Chem. C 111 (2007) 9761-9768.

[357] K.M. Schüttler, L.A. Mancera, T. Diemant, A. Groß, R.J. Behm, Surf. Sci. 650 (2016) 237-254.

[358] P. Zhu, D. Dastan, L. Liu, L. Wu, Z. Shi, Q.-Q. Chu, F. Altaf, M.K.A. Mohammed, J. Mol. Graph. Model. 118 (2023) 108335.

[359] P. Delcroix, M. Pagliai, G. Cardini, D. Bégué, B. Hanoune, J. Phys. Chem. A 119 (2015) 290-298.

[360] Z. Tang, T. Zhang, D. Luo, Y. Wang, Z. Hu, R.T. Yang, ACS Catal. 12 (2022) 13457-13474.

[361] X. Bu, J. Ran, J. Niu, Z. Ou, L. Tang, X. Huang, Mol. Catal. 515 (2021) 111891.

[362] T.G. Gambu, The mobility of oxygen containing species (OCS*) over Pt-based catalyst surfaces: Impact on the oxygen reduction reaction (ORR) activity, PhD-Thesis, University of Cape Town, Cape Town (2020).

[363] J.-H. Wen, D. Guo, G.-C. Wang, Appl. Surf. Sci. 555 (2021) 149690.

[364] S. Wang, I. Agirrezabal-Telleria, A. Bhan, D. Simonetti, K. Takanabe, E. Iglesia, Faraday Discuss. 197 (2017) 9-39.

[365] P. Forzatti, E. Tronconi, A.S. Elmi, G. Busca, Appl. Catal. A: Chem. 157 (1997) 387-408.

[366] E. van Steen, A. Kunene, T. van Heerden, T.G. Gambu, ChemCatChem 12 (2020) 4760-4764.

[367] R. Kumar, H.J. Pant, S. Goswami, V.K. Sharma, A. Dash, S. Mishra, K. Bhanja, S. Mohan, S.M. Mahajani, Appl. Radiat. Isot. 121 (2017) 51-60.

[368] V. Bolis, C. Busco, M. Ciarletta, C. Distasi, J. Erriquez, I. Fenoglio, S. Livraghi, S. Morel, J. Colloid Interface Sci. 369 (2012) 28-39.

[369] G.M. Leteba, Synthesis, Characterisation and Catalytic Investigations of Pt-Based Binary (Bimetallic) and Ternary (Trimetallic) Nanoparticles, PhD-Thesis, University of Cape Town, Macquarie University, Cape Town (2016).

[370] J.M. Thomas, W.J. Thomas, Principles and practice of heterogeneous catalysis, John Wiley & Sons (2014).

[371] I. Chorkendorff, J.W. Niemantsverdriet, Concepts of modern catalysis and kinetics, John Wiley & Sons (2017.

[372] R.J. Madix, J.T. Roberts, The Problem of Heterogeneously Catalyzed Partial Oxidation: Model Studies on Single Crystal Surfaces, in: R.J. Madix (Ed.) Surface Reactions, Springer Berlin Heidelberg, Berlin, Heidelberg (1994) pp. 5-53.

[373] J. Wieser, A.J. Knorpp, D.C. Stoian, P. Rzepka, M.A. Newton, J.A. van Bokhoven, Angew. Chem. Int. Ed. 62 (2023) e202305140.

[374] P. Praus, A. Smýkalová, K. Foniok, V. Matějka, M. Kormunda, B. Smetana, D. Cvejn, Appl. Surf. Sci. 529 (2020) 147086.

[375] L. Zhong, C. Anand, K.S. Lakhi, G. Lawrence, A. Vinu, Sci. Rep. 5 (2015) 12901.

APPENDIX I: METHODOLOGICAL APPROACH

Content:

Section I: Reactor details and flow diagrams

Section II: Gas chromatography analyses procedure

Section III: Reactor loading procedure

SECTION I: REACTOR DETAILS AND FLOW DIAGRAMS

a) Gas-phase fixed bed reactor

The gas-phase, fixed bed reactor set-up (see Fig. A1.1) consists of three main parts, i.e. the main reactor body, the evaporator whose main function is to generate steam, and the reactor lines (both inlet and outlet lines). The main body of the reactor is constructed of a 25 cm ¼" stainless steel (7 mm inner-diameter) casing that houses a quartz liner (see Fig. A1.2). The reactor has three main inlets, one dedicated to argon, which is a pressure balancing gas, one dedicated to the reactive gas mixture, which is composed of O_2 and CH_4, and the helium/steam inlet line. The argon flows outside the quartz sheath and is separated from the reactive gas inlet by a port connector sitting on a fluorocarbon O-ring. Sintered metal filters and non-return valves are placed on the methane (V-103) and oxygen (V-204) lines, which act as flame-arrestors. The flow of gases into the reactor is controlled using Unit 7000 mass flow controllers. The flow rate of the exit gas stream is controlled using a needle valve (V-502). Water is introduced to the reactor from a reservoir placed on a mass balance using a high performance liquid chromatography pump, and goes through a tube constructed of stainless steel packed with Chromosorb P (60-80 Mesh, Sigma Aldrich).

The feed and product lines are constructed of 1/8" Swagelok tubing which are heated with Nichrome wire and are covered in foil, a layer of fibre ceramic blanket and quartz exhaust wrap. The reactor exit lines are connected to an Agilent 6890N gas chromatograph and are fitted with Swagelok® stainless steel minor units.

For catalytic tests, the reactor is placed in a quartz tube between two layers of quartz wool to make a catalyst bed (which is normally 2 cm). The quartz tube is then placed in the stainless steel casing. A thermocouple is placed in contact with the catalyst bed to monitor the ned temperature. The thermocouple is housed in a quartz sheath. The schematic diagram of the main reactor body is presented in Figure A1.2. The full description of the reactor is in [A1].

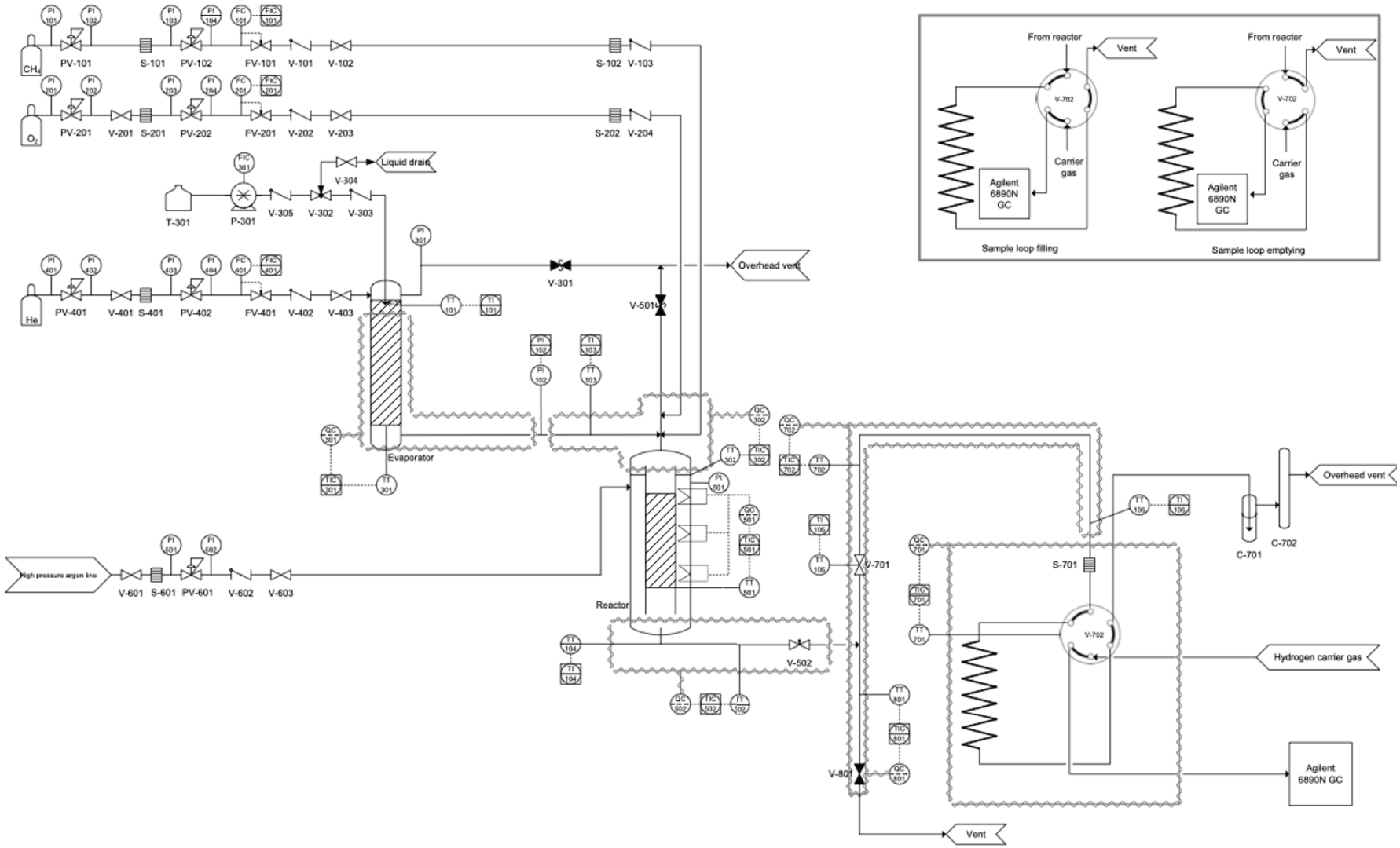

Figure A1.1: Process flow diagram of the gas-phase fixed-bed reactor.

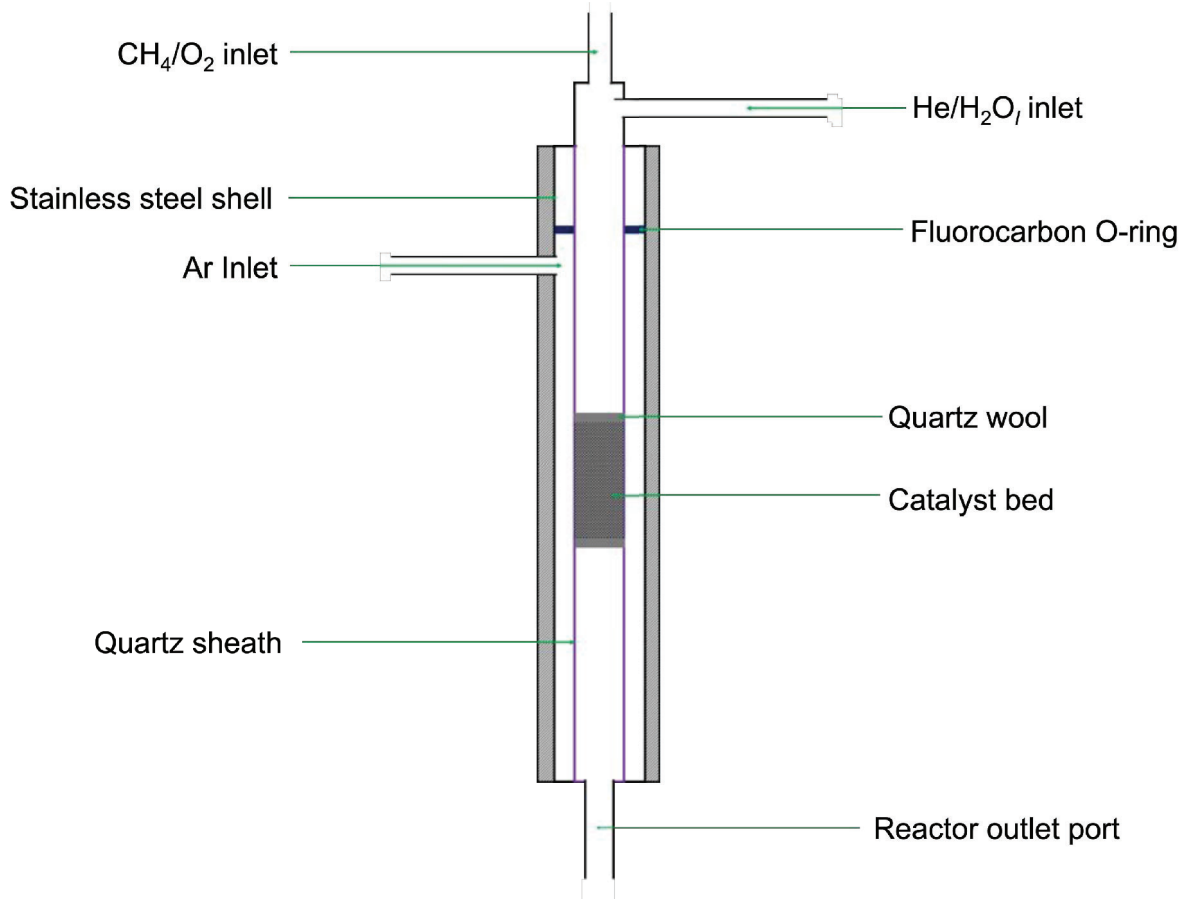

Figure A1.2: Schematic, cross-sectional representation of the fixed bed reactor main body showing the quartz sheath, stainless steel casing and catalyst bed [A1].

b) Trickle-bed reactor

The trickle-bed reactor consists of a quartz sheath that is encased within a stainless steel shell (19.05 mm outer-diameter). The reactor inlet and outlines are constructed with 1/8" stainless steel tubing. The gases are fed from cylinders and the flow is controlled with Brooks® mass flow controllers. The pressure in the reactor is set using argon as a pressure controlling gas, similar to the fixed-bed reactor. The flow out of the reactor is controlled using a needle valve. The trickle-bed reactor process flow diagram is presented in Figure A1.3. For further reactor details, please consult [A2].

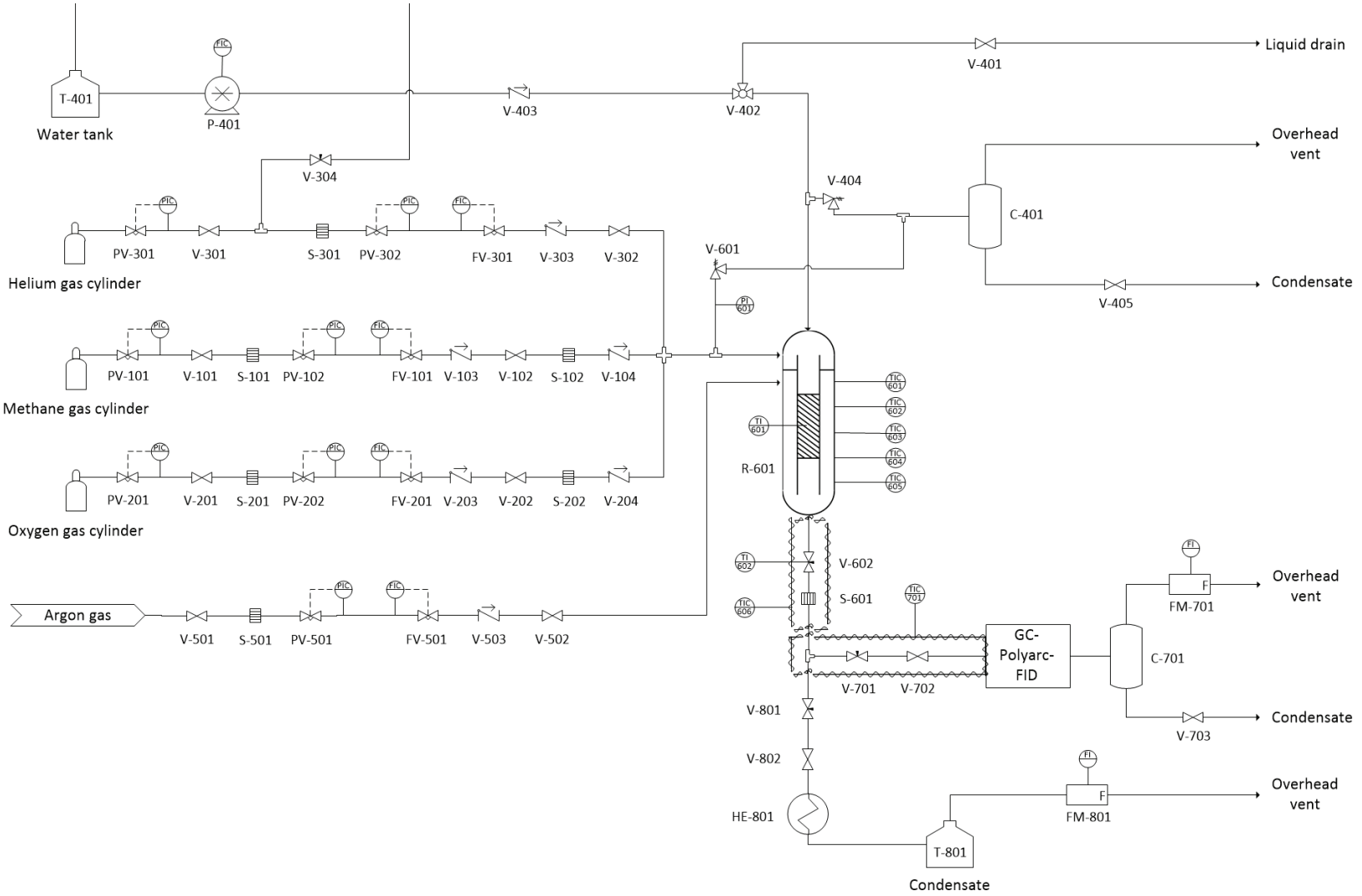

Figure A1.3: Process flow diagram of the trickle-bed reactor.

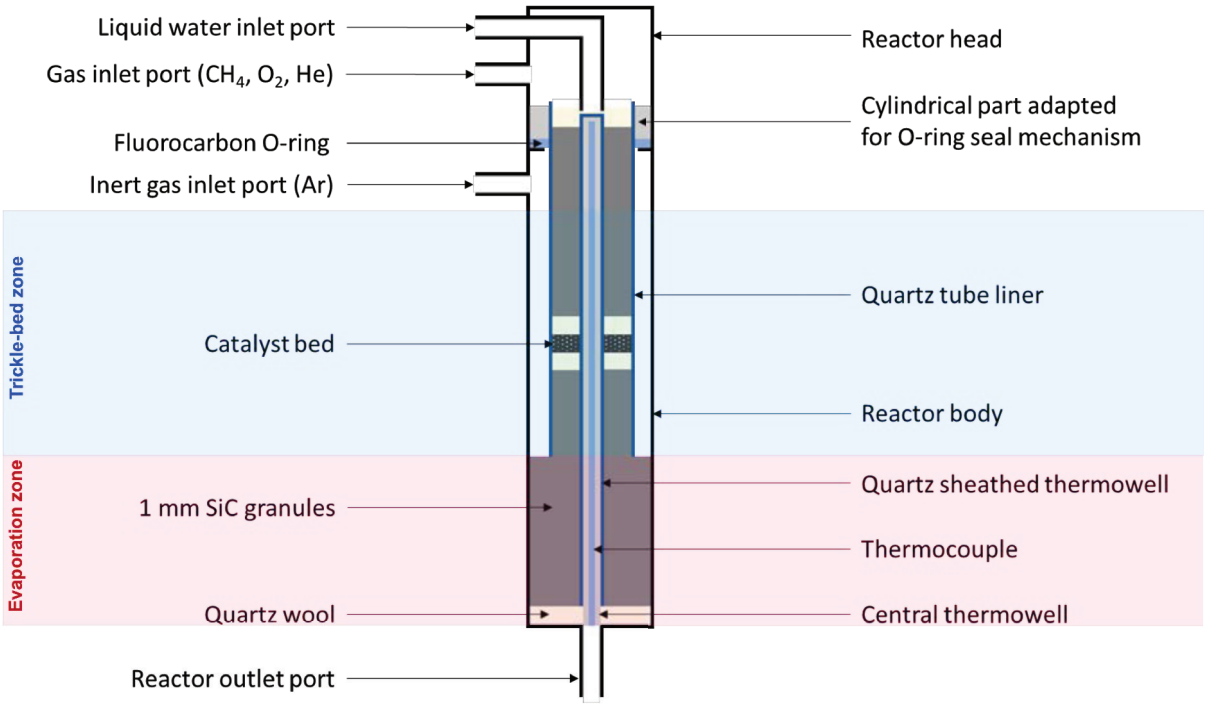

Figure A1.4: Schematic, cross-sectional representation of the trickle-bed reactor main body showing the catalyst bed and the trickle-bed and evaporation zones on the reactor [A2].

SECTION II: GAS CHROMATOGRAPHIC ANALYSES OF PRODUCTS

The analysis of the reaction products is carried out on a gas chromatograph (6890N, Agilent) that is equipped with flame ionisation detector and is interfaced with a PolyArc oxidiser-methaniser (Activated Research Company) to enable the accurate detection and quantification of CO, CO_2, methane, methanol, formaldehyde and other C_1 oxygenates (and their derivatives) [A3]. The GC is periodically calibrated with a mixture of $CO/CO_2/CH_4$ to ensure accuracy of the PolyArc response. Liquid standards are also routinely injected to calibrate the GC.

The effluent leaving the reactor is injected by means of a 6-way valve (Vici Valco). The GC analysis method is summarised in Table A1.1.

Table A1.1: Gas chromatograph instrument details and analysis method

Column	HP-PLOT Q PT
Stationary phase	Polystyrene-divinylbenzene
Diameter	0.32 mm
Length	30 mm
Film thickness	20 μm
Carrier gas	H2
Flowrate	3.5 ml_n/min
Gas sampling	
Loop volume	1 ml
Load time	1 min
Injection time	0.11 min
Valve temperature	180 °C
Injector	Split mode
Temperature	150 °C
Split ratio	10:1
Oven	
Initial temperature	40 °C
Initial time	2 min
Ramp rate	20 °C/min
Ramp time	7 min
Final temperature	180 °C
Final time	6 min
Run time	15 min
Methanator	Polyarc™ reactor
Heater temperature	350 °C
H2 flowrate	35 ml_n/min
Air flowrate	2.5 ml_n/min
Detector	FID
Temperature	250 °C
H2 flowrate	1.5 ml_n/min
Air flowrate	350 ml_n/min
N2 make-up gas flowrate	20 ml_n/min

SECTION III: REACTOR LOADING PROCEDURE AND CATALYTIC MEASUREMENTS

Prior to loading the gas phase reactor, the catalyst is pelletised using a hydraulic press (3 tons of force) then crushed and sieved to between 150-200 μm. The catalyst is then loaded between two quartz wool plugs to form a catalyst bed in a quartz sheath and is placed into the reactor shell. The shell is then placed on the reactor stand, tightened, then subjected to a leak test. Thereafter, the catalyst is pre-treated overnight in a He/O_2 mixture (5% O_2, 150 ml_n/min) at 350°C. The reactor is then cooled to reaction temperature, pressurised to reaction pressure (20 bar, using He first, then Ar to balance the pressure), then the methane is introduced.

The loading procedure for the trickle-bed reactor is slightly different; initially, a quartz wool plug is placed at the bottom of the reactor, followed by the placement of a quartz sheath (14 mm OD) around the thermowell. Thereafter, a bed of silicon carbide is loaded in the evaporation zone (about 370 mm from the top of the reactor). The quartz sheath is placed in the reactor, then loaded with silicon carbide (ca. 90 mm from the top of the reactor), followed by a quartz wool plug to seat the catalyst bed. The catalyst is then loaded, followed by another quartz wool plug. The rest of the space is filled with silicon carbide. The reactor is then sealed, and placed on the furnace. A leak test is performed by pressurising the reactor with argon, and is followed by pre-treatment overnight, following a procedure identical to that used for the fixed-bed reactor. Prior to reaction, the reactor set to the reaction temperature and pressurised to the reaction pressure (30 bar). To start the reaction, the reactive gases are introduced. Water is introduced from a reservoir using a HPLC pump. Deionised water is degassed prior to introduction by bubbling helium through in order to remove any dissolved CO_2. The pump is also typically primed prior to the introduction of water. The GC transfer line is periodically changed to ensure accurate activity measurements as some polyoxymethylene may have been deposited in the lines.

SECTION IV: FORMULAE FOR PRODUCT QUANTIFICATION

The PolyArc oxidiser-methaniser converts all components eluting from the column to methane which enables detection of oxygenate compounds by the flame-ionisation detector. Hence, the response for all components ought to be the same, since what is being detected is methane. It is also assumed that the only source of carbon in the reactor is methane, hence any changes in the methane total peak area is attributed to the products formed and those changes are then taken as the methane conversion. Ultimately, the methane conversion is calculated as thus:

$$X_{CH_4}(\%) = \frac{\Sigma \text{ Peak area of products}}{\Sigma \text{ Total peak areas}} \times 100$$

The rate of methane conversion (which is used as a standard measure of catalytic activity since it standardises the activity based on the weight of catalyst used) was calculated based on the space velocity. The space velocity was calculated as thus;

$$\text{Space Velocity} = \frac{Methane\ molar\ flow\ rate\ (mmol/min)}{Catalyst\ weight\ (g)}$$

The rate of methane conversion was then calculated using the following formulae:

$$-r_{CH_4} = \text{Space velocity} - \text{Space velocity} \times \left(1 - \frac{X_{CH_4}(\%)}{100}\right)$$

The turnover frequency was calculated based on the metal dispersion, which was measured using oxygen chemisorption and/or transmission-electron microscopy measurements. The TOF is thus calculated as:

$$TOF(h) = \frac{number\ of\ methane\ molecules\ converted\ per\ hour}{number\ of\ active\ sites\ per\ catalyst}$$

$$TOF(h) = \frac{M_{w,Pt}\left(\frac{g}{mol}\right) \times (-r_{CH_4})}{\frac{D_{Pt}(\%)}{100} \times \left(\frac{Pt\ loading\ (\%)}{100}\right)}$$

References

[A1] J. Guo, Design, construction and commissioning of a packed bed reactor system for methane to methanol conversion, MSc dissertation, University of Cape Town, Cape Town (2018).

[A2] L.M.N. Hytoolakhan, Selective oxidation of methane in a trickle bed reactor over a platinum-based catalyst, MSc dissertation, University of Cape Town, Cape Town (2022).

[A3] C.S. Spanjers, C.A. Beach, A.J. Jones, P.J. Dauenhauer, Analytical Methods 9 (2017) 1928-1934.

APPENDIX II: SUPPLEMENTAL INFORMATION TO CHAPTER IV

Content:

Section I: Catalyst synthesis and Characterisation

Section II: Catalytic testing

Section III: DFT Studies

SECTION I: CATALYST SYNTHESIS AND CHARACTERISATION

The catalysts were prepared by incipient wetness impregnation of platinic acid in deionized water on titanium dioxide (Sigma Aldrich; Rutile; S_{BET} = 44.5 m^2/g), or alumina (γ-Al_2O_3; Alfa Aesar, 3 Micron APD Powder, LOT: K27Y013, S_{BET} = 73.9 m^2/g) as a support. The support was contacted with an aqueous solution of platinic acid (H_2PtCl_6, Sigma Aldrich) to obtain 10 wt.-% platinum on the support. The solid was dried, calcined at 400°C (air flow rate: 48 $ml_n/min/g$) and subsequently reduced for 5 hrs at 400°C in flowing hydrogen (48 $ml_n/min/g$).

The elemental composition of the materials was determined using inductively coupled plasma-optical emission spectrometry (ICP-OES). The nanoparticles were imaged using transmission electron microscopy (TEM; FEI Tecnai G2 T20 TEM, operating at 200 kV). Specimens for TEM analysis were prepared by casting one-drop of a colloidal suspension in acetone onto 3-mm carbon-coated copper grids. These were then air dried under ambient conditions. The particle size distribution and the average particle size of the nanosized particles representing platinum was determined by measuring between 400-550 nanoparticles using ImageJ® software.

The phase composition of the catalyst samples was determined using powder X-ray diffraction (XRD) on a Bruker D8 ADVANCE diffractometer (Co-Kα radiation: λ = 1.789 Å, 35 kV, 40mA). The platinum particle sizes were determined using Rietveld refinement using Topas v5.0 software (Bruker AXS), which fits the entire XRD pattern. The recovered catalysts were characterized using Fourier transform infrared spectroscopy (FTIR) on a Perkin Elmer Spectrum 100 FTIR Spectrometer in the range 650-4000 cm^{-1} with a resolution of 1 cm^{-1}.

Table A2.1: Metal loading and dispersion of Pt-based catalysts (values in brackets for the recovered catalyst)

Sample	**Pt/Al_2O_3**	**Pt/TiO_2(rutile)**
Pt-loading	10.2	10.3 (10.2)
$T_{reduction}$, °C	400	400
$t_{reduction}$, hrs	5	5
H_2-uptake, cm^3(STP)/g	1.19	0.81 (0.90)
Dispersion	20.6	14.3 (15.7)
d_{Pt}[a], nm	5.5	7.9 (7.2)
d_{Pt}[b], nm	3.2 ± 1.5 (3.6 ± 3.5)	2.1 ± 0.9 (6.1 ± 4.5)

[a]: estimated from $d_{Pt} = \frac{113}{Dispersion(\%)}$; [b]: from TEM-measurement.

SECTION II: CATALYST ACTIVITY TESTS

Catalytic tests were initially performed in a specially-constructed fixed-bed reactor equipped with an evaporator for the generation of steam (see Appendix 1, Figure 1). An impregnated, Pt/TiO_2 catalyst was initially tested in the gas phase, which resulted in the formation of CO_2, methanol, methoxy-methanol and trioxane (at 8.1 bar water). The GC trace obtained under these conditions is presented in Figure A2.1.

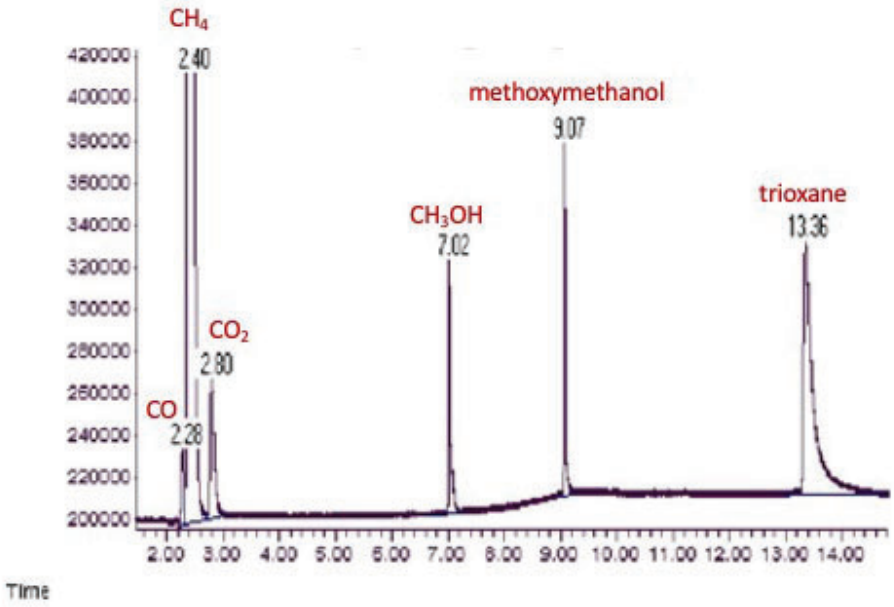

Figure A2.1: GC-trace obtained during the selective oxidation of methane under the gas-phase conditions.

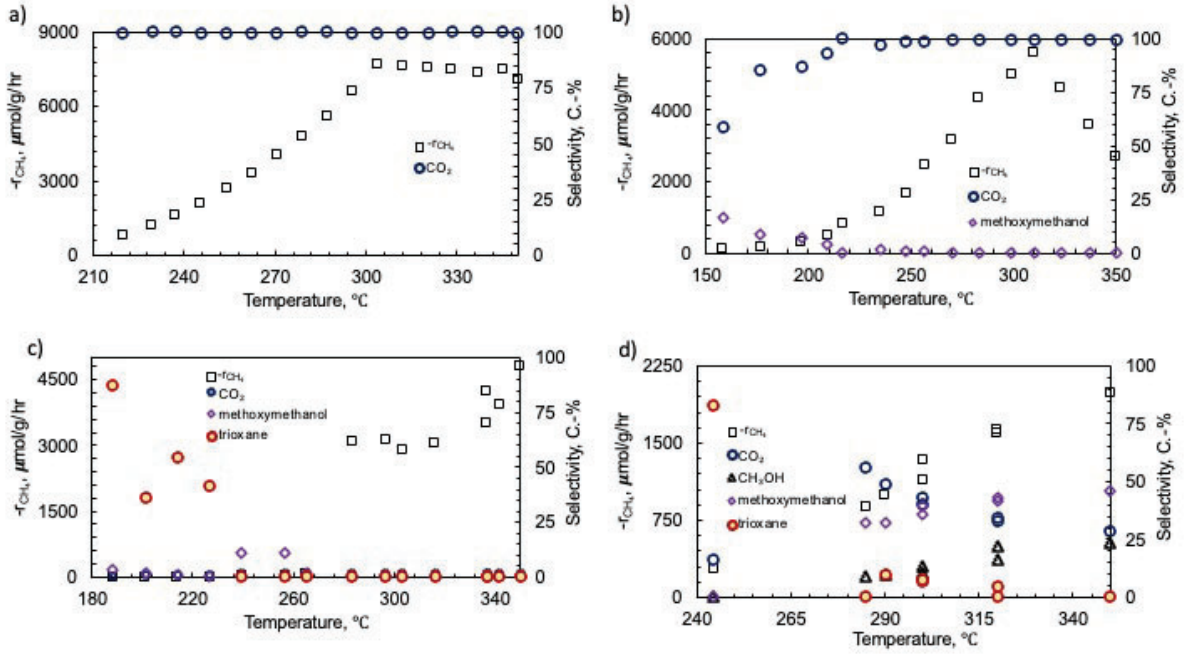

Figure A2.2: Rate of methane oxidation over 10 wt.% Pt/TiO_2 (rutile) conducted in the gas phase reactor, with a $(H_2O/CH_4)_{feed}$ mol/mol ratio of 0 (a), 6 (b), 12 (c) and 50 (d) (CH_4=2 ml_n/min, P_{total}= 20 bar, O_2=16 ml_n/min. The He flow rate was modified to maintain constant inlet partial pressures of CH_4 and O_2.

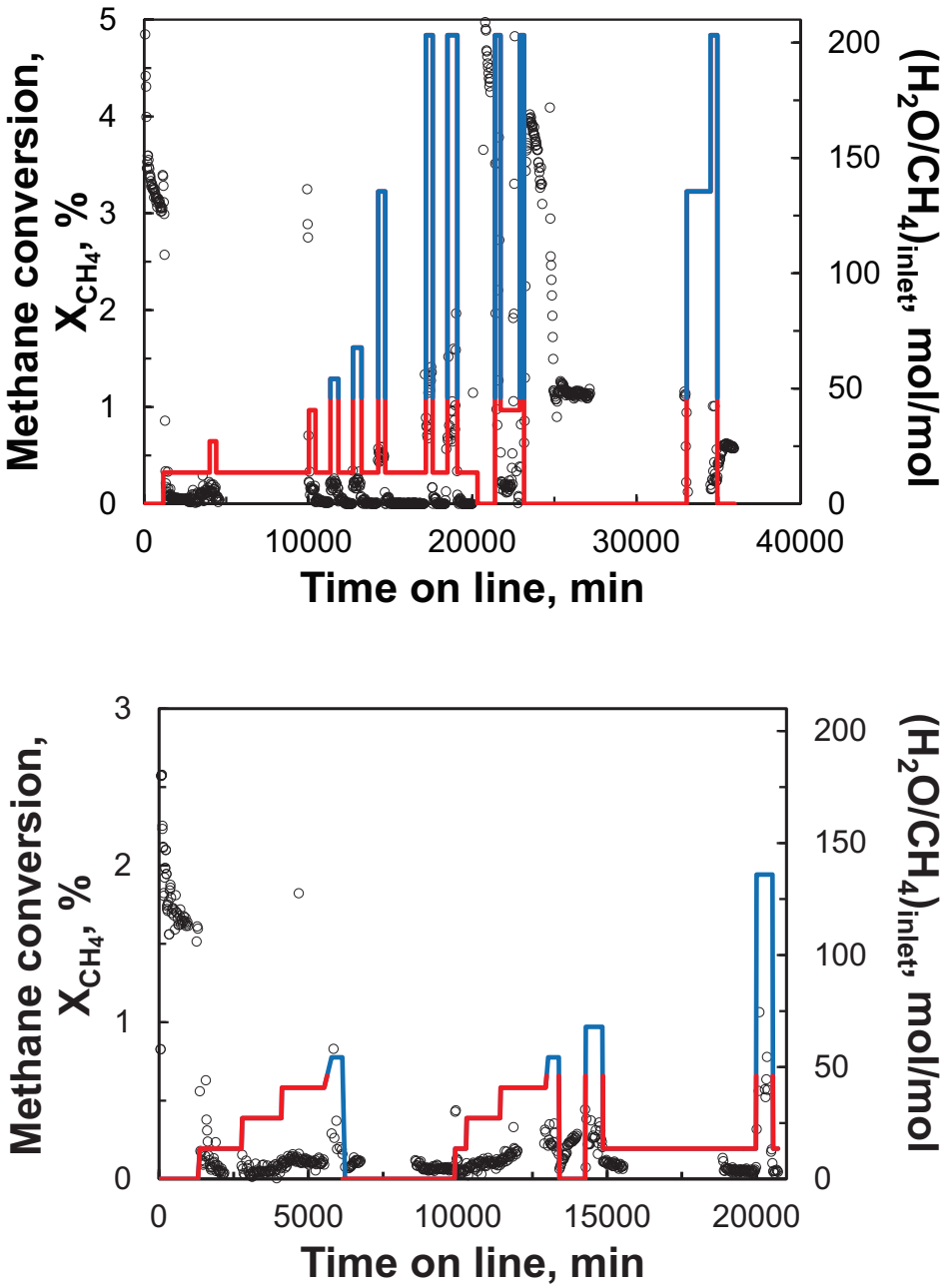

Figure A2.3: Time-on-stream behavior in the oxidation of methane over 10% Pt/TIO_2 (top) and 10% Pt/Al_2O_3 (bottom) at 220°C, 30 bar and $F_{CH4,0}/W$ = 3.23/hr/g (inlet partial pressures p_{CH4} = 0.5 bar; p_{O2} = 1.5 bar; red/blue line indicating the water flow rate to the reactor with the blue line indicating flooding conditions in the reactor).

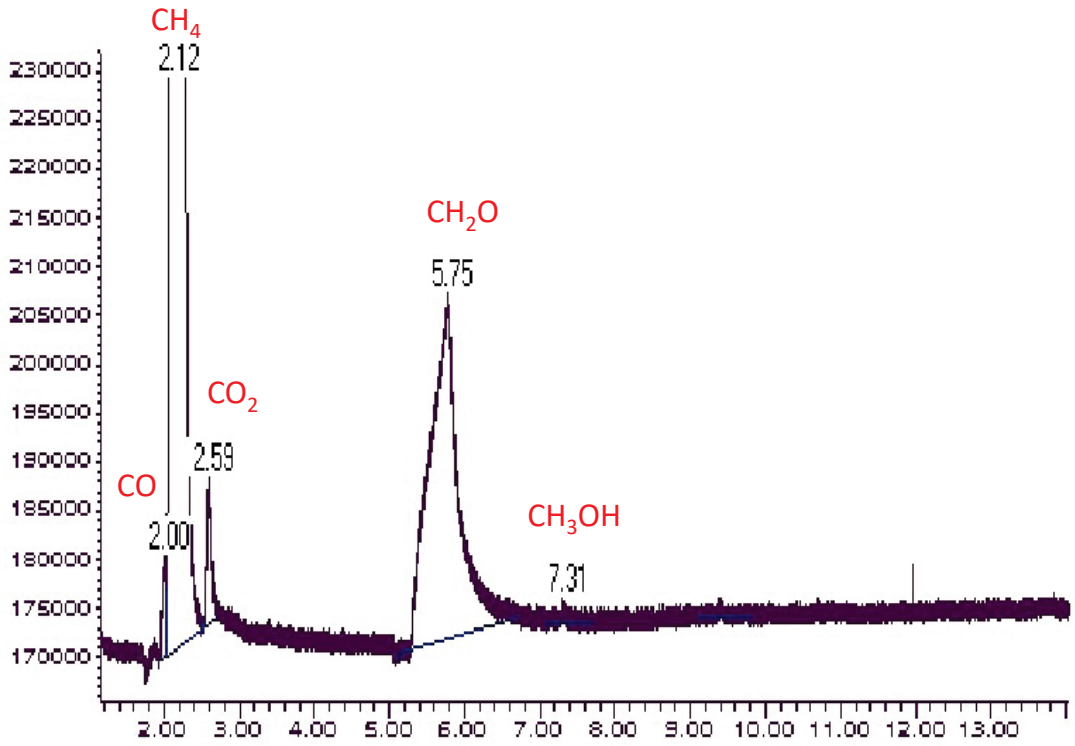

Figure A2.4: GC-trace obtained during the selective oxidation of methane under the trickle-bed conditions over 10% Pt/Al_2O_3.

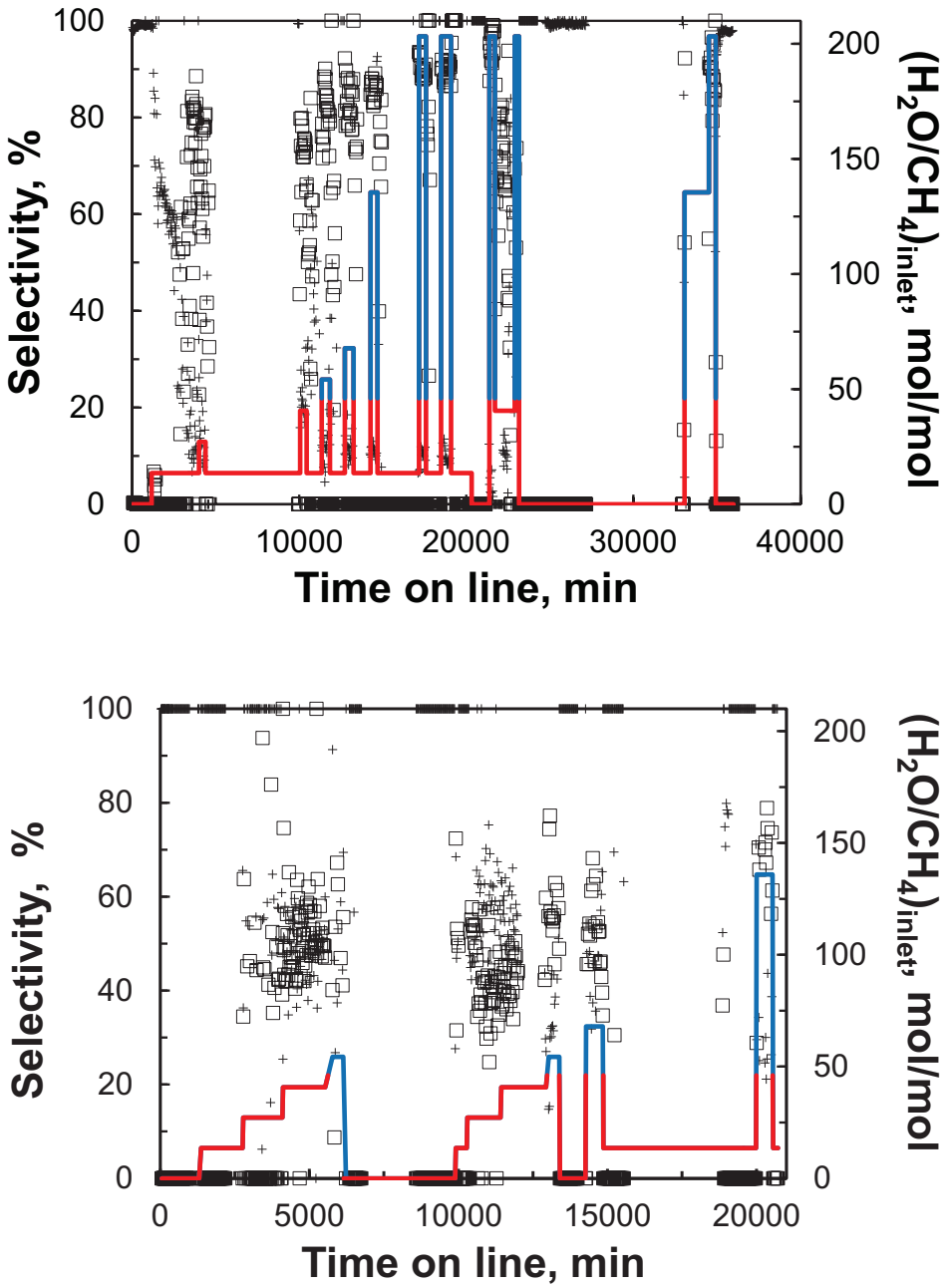

Figure A2.5: Selectivity for the formation of CO_2 (+) and formaldehyde in the oxidation of methane over 10% Pt/TIO_2 (top) and 10% Pt/Al_2O_3 (bottom) at 220°C, 30 bar and $F_{CH4,0}/W$ = 3.23/hr/g (inlet partial pressures p_{CH4} = 0.5 bar; p_{O2} = 1.5 bar; red/blue line indicating the water flow rate to the reactor with the blue line indicating flooding conditions in the reactor).

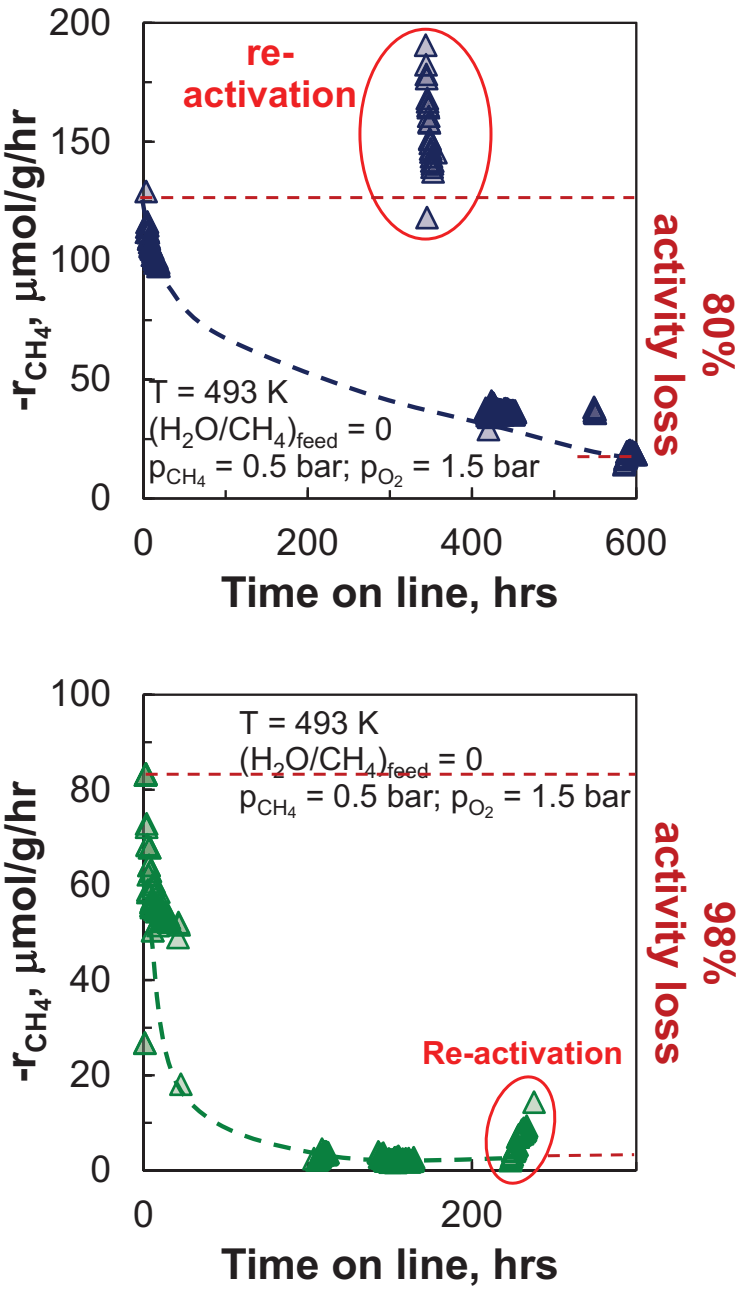

Figure A2.6: Catalyst activity as a function of time on stream over Pt/TiO_2 (top) and Pt/Al_2O_3 (bottom) (220°C, 30 bar and $F_{CH4,0}/W$ = 3.23/hr/g; inlet partial pressures p_{CH4} = 0.5 bar; p_{O2} = 1.5 bar, $(H_2O/CH_4)_{feed}$ = 0).

SECTION III: DFT STUDIES

Spin polarised quantum chemical calculations were performed using VASP [A1-A3] using the GGA-PBE functional [A4] with dispersion correction according to Grimme et al. with Becke-Jonson damping [A5,A6]. The PAW pseudopotentials were used to describe the electron-ion interaction [A2]. Smearing using 1st order Methfessel-Paxton method [A7] was applied with $\sigma=0.05\ eV$ for surface calculations. Brillouin zone was sampled using a Γ-centred Monkhorst-Pack grid [A8] with a plane wave cut-off energy of 500 eV (grid size (√3x√3): 12 x 12 x1; (2x2): 10 x 10 x 1; (3x3): 7 x 7 x 1, respectively). The lattice parameter for bulk FCC platinum was evaluated to be 3.9246 Å with a bulk modulus of 301 GPa in good agreement with the experimental values of 3.9231 Å and 282.7 GPa, respectively [A9].

A five layer Pt(111) slab with a 15 Å vacuum layer was used in this study. For the geometry optimizations, all the atoms were allowed to relax except the bottom two layers of the slabs. Surface structures were optimized with a maximum force of 0.01 eV/Å applying dipole correction in the direction perpendicular to the surface (SCF < 10^{-5} eV). The optimized structures represent local minimums on the potential energy surface as confirmed by a vibrational analysis. The vibrational modes were obtained allowing only the atoms of the adsorbate to move by 0.015 Å.

The obtained energies were referenced to that of the bare surface and the molecules CH_4, O_2, H_2, H, OH, H_2O, methanol, methanediol and formaldehyde, which were optimized by placing each molecule in a 15 Å x 16 Å x 17 Å box (plane wave cut-off energy: 1000 eV; Gaussian smearing, σ = 0.005 eV; Gamma-centered k-point grid: 1x1x1; maximum allowable force: 0.01 eV/Å). The obtained bond distances and vibrational modes of the gas phase molecules were compared with experimentally determined values [A9-A11].

The adsorption energy as reported in Tables A2.3-A2.4 was determined relative to H_2O, O_2 and CH_4 in the gas phase and normalized with respect to the size of the unit cell taking the (2x2) unit cell as a basis:

$$E_{ads} = \frac{E_{C_\alpha H_\beta O_\gamma \text{ on } Pt(111)} - E_{Pt(111)-slab} - \alpha \cdot E_{CH_4} - \frac{\beta - 4\cdot\alpha x}{2} \cdot E_{H_2O(g)} - \frac{2\cdot\gamma - \beta + 4\cdot\alpha x}{4} E_{O_2(g)}}{N^{(a\times a)}}$$

and $$\Delta ZPE = \frac{ZPE_{C_\alpha H_\beta O_\gamma \text{ on } Pt(111)} - ZPE_{Pt(111)-slab} - \alpha \cdot ZPE_{CH_4} - \frac{\beta - 4\cdot\alpha x}{2} \cdot ZPE_{H_2O(g)} - \frac{2\cdot\gamma - \beta + 4\cdot\alpha x}{4} ZPE_{O_2(g)}}{N^{(a\times a)}}$$

with $N^{(\sqrt{3}\times\sqrt{3})} = \frac{3}{4}$; $N^{(2\times2)} = 1$; $N^{(3\times3)} = \frac{9}{4}$.

The most stable structure at a particular condition can be obtained by considering the Gibbs free energy of a particular structure at that condition. The Gibbs free energy associated with a structure was calculated as:

$$G_{structure} = E^{elec}_{structure} - E^{elec}_{bare\ slab} + h^{vib}_{structure} - T \cdot s^{vib}_{structure}$$

with $G_{structure}$: the Gibbs free energy associated with structure (slab + adsorbate)

$E^{elec}_{structure}$: the electronic energy of the structure (slab + adsorbate)

E^{elec}_{slab}: the electronic energy of the bare slab

$h^{vib}_{stucture}$: the enthalpy correction due to vibration of the adsorbate

$s^{vib}_{stucture}$: the entropy correction due to vibration of the adsorbate

After determining the Gibbs free energy of structures on the surface, surface phase diagrams of species on Pt(111) were determined in the presence of water and O_2 and in the presence of water, O_2, and CH_4. Numerous configurations can be obtained considering different species, vacant sites, and different adsorption geometries. Hence, only 63 configurations containing O, OH and H_2O were considered for the surface phase diagram on Pt(111) exposed to water and O_2 (see Table A2.2) A much more limited additional set (10 different configurations) was considered when dealing with methyl and methoxy species on the surface was investigated to construct a surface phase diagram on Pt(111) exposed to water, O_2 and CH_4 (see Table A2.3 and A2.4).

The structure with the lowest Gibbs free energy at a given chemical potential of water, oxygen and methane (as determined by DFT) can be found by searching for the minimum value for:

$$G = \min_i \left(\frac{G_{structure,i} - \alpha \cdot \mu_{CH_4(g)} - \frac{\beta - 4\cdot\alpha x}{2} \cdot \mu_{H_2O(g)} - \frac{2\cdot\gamma - \beta + 4\cdot\alpha x}{4} \cdot \mu_{O_2(g)}}{N^{(a\times a)}} \right)$$

with $G_{structure,i}$: the Gibbs free energy associated with structure i (slab + adsorbate)

α the number of C-atoms in the adsorbate

β the number of H-atoms in the adsorbate

γ the number of O-atoms in the adsorbate

$N^{(a\times a)}$ the number of surface Pt-atoms on one side of the unit cell

The prediction of the chemical potential of oxygen using DFT is improved significantly by relating the enthalpy/chemical potential of oxygen to the DFT-derived enthalpy/chemical potential of hydrogen and water [A12,A13] rather than using the enthalpy/chemical potential of oxygen derived from DFT-generated data:

$$h^o_{O_2} = 2\cdot\left(h^o_{H_2O} - h^o_{H_2} - \Delta_{f,H_2O}H^0\right) \quad \mu^o_{O_2} = 2\cdot\left(\mu^o_{H_2O} - \mu^o_{H_2} - \Delta_{f,H_2O}G^0\right)$$

Hence, the derived phase diagrams in this study refer use water and hydrogen as the reference state for gas phase oxygen.

Table A2.2: Geometric characteristics, energetics, and normal modes of surface structures considered to determine the surface phase diagram of adsorbed O, OH and H_2O on Pt(111)

	Θ_*	Θ_O	Θ_{H2O}	Θ_{OH}	E_{ads}, eV	$\Delta_{ads}ZPE$, eV
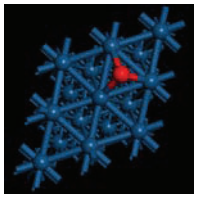	0.75	0.25	-	-	-0.974	0.026
	d_{Pt-O}: 2.047, 2.047, 2.047 Å (O in fcc hollow on 2x2)				470, 367, 366 cm^{-1}	
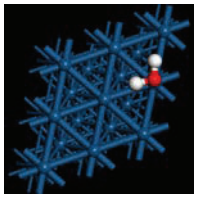	0.75	-	0.25	-	-0.464	0.073
	$d_{Pt-O(H,H)}$: 2.410 Å $d_{(Pt)O-H}$: 0.982, 0.982Å $\angle_{H-O-H}$: 104.4° $\angle_{plane\ through\ H-O-H\ and\ surface}$: 0.8° ($H_2O$ in atop on 2x2)				3658, 3563, 1551, 566, 508, 165, 151, 91, 84 cm^{-1}	
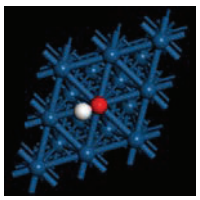	0.75	-	-	0.25	-0.594	0.028
	$d_{Pt-O(H)}$: 1.988 Å $d_{(Pt)O-H}$: 0.980 Å $\angle_{Pt-O-H}$: 106.0° (OH in atop on 2x2)				3650, 928, 518, 126, 118, 80 cm^{-1}	
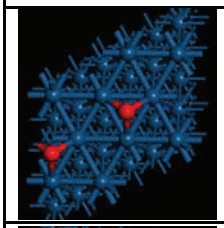	0.67	0.33	-	-	-1.049	0.011
	d_{Pt-O}: 2.070, 2.071, 2.071 Å (O in fcc hollow on √3x√3)				448, 260, 259 cm^{-1}	
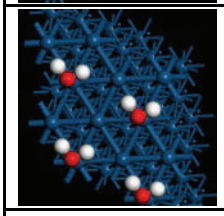	0.67	-	0.33	-	-0.630	0.081
	$d_{Pt-O(H,H)}$: 2.447 Å $d_{(Pt)O-H}$: 0.982, 0.983Å $\angle_{H-O-H}$: 103.6° $\angle_{plane\ through\ H-O-H\ and\ surface}$: 1.6° ($H_2O$ in atop on √3x√3)				3635, 3539, 1554, 584, 471, 150, 88, 75, 40 cm^{-1}	
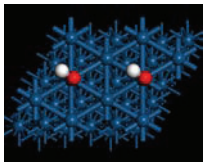	0.67	-	-	0.33	-0.848	0.039
	$d_{Pt-O(H)}$: 1.987Å $d_{(Pt)O-H}$: 0.981 Å $\angle_{Pt-O-H}$: 106.4° (OH in atop on √3x√3)				3638, 940, 520, 152, 107, 81 cm^{-1}	
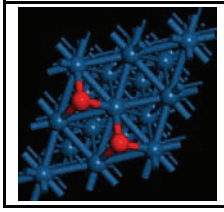	0.50	0.50	-	-	-1.899	0.062
	d_{Pt-O}: 2.028, 2.028, 2.031, 2.031, 2.033, 2.033 Å (O in fcc hollow on 2x2)				490, 471, 442, 413, 382, 371 cm^{-1}	

Table A2.2 (cont.)

	Θ_*	Θ_O	Θ_{H2O}	Θ_{OH}	E_{ads}, eV	$\Delta_{ads}ZPE$, eV
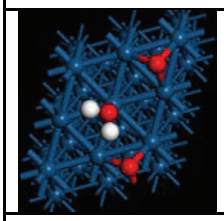	0.50	0.25	0.25	-	-1.858	0.110
	d_{Pt-O}: 2.066, 2.085, 2.090 Å $d_{Pt-O(H,H)}$: 2.380 Å $d_{(Pt)O-H}$: 0.980, 0.982 Å $\angle_{H-O-H}$: 105.2° $\angle_{\text{plane through H-O-H and surface}}$: 8.3° (O in fcc hollow, H_2O in atop on 2x2)				3678, 3583, 1561, 624, 591, 437, 333, 311, 213, 183, 109, 74 cm^{-1}	
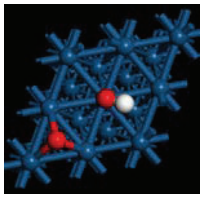	0.50	0.25	-	0.25	-1.858	0.110
	d_{Pt-O}: 2.046, 2.046, 2.059 Å $d_{Pt-O(H)}$: 1.989 Å $d_{(Pt)O-H}$: 0.980 Å $\angle_{Pt-O-H}$: 107.3° (O in fcc hollow, OH in atop on 2x2)				3650, 954, 521, 465, 370, 356, 170, 138, 110 cm^{-1}	
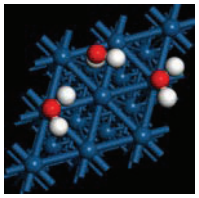	0.50	-	0.50	-	-1.335	0.167
	$d_{Pt-O(H,H)}$: 2.397 Å $d_{Pt-H(O)}$: 2.489, 2.554, 2.711 Å $d_{(Pt)O-H}$: 0.980, 1.001, 0.979, 0.996 Å $\angle_{H-O-H}$: 106.1°, 102.5° $\angle_{\text{plane through H-O-H and surface}}$: 21.6°, 77.6° ($H_2O$ in atop and H_2O above hcp hollow on 2x2)				3674, 3638, 3296, 3192, 1604, 1547, 879, 634, 586, 525, 399, 249, 210, 165, 142, 140, 71, 61 cm^{-1}	
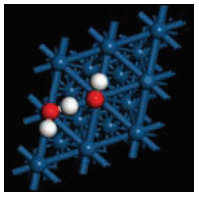	0.50	-	0.25	0.25	-1.664	0.117
	$d_{Pt-O(H)}$: 2.081 Å $d_{Pt-O(H,H)}$: 2.186 Å $d_{(Pt)O-H}$: 0.977 Å $d_{(Pt,H)O-H}$: 0.977, 1.078 Å $\angle_{Pt-O-H}$: 104.9° $\angle_{H-O-H}$: 109.1° $\angle_{\text{plane through H-O-H and surface}}$: 20.9° ($H_2O$ and OH in atop on 2x2)				3690, 3690, 1853, 1539, 1269, 872, 738, 620, 422, 386, 307, 229, 164, 135, 109 cm^{-1} [1]	
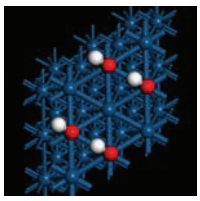	0.50	-	-	0.50	-1.639	0.103
	$d_{Pt-O(H)}$: 1.988, 1.988 Å $d_{(Pt)O-H}$: 0.991, 0.992 Å $\angle_{Pt-O-H}$: 106.2°, 106.2° (OH in atop on 2x2)				3394, 3371, 1144, 1055, 618, 533, 515, 405, 257, 147, 90, 76 cm^{-1}	
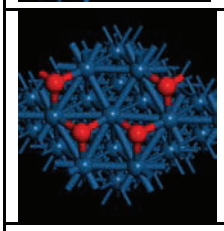	0.33	0.67	-	-	-2.047	0.082
	d_{Pt-O}: 2.038, 2.038, 2.038, 2.038, 2.038, 2.039 Å (O in fcc hollow on √3x√3)				503, 430, 428, 420, 388, 386 cm^{-1}	
	0.33	0.33	0.33	-	[1]	

[1] A structure containing $\theta_* = 0.33$, $\theta_O = 0.33$, $\theta_{H_2O} = 0.33$ on (√3x√3)-Pt(111) optimises to a structure with $\theta_* = 0.33$, $\theta_{OH} = 0.67$.

Table A2.2 (cont.)

	Θ_*	Θ_O	Θ_{H2O}	Θ_{OH}	E_{ads}, eV	$\Delta_{ads}ZPE$, eV
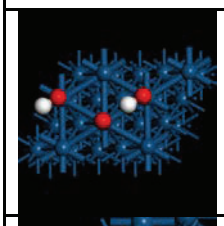	0.33	0.33	-	0.33	-0.959	0.062
	d_{Pt-O}: 1.845 Å $d_{Pt-O(H)}$: 1.957 Å $d_{(Pt)O-H}$: 1.003 Å $\angle_{Pt-O-H}$: 105.6° (O and OH atop on √3x√3)				3139, 1065, 634, 537, 493, 204, 154, 142, 132 cm^{-1}	
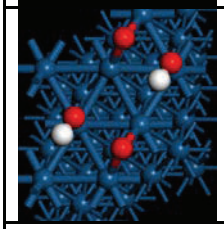	0.33	0.33	-	0.33	-1.141	0.079
	d_{Pt-O}: 1.997, 2.004 Å $d_{Pt-O(H)}$: 1.994 Å $d_{(Pt)O-H}$: 0.981 Å $\angle_{Pt-O-H}$: 107.1° (O in bridge and OH atop on √3x√3)				3639, 906, 500, 476, 367, 317, 186, 168, 150 cm^{-1}	
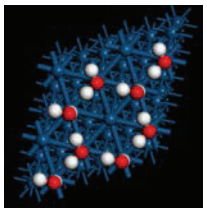	0.33	-	0.67	-	-1.994	0.246
	$d_{Pt-O(H,H)}$: 2.536 Å $d_{Pt-H(O,H)}$: 2.087 Å $d_{(Pt, H)O-H}$: 0.996, 0.997, 0.993, 1.009 Å $\angle_{H-O-H}$: 106.4°,100.0° $\angle_{plane\ through\ H-O-H\ and\ surface}$: 0.4°, 89.7° ($H_2O$ alternating in atop and perpendicular orientation on √3x√3)				3402, 3272, 3254, 3017, 1640, 1544, 956, 875, 854, 588, 502, 429, 280, 233, 231, 114, 70, 43 cm^{-1}	
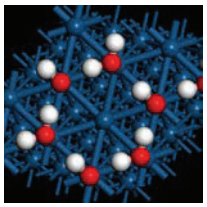	0.33	-	0.33	0.33	-2.831	0.225
	$d_{Pt-O(H)}$: 2.101 Å $d_{Pt-O(H,H)}$: 2.201Å $d_{(Pt)O-H}$: 0.985 Å $d_{(Pt,H)O-H}$:1.017, 1.018 Å $\angle_{Pt-O-H}$: 102.8° $\angle_{H-O-H}$: 112.1° $\angle_{plane\ through\ H-O-H\ and\ surface}$: 14.9 ° ($H_2O$ and OH in atop on √3x√3)				3528, 2868, 2823, 1537, 1071, 1016, 961, 958, 623, 408, 336, 254, 197, 140, 128 cm^{-1}	
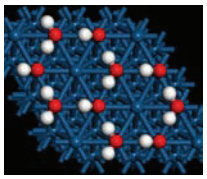	0.33	-	0.33	0.33	-2.756	0.232
	$d_{Pt-O(H)}$: 2.101, 2.101, 2.101 Å $d_{Pt-O(H,H)}$:2.200, 2.200, 2.200 Å $d_{(Pt)O-H}$: 0.985, 0.985, 0.985 Å $d_{(Pt,H)O-H}$:1.017, 1.017, 1.017 Å 1.019, 1.019, 1.019 Å $\angle_{Pt-O-H}$: 102.7°, 102.7°, 102.7° $\angle_{H-O-H}$: 112.4°, 112.4°, 112.4° $\angle_{plane\ through\ H-O-H\ and\ surface}$: 14.8°, 14.8°, 14.8° ($H_2O$ and OH in atop on 3x3)				3529, 3524, 3520, 2918, 2916, 2869, 2823, 2814, 2812, 1552, 1552, 1539, 1084, 1084, 1073, 1021, 986, 985, 975, 973, 965, 960, 846, 846, 773, 771, 626, 408, 397, 396, 338, 321, 317, 257, 228, 227, 205, 204, 200, 186, 185, 173, 171, 141, 134 cm^{-1}	
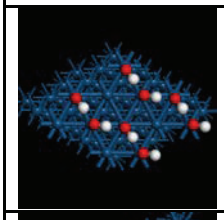	0.33	-	0.67	-	-2.270	0.152
	$d_{Pt-O-(H)}$: 1.984, 1.984 Å $d_{(Pt)O-H}$: 1.008, 1.009 Å $\angle_{Pt-O-H}$: 104.4°, 104.7° (OH atop on √3x√3)				3068, 2995, 1201, 1154, 823, 682, 541, 505, 331, 203, 160, 121 cm^{-1}	
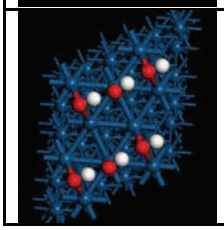	0.33	-	0.67	-	-2.155	0.137
	$d_{Pt-O-(H)}$: 2.009, 2.119, 2.178 Å $d_{(Pt)O-H}$: 0.995, 1.037 Å $\angle_{Pt-O-H}$: 103.7°, 104.2°, 105.9° (bridging OH + OH atop on √3x√3)				3252, 2427, 1259, 1077, 1009, 626, 592, 486, 390, 206, 188, 86 cm^{-1}	

Table A2.2 (cont.)

	Θ_*	Θ_O	Θ_{H2O}	Θ_{OH}	E_{ads}, eV	$\Delta_{ads}ZPE$, eV
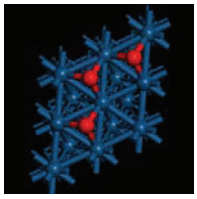	0.25	0.75	-	-	-1.700	0.091
	d_{Pt-O}: 2.028, 2.028, 2.028, 2.029, 2.029, 2.029, 2.034, 2.035 2.035 Å (O on fcc hollow on 2x2)				494, 469, 444, 444, 423, 422, 377, 377, 361 cm^{-1}	
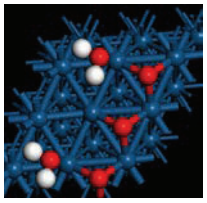	0.25	0.50	0.25	-	-2.218	0.117
	d_{Pt-O}: 2.028, 2.032, 2.033, 2.045, 2.051, 2.052Å $d_{Pt-O(H,H)}$:3.327Å $d_{(H)O-H}$: 0.973, 0.977 Å $\angle_{H-O-H}$: 104.8° $\angle_{plane\ through\ H-O-H\ and\ surface}$: 48.4° (O on fcc hollow and H_2O atop on 2x2)				3780, 3673, 1582, 488, 465, 446, 402, 399, 374, 370, 220, 189, 117, 56, 27 cm^{-1}	
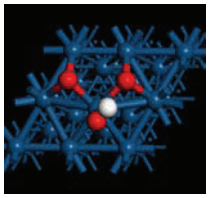	0.25	0.50	-	0.25	-1.824	0.103
	d_{Pt-O}: 2.007, 2.011, 2.046, 2.049, 2.061, 2.072 Å $d_{Pt-O(H)}$: 1.979 Å $d_{(Pt)O-H}$: 0.982 Å $\angle_{Pt-O-H}$: 103.6° (O on fcc hollow and OH atop on 2x2)				3626, 1036, 527, 494, 467, 449, 416, 402, 353, 214, 127, 93 cm^{-1}	
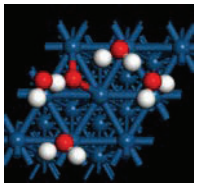	0.25	0.25	0.50	-	-2.627	0.220
	d_{Pt-O}: 2.069, 2.081, 2.121 Å $d_{Pt-O(H,H)}$:2.295, 3.592 Å $d_{(Pt)O-H}$: 0.973, 0.982, 0.995, 1.021 Å $\angle_{H-O-H}$: 105.2°, 105.1° $\angle_{plane\ through\ H-O-H\ and\ surface}$: 28.8°, 47.6° (O on fcc hollow, H_2O atop on 2x2)				3780, 3586, 3312, 2838, 1629, 1585, 1031, 768, 714, 575, 469, 406, 351, 343, 322, 280, 211, 169, 140, 105, 48 cm^{-1}	
	0.25	0.25	0.25	0.25	[2]	
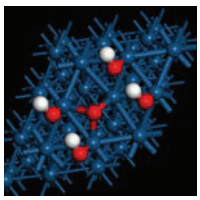	0.25	0.25	-	0.50	-1.460	0.141
	d_{Pt-O}: 1.984, 2.043, 2.066 Å $d_{Pt-O(H)}$: 1.989, 2.005 Å $d_{(Pt)O-H}$: 0.990, 0.993 Å $\angle_{Pt-O-H}$: 105.4°, 106.2° (O on fcc hollow, OH atop on 2x2)				3451, 3343, 1166, 1087, 571, 526, 517, 496, 423, 400, 374, 273, 194, 121, 64 cm^{-1}	
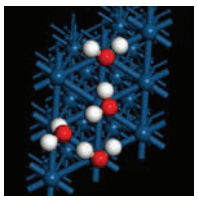	0.25	-	0.75	-	-2.024	0.289
	$d_{Pt-O(H,H)}$: 2.314,3.357 Å $d_{Pt-H(O)}$: 2.311 Å $d_{(Pt)O-H}$: 0.980, 0.982, 0.987, 0.993, 1.000, 1.023 Å $\angle_{H-O-H}$: 103.8°, 103.9°, 105.8° $\angle_{plane\ through\ H-O-H\ and\ surface}$: 23.8°, 30.8°, 78.1° ($H_2O$ on/above atop on 2x2)				3627, 3611, 3477, 3354, 3222, 2777, 1673, 1602, 1574, 1097, 804, 677, 646, 625, 545, 515, 454, 389, 365, 257, 204, 172, 146, 122, 94, 68, 50 cm^{-1}	

[2] Starting from a structure containing $\theta_* = 0.25$, $\theta_O = 0.25$, $\theta_{H_2O} = 0.25$ and $\theta_{OH} = 0.25$ on (2x2)-Pt(111)optimises to a structure with $\theta_* = 0.25$ and $\theta_{OH} = 0.75$.

Table A2.2 (cont.)

	Θ_*	Θ_O	Θ_{H2O}	Θ_{OH}	E_{ads}, eV	$\Delta_{ads}ZPE$, eV
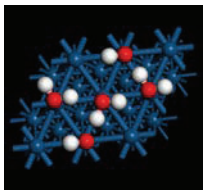	0.25	-	0.50	0.25	-2.591	0.253
	$d_{Pt-O(H)}$: 2.149 Å $d_{Pt-O(H,H)}$: 2.323, 2.333 Å $d_{(Pt,H)O-H}$: 0.983, 1.043 Å 0.984, 1.043 Å $d_{(Pt)O-H}$: 0.975 Å $\angle_{H-O-H}$: 107.8°, 107.9° $\angle_{Pt-O-H}$[a]: 96.4° $\angle_{plane\ through\ H-O-H\ and\ surface}$: 16.6°, 16.6° ($H_2O$ and OH atop on 2x2)				3706, 3558, 3505, 2469, 2305, 1681, 1533, 1171, 1135, 868, 792, 722, 689, 630, 519, 393, 386, 337, 225, 196, 180, 147, 115, 113 cm^{-1}	
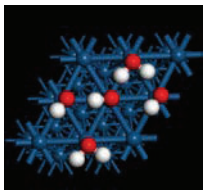	0.25	-	0.25	0.50	-2.873	0.210
	$d_{Pt-O(H)}$: 2.034,2.066 Å $d_{Pt-O(H,H)}$: 2.126 Å $d_{(Pt,H)O-H}$: 1.017, 1.064 Å $d_{(Pt)O-H}$: 0.978, 1.004 Å $\angle_{H-O-H}$: 95.9° $\angle_{Pt-O-H}$: 100.1°, 100.1° $\angle_{plane\ through\ H-O-H\ and\ surface}$: 9.5° ($H_2O$ and OH atop on 2x2)				3670, 3109, 2942, 2114, 1589, 1272, 1166, 1097, 942, 876, 646, 492, 465, 451, 425, 324, 284, 206, 151, 134, 133 cm^{-1}	
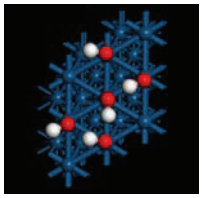	0.25	-	-	0.75	-2.365	0.165
	$d_{Pt-O(H)}$: 1.980, 1.988, 1.985 Å $d_{(Pt)O-H}$: 1.007, 1.007, 1.015 Å $\angle_{Pt-O-H}$: 103.4°, 103.7°, 104.6° (OH atop on 2x2)				3080, 3021, 2865, 1247, 1179, 1135, 933, 697, 605, 541, 519, 492, 358, 270, 245 cm^{-1}	
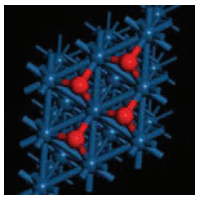	-	1.00	-	-	-0.984	0.100
	d_{Pt-O}: 2.041, 2.041, 2.041, 2.044, 2.044, 2.044, 2.044, 2.044, 2.044, 2.044, 2.044, 2.044 Å (O on fcc-hollow on 2x2)				496, 429, 428, 427, 419, 417, 416, 369, 368, 366, 310, 305 cm^{-1}	
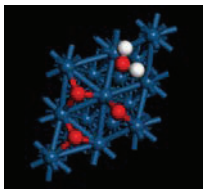	-	0.75	0.25	-	-1.818	0.171
	d_{Pt-O}: 1.967, 1.968, 1.994, 1.998, 2.038, 2.046, 2.052, 2.059 Å $d_{Pt-O(H,H)}$: 3.265 Å $d_{(H)O-H}$: 0.973, 0.980 Å $\angle_{H-O-H}$: 105.3° $\angle_{plane\ through\ H-O-H\ and\ surface}$: 14.8 ° (O on fcc-hollow; H_2O above bridge on 2x2)				3785, 3592, 1579, 577, 546, 510, 487, 455, 441, 425, 411, 379, 298, 272, 217, 118, 94, 79 cm^{-1}	
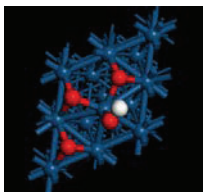	-	0.75	-	0.25	-1.517	0.136
	d_{Pt-O}: 2.013, 2.015, 2.021, 2.022, 2.036, 2.038, 2.044, 2.064, 2.072 Å $d_{Pt-O(H)}$: 1.982 Å $d_{(Pt)-O-H}$: 0.982 Å $\angle_{Pt-O-H}$: 104.1° (O on fcc-hollow; OH atop on 2x2)				3632, 1035, 520, 489, 477, 467, 450, 438, 435, 413, 381, 360, 188, 126, 106 cm^{-1}	

Table A2.2 (cont.)

	Θ_*	Θ_O	Θ_{H2O}	Θ_{OH}	E_{ads}, eV	$\Delta_{ads}ZPE$, eV
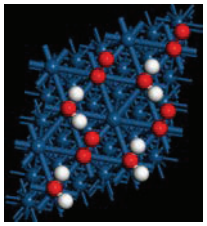	-	0.67[3]	0.33	-	-1.683[4]	0.141
	d_{Pt-O}: 2.032 Å d_{O-O}: 1.344 Å $d_{Pt-O(H,H)}$: 2.074 Å $d_{(H)O-H}$: 0.993, 1.090 Å $\angle_{Pt-O-O}$: 119.7° $\angle_{H-O-H}$: 105.5° $\angle_{plane\ through\ H-O-H\ and\ surface}$: 10.7° ($H_2O$ and O_2 atop on √3x√3)				3315, 1647, 1618, 1079, 993, 972, 624, 558, 460, 316, 289, 233, 158, 94, 73 cm^{-1}	
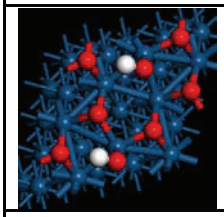	-	0.67	-	0.33	-1.830	0.161
	d_{Pt-O}: 2.015, 2.019, 2.020, 2.027, 2.066, 2.067 Å $d_{Pt-O(H)}$: 1.977 Å $d_{(Pt)O-H}$: 0.983 Å $\angle_{Pt-O-H}$: 104.1° (O in fcc hollow; OH atop on √3x√3)				3606, 1068, 541, 522, 511, 473, 427, 402, 392, 260, 147, 137 cm^{-1}	
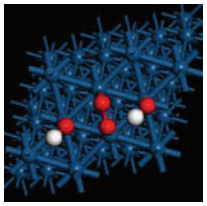	-	0.67[3]	-	0.33	-1.632	0.167
	$d_{Pt-O(O)}$: 2.004, 2.042 Å d_{O-O}: 1.389 Å $d_{Pt-O(H)}$: 1.959 Å $d_{(Pt)O-H}$: 0.986 Å $\angle_{Pt-O-O}$: 109.0°, 109.3° $\angle_{Pt-O-H}$: 108.3° (O_2 on bridge; OH atop on √3x√3)				3437, 1017, 801, 582, 562, 522, 417, 380, 286, 243, 165, 151 cm^{-1}	
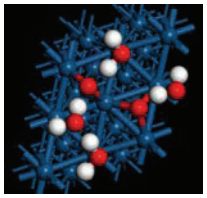	-	0.50	0.50	-	-3.174	0.247
	d_{Pt-O}: 2.032, 2.034, 2.045, 2.047, 2.050 Å $d_{Pt-O(H,H)}$: 2.127, 3.561 Å $d_{(H)O-H}$: 0.976, 1.006, 1.039, 1.043 Å $\angle_{H-O-H}$: 103.3°, 104.5° $\angle_{plane\ through\ H-O-H\ and\ surface}$: 28.2°, 40.7° (O in fcc hollow and bridge; H_2O atop on 2x2)				3727, 3094, 2510, 2419, 1645, 1610, 1178, 1126, 930, 817, 550, 517, 464, 441, 440, 413, 376, 367, 363, 292, 224, 150, 125, 96 cm^{-1}	
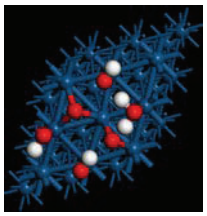	-	0.50	0.25	0.25	-2.306	0.216
	d_{Pt-O}: 1.966, 1.975, 2.022, 2.037, 2.050 Å $d_{Pt-O(H)}$: 2.031 Å $d_{Pt-O(H,H)}$: 2.166 Å $d_{(Pt)O-H}$: 0.995 Å $d_{(H)O-H}$: 1.032, 1.043 Å $\angle_{Pt-O-H}$: 98.1° $\angle_{H-O-H}$: 102.8° $\angle_{plane\ through\ H-O-H\ and\ surface}$: 0.0° (O in fcc hollow and bridge; H_2O and OH atop on 2x2)				3324, 2604, 2374, 1613, 1192, 1099, 1020, 861, 617, 560, 530, 507, 477, 444, 413, 362, 343, 302, 240, 169, 138 cm^{-1}	
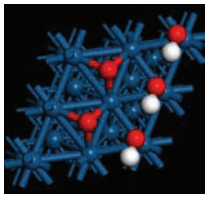	-	0.50	-	0.50	-1.942	0.184
	d_{Pt-O}: 2.012, 2.012, 2.017, 2.017, 2.022, 2.022 Å $d_{Pt-O(H)}$: 2.010, 2.011 Å $d_{(Pt)O-H}$: 0.992, 0.992 Å $\angle_{Pt-O-H}$: 105.0°, 105.1° (O in fcc hollow; OH atop on 2x2)				3405, 3380, 1152, 1066, 560, 512, 502, 501, 473, 461, 456, 434, 404, 388, 256, 200, 195, 131 cm^{-1}	

[3] In this configuration molecularly adsorbed O_2 is on the surface rather than 2O

[4] The same coverage with O in the fcc hollow site is more stable (Eads = -2.527 eV), but vibrational analysis resulted in a single imaginary frequency

Table A2.2 (cont.)

	Θ_*	Θ_O	Θ_{H2O}	Θ_{OH}	E_{ads}, eV	$\Delta_{ads}ZPE$, eV
	-	0.33	0.67		[5]	
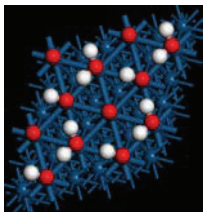	-	0.33	0.33	0.33	-3.064	0.262
	d_{Pt-O}: 1.840 Å $d_{Pt-O(H)}$: 2.053 Å $d_{Pt-O(H,H)}$: 2.142 Å $d_{(Pt)O-H}$: 0.987 Å $d_{(H)O-H}$: 1.016, 1.017 Å $\angle_{Pt-O-H}$: 104.0° $\angle_{H-O-H}$: 110.7° $\angle_{\text{plane through H-O-H and surface}}$: 17.9° (O, H_2O and OH atop on √3x√3)				3491, 2903, 2874, 1494, 1104, 1073, 1024, 830, 656, 502, 447, 375, 294, 278, 238, 205, 156, 143 cm^{-1}	
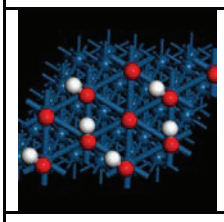	-	0.33	-	0.67	-2.259	0.173
	d_{Pt-O}: 1.831 Å $d_{Pt-O(H)}$: 1.971, 1.971 Å $d_{(Pt)O-H}$: 1.005, 1.005 Å $\angle_{Pt-O-H}$: 105.4°, 105.4° (O and OH atop on √3x√3)				3126, 3087, 1180, 1127, 739, 651, 563, 531, 512, 290, 244, 213, 212, 180, 170 cm^{-1}	
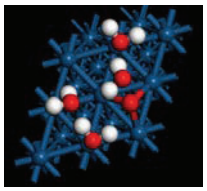	-	0.25	0.75	-	-3.313	0.321
	d_{Pt-O}: 2.058, 2.063, 2.083 Å $d_{Pt-O(H,H)}$: 2.315, 3.399,4.371 Å $d_{(H)O-H}$: 0.975, 0.982, 0.985, 0.988, 1.011, 1.042 Å $\angle_{H-O-H}$: 103.3°, 105.4°,105.0° $\angle_{\text{plane through H-O-H and surface}}$: 23.0°, 60.7°, 45.2° (O in fcc hollow; H_2O atop on 2x2)				3730, 3598, 3525, 3448, 3033, 2467, 1656, 1619, 1583, 1201, 931, 732, 722, 624, 550, 468, 456, 442, 416, 377, 357, 335, 271, 237, 162, 143, 135, 103, 73, 45 cm^{-1}	
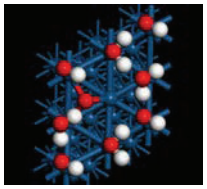	-	0.25	0.50	0.25	-3.194	0.281
	d_{Pt-O}: 2.025, 2.046, 2.082 Å $d_{Pt-O(H)}$: 2.128Å $d_{Pt-O(H,H)}$: 2.138, 3.465 Å $d_{(Pt)O-H}$: 0.978 Å $d_{(H)O-H}$: 0.978, 1.018, 1.023, 1.052 Å $\angle_{Pt-O-H}$: 100.9° $\angle_{H-O-H}$: 97.4°, 102.4° $\angle_{\text{plane through H-O-H and surface}}$: 26.9°, 35.4° (O in fcc hollow; H_2O, OH atop on 2x2)				3679, 3670, 2886, 2780, 2332, 1657, 1641, 1210, 1122, 1014, 861, 810, 615, 522, 500, 462, 442, 398, 372, 323, 303, 266, 255, 168, 123, 119, 86 cm^{-1}	
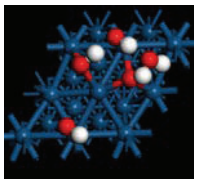	-	0.25	0.25	0.50	-2.373	0.216
	d_{Pt-O}: 1.990, 2.006, 2.073 Å $d_{Pt-O(H)}$: 2.068, 2.094, 2.159 Å $d_{(Pt)O-H}$: 1.015, 1.085 Å $d_{(H)O-H}$: 0.973, 0.995 Å $\angle_{Pt-O-H}$: 100.5°, 104.8°, 105.9° $\angle_{H-O-H}$: 104.3° $\angle_{\text{plane through H-O-H and surface}}$: 45.9° (O in fcc hollow; H_2O atop, OH bridge on 2x2)				3772, 3316, 2945, 1725, 1606, 1343, 1306, 1188, 930, 761, 515, 486, 469, 450, 428, 375, 364, 311, 284, 265, 170, 150, 136, 72 cm^{-1}	

[5] A structure containing $\theta_O = 0.33$, $\theta_{H_2O} = 0.67$ on (√3x√3)-Pt(111) optimises to a structure with $\theta_{H_2O} = 0.33$, $\theta_{OH} = 0.67$

Table A2.2 (cont.)

	Θ_*	Θ_O	Θ_{H2O}	Θ_{OH}	E_{ads}, eV	$\Delta_{ads}ZPE$, eV
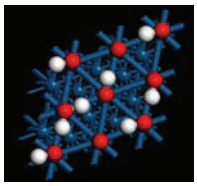	-	0.25	0.25	0.50	-3.148	0.217
	d_{Pt-O}: 1.861Å $d_{Pt-O(H)}$: 2.005, 2.006 Å $d_{Pt-O(H,H)}$: 2.081 Å $d_{(Pt)O-H}$: 0.994, 0.995 Å $d_{(H)O-H}$: 1.030, 1.031 Å $\angle_{Pt-O-H}$: 104.1°, 104.2° $\angle_{H-O-H}$: 113.9° $\angle_{\text{plane through H-O-H and surface}}$: 18.8° (O, H_2O and OH atop on 2x2)				3322, 3312, 2620, 2608, 1404, 1206, 1146, 1075, 1064, 810, 630, 564, 484, 479, 421, 414, 315, 291, 260, 245, 211, 193, 156, 152 cm^{-1}	
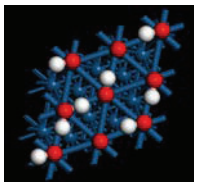	-	0.25	0.25	0.50	-3.179	0.234
	d_{Pt-O}: 1.880 Å $d_{Pt-O(H)}$: 1.990, 1.991 Å $d_{Pt-O(H,H)}$: 2.098 Å $d_{(Pt)O-H}$: 1.000, 1.005 Å $d_{(H)O-H}$: 1.018, 1.020 Å $\angle_{Pt-O-H}$: 103.9°, 104.3° $\angle_{H-O-H}$: 111.1° $\angle_{\text{plane through H-O-H and surface}}$: 17.2° (O, H_2O and OH atop on 2x2)				3198, 3098, 2842, 2810, 1418, 1175, 1141, 1124, 1065, 758, 686, 595, 526, 512, 495, 405, 325, 290, 250, 244, 226, 175, 156, 144 cm^{-1}	
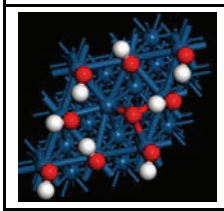	-	0.25	-	0.75	-1.971	0.216
	d_{Pt-O}: 1.942, 2.043, 2.066 Å $d_{Pt-O(H)}$: 1.954, 1.973, 2.074 Å $d_{(Pt)O-H}$: 0.982, 1.010, 1.013 Å $\angle_{Pt-O-H}$: 101.2°, 103.6°, 105.3° (O on fcc hollow, OH atop on 2x2)				3618, 3015, 2897, 1241, 1191, 988, 816, 749, 592, 534, 525, 433, 424, 403, 393, 348, 298, 212, 198, 166, 142 cm^{-1}	
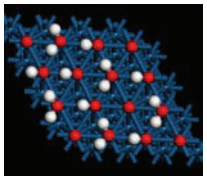	-	0.22	0.33	0.44	-3.273	0.283
	d_{Pt-O}: 1.843, 1.843 Å $d_{Pt-O(H)}$: 1.989, 2.052, 2.062, 2.062 Å $d_{Pt-O(H,H)}$: 2.134, 2.145, 2.148 Å $d_{(Pt)O-H}$: 0.985, 0.986, 0.986, 0.986 Å $d_{(Pt,H)O-H)}$:0.999, 1.000, 1.018, 1.018, 1.040, 1.042 Å $\angle_{Pt-O-H}$: 104.0°, 104.1°, 104.8°, 106.0° $\angle_{H-O-H}$: 103.4°, 104.8°, 108.0° $\angle_{\text{plane through H-O-H and surface}}$: 15.3°, 15.4°, 18.5° (O, H_2O, OH atop on 3x3)				3525, 3523, 3495, 3458, 3248, 3227, 2894, 2870, 2455, 2429, 1547, 1542, 1500, 1174, 1169, 1132, 1102, 1065, 1041, 1036, 1034, 986, 981, 818, 742, 675, 668, 660, 602, 595, 506, 497, 463, 386, 378, 359, 316, 300, 296, 254, 249, 246, 230, 223, 210, 187, 185, 167, 148, 145, 100 cm^{-1}	
	-	0.11	0.44	0.44	[6]	

[6] A structure containing $\theta_O = 0.11$, $\theta_{H_2O} = 0.44$ and $\theta_{OH} = 0.44$ on (3x3)-Pt(111) optimises to a structure with $\theta_{H_2O} = 0.33$, $\theta_{OH} = 0.67$

Table A2.2 (cont.)

	Θ_*	Θ_O	Θ_{H2O}	Θ_{OH}	E_{ads}, eV	$\Delta_{ads}ZPE$, eV
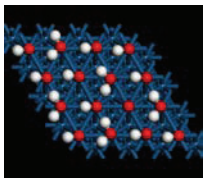	-	0.11	0.33	0.55	-3.519	0.307
	d_{Pt-O}: 1.841 Å $d_{Pt-O(H)}$: 1.998, 2.001, 2.060, 2.064, 2.072 Å $d_{Pt-O(H,H)}$: 2.135, 2.148, 2.151 Å $d_{(Pt)O-H}$: 0.983, 0.983, 0.984, 0.984, 0.986 Å $d_{(Pt,H)O-H)}$:0.996, 0.996, 1.022, 1.027, 1.043, 1.046 Å $\angle_{Pt-O-H}$: 104.5°, 104.7°, 104.8, 105.9°, 106.3° $\angle_{H-O-H}$: 107.0°, 107.2°, 110.7° $\angle_{plane\ through\ H-O-H\ and\ surface}$: 13.8°, 14.6°, 15.2° (O, H_2O, OH atop on 3x3)				3564, 2548, 3512, 2496, 2486, 3328, 3319, 2778, 2688, 2473, 2330, 1572, 1567, 1554, 1203, 1171, 1154, 1124, 1077, 1057, 1032, 1024, 1011, 1001, 988, 877, 720, 685, 651, 607, 555, 543, 506, 486, 473, 450, 433, 421, 414, 386, 380, 348, 332, 332, 317, 295, 293, 288, 277, 260, 256, 235, 228, 215, 203, 179, 151, 147, 144, 110 cm^{-1}	
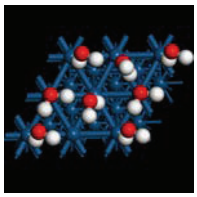	-	-	1.00	-	-2.733	0.389
	$d_{Pt-O(H,H)}$: 2.240 Å $d_{Pt-H(O)}$: 2.370, 2.377, 4.946 Å $d_{(Pt)O-H}$: 1.036, 1.036 Å $d_{(Pt)O-H}$: 0.972,0.988, 0.989, 0.990, 0.998, 1.007 Å $\angle_{H-O-H}$: 100.7°, 104.8°, 104.8°, 105.8° $\angle_{plane\ through\ H-O-H\ and\ surface}$: 26.3°, 60.7°, 61.4°, 89.8° (H_2O, OH on/above atop on 2x2)				3795, 3423, 3392, 3312, 3231, 3051, 2607, 2484, 1676, 1633, 1589, 1585, 1200, 1143, 1033, 847, 843, 739, 594, 560, 526, 470, 465, 398, 351, 338, 314, 245, 235, 171, 161, 155, 129, 109, 59, 49 cm^{-1}	
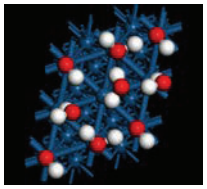	-	-	0.75	0.25	-3.118	0.312
	$d_{Pt-O(H)}$: 2.071 Å $d_{Pt-O(H,H)}$: 2.145, 3.222, 4.268 Å $d_{(Pt)O-H}$: 0.981 Å $d_{(H)O-H}$: 0.974, 0.991, 0.999, 1.014, 1.025, 1.094 Å $\angle_{Pt-O-H}$: 108.3° $\angle_{H-O-H}$: 106.6°, 102.0°,105.7° $\angle_{plane\ through\ H-O-H\ and\ surface}$: 26.1°, 81.4°, 52.8° ($H_2O$, OH on/above atop on 2x2)				3757, 3594, 3390, 3213, 3003, 2706, 1635, 1618, 1588, 1576, 1336, 1245, 1072, 929, 897, 736, 719, 554, 483, 469, 427, 396, 355, 327, 300, 251, 213, 169, 155, 139, 101, 78, 52 cm^{-1}	
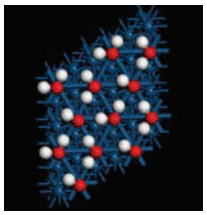	-	-	0.67	0.33	-3.241	0.398
	$d_{Pt-O(H)}$: 2.186 Å $d_{Pt-O(H,H)}$: 2.340, 2.362 Å $d_{(Pt)O-H}$: 0.983 Å $d_{(H)O-H}$: 0.991, 0.992, 0.996, 0.997 Å $\angle_{Pt-O-H}$: 105.2° $\angle_{H-O-H}$: 106.4°, 106.3° $\angle_{plane\ through\ H-O-H\ and\ surface}$: 10.6°, 11.1° ($H_2O$, OH on atop on √3x√3)				3569, 3370, 3332, 3241, 3186, 1639, 1611, 922, 897, 823, 796, 748, 733, 641, 520, 354, 338, 317, 288, 280, 191, 115, 110, 84 cm^{-1}	
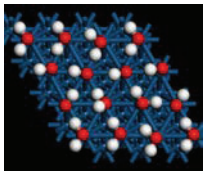	-	-	0.55	0.44	-3.604	0.332
	$d_{Pt-O(H)}$: 2.100, 2.102, 2.121, 2.138 Å $d_{Pt-O(H,H)}$: 2.153, 2.161, 2.183, 2.211, 3.386 Å $d_{(Pt)O-H}$: 0.972, 0.981, 0.982, 0.996 Å $d_{(H)O-H}$: 0.972, 0.990, 0.991, 0.998, 1.004, 1.010, 1.024, 1.029, 1.034, 1.042 Å $\angle_{Pt-O-H}$: 100.6°, 101.0°, 105.3°, 107.2° $\angle_{H-O-H}$: 102.9°, 105.5°, 110.0°, 110.4 °, 111.0° $\angle_{plane\ through\ H-O-H\ and\ surface}$: 6.3°, 12.9°, 14.5°, 60.8° (H_2O, OH on atop on 3x3)				3739, 3716, 3595, 3494, 3388, 3312, 3277, 3179, 3162, 2886, 2772, 2585, 2478, 2456, 1626, 1612, 1564, 1537, 1511, 1188, 1164, 1154, 1098, 1065, 1057, 1026, 1016, 1003, 956, 929, 922, 866, 857, 820, 804, 705, 689, 640, 569, 456, 423, 413, 402, 388, 384, 372, 348, 339, 328, 307, 299, 287, 277, 272, 259, 253, 250, 239, 221, 217, 205, 191, 177, 140, 135, 127, 111, 88, 40 cm^{-1}	

Table A2.2 (cont.)

	Θ_*	Θ_O	Θ_{H2O}	Θ_{OH}	E_{ads}, eV	$\Delta_{ads}ZPE$, eV
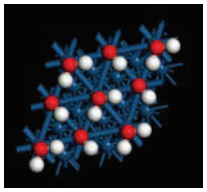	-	-	0.50	0.50	-4.039	0.383
	$d_{Pt-O(H)}$: 2.123, 2.124 Å $d_{Pt-O(H,H)}$: 2.173, 2.174 Å $d_{(Pt)O-H}$: 0.983, 0.983 Å $d_{(H)O-H}$: 1.011, 1.012, 1.012, 1.013 Å $\angle_{Pt-O-H}$: 105.0°, 104.9° $\angle_{H-O-H}$: 109.7°, 109. 7° $\angle_{plane\ through\ H-O-H\ and\ surface}$: 14.0°, 14.1° ($H_2O$, OH on atop on 2x2)				3553, 3502, 2999, 2978, 2909, 2892, 1566, 1537, 1086, 1073, 1069, 1025, 947, 893, 816, 796, 725, 687, 420, 394, 383, 340, 331, 300, 282, 269, 222, 176, 139, 137 cm^{-1}	
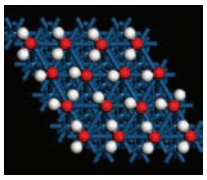	-	-	0.44	0.55	-3.846	0.357
	$d_{Pt-O(H)}$: 2.060, 2.069, 2.072, 2.077, 2.121 Å $d_{Pt-O(H,H)}$: 2.144, 2.145, 2.157, 2.237 Å $d_{(Pt)O-H}$: 0.976, 0.981, 0.989, 0.990, 0.991 Å $d_{(H)O-H}$: 0.989, 0.993, 1.009, 1.014, 1.023, 1.031, 1.031, 1.043 Å $\angle_{Pt-O-H}$: 102.5°, 103.3°, 104.2°, 105.2°, 106.6° $\angle_{H-O-H}$: 108.2°, 108.8°, 109.4°, 109.5° $\angle_{plane\ through\ H-O-H\ and\ surface}$: 14.2°, 14.2°, 15.8°, 17.4° (H_2O, OH on atop on 3x3)				3662, 3560, 3427, 3406, 3394, 3356, 3322, 3005, 2899, 2771, 2594, 2589, 2396, 1586, 1574, 1543, 1513, 1193, 1171, 1141, 1120, 1090, 1063, 1049, 1027, 1006, 1000, 983, 950, 925, 862, 845, 756, 743, 714, 665, 647, 571, 453, 447, 440, 426, 407, 399, 393, 379, 370, 366, 351, 332, 324, 306, 300, 291, 280, 268, 251, 239, 229, 208, 198, 171, 159, 144, 137, 130 cm^{-1}	
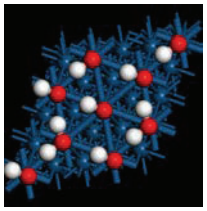	-	-	0.33	0.67	-3.782	0.336
	$d_{Pt-O(H)}$: 1.998, 2.078 Å $d_{Pt-O(H,H)}$: 2.155 Å $d_{(Pt)O-H}$: 0.981, 0.983 Å $d_{(H)O-H}$: 1.014, 1.015 Å $\angle_{Pt-O-H}$: 104.4°, 106.4° $\angle_{H-O-H}$: 106.4° $\angle_{plane\ through\ H-O-H\ and\ surface}$: 13.9° ($H_2O$, OH on atop on $\sqrt{3}x\sqrt{3}$)				3566, 3540, 2964, 2888, 1531, 1124, 1075, 1012, 991, 877, 514, 507, 426, 420, 380, 351, 300, 229, 211, 135, 134 cm^{-1}	
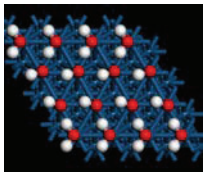	-	-	0.33	0.67	-4.049	0.330
	$d_{Pt-O(H)}$: 2.045, 2.045, 2.045, 2.046, 2.046, 2.046 Å $d_{Pt-O(H,H)}$: 2.112, 2.112, 2.112 Å $d_{(Pt)O-H}$: 0.986, 0.986, 0.986, 0.987, 0.987, 0.987 Å $d_{(Pt,H)O-H)}$:1.030, 1.031, 1.031, 1.032, 1.032, 1.032 Å $\angle_{Pt-O-H}$: 104.2°, 104.2°, 104.2°, 104.3°, 104.3°, 104.3° $\angle_{H-O-H}$: 110.6°, 110.6°, 110.7° $\angle_{plane\ through\ H-O-H\ and\ surface}$: 14.9°, 14.9°, 14.9° ($H_2O$, OH on atop on 3x3)				3525, 3523, 3495, 3458, 3248, 3227, 2894, 2870, 2455, 2429, 1547, 1542, 1500, 1174, 1169, 1132, 1102, 1065, 1041, 1036, 1034, 986, 981, 818, 742, 675, 668, 660, 602, 595, 506, 497, 463, 444, 437, 435, 386, 378, 359, 316, 300, 296, 294, 276, 265, 254, 249, 246, 230, 223, 210, 187, 185, 167, 148, 145, 100 cm^{-1}	
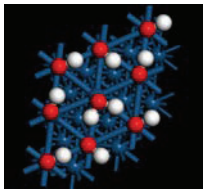	-	-	0.25	0.75	-3.927	0.304
	$d_{Pt-O(H)}$: 2.008, 2.028, 2.036 Å $d_{Pt-O(H,H)}$: 2.126 Å $d_{(Pt)O-H}$: 1.004, 1.005, 1.016 Å $d_{(H)O-H}$: 1.023, 1.033 Å $\angle_{Pt-O-H}$: 101.9°, 102.9°, $\angle_{H-O-H}$: 97.6° $\angle_{plane\ through\ H-O-H\ and\ surface}$: 9.9° ($H_2O$, OH on atop on 2x2)				3125, 3086, 2855, 2817, 2612, 1579, 1244, 1194, 1172, 1137, 1107, 1065, 865, 718, 544, 502, 493, 462, 426, 377, 319, 308, 253, 237, 182, 153, 151cm^{-1}	

Table A2.2 (cont.)

	Θ_*	Θ_O	Θ_{H2O}	Θ_{OH}	E_{ads}, eV	Δ_{ads}ZPE, eV
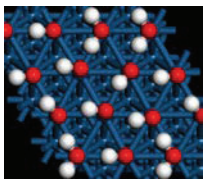	-	-	0.22	0.77	-3.800	0.291
	$d_{Pt-O(H)}$: 1.982, 2.005, 2.008, 2.024, 2.024, 2.025, 2.026 Å $d_{Pt-O(H,H)}$: 2.079, 2.146 Å $d_{(Pt)O-H}$: 0.987, 0.990, 0.991, 0.996, 0.997, 0.997, 0.997 Å $d_{(H)O-H}$: 1.021, 1.021, 1.047, 1.051 Å $\angle_{Pt-O-H}$: 102.7°, 102.9°, 103.1°, 103.4°, 104.3°, 104.4°, 107.1° $\angle_{H-O-H}$: 109.1°, 112.0° $\angle_{\text{plane through H-O-H and surface}}$: 9.7°, 15.3° ($H_2O$, OH on atop on 3x3)				3518, 3462, 3435, 3329, 3298, 3287, 3204, 2863, 2716, 2342, 2211, 1540, 1493, 1327, 1248, 1176, 1157, 1144, 1125, 1120, 1116, 1103, 1099, 1093, 957, 838, 714, 697, 632, 564, 543, 531, 488, 477, 473, 470, 461, 450, 450, 435, 429, 375, 333, 316, 314, 303, 291, 289, 279, 276, 261, 245, 217, 213, 201, 187, 179, 159, 144, 26 cm^{-1}	
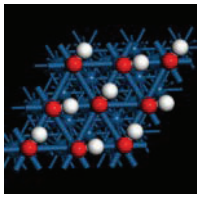	-	-	-	1.00	-3.369	0.250
	$d_{Pt-O(H)}$: 1.975, 1.976, 1.976, 1.976 Å $d_{(Pt)O-H}$: 1.003, 1.003, 1.003, 1.004 Å $\angle_{Pt-O-H}$: 104.4°, 104.4°, 104.4°, 104.4° (H_2O, OH on atop on 2x2)				3141, 3137, 3133, 3107, 1209, 1164, 1164, 1154, 747, 744, 717, 543, 512, 512, 511, 493, 312, 304, 302, 243, 224, 223, 166, 165 cm^{-1}	

Table A2.3: Geometric characteristics, energetics, and normal modes of surface structures of proposed intermediates in the aerobic oxidation of methane on Pt(111)

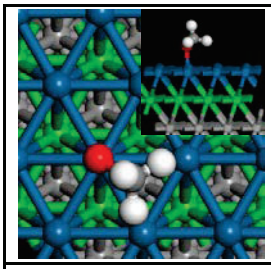	Methoxy $d_{Pt-O(C)}$: 1.990 Å $d_{(Pt)O-C}$: 1.404 Å $d_{(O)C-H}$: 1.104 Å, 1.112 Å, 1.114 Å $\angle_{Pt-O-C}$: 116.5° $\angle_{O-C-H}$: 106.8°, 112.3°, 112.3°	E_{ads}, eV	-2.154
		$\Delta_{ads}ZPE$, eV	0.084
		2975, 2821, 2796, 1389, 1373, 1362, 1084, 1079, 1004, 471, 259, 235, 131, 81, 47 cm^{-1}	
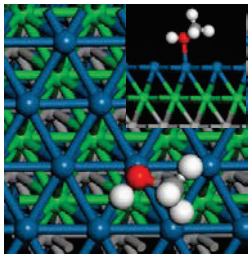	Methanol d_{Pt-O}: 2.290 Å d_{O-H}: 0.982 Å d_{O-C}: 1.452 Å d_{C-H}: 1.095, 1.099, 1.101 Å $\angle_{Pt-O-H}$: 96.1° $\angle_{Pt-O-C}$: 117.3° $\angle_{H-O-C}$: 109.3° $\angle_{O-C-H}$: 106.2°, 108.8°, 110.9°	E_{ads}, eV	-1.702
		$\Delta_{ads}ZPE$, eV	0.185
		3583, 3087, 3035, 2976, 1440, 1430, 1401, 1297, 1123, 1058, 947, 576, 272, 215, 175, 140, 115, 58 cm^{-1}	
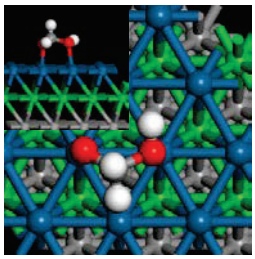	Hydroxy-methoxy $d_{Pt-O(C)}$: 2.048 Å $d_{Pt-O(C,H)}$: 2.238 Å $d_{(Pt)O-H}$: 0.982 Å $d_{(Pt,H)O-C}$: 1.499 Å $d_{(Pt)O-C}$: 1.351 Å d_{C-H}: 1.105 Å, 1.114 Å $\angle_{Pt-O(H)-C}$: 111.7° $\angle_{Pt-O-C}$: 115.9° $\angle_{Pt-O-H}$: 101.1° $\angle_{O-C-O}$: 113.9° $\angle_{O-C-H}$: 101.6°, 105.7° $\angle_{O(H)-C-H}$: 108.8°, 115.1°	E_{ads}, eV	-4.388
		$\Delta_{ads}ZPE$, eV	0.197
		3602, 2958, 2790, 1401, 1329, 1248, 1172, 1106, 987, 742, 603, 487, 408, 303, 248, 138, 104, 84 cm^{-1}	
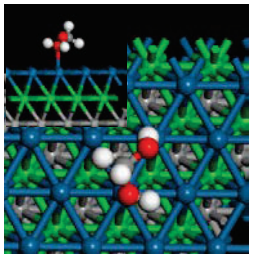	Methanediol $d_{Pt-O(C)}$: 2.264 Å $d_{(Pt,H)-O-C}$: 1.475 Å $d_{(H)-O-C}$: 1.379 Å $d_{(Pt)O-H}$: 0.981 Å d_{O-H}: 0.996 Å d_{C-H}: 1.099 Å, 1.104 Å $\angle_{Pt-O(H)-C}$:119.3° $\angle_{Pt-O-H}$: 104.4° $\angle_{O-C-O}$: 112.9° $\angle_{O-C-H}$: 103.3°, 106.6° $\angle_{C-O-H}$: 108.8°	E_{ads}, eV	-3.967
		$\Delta_{ads}ZPE$, eV	0.250
		3627, 3268, 3034, 2937, 1441, 1373, 1359, 1269, 1173, 1068, 986, 835, 579, 524, 439, 265, 187, 149, 124, 92, 26 cm^{-1}	

Table A2.4: Geometric characteristics, energetics, and normal modes of surface structures of proposed intermediates in the aerobic oxidation of methane on Pt(111) covered with O, OH and H_2O

Initial structure 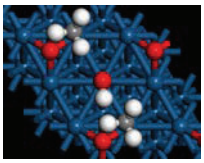 Θ_{CH3} = 0.25 Θ_{O} = 0.25 Θ_{OH} = 0.25	Final structure 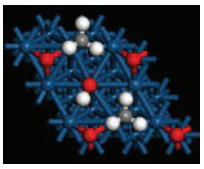 Θ_{CH3} = 0.25 Θ_{O} = 0.25 Θ_{OH} = 0.25	d_{Pt-O}: 2.043, 2.052, 2.058 Å $d_{Pt-O(H)}$: 2.007 Å d_{O-H}: 0.978 Å $d_{Pt-C(H)}$: 2.005 Å d_{C-H}: 1.093, 1.093, 1.094 Å $\angle_{Pt-O-H}$: 105.9° $\angle_{Pt-C-H}$: 102.7°, 108.3°, 108.4°	E_{ads}, eV	-1.551
			$\Delta_{ads}ZPE$, eV	0.132
			3669, 3126, 3112, 2993, 1404, 1368, 1200, 953, 845, 825, 505, 499, 471, 407, 365, 268, 226, 193, 168, 141, 102 cm^{-1}	
Initial structure 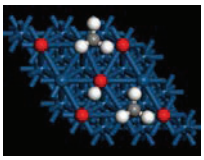 Θ_{CH3} = 0.25 Θ_{O} = 0.25 Θ_{OH} = 0.25	Final structure 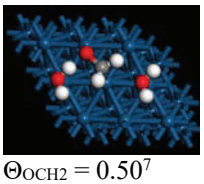 Θ_{OCH2} = 0.50[7] Θ_{H2O} = 0.25	$d_{Pt-O(C)}$: 2.175 Å $d_{Pt-O(H)}$: 2.221 Å d_{O-H}: 0.975, 1.044 Å d_{O-C}: 1.379 Å d_{C-H}: 1.101, 1.106 Å $\angle_{Pt-O-C}$: 103.8° $\angle_{O-C-H}$: 112.7°, 113.3° $\angle_{H-O-H}$: 111.9° $\angle_{plane\ through\ H-O-H\ and\ surface}$: 22.9°	E_{ads}, eV	-3.100
			$\Delta_{ads}ZPE$, eV	0.171
			3711, 2979, 2902, 2377, 1559, 1399, 1184, 1130, 1106, 956, 725, 679, 546, 511, 356, 326, 276, 251, 202, 166, 139 cm^{-1}	
Initial structure 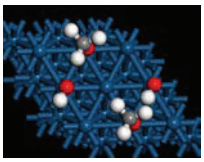 Θ_{OCH3} = 0.25 Θ_{OH} = 0.25	Final structure 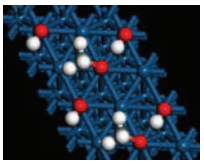 Θ_{OCH3} = 0.25 Θ_{OH} = 0.25	$d_{Pt-O(H)}$: 1.980 Å $d_{Pt-O(C)}$: 2.028 Å d_{O-H}: 1.054 Å d_{C-H}: 1.104, 1.111, 1.118 Å $\angle_{Pt-O-H}$: 103.1° $\angle_{Pt-O-C}$: 115.1° $\angle_{Pt-O-C}$: 107.4° 111.5°, 112.7°	E_{ads}, eV	-2.047
			$\Delta_{ads}ZPE$, eV	0.156
			3140, 2976, 2846, 2734, 1393, 1373, 1344, 1172, 1089, 1078, 997, 722, 539, 445, 325, 283, 243, 194, 135, 115, 96 cm^{-1}	
Initial structure 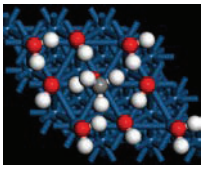 Θ_{OCH3} = 0.25 Θ_{H2O} = 0.50 Θ_{OH} = 0.25	Final structure 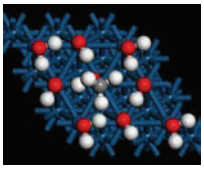 Θ_{HOCH3} = 0.25 Θ_{H2O} = 0.25 Θ_{OH} = 0.50	$d_{Pt-O(C)}$: 2.838 Å $d_{(Pt)O-C}$: 1.430 Å d_{O-H}: 1.022 Å d_{C-H}: 1.097, 1.100, 1.103 Å $\angle_{Pt-O-C}$: 146.5° $\angle_{Pt-O-H}$: 89.0° $\angle_{O-C-H}$: 108.0°, 109.1°, 110.8° $d_{Pt-O(H)}$: 2.061, 2.064 Å $d_{Pt-O(H,H)}$: 2.139 Å $d_{(Pt)O-H}$: 1.006, 1.020 Å $d_{(Pt,H)O-H}$: 1.032, 1.036 Å $\angle_{Pt-O-H}$: 101.8°, 104.9° $\angle_{H-O-H}$: 96.7° $\angle_{plane\ through\ H-O-H\ and\ surface}$: 6.9°	E_{ads}, eV	-3.761
			$\Delta_{ads}ZPE$, eV	0.411
			3076, 3058, 3008, 2949, 2827, 2698, 2676, 2499, 1610, 1474, 1445, 1440, 1424, 1256, 1235, 1181, 1157, 1136, 1126, 1102, 1023, 931, 838, 693, 487, 459, 438, 384, 341, 317, 277, 231, 207, 169, 148, 110, 90, 78, 68 cm^{-1}	

[7] Di-σ surface species

Table A2.4 (cont.):

<table>
<tr>
<td>Initial structure
 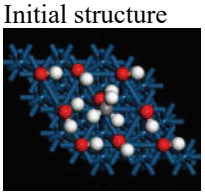
Θ_{HOCH3} = 0.25
Θ_{H2O} = 0.25
Θ_{OH} = 0.50</td>
<td>Final structure
 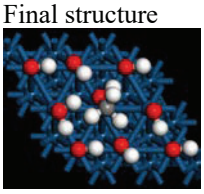
Θ_{HOCH3} = 0.25
Θ_{H2O} = 0.25
Θ_{OH} = 0.50</td>
<td>$d_{Pt\text{-}O(C)}$: 3.185 Å
$d_{(Pt)O\text{-}C}$: 1.430 Å
$d_{O\text{-}H}$: 1.025 Å
$d_{C\text{-}H}$: 1.098, 1.099, 1.102 Å
$\angle_{Pt\text{-}O\text{-}C}$: 137.7°
$\angle_{Pt\text{-}O\text{-}H}$: 73.3°
$\angle_{O\text{-}C\text{-}H}$: 108.0°, 110.0°, 110.9°
$d_{Pt\text{-}O(H)}$: 2.041, 2.056 Å
$d_{Pt\text{-}O(H,H)}$: 2.148 Å
$d_{(Pt)O\text{-}H}$: 0.987, 1.030 Å
$d_{(Pt,H)O\text{-}H}$: 1.000, 1.046 Å
$\angle_{Pt\text{-}O\text{-}H}$: 99.9°, 110.4°
$\angle_{H\text{-}O\text{-}H}$: 98.8°
$\angle_{\text{plane through H-O-H and surface}}$: 14.4°</td>
<td>E_{ads}, eV</td><td>-3.804</td>
</tr>
<tr>
<td colspan="2"></td>
<td></td>
<td>Δ_{ads}ZPE, eV</td><td>0.406</td>
</tr>
<tr>
<td colspan="2"></td>
<td></td>
<td colspan="2">3437, 3243, 3052, 3023, 2957, 2734, 2556, 2366, 1620, 1507, 1453, 1440,
1415, 1276, 1192, 1143, 1135, 1073, 1036, 1004, 973, 924, 776, 528, 474, 454, 435, 417, 337, 295, 266, 217, 168, 149, 134, 109, 103, 90, 74 cm^{-1}</td>
</tr>
<tr>
<td>Initial structure
 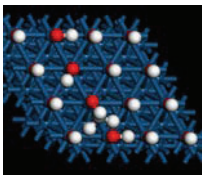
Θ_{OCH3} = 0.11
Θ_{OH} = 0.88</td>
<td>Final structure
 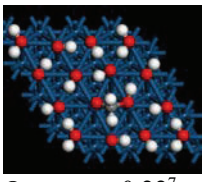
Θ_{OCH2OH} = 0.22[7]
Θ_{H2O} = 0.11
Θ_{OH} = 0.66</td>
<td>$d_{Pt\text{-}O(C)}$: 2.039 Å
$d_{Pt\text{-}O(C,H)}$: 2.180 Å
$d_{(Pt)O\text{-}C}$: 1.371 Å
$d_{(Pt,H)O\text{-}C}$: 1.471 Å
$d_{O\text{-}H}$: 1.013 Å
$d_{C\text{-}H}$: 1.098, 1.104 Å
$\angle_{Pt\text{-}O\text{-}C}$: 124.8°
$\angle_{Pt\text{-}O(H)\text{-}C}$: 116.1°
$\angle_{Pt\text{-}O\text{-}H}$: 102.2°
$\angle_{O\text{-}C\text{-}O}$: 115.7°
$d_{Pt\text{-}O(H)}$: 1.979, 1.981, 1.987, 2.020, 2.045, 2.055 Å
$d_{Pt\text{-}O(H,H)}$: 2.097 Å
$d_{(Pt)O\text{-}H}$: 0.984, 0.994, 1.000, 1.003, 1.008, 1.015 Å
$d_{(Pt,H)O\text{-}H}$: 1.001, 1.050 Å
$\angle_{Pt\text{-}O\text{-}H}$: 100.0°, 100.6°,101.5°, 103.1°, 104.1°, 105.5°
$\angle_{H\text{-}O\text{-}H}$: 111.4°
$\angle_{\text{plane through H-O-H and surface}}$: 19.5°</td>
<td>E_{ads}, eV</td><td>-4.740</td>
</tr>
<tr>
<td colspan="2"></td>
<td></td>
<td>Δ_{ads}ZPE, eV</td><td>0.320</td>
</tr>
<tr>
<td colspan="2"></td>
<td></td>
<td colspan="2">3625, 3374, 3268, 3239, 3205, 3021, 2947, 2912, 2894, 2817, 2222, 1540, 1406, 1352, 1308, 1260, 1205, 1197, 1188, 1175, 1165, 1082, 1062, 1052, 1048, 1026, 959, 850, 831, 800, 774, 712, 642, 607, 561, 515, 507, 504, 477, 445, 434, 425, 410, 379, 375, 366, 334, 328, 312, 294, 276, 269, 263, 258, 254, 227, 202, 193, 184, 172, 152, 138, 129 cm^{-1}</td>
</tr>
<tr>
<td>Initial structure
 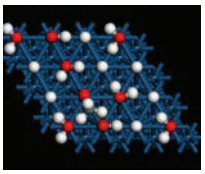
Θ_{OCH3} = 0.11
Θ_{H2O} = 0.11
Θ_{OH} = 0.77</td>
<td>Final structure
 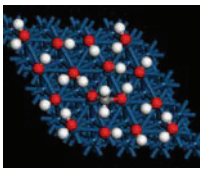
Θ_{OCH2OH} = 0.22[7]
Θ_{H2O} = 0.22
Θ_{OH} = 0.55</td>
<td>$d_{Pt\text{-}O(C)}$: 2.078 Å
$d_{Pt\text{-}O(C,H)}$: 2.184 Å
$d_{(Pt)O\text{-}C}$: 1.382 Å
$d_{(Pt,H)O\text{-}C}$: 1.474 Å
$d_{O\text{-}H}$: 1.013 Å
$d_{C\text{-}H}$: 1.094, 1.101 Å
$\angle_{Pt\text{-}O\text{-}C}$: 126.5°
$\angle_{Pt\text{-}O(H)\text{-}C}$: 119.4°
$\angle_{Pt\text{-}O\text{-}H}$: 102.8°
$\angle_{O\text{-}C\text{-}O}$: 115.3°
$d_{Pt\text{-}O(H)}$: 1.992, 2.036, 2.043, 2.055, 2.066 Å
$d_{Pt\text{-}O(H,H)}$: 2.105, 2.126 Å
$d_{(Pt)O\text{-}H}$: 0.993, 0.997, 1.010, 1.011, 1.016 Å
$d_{(Pt,H)O\text{-}H}$: 1.003, 1.003, 1.050, 1.056 Å
$\angle_{Pt\text{-}O\text{-}H}$: 100.1°, 101.1°, 101.8°, 102.1°, 103.8°
$\angle_{H\text{-}O\text{-}H}$: 101.8°, 106.9°
$\angle_{\text{plane through H-O-H and surface}}$: 12.8°, 15.7°</td>
<td>E_{ads}, eV</td><td>-4.866</td>
</tr>
<tr>
<td colspan="2"></td>
<td></td>
<td>Δ_{ads}ZPE, eV</td><td>0.355</td>
</tr>
<tr>
<td colspan="2"></td>
<td></td>
<td colspan="2">3497, 3411, 3267, 3181, 3104, 3087, 2951, 2935, 2587, 2771, 2363, 2113,
1624, 1566, 1412, 1379, 1323, 1270, 1260, 1239, 1227, 1199, 1161, 1111,
1096, 1084, 1072, 1058, 1036, 980, 966, 927, 865,
803, 760, 698, 626, 576, 546, 504, 464, 449, 440, 425, 408, 405, 378, 357,
354, 332, 312, 308, 306, 292, 283, 273, 264, 244, 223, 203, 191, 183, 180,
143, 130, 117 cm^{-1}</td>
</tr>
</table>

Table A2.4 (cont.)

Initial structure 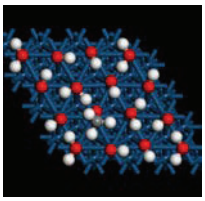 Θ_{OCH3} = 0.11 Θ_{H2O} = 0.33 Θ_{OH} = 0.55	Final structure 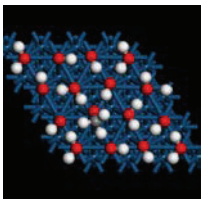 Θ_{OCH3} = 0.11 Θ_{H2O} = 0.33 Θ_{OH} = 0.55	$d_{Pt-O(C)}$: 2.133 Å $d_{(Pt)O-C}$: 1.431 Å d_{C-H}: 1.101, 1.01, 1.103 Å $\angle_{Pt-O-C}$: 132.3° $\angle_{O-C-H}$: 108.0°, 110.1°, 110.4° $d_{Pt-O(H)}$: 1.973, 2.040, 2.056 Å 2.075, 2.077 Å $d_{Pt-O(H,H)}$: 2.080, 2.106, 1.141 Å $d_{(Pt)O-H}$: 0.985, 1.000, 1.001, 1.003, 1.005 Å $d_{(Pt,H)O-H}$: 0.983, 1.024, 1.033, 1.038, 1.047, 1.055 Å $\angle_{Pt-O-H}$: 100.5°, 101.0°, 101.3° 102.6°, 103.6° $\angle_{H-O-H}$: 111.4°, 111.7°, 112.4° $\angle_{plane\ through\ H-O-H\ and\ surface}$: 17.0°, 17.2°, 25.9°	E_{ads}, eV	-4.198
			$\Delta_{ads}ZPE$, eV	0.586
			3596, 3449, 3274, 3219, 3111, 3065, 3034, 2989, 2913, 2781, 2645, 2418, 2258, 2240, 1562, 1527, 1487, 1452, 1432, 1386, 1296, 1228, 1201, 1199, 1186, 1159, 1152, 1139, 1132, 1124, 1078, 1047, 1005, 992, 948, 925, 867, 793, 745, 659, 576, 557, 514, 485, 453, 447, 431, 416, 408, 401, 374, 362, 358, 348, 340, 310, 306, 297, 276, 269, 256, 246, 235, 231, 224, 214, 187, 178, 172, 147, 128, 119 cm^{-1}	
Initial structure 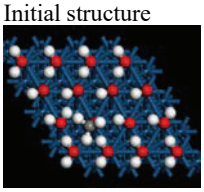 Θ_{OCH3} = 0.11 Θ_{H2O} = 0.44 Θ_{OH} = 0.44	Final structure 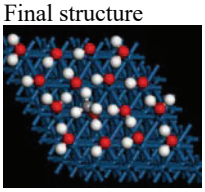 Θ_{HOCH3} = 0.11 Θ_{H2O} = 0.33 Θ_{OH} = 0.55	$d_{Pt-O(C,H)}$: 2.969 Å $d_{(Pt)O-C}$: 1.432 Å d_{O-H}: 1.017 Å d_{C-H}: 1.097, 1.100, 1.102 Å $d_{Pt-O(H)}$: 2.050, 2.059, 2.068, 2.071, 2.094 Å $d_{Pt-O(H,H)}$:2.089, 2.137, 2.163 Å $d_{(Pt)O-H}$: 0.985, 0.990, 0.990, 0.998, 1.011 Å $d_{(Pt,H)O-H}$: 0.990, 1.018, 1.028, 1.055, 1.058, 1.075 Å $\angle_{Pt-O-H}$: 101.6°, 102.0°,102.2°, 102.3°, 104.0° $\angle_{H-O-H}$: 97.6°, 107.5°, 111.3° $\angle_{plane\ through\ H-O-H\ and\ surface}$: 9.6°, 14.5°, 26.9°	E_{ads}, eV	-4.407
			$\Delta_{ads}ZPE$, eV	0.381
			3696, 3508, 3417, 3396, 3295, 3132, 3087, 3064, 3037, 2966, 2861, 2653, 2593, 2573, 2312, 1579, 1533, 1515, 1480, 1452, 1445, 1422, 1224, 1223, 1211, 1143, 1142, 1140, 1114, 1108, 1085, 1074, 1054, 1046, 1019, 1005, 933, 899, 788, 775, 756, 704, 658, 528, 455, 452, 440, 430, 419, 411, 402, 396, 354, 352, 335. 330, 315, 301, 289, 277, 274, 262, 240, 215, 214, 203, 200, 186, 135, 132, 126, 113, 94, 76, 29 cm^{-1}	
Initial structure 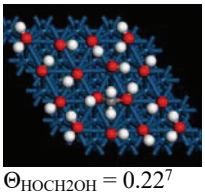 $\Theta_{HOCH2OH}$ = 0.22[7] Θ_{H2O} = 0.11 Θ_{OH} = 0.66	Final structure 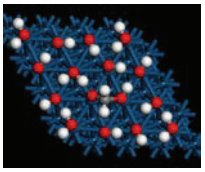 Θ_{OCH2OH} = 0.22[7] Θ_{H2O} = 0.22 Θ_{OH} = 0.55	$d_{Pt-O(C)}$: 2.078 Å $d_{Pt-O(C,H)}$: 2.184 Å $d_{(Pt)O-C}$: 1.382 Å $d_{(Pt,H)O-C}$: 1.474 Å d_{O-H}: 1.013 Å d_{C-H}: 1.094, 1.101 Å $\angle_{Pt-O-C}$: 126.5° $\angle_{Pt-O(H)-C}$: 119.4° $\angle_{Pt-O-H}$: 102.8° $\angle_{O-C-O}$: 115.3° $d_{Pt-O(H)}$: 1.992, 2.036, 2.043, 2.055, 2.066 Å $d_{Pt-O(H,H)}$: 2.105, 2.126 Å $d_{(Pt)O-H}$: 0.993, 0.997, 1.010, 1.011, 1.016 Å $d_{(Pt,H)O-H}$: 1.003, 1.003, 1.050, 1.056 Å $\angle_{Pt-O-H}$: 100.1°, 101.1°, 101.8°, 102.1°, 103.8° $\angle_{H-O-H}$: 101.8°, 106.9° $\angle_{plane\ through\ H-O-H\ and\ surface}$: 12.8°, 15.7°	E_{ads}, eV	-4.866
			$\Delta_{ads}ZPE$, eV	0.355[8]

[8] Not determined as structure is identical to structure starting from Θ_{OCH3} = 0.11, Θ_{H2O} = 0.11 and Θ_{OH} = 0.77

References

[A1] G. Kresse, J. Hafner: Ab initio molecular dynamics for liquid metals. *Physical Review B Condensed Matter* **1993**, *47*, 558-561.

[A2] G. Kresse, J. Furthmüller: Efficient iterative schemes for ab initio total-energy calculations using a plane-wave basis set. *Physical Review B* **1996**, *54*, 11169–11186.

[A3] G. Kresse, D. Joubert: From ultrasoft pseudopotentials to the projector augmented-wave method. *Physical Review B* **1999**, *59*, 1758–1775.

[A4] J.P. Perdew, K. Burke, M. Ernzerhof: Generalized gradient approximation made simple. *Physical Review Letters* **1996**, *77* (1996), 3865-3868.

[A5] S. Grimme, J. Antony, S. Ehrlich, S. Krieg: A consistent and accurate *ab initio* parametrization of density functional dispersion correction (DFT-D) for the 94 elements H-Pu. *Journal of Chemical Physics* **2010**, *132*, 154104.

[A6] S. Grimme, S. Ehrlich, L. Goerigk: Effect of the damping function in dispersion corrected density functional theory. *Journal of Computational Chemistry* **2011**, *32*, 1456-1465.

[A7] M. Methfessel, A.T. Paxton: High precision sampling for Brillouin zone integration in metals. *Physical Review B.* **1989**, *40*, 3616-3621.

[A8] H.J. Monkhorst, J.D. Pack: Special points for Brillouin-zone integration. *Physical Review B* **1976**, *13*, 5188-5192.

[A9] W.M. Haynes, D.R. Lide, Eds.: *Handbook of Chemistry and Physics*. 91st ed., CRC Press, Boca Raton, **2010**.

[A10] NIST Chemistry Webbook (https://webbook.nist.gov/cgi/cbook.cgi)

[A11] D.R. Kent IV, S.L. Widicus, G.A. Blake, W.A. Goddard III: A theoretical study of the conversion of gas phase methanediol to formaldehyde. *Journal of Chemical Physics* **2003**, *119*, 5117-5120.

[A12] J. Rossmeisl, A. Logadottir, J.K. Nørskov: Electrolysis of water on (oxidized) metal surfaces. *Chemical Physics* **2005**, *319*, 178–184.

[A13] E.M. Karp, C.T. Campbell, F. Studt, F. Abild-Pedersen, J.K. Nørskov: Energetics of oxygen adatoms, hydroxyl species and water dissociation on Pt(111). *J. Phys. Chem. C* **2012**, *116(49)*, 25772-25775.

APPENDIX III: SUPPLEMENTAL MATERIAL TO CHAPTER V

Section I: Catalyst Synthesis

Section II: Characterisation

Section III: Catalytic activity measurements

SECTION I: CATALYST SYNTHESIS

In a typical preparation, an aqueous solution (250 mL) of chloroplatinic acid hexahydrate ($H_2PtCl_6 \cdot 6H_2O$, Merck; 0.002 mol/dm^3) was contacted with 9.9 g of either titania (TiO_2, Degussa P25 Aeroxide, 47 m^2/g, Evonik or TiO_2, rutile phase, Merck, 25 m^2/g), alumina (γ-Al_2O_3, Alpha-Aesar, 80-120 m^2/g) or carbon black (Vulcan XC-72R, FuelCellStore, 250 m^2/g) at room temperature. Excess water was slowly evaporated at 60°C and 72 mbar in a rotary evaporator. The solid was dried overnight at 120°C in an oven under static air. The catalyst was calcined at 400°C in air (flow rate: 48 ml$_n$/min/g) for 5 hours and subsequently reduced in hydrogen (48 ml$_n$/min/g) at 400°C for 5 hours.

SECTION II: CATALYST CHARACTERISATION

The platinum loading on the oxide supported catalysts (Pt/TiO_2-Rutile, Pt/TiO_2-P25, Pt/Al_2O_3) was determined using inductively coupled plasma-optical emission spectroscopy (ICP-OES). The catalysts were digested in aqua regia using a Mars 5 microwave digestion unit and analysed on a Varian ES 730 inductively coupled plasma-optical emission spectrometer. The metal loading on the carbon supported catalyst (Pt/C) was determined using thermogravimetric analysis which was conducted on a SDT650 Thermal Analysis Instrument. For the analysis, the Pt/C sample was heated to 900°C under a flow of air (10 ml$_n$/min), at a heating rate of 10°C/min whilst monitoring the weight loss.

The phases present in the catalysts were determined using powder X-ray diffraction (XRD) on a Bruker D8 ADVANCE diffractometer (Co-Kα radiation: λ = 1.789 Å, 35 kV, 40mA). The scan was taken from 2θ = 20° to 100°. The morphology and diameter of the supported platinum nanoparticles was determined by transmission electron microscopy imaging on a FEI Tecnai G2 T20 TEM, operating at 200 kV. The samples were first dispersed in ethanol via sonication at room temperature, then drop-casted on carbon-coated copper grids. The images were analysed using ImageJ® software to determine the particle size distribution of the platinum nanoparticles.

The BET-surface area of the samples was determined using nitrogen adsorption at -196°C on a Micrometrics Tristar II 3020, after degassing the sample at 200°C for 3hrs. The available active metal surface of the freshly prepared and recovered catalysts was determined through

the chemisorption of hydrogen. The catalysts were first degassed under vacuum overnight at 250°C, and subsequently analysed on a Micromeritics ASAP 2020 Chemisorption Analyser. The hydrogen uptake was determined at 80°C in the pressure range of 0.1–600 mmHg. The platinum dispersion was determined assuming an adsorption stoichiometry of $H:Pt_{surface}=1$.

The Brønsted acidity of the catalysts was determined using temperature programmed desorption (TPD) of isopropyl amine, which was performed on an Autochem II (Micromeritics Corporation, USA) coupled to a Cirrus mass spectrometer (MKS, USA) to determine the effluent gas composition. Prior to adsorption of isopropyl amine (99% purity, GC grade, Merck), the catalyst (ca. 0.1 g) was heated to 200°C and kept at this temperature for 15min under hydrogen flow (50 ml_n/min). Thereafter, it was kept at 200°C for 1 hr under helium flow (50ml_n/min). The catalyst was then cooled to 100°C and isopropyl amine was pulsed over the catalyst to saturate its surface. The desorption experiment was performed in a flow of helium (25 ml_n/min) from 100°C to 800°C with mass spectrometry used to analyse the gases formed. Isopropyl amine reacts with Brønsted acid sites to produce propylene and ammonia gas and the desorption of propylene indicates the strength and quantity of the Brønsted acid site(s).[302, 303] The same instrument and methodology were used for the temperature programmed desorption of CO_2 (pulse adsorption of CO_2 at 40^{o}C), which was performed to characterise the Brønsted basicity of the catalysts.

The catalysts were also characterized using Fourier transform infrared spectroscopy (FTIR) to determine the presence of organic deposits on the catalyst. The measurement was performed on a Perkin Elmer Spectrum 100 FTIR Spectrometer in the ATR mode in the range 650-4000 cm^{-1} with a resolution of 1 cm^{-1}.

The organic species on the recovered catalysts were further analysed using temperature programmed decomposition/desorption by flowing helium over the catalyst whilst heating from 100 to 850°C on the Autochem II (Micromeritics Corporation, USA). The composition of the effluent was monitored with a Cirrus mass spectrometer (MKS, USA).

The TGA-DSC profiles of the fresh and recovered Pt/C catalyst is presented in Fig. A3.1.

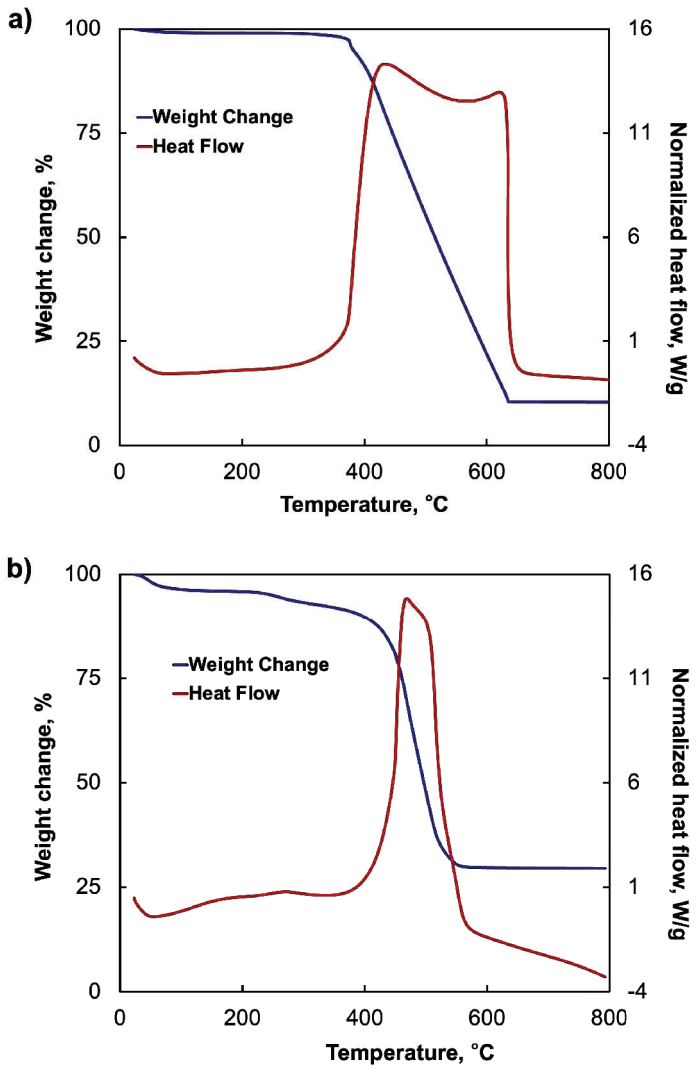

Figure A3.1: Thermogravimetric analysis to determine the Pt-loading in the freshly reduced Pt/C catalyst (a) and recovered Pt/C (b) catalyst.

SECTION III: CATALYST ACTIVITY TESTS

The catalysts (ca. 1.5 g) were pelletized and crushed to form particles (d_p = 150-200 μm) and loaded into a quartz reactor that was then placed in the trickle bed reactor stainless steel casing [262]. The pre-reduced catalyst was pre-conditioned at 220°C at atmospheric pressure in helium (100 ml_n/min) for 8 hours. The reactor was subsequently pressurized to 30 bar. Thereafter, methane, oxygen and helium were simultaneously introduced using Brooks thermal mass flow controllers. De-ionized water was introduced via a high-performance liquid chromatography (HPLC)-pump. The partial pressure of methane and oxygen at the reactor inlet were maintained at 0.5 and 1.5 bar respectively by keeping their volumetric flow rates constant. The space velocity was kept constant at 3.23 CH_4/g/hr. During the catalytic measurements, the molar feed ratio of water to methane was varied and the helium flow rate was adjusted to compensate for the steam flow rate (assuming vapor-liquid equilibrium at the start of the catalyst bed). The gas mixture leaving the reaction zone was diluted with argon and the reactor effluent was subsequently expanded to atmospheric pressure.

The gas composition was analysed online on a 6890N Agilent Gas Chromatograph (GC) equipped with a flame ionization detector (FID) interfaced with a PolyArc oxidizer-methanizer reactor (Quantum Analytics, USA). This enabled the detection of all carbon containing compounds, including CO, CO_2, and formaldehyde using an FID. The GC-methanizer-FID was calibrated with a $CO/CO_2/CH_4$ gas mixture as well as liquid mixtures containing oxygenates such as methanol, formaldehyde, formic acid, methoxy methanol and dimethyl-ether to ensure the accurate detection and quantification of these compounds.

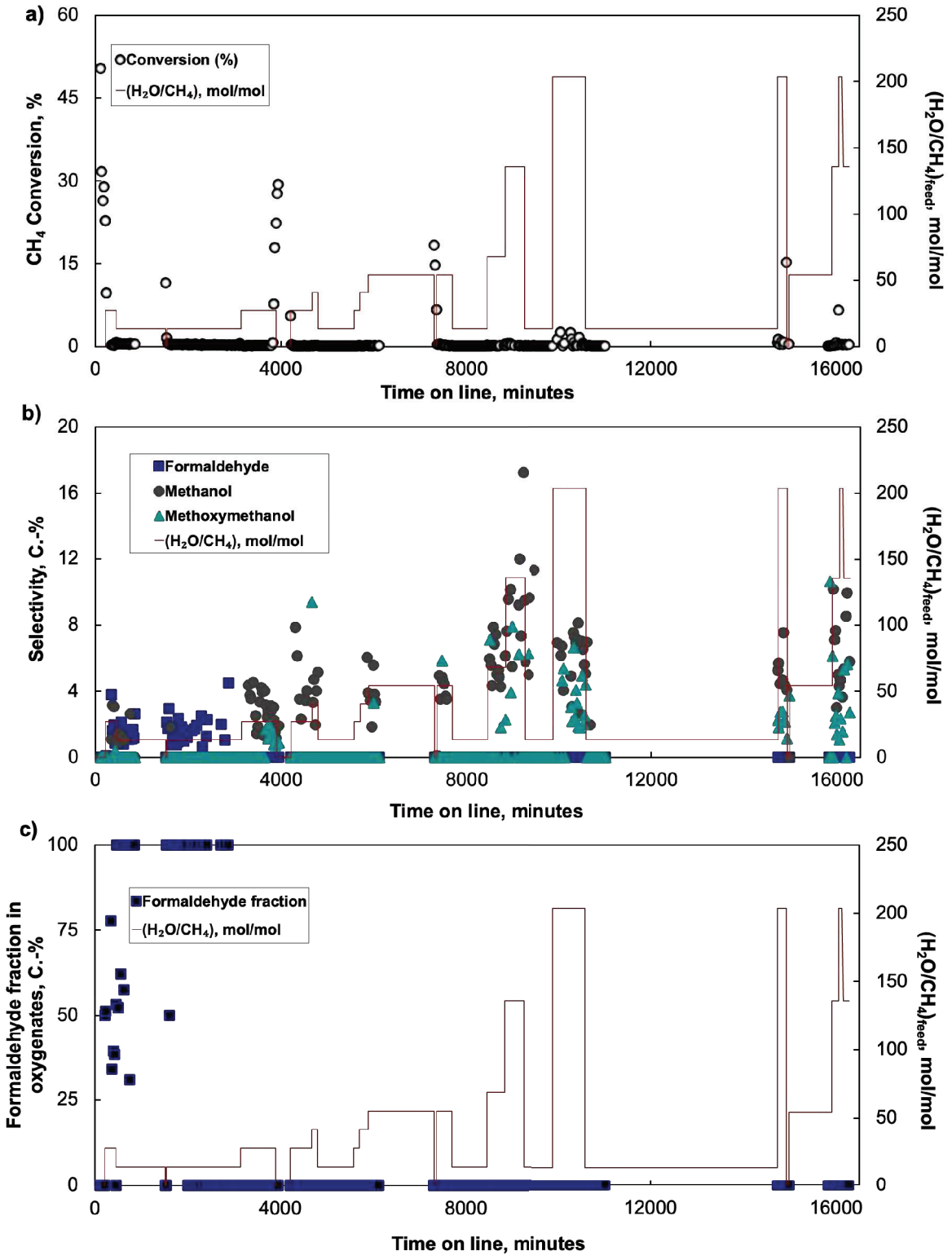

Figure A3.2: Methane conversion (a), oxygenate selectivity (b) and formaldehyde content in the fraction of oxygenates (c) formed over Pt/TiO_2-P25 as a function of time. **Conditions**: T=220°C, p=30 bar, $p_{CH4,inlet}$=0.5 bar, $p_{O2,inlet}$=1.5 bar, space velocity = 3.23 $CH_4/g_{catalyst}/hr$.

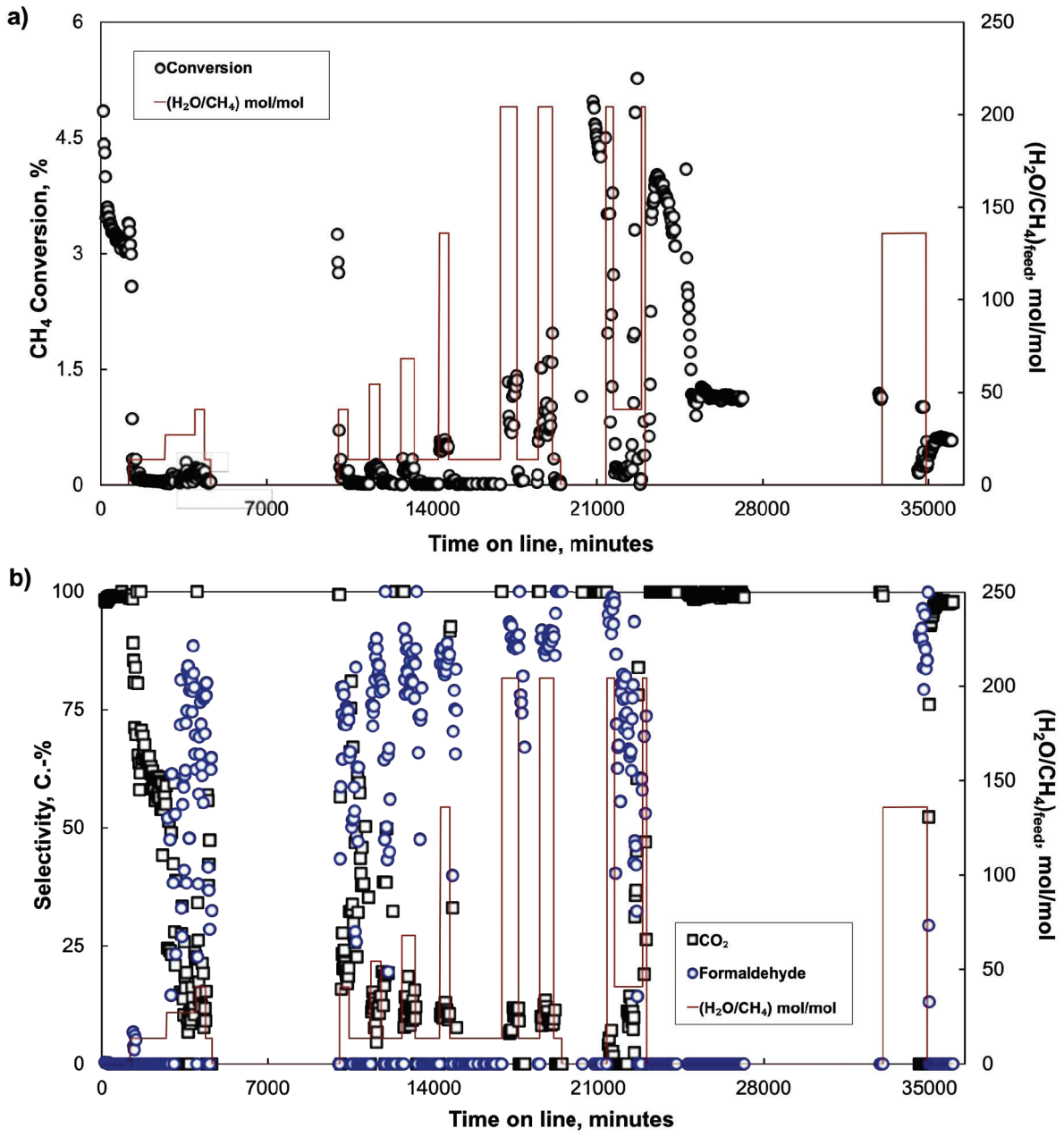

Figure A3.3: Methane conversion (a) and selectivity for the formation of formaldehyde and CO_2 over Pt/TiO_2-Rutile as a function of time. **Conditions**: T=220°C, p=30 bar, $p_{CH4,inlet}$=0.5 bar, $p_{O2,inlet}$=1.5 bar, space velocity = 3.23 $CH_4/g_{catalyst}$/hr.

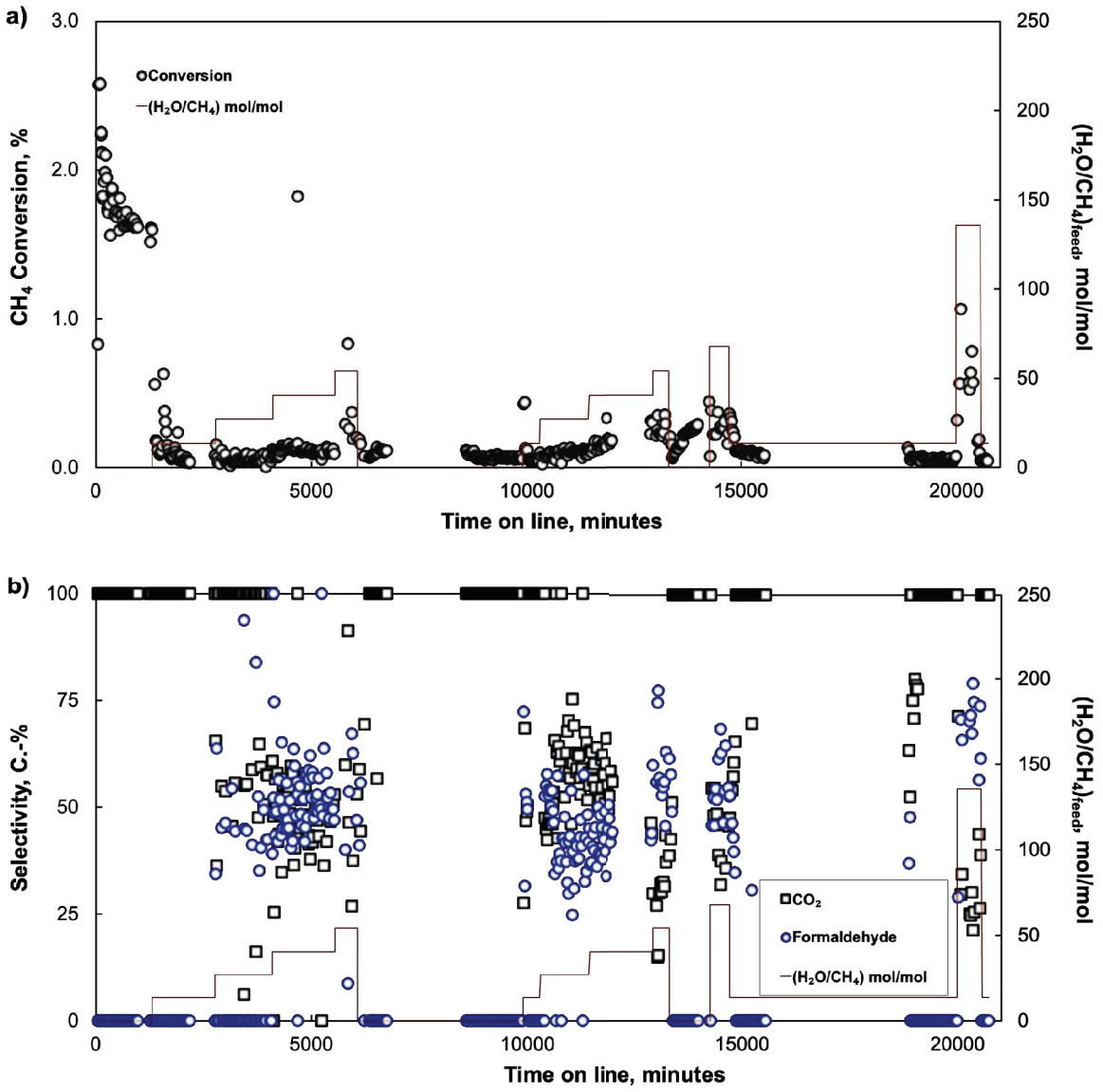

Figure A3.4: Methane conversion (a), and selectivity for the formation of CO_2 and formaldehyde (b) over Pt/Al_2O_3 as a function of time. **Conditions**: T=220°C, p=30 bar, $p_{CH4,inlet}$=0.5 bar, $p_{O2,inlet}$=1.5 bar, space velocity = 3.23 $CH_4/g_{catalyst}$/hr.

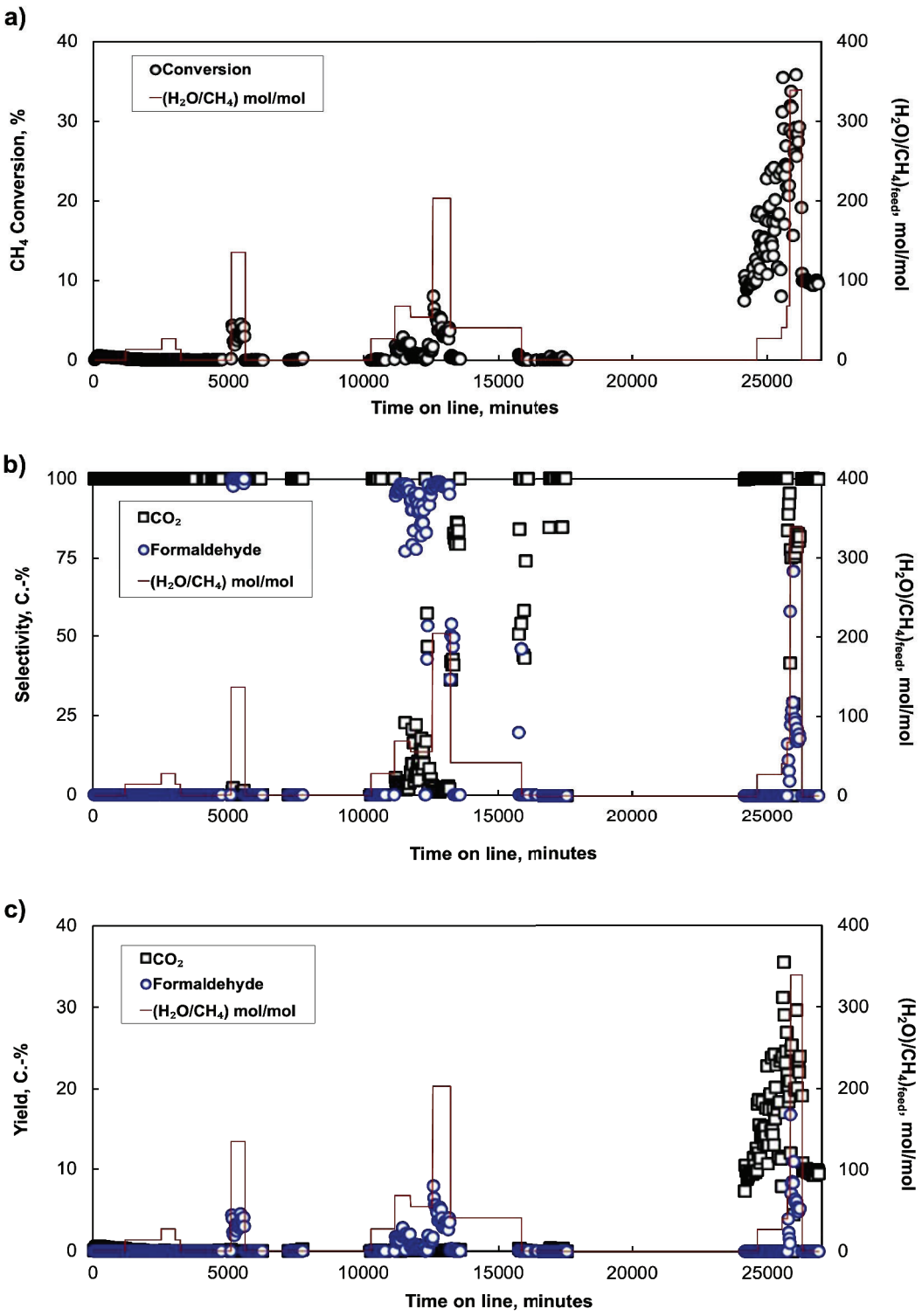

Figure A3.5: Methane conversion (a), selectivity for the formation of formaldehyde and CO_2 (b) and the formaldehyde and CO_2 yield over Pt/C as a function of time. **Conditions**: T=220°C, p=30 bar, $p_{CH4,inlet}$=0.5 bar, $p_{O2,inlet}$=1.5 bar, space velocity = 3.23 $CH_4/g_{catalyst}$/hr.

Table A3.1: Quantity of isopropyl amine adsorbed by the fresh and recovered catalysts during pulse chemisorption

Catalyst	$n_{ads,\ IPA}$, μmol/m^2
Pt/TiO_2-P25-Fresh	6.8
Pt/TiO_2-P25-Used	3.8
Pt/TiO_2-Rutile-Fresh	3.1
Pt/TiO_2-Rutile-Used	1.4
Pt/Al_2O_3-Fresh	7.8
Pt/Al_2O_3-Used	2.8
Pt/C-Fresh	1.2
Pt/C-Used	4.7

Table A3.2: Comparison of the catalytic performance of the Pt/TiO_2-Rutile and Pt/C-catalysts with the activity of systems recently reported in literature

Entry	Catalyst	T, °C	Reactants	X_{CH4}, %	S_{CH2O}	S_{CO2}	Reference
1	Pt/TiO_2-Rutile	220	CH_4, H_2O, O_2	1.0	90	10	This study
2	Pt/C	220	CH_4, H_2O, O_2	4.2	98	2	This study
3	Fe/SiO_2	600	CH_4, H_2O, O_2	2.3	41	13	A1
4	B_2O_3/Al_2O_3	550	CH_4, H_2O, O_2	6.8	46	2.7	A2
5	Co/SiO_2	400	CH_4, H_2O, O_2	-[a]	100	-	A3
6	V-SBA-15	640	CH_4, H_2O[b], O_2	1.5	65	1	A4

[a]Conversion very low, less than 0.01%

[b]Water = 10% in the feed.

Table A3.3: The uptake of H_2 and O_2 by the fresh and recovered catalysts

Catalyst	**H_2-uptake μmol/g**	**O_2-uptake μmol /g**
Pt/TiO_2-P25-F	71	67
Pt/TiO_2-P25-U	67	62
Pt/TiO_2-Rutile-F	62	58
Pt/TiO_2-Rutile-U	62	58
Pt/Al_2O_3-F	89	58
Pt/Al_2O_3-U	9	9
Pt/C-F	107	116
Pt/C-U	45	80

References

[A1] K. Wachi, T. Yabe, T. Suzuki, K. Yanesato, K. Suzuki, K. Yamaguchi, Appl. Catal. B: Environ. 341 (2022) 121420.

[A2] J. Tian, J. Tan, Z.Zhang, P.Han, M. Yin, S. Wan, J. Lin, S. Wang, Y. Wang, Nat. Commun. 11 (2020) 5693.

[A3] J. Ohyama, D. Abe, A. Hirayama, H. Iwai, Y. Tsuchimura, K. Sakamoto, M. Irikura, Y. Nakamura, H. Yoshida, M. Machida, S. Nishimura, T. Yamamoto, S. Matsumura, K. Takahashi, J. Phys. Chem. C 126 (2022) 1785-1792.

[A4] B. Kunkel and S. Wohlrab, Catal. Commun. 155 (2021) 106317.

APPENDIX IV: SUPPLEMENTAL MATERIAL TO CHAPTER VI

Contents:

SECTION I: CATALYST SYNTHESIS

Platinum(II) acetyl acetonate ($Pt(acac)_2$, 97%, Merck), silver nitrate ($AgNO_3$, 99%, Merck), copper(II) acetyl acetonate ($Cu(acac)_2$, 99.9% trace metal basis, Merck) and gold chloride trihydrate ($HAuCl_4 \cdot 3\ H_2O$, 99.9% trace metal basis, Merck) were dissolved in a mixture containing benzyl ether (BE, 98%, Merck), oleylamine (OAm, 70%, Merck) and oleic acid (technical grade, 90%, Merck) in a volumetric ratio of 1.2:1:1 under continuous stirring at 150°C. Thereafter, the resulting mixture was heated to 250°C, followed by the addition of molybdenum hexacarbonyl ($Mo(CO)_6$, 98%, Merck) as a reducing agent, based on a method developed in-house. Reduction with molybdenum hexacarbonyl was found previously to lead to the formation of high-index faceted nanoparticles, and allows for the tailoring of the nanoparticle structure [A1]. The mixture was subsequently cooled, and the nanoparticles were precipitated out with ethanol. The nanoparticles were cleaned with ethanol, then re-dispersed in chloroform. The support was added to the chloroform suspension, sonicated, dried, then successively washed with ethanol. Thereafter, the impregnated support was dried to yield the supported catalyst.

SECTION II: CATALYST CHARACTERISATION

The elemental composition of the supported nanoalloys and the overall metal loading was determined by first digesting the materials in aqua-regia (HCl, HNO_3 and HF) using a Mars 5 microwave digestion unit, followed by analysis by inductively coupled plasma-optical emission spectroscopy (ICP-OES) on a Varian ES 730 spectrometer.

Powder X-ray diffraction (Bruker D8 Advance, Co-Kα radiation: $\lambda = 1.789$ Å, 35 kV, 40mA) was used to determine the phases present in the materials as well as to confirm the formation of alloys. The scans were obtained at 2θ angles ranging from 20° to 120°.

Transmission electron microscopy was also used to determine morphology and sizes of the supported nanoparticles, with High Angular Annular Dark Field (HAADF) imaging and scanning transmission electron microscopy being used to characterise the alloy structure.

High-resolution transmission electron microscopy (HRTEM) images were obtained on a double-aberration corrected JEOL ARM 200F transmission electron microscope operating at 200kV at the Centre for High Resolution Electron Microscopy at the Nelson Mandela University. The samples were first dispersed in ethanol using ultrasonication, then transferred to a holey-carbon copper grids (for non-copper containing samples) and nickel grids. Images were obtained in the high angle annular dark field and bright field analysis modes.

Oxygen chemisorption was used to determine the available active metal surface. The samples were first degassed at 250°C under vacuum overnight and analysed on a Micromeritics ASAP 2020 Chemisorption analyser. The oxygen uptake was measured at 220°C in a pressure range of 0.1-600 mmHg.

Infrared spectroscopy was used to determine the presence of organic deposits on the catalyst. The measurement was performed on a Perkin Elmer Spectrum 100 FTIR Spectrometer in the ATR mode in the range 650-4000 cm^{-1} with a resolution of 1 cm^{-1}.

The Particle-size distribution plots of the as-synthesised nanoparticles are presented in Figure A4.1.

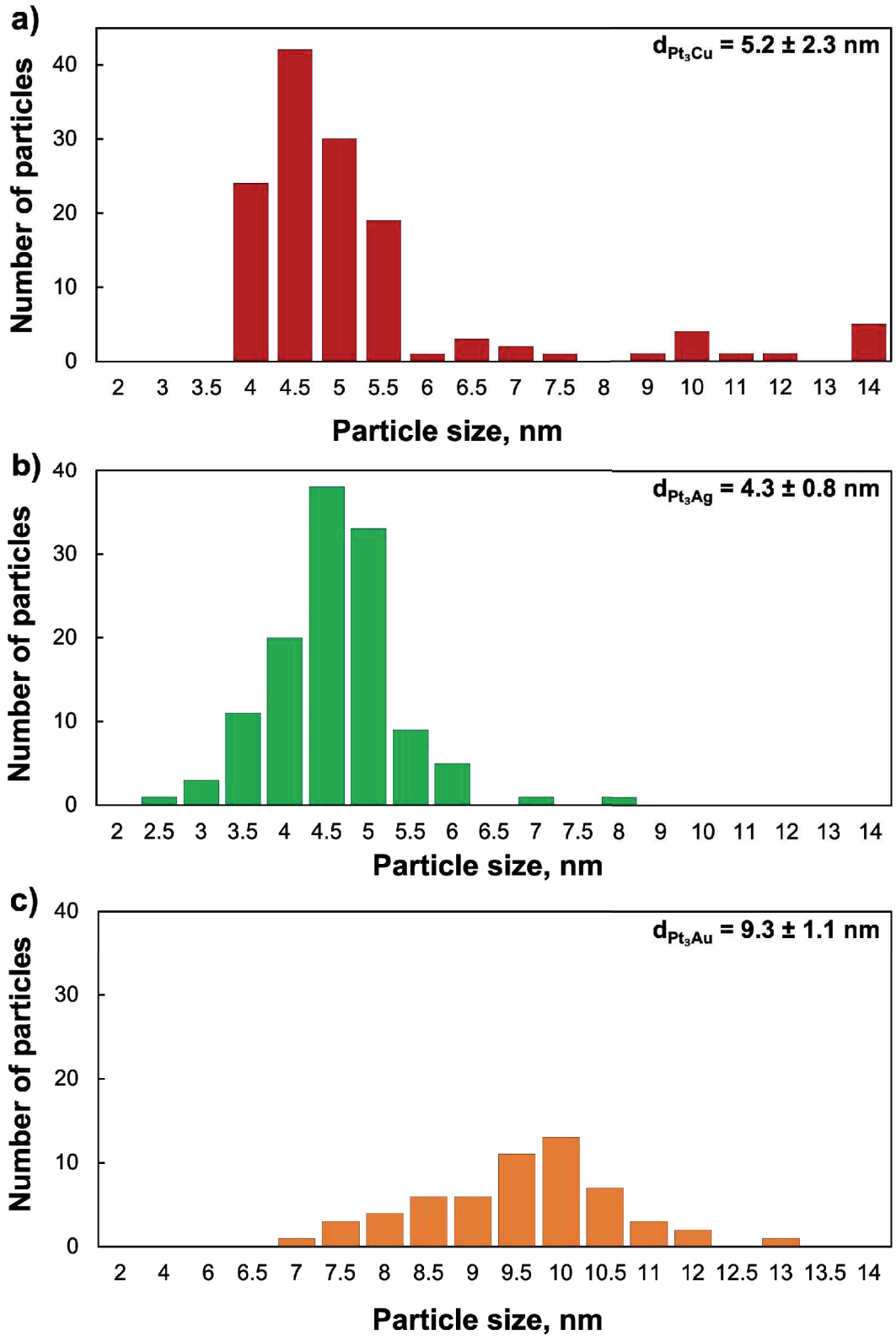

Figure A4.1: Particle size distribution histograms of the unsupported a) Pt_3Cu, b) Pt_3Ag and c) Pt_3Au nanoparticles.

Table A4.1: Lattice parameters and crystalline domain sizes of the annealed, supported nanoparticles as determined from Rietveld refinement

Catalyst	Lattice parameter, nm	Crystalline domain size, nm	X_{Pt}	X_M*
Pt	0.391		1	0
Pt_3Cu/TiO_2	0.391	21	1	0
Pt_3Ag/TiO_2	0.393	8.9	8	2
Pt_3Au/TiO_2	0.394	27	8	2

*Alloying element composition according to Vegard's law

The scanning transmission electron microscopy energy dispersive X-ray spectroscopy (STEM-EDX) scans were obtained for multiple metallic particles over the different alloys in order to establish if there was a size correlation in the metallic compositions of the particles. Over the Pt_3Cu/TiO_2 annealed samples (Fig. A4.2), it was found that the large particles (~ 10 nm) were platinum-enriched, with a Pt:Cu atomic ratio of ca. 4:1, whilst the smaller particles (~5 nm) were relatively copper enriched, with a Pt:Cu ratio of 2:1.

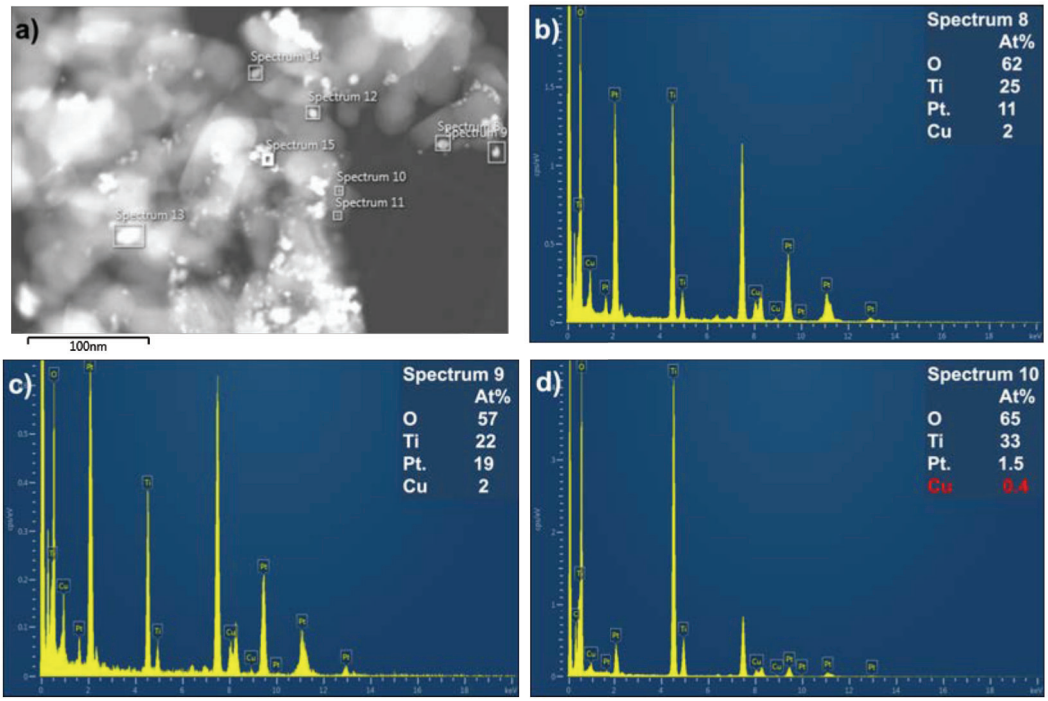

Figure A4.2: a) The dark-field TEM image and corresponding EDX spectra (b-d) of the annealed Pt_3Cu/TiO_2 catalyst.

The STEM-EDX scans of the unannealed and annealed Pt_3Ag/TiO_2 catalyst (Fig. A4.3) show a variation in the Pt:Ag ratio which in this case does not seem to be particle size dependent. However, annealing results in the formation of large platinum-rich clusters, with some large particles having a Pt:Ag ratio of 10:1, and small particles with having a ratio of 4:1.

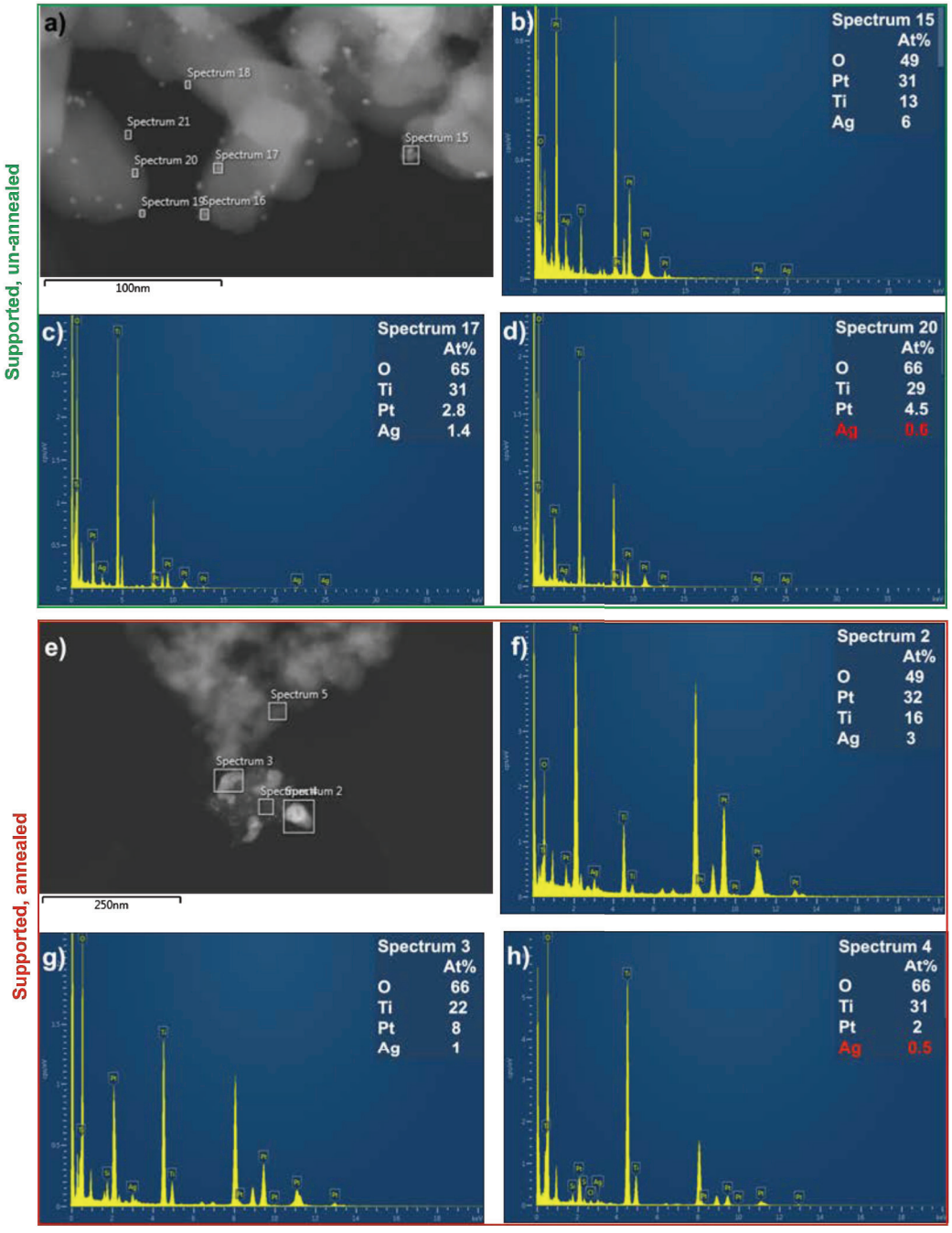

Figure A4.3: The dark-field TEM images of the a) unannealed and e) annealed Pt_3Ag/TiO_2 catalyst and corresponding EDX spectra of the unannealed (b-d) and annealed (f-h) Pt_3Ag/TiO_2 catalyst.

The STEM-EDX scans of the annealed Pt_3Au/TiO_2 catalyst show the variation in the Pt:Au composition to be size dependent, with platinum-enriched large particles (~ 15 nm) (with a Pt:Au ratio of 5:1), and gold enriched small nanoparticles (i.e. Pt:Au ratio of 3:1).

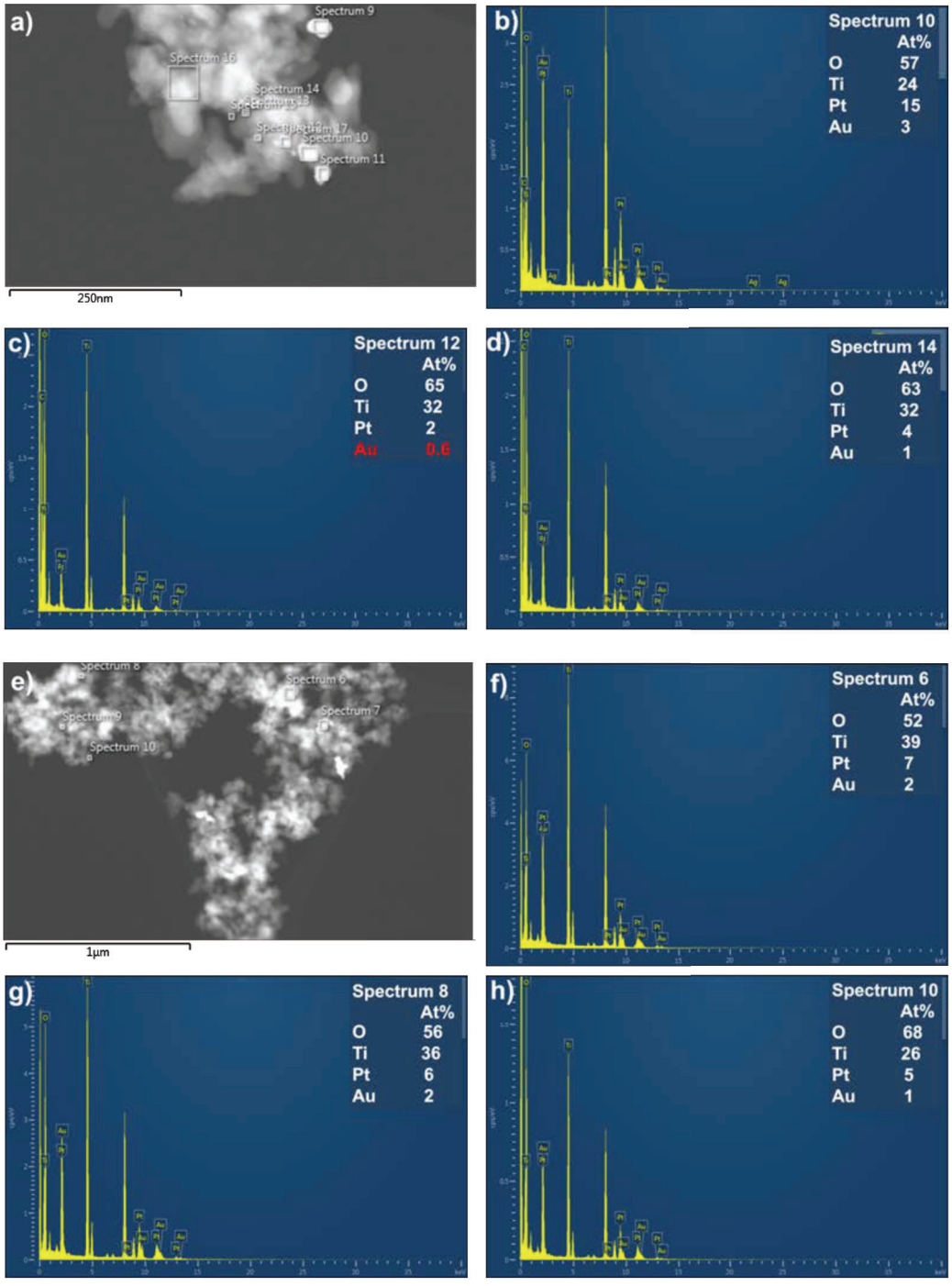

Figure A4.4: The dark-field TEM images of the annealed Pt_3Au/TiO_2 catalyst (a and e) and corresponding EDX spectra of the nanoparticles (b-d) and large clusters (f-h) of the annealed Pt_3Au/TiO_2 catalyst.

SECTION III: CATALYST ACTIVITY TESTS

The catalysts were pelletized and subsequently crushed to a particle size 100-15 μm. A mass of ~0.5g of catalyst was loaded between glass wool plugs in a quartz tube which was placed in a stainless-steel shell. The catalysts were pre-treated by flowing oxygen (16 ml_n/min^{-1}) and He (96 ml_n/min^{-1}) at 350°C overnight. The catalysts were tested for the selective oxidation of methane at 220°C, at a pressure of 20 bar ($p_{O_2,inlet}$ = 1.5 bar, $p_{CH_4,\ inlet}$ = 0.5 bar), co-feeding varying amounts of liquid water (with the highest flow-rate being 0.16 $ml{\cdot}min^{-1}$, which corresponds to 15 bar of water in the gas phase). Helium was used to keep the total gas flow rate through the reactor at 160 ml_n/min.

The pelletized and crushed catalysts were also loaded into the trickle-bed reactor in a quartz tube between quartz wool plugs, then placed in the trickle bed reactor stainless steel casing. The catalysts were pretreated by annealing in a similar fashion to that employed in the fixed bed reactor. The reactor was cooled to 220°C, pressurized to 30 bar with argon, before the reactive gases were introduced. The partial pressures of methane and oxygen were maintained at 0.5 bar and 1.5 bar respectively, while that of helium was varied when water was introduced to keep the methane and oxygen partial pressures constant.

The product analysis was carried online via injection on a 6890N GC equipped with an oxidizer-methaniser reactor, via a 6-way valve (see Appendix 1).

The time on line performance of the Pt nanoparticles (supported on rutile) and the nanoalloy catalysts is presented in Figures A4.5-A4.8.

From the graphs, it can be seen that the selectivity increases with an increase in conversion in the presence of water.

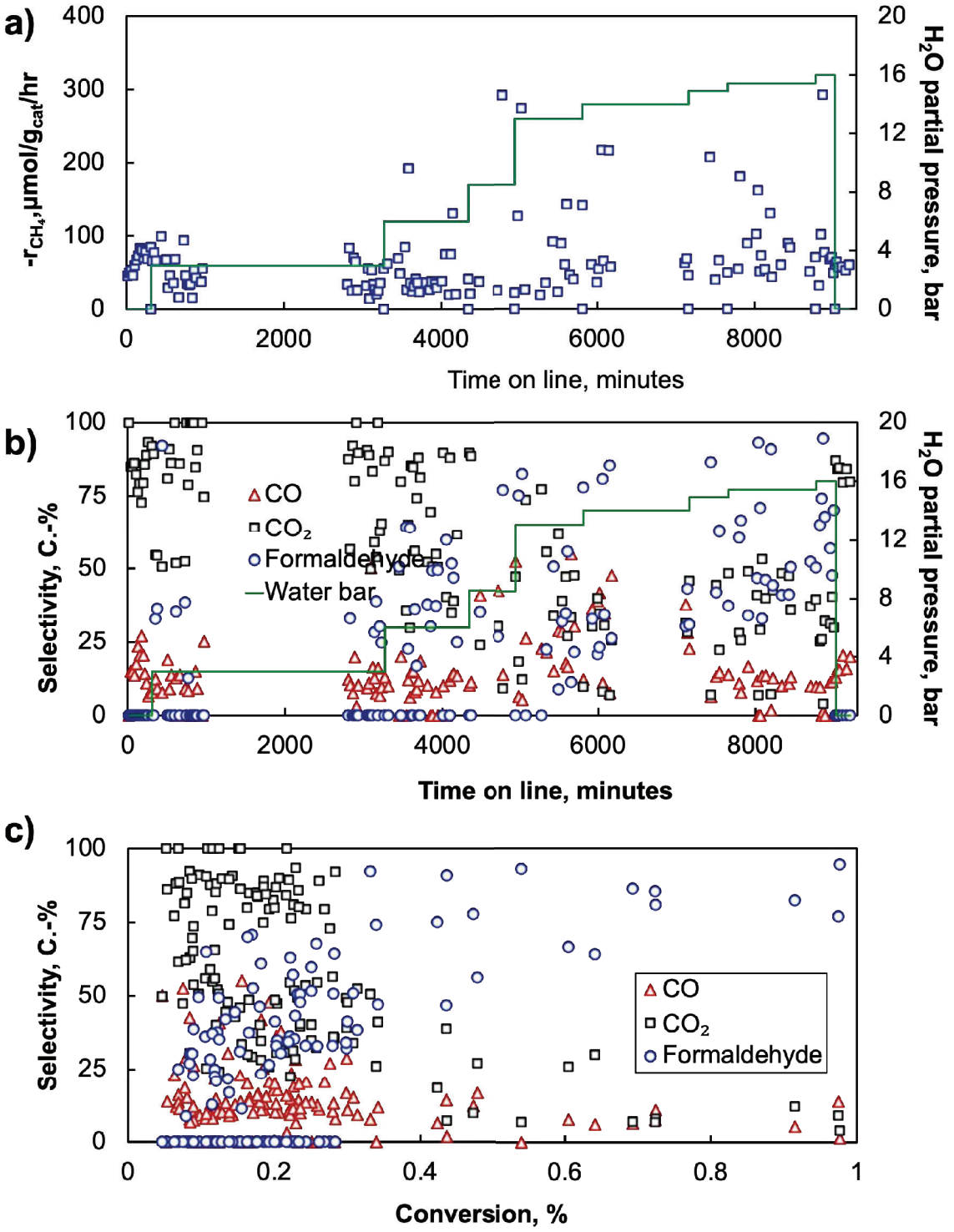

Figure A4.5: The time on line performance of the Pt/TiO_2 catalyst (a), the selectivity towards oxygenates as a function of time (b) and the conversion/selectivity relationship (c).

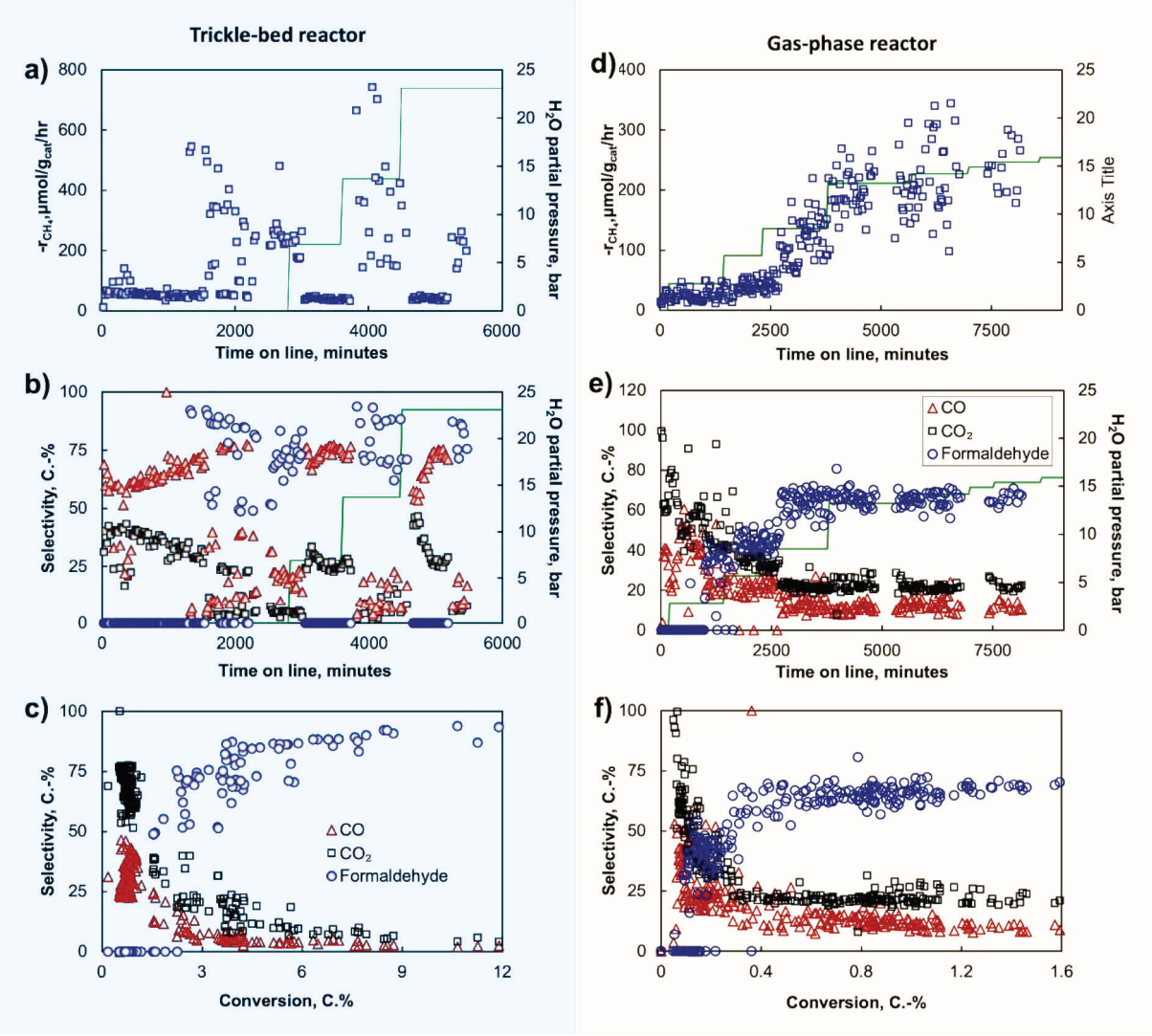

Figure A4.6: The rate of methane conversion (a,d) and oxygenate selectivity (b,e) as a function of time during the selective oxidation of methane over Pt_3Cu/TiO_2 in the trickle-bed reactor (left) and the gas-phase reactor (right). The conversion/selectivity relationship is also plotted (c,f).

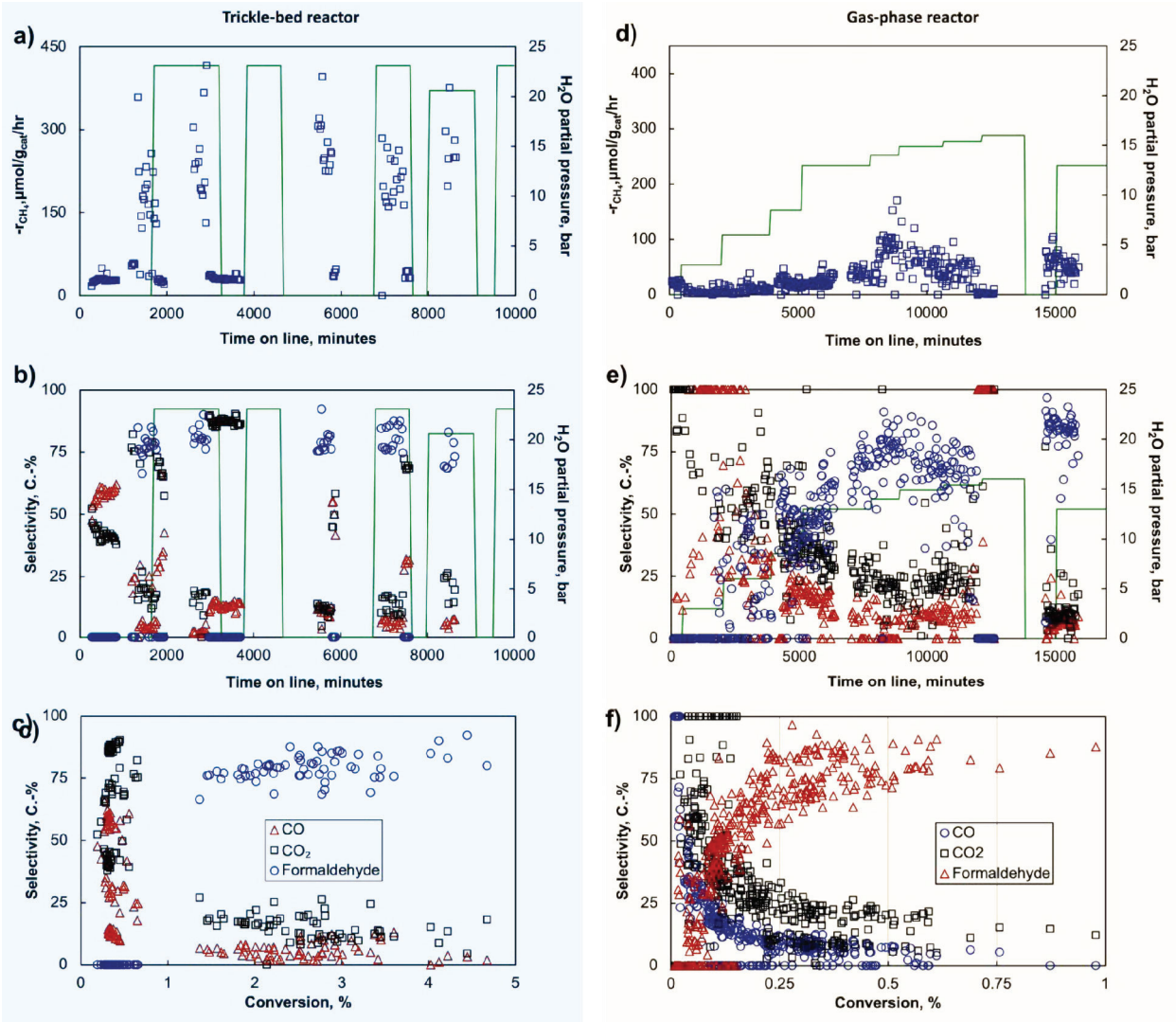

Figure A4.7: The rate of methane conversion (a,d) and oxygenate selectivity (b,e) as a function of time during the selective oxidation of methane over Pt_3Ag/TiO_2 in the trickle-bed reactor (left) and the gas-phase reactor (right). The conversion/selectivity relationship is also plotted (c,f).

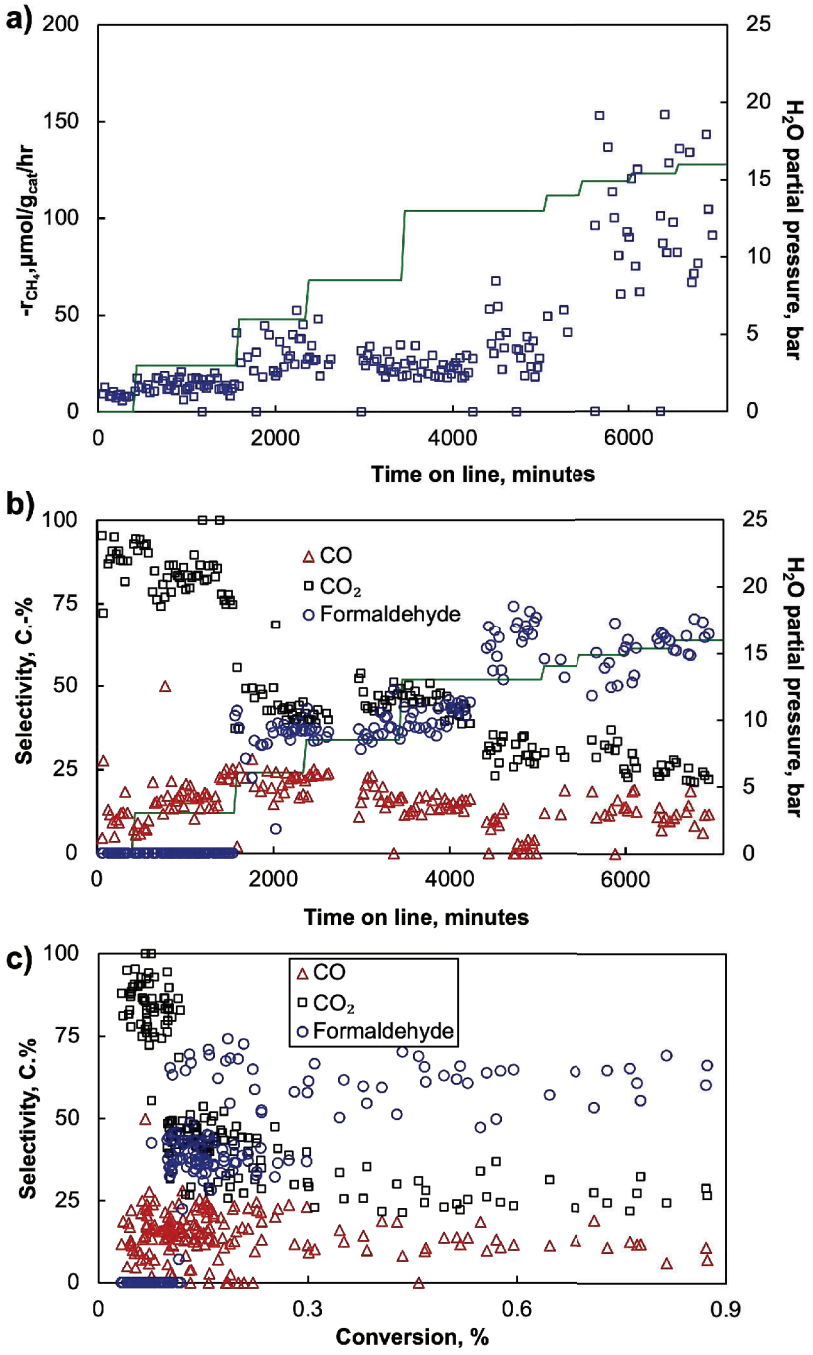

Figure A4.8: The rate of methane conversion as a function of time (a), the selectivity as a function of time (b) over the Pt_3Au/TiO_2 catalyst and the conversion/selectivity relationship. Catalytic testing performed in the gas-phase reactor.

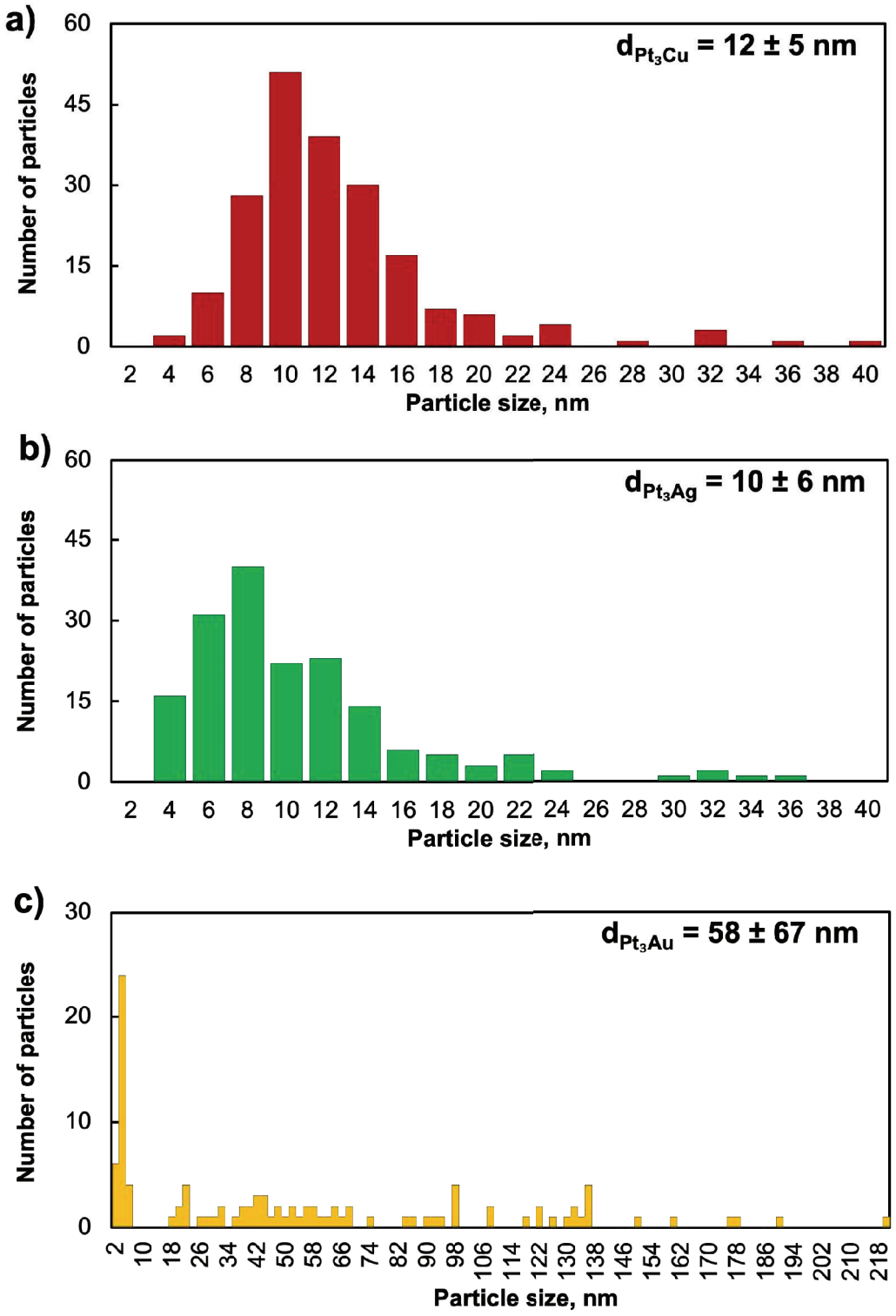

Figure A4.9: Particle size distribution on the recovered a) Pt_3Cu/TiO_2, b) Pt_3Ag/TiO_2 and c) Pt_3Au/TiO_2 catalysts recovered from the gas phase.

The TEM images of the recovered Pt_3Ag/TiO_2 and Pt_3Au/TiO_2 catalysts showed signs of carbon deposition, through the presence of an amorphous material that was not observed for the fresh or the annealed samples. EDX scans of the materials showed it to be carbon based (Fig. A4.5).

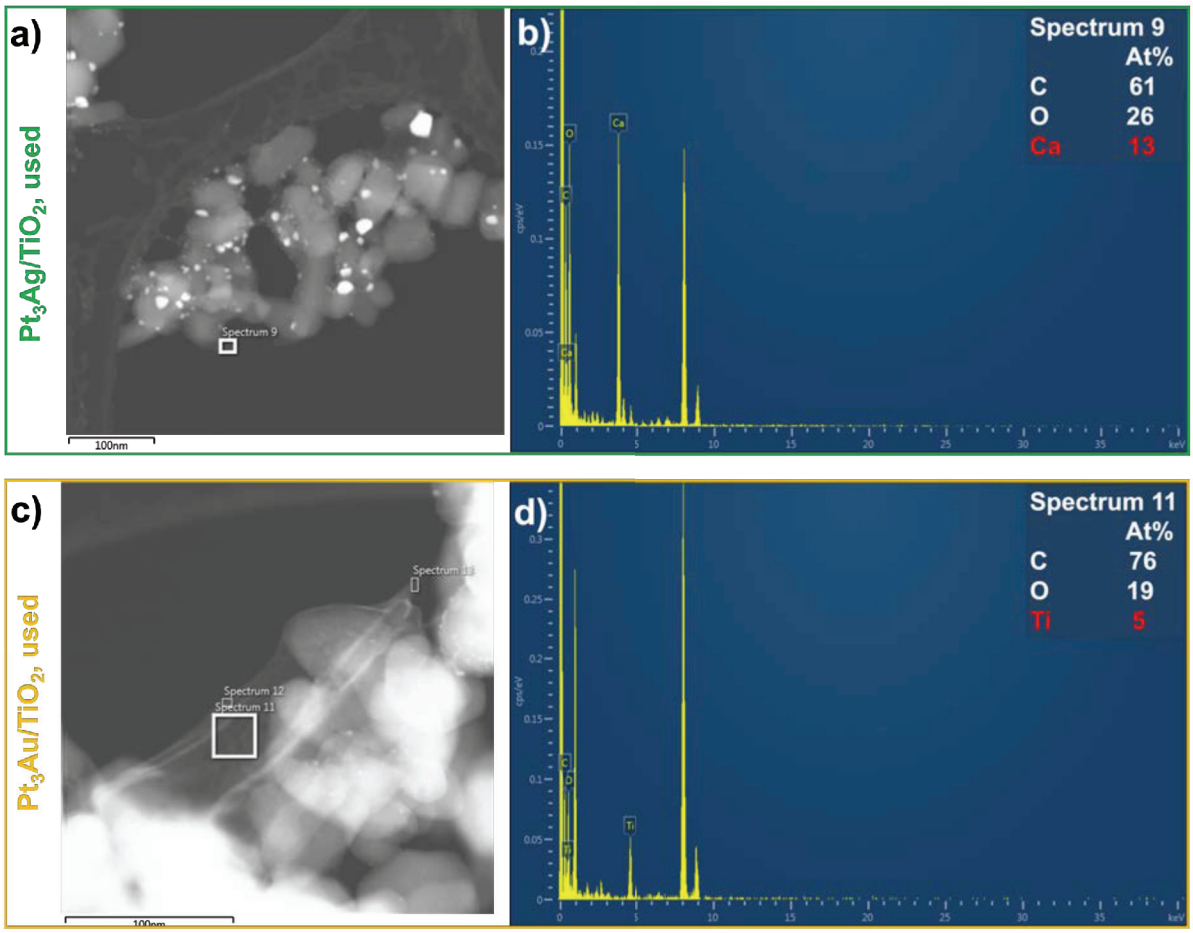

Figure A4.10: Dark field TEM images of the recovered Pt_3Ag/TiO_2 (a) and Pt_3Au/TiO_2 (c) catalysts showing the amorphous material on the catalyst, and corresponding EDX spectra of the amorphous material on the recovered Pt_3Ag/TiO_2 (b) and Pt_3Au/TiO_2 (d) catalysts.

Elemental analysis was also performed on the recovered catalysts in order to ensure that the alloys were stable against leaching. The elemental compositions of the recovered catalysts are presented in Table A4.1.

Table A3.2: The metal weight loading on the titania support, and corresponding molar compositions of the Pt and M components on the Pt_3M alloys

Catalyst	Pt (wt.%)	M (wt.%)	Pt (μmoles)	M (μmoles)	Pt:M (mole ratio)	Lattice parameter, nm
Pt_3Cu (F)	7.0	0.68	18.77	5.60	3.4 : 1	0.382
Pt_3Cu (R)	7.1	0.75	17.87	5.80	3.1 : 1	0.391
Pt_3Ag (F)	7.7	1.8	19.97	8.44	2.4 : 1	0.399
Pt_3Ag (R)	7.9	1.7	20.24	7.88	2.6 : 1	0.393
Pt_3Au (F)	7.3	0.66	19.24	1.74	11.2 : 1*	0.394
Pt_3Au (R)	7.0	0.93	18.01	2.37	7.4 : 1	0.394

*Error in analysis

The bright-field transmission electron microscope images of the fresh and recovered Pt/TiO_2 catalyst (Fig. A4.7 a and b) show well-dispersed platinum nanoparticles in the particle size range of 4.5 to 8 nm for the fresh catalyst, and 4-10 nm on the recovered catalyst, indicating minor sintering that may have occurred during the catalytic pre-treatment. The powder XRD pattern of the recovered catalyst shows an increase in the crystalline character of the supported platinum. The ATR-IR spectrum of the fresh, unannealed catalyst shows two bands at c. 1500 cm^{-1} which correspond to the surfactant used during the synthesis of the platinum nanoparticles. This bands are absent on the recovered catalyst spectrum, which shows the appearance of new bands at 1030 and 1220 cm^{-1}. These bands have been identified as the C-O-C stretching vibrations (former) and CH_2 rocking transitions (latter) [A2].

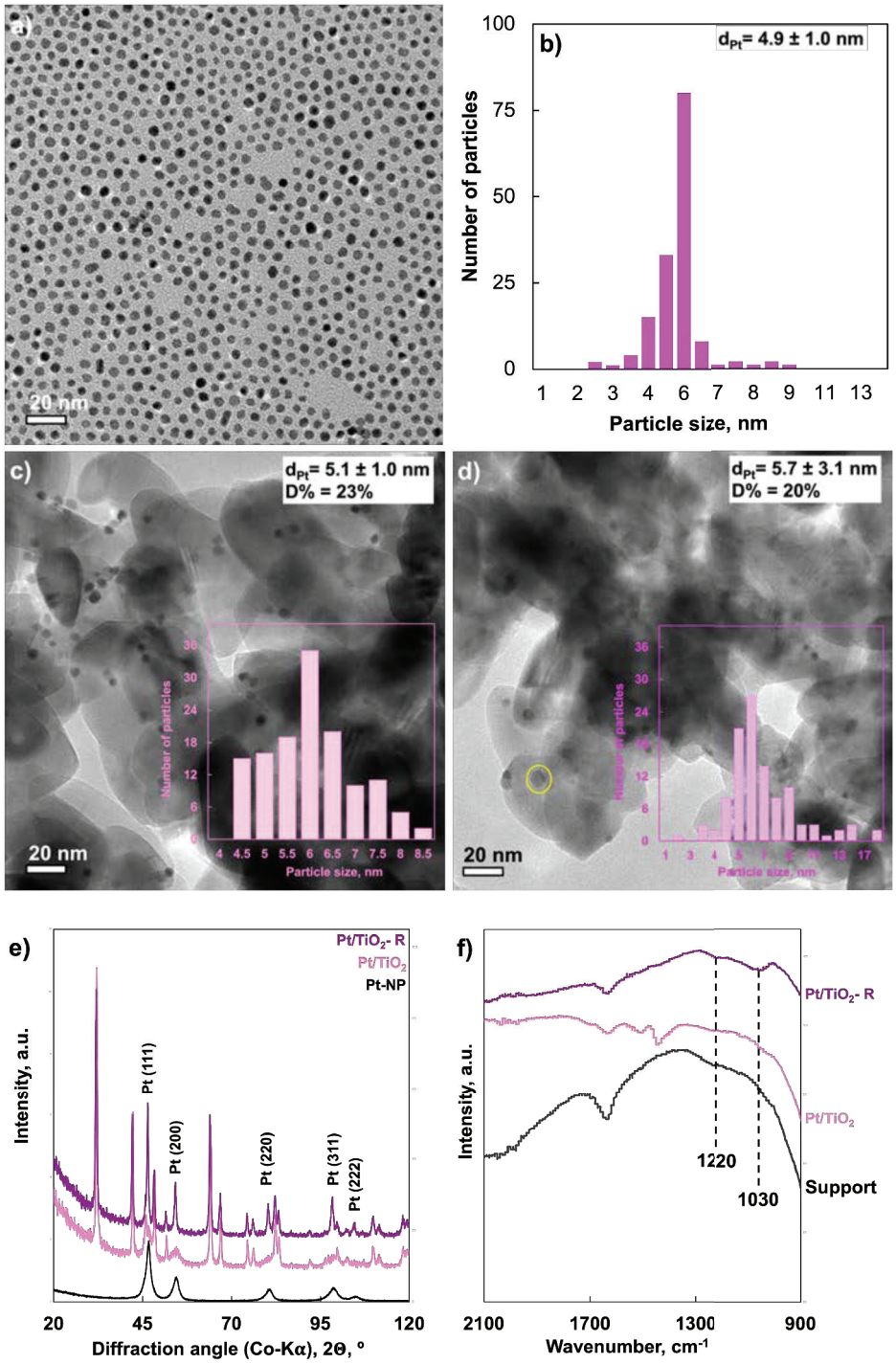

Figure A4.11: a) Bright-field TEM image of the unsupported, b) particle size distribution of the unsupported Pt nanoparticles, c) the bright-field TEM image of the supported, unannealed Pt nanoparticles on titania support, d) the bright field TEM image of the recovered catalyst, e) the powder XRD patterns of the unsupported nanoparticles and the unannealed and recovered catalyst and f) the FTIR spectra of the rutile support, the unannealed and the recovered Pt/TiO_2 catalyst.

SECTION V: CATALYST DEACTIVATION

The stability of the Pt_3Ag/TiO_2 catalyst was evaluated by returning to baseline operating conditions, where the flow of water into the reactor was stopped in order to assess the activity of the catalyst after the introduction of water, and to ascertain that water did not leads to catalyst deactivation. This was done in both the gas-phase reactor and the trickle bed reactor. The catalyst in the gas phase reactor showed signs of deactivation, and time on stream experiments in the absence of water (after the catalyst was exposed to water) show the decline in catalytic activity (Fig. AE.6a). This corresponds to a 93% activity loss with time. The catalyst appears more stable in the trickle-bed reactor (Fig. A4.8b).

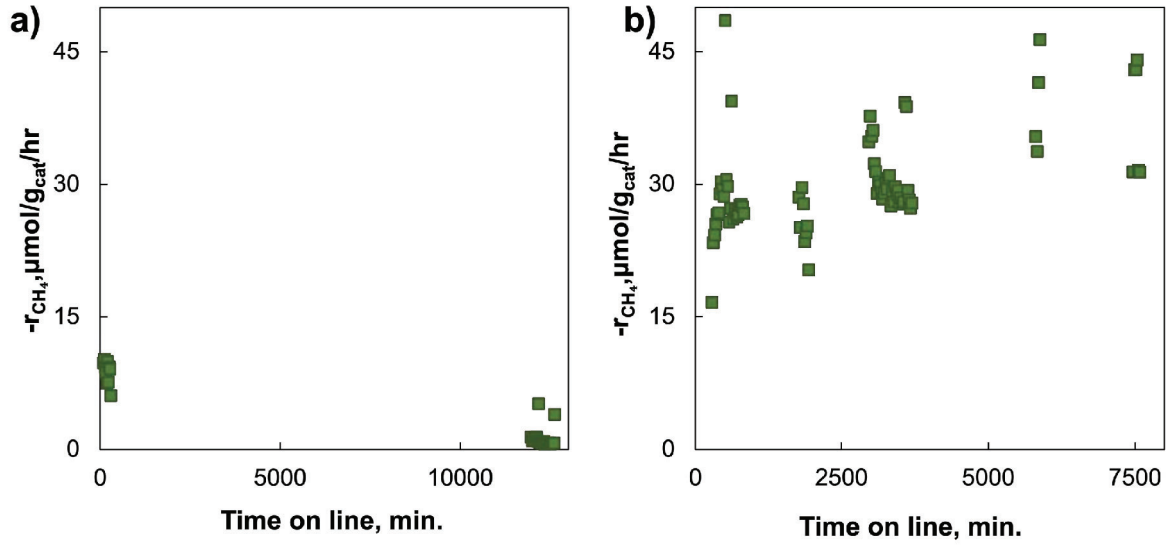

Figure A4.12: Time on line performance of Pt_3Ag/TiO_2 in a) the fixed bed reactor (at 20 bar) and b) trickle-bed reactor (at 30 bar), in the absence of water (p_{CH_4} = 0.5 bar, p_{O_2} = 1.5 bar, 220°C).

References

[A1] G. M. Leteba, D. R. Mitchell, P. B. J. Leveque, E. van Steen, C. I. Lang, Nanomaterials 11 (2021) 1825.

[A2] T. Kecskés, J. Raskó, J. Kiss, Appl.Catal. A: Gen. 273 (2004) 55-62.

CONFERENCE CONTRIBUTIONS

ORAL PRESENTATION

2023

1. Breaking the selectivity-conversion shackles in the platinum catalysed methane oxidation to formaldehyde

S.V.L. Mahlaba, N. Hytoolakhan Lal Mahomed, J. Guo, G.M. Leteba, A. Govender and E. van Steen

28th North American Meeting of the North American Catalysis Society (NAM)

Rhode Island Convention Center, Providence, Rhode Island, United States of America

POSTER PRESENTATIONS

2022

1. Enhanced activity in the aerobic, selective oxidation of methane over Pt-based nanoalloy catalysts

   S.V.L. Mahlaba, J. Guo, G. Leteba, E.J. Olivier and E. van Steen

   27th North American Meeting of the North American Catalysis Society

   New York Hilton Midtown, New York City, New York, United States of America

2. Highly selective oxidation of methane to formaldehyde over platinum

   E. van Steen, S.V.L. Mahlaba, N. Hytoolakhan Lal Mahomed, J. Guo, G.M. Leteba, and P.L. Cilliers

   27th North American Meeting of the North American Catalysis Society

   New York Hilton Midtown, New York City, New York, United States of America

3. In support of selective methane oxidation: Support effects on the activity and product selectivity during the aerobic, water-assisted oxidation of methane

   S.V.L. Mahlaba, N. Hytoolakhan Lal Mahomed, J. Guo, G.M. Leteba, A. Govender and E. van Steen

   32nd Annual meeting of the Catalysis Society of South Africa (CATSA)

   Champagne Sports Resort, Drakensberg, South Africa

LIST OF PUBLICATIONS/OUTPUTS

1. PUBLICATIONS

1.1. **Mahlaba SVL,** Hytoolakhan Lal Mahomed N, Guo J, Govender A, Leteba GM, Cilliers PL, van Steen E "Platinum-catalysed selective aerobic oxidation of methane to formaldehyde in the presence of liquid water", *Angewandte Chemie International Edition*. 2022 Sept Vol. 62 No. 38, pe202206841.*

1.2. Van Steen E, Guo J, Hytoolakhan Lal Mahomed N, Leteba GM, **Mahlaba SVL** "Selective, aerobic oxidation of methane to formaldehyde over platinum-a review", *ChemCatChem*. 2023 April Vol. 15 No. 8 e202201238.*

1.3. **Mahlaba SVL**, Hytoolakhan Lal Mahomed N, Leteba GM, Govender A, van Steen E "Role of the support in the selective, aerobic methane oxidation to formaldehyde over Pt/TiO_2" (Submitted to ACS Catalysis, accepted).*